

Turkish Journal of

Analytical Chemistry

Volume 5

Issue 2

December 2023

<https://dergipark.org.tr/tr/pub/turkjac>

Turkish Journal of
**Analytical
Chemistry**
TurkJAC

Volume 5
Issue 2
December 2023

Publication Type: Peer-reviewed scientific journal

Publication Date: December 29, 2023

Publication Language: English

Published two times in a year (June, December)

Owner

Prof. Miraç Ocak

Karadeniz Technical University, Faculty of Sciences, Department of Chemistry

Executive Editor

Prof. Ümmühan Ocak

Karadeniz Technical University, Faculty of Sciences, Department of Chemistry

Co-Editor

Ender Çekirge

Karadeniz Technical University, Institute of Forensic Sciences

Layout Editor

Ender Çekirge

Karadeniz Technical University, Institute of Forensic Sciences

Editorial Secretary

Ender Çekirge

Karadeniz Technical University, Institute of Forensic Sciences

Language Editors

Nurhayat Özbek

Karadeniz Technical University, Faculty of Sciences, Department of Chemistry

Prof. Miraç Ocak

Karadeniz Technical University, Faculty of Sciences, Department of Chemistry

Copyeditor

Nurhayat Özbek

Karadeniz Technical University, Faculty of Sciences, Department of Chemistry

Aslıhan Yılmaz Çamoğlu

Karadeniz Technical University, Faculty of Sciences, Department of Chemistry

Prof. Miraç Ocak

Karadeniz Technical University, Faculty of Sciences, Department of Chemistry

Proofreader

Nurhayat Özbek

Karadeniz Technical University, Faculty of Sciences, Department of Chemistry

Editors

Prof. Ümmühan Ocak

Karadeniz Technical University, Faculty of Sciences, Department of Chemistry

Prof. Miraç Ocak

Karadeniz Technical University, Faculty of Sciences, Department of Chemistry

Prof. Selehattin Yılmaz	Çanakkale Onsekiz Mart University, Faculty of Science and Literature, Department of Chemistry
Prof. Ali Gündoğdu	Karadeniz Technical University, Maçka Vocational School, Department of Pharmacy Services

Section Editors

Prof. Salih Zeki Yıldız	Sakarya University, Faculty of Science and Literature, Department of Chemistry
Prof. Hüseyin Şahin	Giresun University Espiye Vocational School, Department of Property Protection and Security
Asst. Prof. Bülent Akar	Gümüşhane University, Faculty of Engineering and Natural Sciences, Department Of Food Engineering

Editor Board

Prof. Selehattin Yılmaz	Çanakkale Onsekiz Mart University, Faculty of Science and Literature, Department of Chemistry
Prof. Celal Duran	Karadeniz Technical University, Faculty of Sciences, Department of Chemistry
Prof. Hakan Alp	Karadeniz Technical University, Faculty of Sciences, Department of Chemistry
Prof. Volkan Numan Bulut	Karadeniz Technical University, Maçka Vocational School, Department of Chemistry and Chemical Processing Technologies
Prof. Ali Gündoğdu	Karadeniz Technical University, Maçka Vocational School, Department of Pharmacy Services
Asst. Prof. Aysel Başoğlu	Gümüşhane University, Faculty of Health Sciences, Department of Occupational Health and Safety
Prof. Ayşegül İyidoğan	Gaziantep University, Faculty of Science and Literature, Department of Chemistry
Prof. Sevgi Kolaylı	Karadeniz Technical University, Faculty of Sciences, Department of Chemistry
Prof. Hüseyin Serencam	Trabzon University, College of Applied Sciences, Department of Gastronomy and culinary arts
Assoc. Prof. Fatma Ağin	Karadeniz Technical University, Faculty of Pharmacy, Department of Basic Pharmaceutical Sciences
Prof. Duygu Özdeş	Gümüşhane University, Gümüşhane Vocational School, Department of Chemistry and Chemical Processing Technologies
Dr. Mustafa Z. Özel	University of York, Department of Chemistry

Prof. Małgorzata Wiśniewska	University of Maria Curie- Sklodowska, Faculty of Chemistry, Institute of Chemical Sciences, Department of Radiochemistry and Environmental Chemistry
Prof. Dilek Kul	Karadeniz Technical University, Faculty of Pharmacy, Department of Basic Pharmaceutical Sciences
Prof. Sławomira Skrzypek	University of Lodz, Faculty of Chemistry, Department of Inorganic and Analytical Chemistry
Prof. Fatih İslamoğlu	Recep Tayyip Erdoğan University, Faculty of Science and Literature, Department of Chemistry
Asst. Prof. Zekeriyya Bahadır	Giresun University, Faculty of Science and Literature, Department of Chemistry
Asst. Prof. Yasemin Çağlar	Giresun University, Faculty of Engineering, Department of Genetic and Bioengineering
Prof. Agnieszka Nosal-Wiercińska	University of Maria Curie- Sklodowska, Faculty of Chemistry, Institute of Chemical Sciences, Department of Analytical Chemistry
Assoc. Prof. Dr. Halit Arslan	Gazi University, Faculty of Science, Department of Chemistry
Assoc. Prof. Cemalettin Baltacı	Gümüşhane University, Faculty of Engineering and Natural Sciences, Department of Food Engineering
Asst. Prof. Zafer Ocak	Kafkas University, Education Faculty, Mathematics and Science Education
Prof. Mustafa İmamoğlu	Sakarya Univer.sity, Faculty of Science and Literature, Department of Chemistry
Assoc. Prof. Esra Bağda	Sivas Cumhuriyet University, Faculty of Pharmacy, Department of Basic Pharmaceutical Sciences, Analytical Chemistry Division
Assoc. Prof. Hüseyin Altundağ	Sakarya University, Faculty of Science and Literature, Department of Chemistry
Asst. Prof. Mehmet Başoğlu	Gümüşhane University, Faculty of Engineering and Natural Sciences, Department of Energy Systems Engineering

Publishing Board

Prof. Latif Elçi	Pamukkale University, Faculty of Science and Literature, Department of Chemistry
Prof. Münevver Sökmen	Konya Food and Agriculture University, Faculty of Engineering and Architecture, Department of Bioengineering
Prof. Atalay Sökmen	Konya Food and Agriculture University, Faculty of Engineering and Architecture, Department of Bioengineering
Prof. Kamil Kaygusuz	Karadeniz Technical University, Faculty of Sciences, Department of Chemistry
Prof. Yaşar Gök	Pamukkale University, Faculty of Science and Literature, Department of Chemistry

Prof. Ayşegül Gölcü	İstanbul Technical University, Faculty of Science and Literature, Department of Chemistry
Prof. Mustafa Tüzen	Gaziosmanpaşa University, Faculty of Science and Literature, Department of Chemistry
Prof. Mustafa Soylak	Erciyes University, Faculty of Sciences, Department of Chemistry
Prof. Fikret Karadeniz	Kafkas University, Faculty of Science and Literature, Department of Chemistry
Prof. Mehmet Yaman	Fırat University, Faculty of Sciences, Department of Chemistry
Prof. Halit Kantekin	Karadeniz Technical University, Faculty of Sciences, Department of Chemistry
Prof. Esin Canel	Ankara University, Faculty of Sciences, Department of Chemistry
Prof. Dilek Ak	Anadolu University, Faculty of Pharmacy, Department of Basic Pharmaceutical Sciences
Prof. Mustafa Küçükislamoğlu	Sakarya University, Faculty of Science and Literature, Department of Chemistry
Prof. Salih Zeki Yıldız	Sakarya University, Faculty of Science and Literature, Department of Chemistry
Prof. Recai İnam	Gazi University, Faculty of Sciences, Department of Chemistry
Prof. Dr. Durişehvar Ünal	İstanbul University, Faculty of Pharmacy, Department of Basic Pharmaceutical Sciences
Prof. Mehmet Tüfekçi	Avrasya University, Faculty of Science and Literature, Department of Biochemistry
Prof. Hüseyin Kara	Selçuk University, Faculty of Sciences, Department of Chemistry
Prof. Sezgin Bakirdere	Yıldız Technical University, Faculty of Science and Literature, Department of Chemistry
Prof. Hasan Basri Şentürk	Karadeniz Technical University, Faculty of Sciences, Department of Chemistry
Prof. Yusuf Atalay	Sakarya University, Faculty of Science and Literature, Department of Physics
Prof. Salih Zeki Yıldız	Sakarya University, Faculty of Science and Literature, Department of Chemistry

Authorship, Originality, and Plagiarism: The authors accept that the work is completely original and that the works of others have been appropriately cited or quoted in the text with the necessary permissions. The authors should avoid plagiarism. It is recommended that they check the article using appropriate software such as Ithenticate and CrossCheck. The responsibility for this matter rests entirely with the authors. All authors will be notified when the manuscript is submitted. If a change of author is needed, the reason for the change should be indicated. Once the manuscript is accepted, no author changes can be made.

Aims and Scope

“Turkish Journal of Analytical Chemistry” publishes original full-text research articles and reviews covering a variety of topics in analytical chemistry. Original research articles may be improved versions of known analytical methods. However, studies involving new and innovative methods are preferred. Topics covered include:

- Analytical materials
- Atomic methods
- Biochemical methods
- Chromatographic methods
- Electrochemical methods
- Environmental analysis
- Food analysis
- Forensic analysis
- Optical methods
- Pharmaceutical analysis
- Plant analysis
- Theoretical calculations
- Nanostructures for analytical purposes
- Chemometric methods
- Energy

ETHICAL GUIDELINES

TurkJAC follows ethical tasks and responsibilities are defined by the Committee on Publication Ethics (COPE) in publication procedure. Based on this guide, the rules regarding publication ethics are presented in the following sections.

Ethical Approval

Ethics committee approval must be obtained for studies on clinical and experimental regarding human and animals that require an ethical committee decision, this approval must be stated in the article and documented in the submission. In such articles, the statement that research and publication ethics are complied with should include. Information about the approval such as committee name, date, and number should be included in the method section and also on the first/last page of the article.

Editors

1. In the preliminary evaluation of a submission, the editor of the journal evaluates the article's suitability for the purpose and scope of the journal, whether it is similar to other articles in the literature, and whether it meets the expectations regarding the language of writing. When it meets the mentioned criteria, the scientific evaluation process is started by assigning a section editor if necessary.
2. A peer-reviewed publication policy is employed in all original studies, taking into full account of possible problems due to related or conflicting interests.

3. Section editors work on the articles with a specific subject and their suggestion is effective in the journal editor's decision about acceptance or rejection of the article.
4. No section editor contacts anyone except the authors, reviewers, and the journal editor about articles in the continued evaluation process.
5. In the journal editor's decision to accept or reject an article, in the addition of section editor's suggestion in consequence of scientific reviewing, the importance of the article, clarity and originality are decisive. The final decision, in this case, belongs to the journal editor.

Authors

1. The authors should actively contribute to the design and execution of the work. Authorship should not be given to a person who does not have at least one specific task in the study.
2. Normally all authors are responsible for the content of the article. However, in interdisciplinary studies with many authors, the part that each author is responsible for should be explained in the cover letter.
3. Before the start of the study, it would be better to determine the authors, contributors, and who will be acknowledged in order to avoid conflict in academic credits.
4. The corresponding author is one of the authors of the article submitted to the journal for publication. All communications will be conducted with this person until the publication of the article. The copyright form will be signed by the corresponding author on all the authors' behalf.
5. It is unacceptable to submit an article that has already been published entirely or partly in other publication media. In such situation, the responsibility lies with all authors. It is also unacceptable that the same article has been sent to TurkJAC and another journal simultaneously for publication. Authors should pay attention to this situation in terms of publication ethics.
6. Plagiarism from others' publications or their own publications and slicing of the same study is not acceptable.
7. All authors agree that the data presented in the article are real and original. In case of an error in the data presented, the authors have to be involved in the withdraw and correction process.
8. All authors must contribute to the peer-reviewed procedure.

Reviewers

1. Peer reviewers worked voluntarily are external experts assigned by editors to improve the submitted article.
2. It is extremely important that the referee performs the review on time so that the process does not prolong. Therefore, when the invitation is agreed upon, the reviewer is expected to do this on time. Also, the reviewer agrees that there are no conflicts of interest regarding the research, the authors, and/or the research funders.
3. Reviewers are expected not to share the articles reviewed with other people. The review process should be done securely.
4. Reviewers are scored according to criteria such as responding to the invitations, whether their evaluations are comprehensive and acting in accordance with deadlines, and the article submissions that they can make to TurkJAC are handled with priority.



Contents

Research Articles

- 1 – The effects of mechanical activation on corrosion resistance of cordierite ceramics **83–88**
Can Serkan Keskin, Ceren Ayna Çakır, Hüseyin Altundağ, Nil Toplan, Hüseyin Özkan Toplan*
- 2 – A green liquid chromatographic method using ethanol in mobile phase for the determination of nimesulide and naproxen in gel formulations **89–97**
Sercan Yıldırım
- 3 – Electrochemical properties of non-peripherally and peripherally tetra-[(1-benzylpiperidin-4-yl)oxy] substituted phthalocyanines **98–106**
Asiye Nas, Gülsev Dilber, Zekeriya Biyiklioglu*
- 4 – Adsorption of hexavalent chromium from aqueous solution onto corn cobs – activated carbon **107–117**
*Pinar Bozbeyoglu, Ali Gundogdu**
- 5 – Green synthesis and structural characterization of ZnO nanoparticles and ZnO@TiO₂ nanocomposites by *Cinnamomum verum* bark extract **118–123**
*Gökçenur Selva Keleşoğlu, Mesut Özdiñcer, Aslıhan Dalmaz, Kübra Zenkin, Sefa Durmuş**
- 6 – Geochemical evaluation of the genetic relationship of Kısacık (Ayvacık, Çanakkale/Türkiye) epithermal gold mineralization using trace and rare earth elements **124–136**
Alaaddin Vural
- 7 – Synthesis of axially di- and peripherally tetra-(4-[(1E)-(4-methoxyphenyl)-methylene]amino)phenoxy) group substituted metallophthalocyanines and their electrochemistry **137–142**
Hüseyin Baş, Zekeriya Biyiklioglu*
- 8 – Antioxidant activity and in vitro/in silico acetylcholinesterase and urease enzyme inhibition effects of amygdalin **143–150**
Zehra Can, Yakup Kar, Halil İbrahim Güler, Ceren Birinci, Sevgi Kolaylı*
- 9 – Evaluation of biological activities of silver nanoparticles (AgNPs) synthesized by green nanotechnology from birch (*Betula* spp.) branches extract **151–161**
Burçin Özçelik, Aslı Kara*



The effects of mechanical activation on corrosion resistance of cordierite ceramics

Can Serkan Keskin^{1,2*} , Ceren Ayna Çakır³ , Hüseyin Altundağ^{1,2} , Nil Toplan⁴ , Hüseyin Özkan Toplan⁴ 

¹Sakarya University, Faculty of Sciences, Department of Chemistry, 54050, Sakarya, Türkiye

²Sakarya University, Biomedical, Magnetic and Semiconductor Materials Application and Research Center, 54050, Sakarya, Türkiye

³Sakarya University, Institute of Natural Sciences, 54050, Sakarya, Türkiye

⁴Sakarya University, Faculty of Engineering, Metallurgy and Materials Engineering, 54050, Sakarya, Türkiye

Abstract

The corrosion degrees of produced non-activated and activated cordierite-based ceramics were investigated in hydrochloric and sulfuric acid solutions. The composition of talc, alumina, and kaolinite powders was mechanically activated in a planetary mill. The concentrations of aluminum, magnesium, silicon, calcium, and potassium leached to the acid solutions from non-activated and activated cordierites were measured using ICP-OES. The amorphization of the structures was examined by XRD analysis. As a result, it has been determined that activated cordierite-based ceramics are more durable, and sulfuric acid solution causes more corrosion than hydrochloric acid.

Keywords: Cordierite, mechanical activation, corrosion resistance

1. Introduction

One of the crucial phases of the triple MgO-SiO₂-Al₂O₃ ceramic system, along with mullite, forsterite, tridymite, cristobalite, enstatite, and sapphire phases, is the cordierite phase (2MgO-2Al₂O₃-5SiO₂) [1,2]. These ceramics find substantial usage in circuit boards, filters, thermal insulation materials, catalytic converters, membranes, furnaces, refractories, electrical porcelain, and other applications because they have good thermo-mechanical, chemical, and dielectric qualities [3,4].

The cordierite phase is created using a variety of starting materials. Simple compounds like oxides, hydroxides, and carbonates are the earliest of them. The second is binary compounds, which include clays, talc, and sepiolite; the third is ternary compounds, which include chlorite. Industrial wastes such as magnesite and glass slag are also used in cordierite production [4,5].

Although the kaolin-talc system is suitable for producing cordierite ceramics, the specifications of the produced cordierites vary due to the presence of impurities in different kaolinites. For this reason, selecting the appropriate kaolin is crucial to preparing high-performance cordierite ceramics. The sintering of

cordierite ceramics is difficult due to the narrow sintering temperature range (1300 – 1400 °C) [6,7]. It is possible to reduce the production temperature and increase the physical properties of cordierite by using different methods such as co-precipitation, solid-state synthesis, or sol-gel.

Since cordierite-based ceramics dissolve more in acidic solutions [8,9], they are susceptible to acid corrosion. There are few studies on the acid solubility of these ceramics. Kang et al. [10] found that μ -cordierite in the cordierite-based glass ceramics they produced was more resistant to acid solutions (especially H₂SO₄) than α -cordierite. Baitalik and Kaya [11] subjected the cordierite-silica-based porous ceramics they produced to the acid corrosion test at 90 °C using a 20% by-weight HCl solution. According to their corrosion test, it was observed that the cordierite phase was completely dissolved in ten days in an acidic medium.

With the mechanical processes carried out in the solid phase, the phase structure of the solids can be changed, and smaller powder particle sizes can be obtained. Therefore, the powder particles exposed to the

Citation: C.S. Keskin, C.A. Çakır, H. Altundağ, N. Toplan, H.Ö. Toplan, The effects of mechanical activation on corrosion resistance of cordierite ceramics, Turk J Anal Chem, 5(2), 2023, 83–88.

 <https://doi.org/10.51435/turkjac.1333631>

Author of correspondence: ckeskin@sakarya.edu.tr

Received: July 27, 2023

Tel: +90 (264) 295 60 37

Accepted: November 06, 2023

Fax: +90 (264) 295 59 50

mechanical process can react at a lower sintering temperature due to increased surface area [12,13]. Obradović et al. [14] investigated the effect of mechanical activation and two-step sintering on cordierite-based ceramics' structure and electrical properties. The mechanical activation provides better homogeneity of powder mixture and powder activity. Also, the obtained densities increased and led to higher dielectric permittivity. Nath et al. [15] reported the mechanical activation effect on cordierite synthesis at lower temperatures. The cordierite was obtained with better properties, such as a higher quantity of cordierite phase and improved physical properties. Đorđević and Jovanić [16] studied mechanical activation influence on electrical properties of cordierite ceramics. The formation temperature of cordierite was affected by activation time, and no significant changes were observed in electrical properties. Yalamaç and Akkurt [17] analyzed the effect of additives and grinding on the synthesis of cordierite. The synthesis temperature successfully decreased to a lower value using additives and grinding. Wu et al. [18] investigated the corrosion resistance of zircon-modified cordierite–spodumene composite ceramics. The corrosion resistance and mechanical strength were improved with zircon modification. Çitak et al. [19] studied the corrosion properties of cordierite-based ZrO₂ composite. The resistance was increased with ZrO₂ addition. In the present study, the effects of structural disorder (amorphization) provided by mechanical activation of the ceramic system (talc-kaolinite-alumina) were determined by X-ray diffraction (XRD) analysis. The microstructural change was analyzed using scanning electron microscopy (SEM). The corrosion resistance of the mixed ceramic systems against two strong acids (H₂SO₄ and HCl) that the material may encounter was examined by ICP-OES.

2. Material and methods

In the present study, the used raw materials are alumina, kaolin, and talc for the production of cordierite-based ceramics, which were supplied by Durovit Company from Turkey. Table 1 shows the company's values of the used raw material's chemical compositions.

Table 1. Chemical composition of raw materials

Compounds (wt.%)	Talc	Kaolin	Alumina
SiO ₂	63	52.12	0.52
Al ₂ O ₃	0.40	33.83	99.425
Fe ₂ O ₃	0.25	0.55	—
CaO	0.40	0.15	—
K ₂ O	0.04	0.13	—
Na ₂ O	0.08	0.01	0.055
MgO	30	0.05	—
TiO ₂	—	0.45	—
L.O.I*	4.83	12.45	—

* Loss on ignition, wt: weight

16 wt.% alumina, 43 wt.% kaolin, and 41 wt.% talc were mixed at 110 °C 24h. A high-energy planetary ball mill (600 rpm) (Fritsch) was used for the mechanical activation of the mixture for 1 hour. An X-ray diffraction investigation was carried out by an X-ray diffractometer (Rigaku Ultima) and CuKα radiation. For the morphological examination of mixed powders that had been activated and non-activated, a Joel 6060 LV SEM was employed. Eq. 1 was used to determine the percentage of amorphization (A%) of mechanically activated powders [20, 21].

$$A\% = \left[1 - \frac{B_o \cdot I_x}{B_x \cdot I_o} \right] \times 100 \quad (1)$$

Where I_o is the diffraction peak's integral intensity, and B_o is the peak's background for the unactivated mixture. B_x and I_x are the same values for the mixture that has been mechanically activated. One axial hydraulic press operating at less than 100 MPa shaped the mixture of activated and non-activated powders. The sintering process of the shaped samples was carried out under atmospheric conditions by keeping them at 1250 °C for 1 hour with a heating rate of 10 °C/min. The cordierite phase formed after sintering was determined by XRD analysis. The microstructural examinations were carried out using SEM. The images were taken from the fractured surface of the samples. For the corrosion tests of the produced cordierite-based ceramics, 2%, 5%, and 10% HCl and H₂SO₄ solutions were prepared. Sintered pellets were kept in acidic solutions with two different acids and three concentrations for 1 and 10 days. Al, Mg, Si, Ca, and K concentrations in leach solutions were measured with a Spectro Arcos model ICP-OES (Spectro Analytical Instruments Dusseldorf, Germany).

3. Results and discussions

Figure 1 shows the XRD patterns of activated and non-activated alumina-talc-kaolinite mixture powders. Most of the crystalline peaks disappeared after mechanical activation due to the amorphization and structural deterioration in the structure of kaolin talc and alumina. The mechanical activation process causes the mineral particles to become amorphous depending on the rotation speed and duration [22]. It means that mechanical activation decreased the grain size and caused amorphization of the mineral particles of the structure [20,22]. The mechanical activation disrupts the crystal structure and makes it unstable. Some reactions occur during operation, and energy consumption is reduced. The grain size decreases, and the surface area increases, which increases the ability to react.

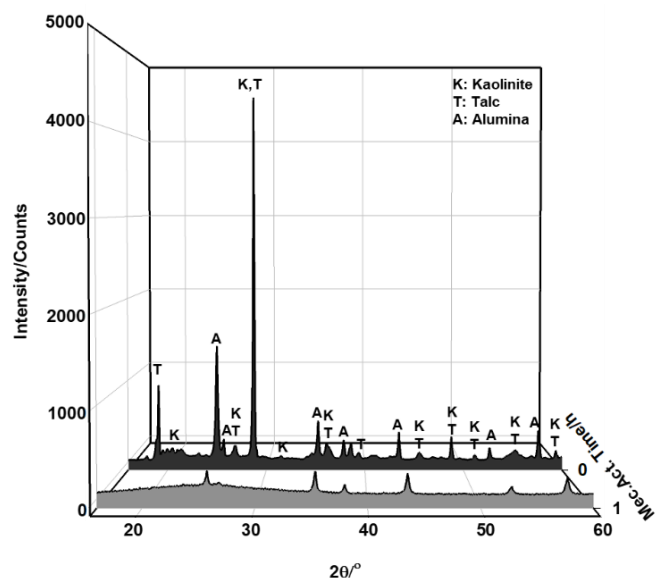


Figure 1. XRD patterns of activated and non-activated alumina-talc-kaolinite-powders

Thus, solid-solid reactions at high temperatures are carried out at lower temperatures. In two studies, Tromans and Meech [23,24] demonstrated that mechanical activation led to the growth of a significant number of dislocations and the corresponding strain fields, which might result in a general decline in long-range lattice periodicity. The loss of diffraction peaks and line broadening occurred in the X-ray patterns after extensive milling, and this might be seen as forming a metastable "amorphous phase".

Fig. 2a and b show scanning electron micrographs (SEM) of powder mixtures made of talc, kaolinite, and alumina that have been activated and not activated. The non-activated mixture has particles larger than 5 μm in size (Fig. 2a). The powder combination is mechanically activated and then agglomerated. Moreover, Eq. 1 was used to determine the degrees of amorphization of alumina, talc, and kaolinite. Alumina, talc, and kaolinite all had amorphization degrees around 75, 95, and 95%, respectively.

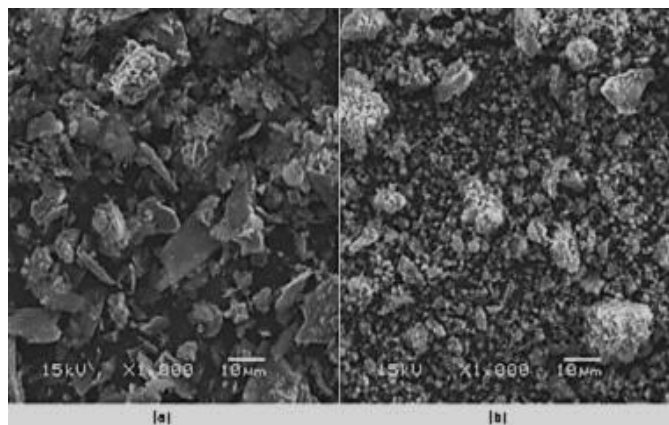


Figure 2. SEM micrographs of non-activated (a) and activated (b) alumina-talc-kaolinite powders

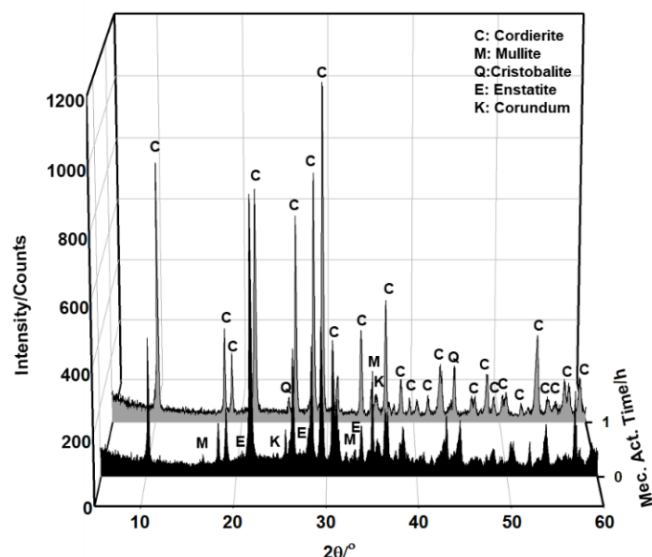


Figure 3. XRD patterns of non-activated and activated samples were sintered at 1250 °C for 1 h.

The activated mixture powders are shaped and sintered at 1250 °C for 1h. The mechanical activation caused decreased grain size and increased surface area. Therefore, the sintering temperature was reduced due to the easier powder reaction. Fig. 3 shows the XRD patterns. The XRD pattern of the non-activated sintered sample indicates that cordierite, corundum, enstatite, mullite, and quartz phases are present. The activated sintered samples' diffraction patterns show well-crystallized sharp peaks of cordierite and a small amount of corundum and quartz. The cordierite phase intensity of the activated sample increased. Elmas et al. [25] studied the effect of mechanical activation on the formation of mullite in their study on the Alumina-Quartz system and stated that mechanical activation supports the formation of the mullite phase.

SEM micrographs of activated and non-activated sintered pellets are shown in Fig. 4a and 4b. Non-activated pellets show high porosity between grains (Fig. 4a). However, porosities are smaller in activated pellets (Fig. 4b).

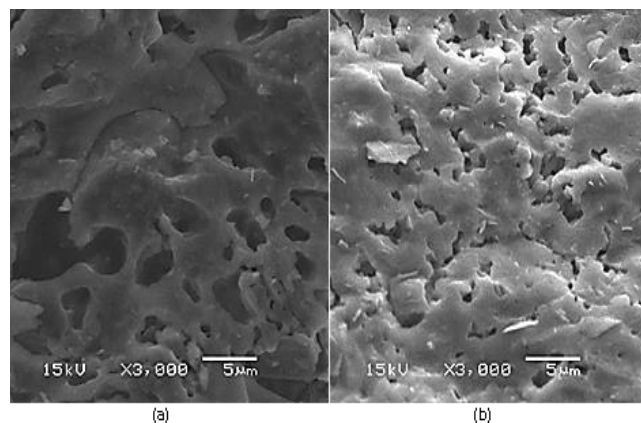


Figure 4. SEM images of (a) non-activated and activated (b) samples sintered at 1250 °C for 1 h.

Based on the SEM images, we can say that mechanical activation has a porosity-reducing effect on the sintering process. Ceramics are porous materials and resistant to acidic corrosion. The amount of porosity was reduced by mechanical activation, and corrosion resistance was increased. Obradovic et al. [1] reported that mechanical activation decreased open porosity and increased density value.

The acidic corrosion rates of activated and non-activated cordierite-based ceramics are shown in Fig. 5. Aluminum was the most dissolved metal in non-activated cordierite-based ceramics. After one day of treatment, the leached Al concentrations from non-activated ceramics in 10% HCl and 10% H₂SO₄ solutions were ~62.0 and ~81.0 mg/L, respectively. In activated ceramics, these concentrations were decreased to ~6.0 mg/L (in HCl solution) and ~8.0 mg/L (in H₂SO₄ solution). The activation process significantly reduced the amount of dissolved Al. Similar results were obtained with Mg and Si except for Ca and K. Although the dissolution of other metals decreased with the activation process, no significant change occurred for Ca. K and Ca were impurities and not parts of the cordierite structure. They were mostly at the grain boundaries [26] and not significantly affected by the activation process. Potassium was affected more than calcium due to binding energy. Also, the bulk densities were measured before and after corrosion, but no difference was observed in the results.

The effect of time on the leached metal concentrations from activated ceramics is shown in Fig. 6. The highest corrosions occurred on the first day, and the concentrations of dissolved metals decreased in ten days. It was observed that after 10 days, there was no Ca, which was found in the grain boundaries, and Mg, which was weakly bound to the structure. Mg was removed easily on the first days of the leaching process and could not be detected in the leaching solution after ten days because it did not remain in the structure. On the first day, the acid dissolved the metals outside the lattice. The concentration of dissolved metals decreased in 10 days because the amount of acid that could enter the lattice was limited.

Fig. 7 demonstrates the effect of acid concentration on the corrosion of activated ceramic. Except for Ca, increased acid concentration increased the concentration of all leached metals as predicted. The leached Ca concentrations were the same in 2% and 10% acids because all Ca were dissolved in 2% HCl and H₂SO₄ solutions. Also, it was concluded that the corrosion strength of H₂SO₄ on activated cordierite-based ceramics was higher than HCl solutions due to the higher acidity of the sulphuric acid.

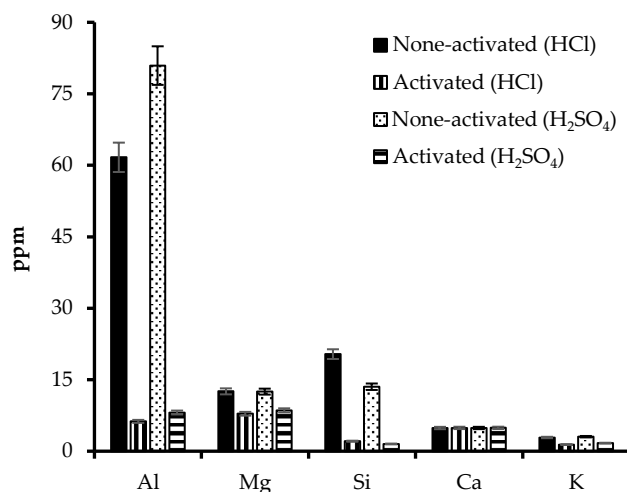


Figure 5. The leached metal concentration of non-activated and activated cordierite-based ceramics (10% acids, 1 day)

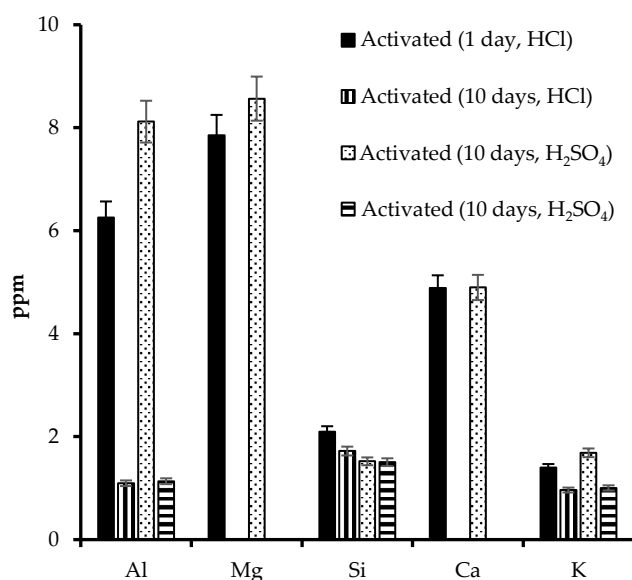


Figure 6. The effect of time on the leached metal concentrations from activated ceramics (10% acids)

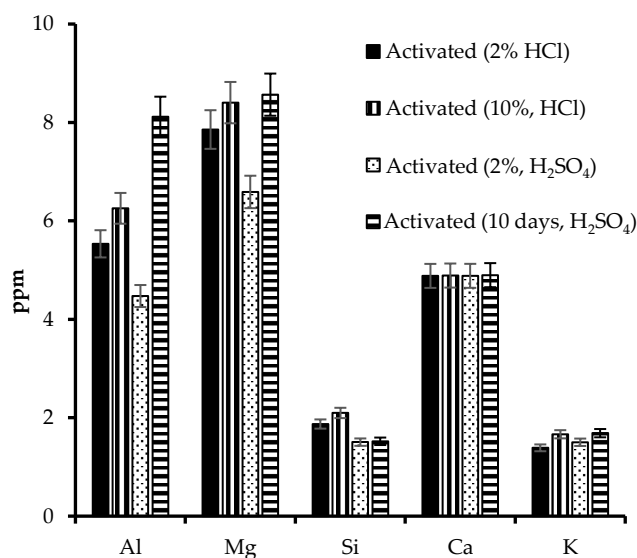


Figure 7. The effect of acid concentration on the leached metal concentrations from activated ceramics (1 day)

4. Conclusions

In the present study, mechanically activated and non-activated cordierite-based ceramics materials were prepared. The amorphization and structural deterioration, microstructure, and corrosion resistance of the bulk materials in HCl and H₂SO₄ were characterized systematically. The most important conclusions are:

1. The mechanical activation in talc, kaolinite, and alumina led to amorphization and structural disordering. Alumina, talc, and kaolinite all had amorphization degrees around 75, 95, and 95%, respectively.
2. The activated and non-activated mixture powders are shaped and sintered at 1250 °C for 1 h. The intensity of the cordierite phase increased in the activated sample.
3. It has been established that mechanical activation lowers open porosity in pellets after sintering.
4. Activated cordierite is approximately 10 times more durable against acidic corrosion than non-activated cordierite. The corrosion degrees are raised by increased acid concentration and strength. The corrosion rates reached a maximum on the first day and then decreased over time due to the limited amount of acid that can enter the lattice.

Acknowledgments

—

Funding

The author (s) has no received any financial support for the research, authorship, or publication of this study.

Authors' contribution

The authors contributed equally to the study.

The declaration of conflict of interest/ common interest

No conflict of interest or common interest has been declared by the authors.

The declaration of ethics committee approval

This study does not require ethics committee permission or any special permission.

The Declaration of Research and Publication Ethics

The authors of the paper declare that they comply with the scientific and ethical rules of the Turkish Journal of Analytical Chemistry. In addition, they declare that this study has not been evaluated in any journal.

References

- [1] C.N. Obradovic, N. Dordevic, S. Filipovic, N. Nikolic, D. Kosanovic, M. Mitric, S. Markovic, V. Pavlovic, Influence of mechanochemical activation on the sintering of cordierite ceramics in the presence of Bi₂O₃ as a functional additive, *Powder Technol*, 218, 2012, 157–161.
- [2] J. Liao, G. Qing, B. Zhao, Phase equilibria studies in the CaO-MgO-Al₂O₃-SiO₂ system with Al₂O₃/SiO₂ weight ratio of 0.4, *Metals*, 13(224), 2023, 2–26.
- [3] W. N. Obradović, V. Pavlović, M. Kachlik, K. Maca, D. Olćan, A. Đorđević, A. Thantshapanyan, B. Vlahović, V. Pavlović, Processing and properties of dense cordierite ceramics obtained through solid-state reaction and pressure-less sintering, *Adv Appl Ceram*, 118(5), 2019, 241–248.
- [4] S. Yürüyen, N. Toplan, K. Yıldız, H.Ö. Toplan, The non-isothermal kinetics of cordierite formation in mechanically activated talc-kaolinite-alumina ceramics system, *J Therm Anal Calorim*, 125(2), 2016, 803–808.
- [5] C. Başaran, N. Canikoğlu, H. Ö. Toplan, N. Toplan, The crystallization kinetics of the MgO-Al₂O₃-SiO₂-TiO₂ glass ceramics system produced from industrial waste, *J Therm Anal Calorim*, 125(2), 2016, 695–701.
- [6] A. Peles, N. Đorđević, N. Obradovic, N. Tadic, V.B. Pavlovic, Influence of prolonged sintering time on density and electrical properties of isothermally sintered cordierite-based ceramics, *Sci Sinter*, 45(2), 2013, 157–164.
- [7] Y. Kobayashi, K. Sumi, E. Kato, Preparation of dense cordierite ceramics from magnesium compounds and kaolinite without additives, *Ceram Int*, 26(7), 2000, 739–43.
- [8] P.Y. Azimov, S.A. Bushmin, Solubility of minerals of metamorphic and metasomatic rocks in hydrothermal solutions of varying acidity: thermodynamic modeling at 400–800 °C and 1–5 kbar, *Geochem. Int+*, 45(1), 2007, 1210–1234.
- [9] A. Harrati, Y. Arkame, A. Manni, A. El Haddar, B. Achiou, A. El Bouari, I. E. A. El Hassani, A. Sdiri, C. Sadik, Cordierite-based refractory ceramics from natural halloysite and peridotite: Insights on technological properties, *J Indian Chem Soc*, 99(6), 2022, 100496.
- [10] J. Kang, J. Wang, X. Zhou, J. Yuan, Y. Hou, S. Qian, S. Li, Y. Yue, Effects of alkali metal oxides on crystallization behavior and acid corrosion resistance of cordierite-based glass-ceramics, *J Non-Cryst Solids*, 481, 2017, 184–190.
- [11] S. Baitalik, N. Kaya, Processing and properties of cordierite-silica bonded porous SiC ceramics, *Ceram Int*, 43(17), 2018, 14683–14692.
- [12] S. Koç, N. Toplan, K. Yıldız, H. O. Toplan, Effects of mechanical activation on the non-isothermal kinetics of mullite formation from kaolinite, *J Therm Anal Calorim*, 103, 2011, 791–796.
- [13] J. Ding, J. Wang, H. Yang, Z. Liu, C. Yu, X. Li, C. Deng, H. Zhu, Improvement of mechanical properties of composites with surface modified B₄C for precision machining, *Materials*, 16(882), 2023, 2–10.
- [14] N. Obradović, S. Filipović, N. Đorđević, D. Kosanović, S. Marković, V. Pavlović, D. Olćan, A. Djordjević, M. Kachlik, K.I. Maca, Effects of mechanical activation and two-step sintering on

- the structure and electrical properties of cordierite-based ceramics, *Ceram Int*, 42, 2016, 13909–13918.
- [15] S.K. Nath, S. Kumar, R. Kumar, Effect of mechanical activation on cordierite synthesis through solid-state sintering method, *B Mater Sci*, 37(6), 2014, 1221–1226.
- [16] N.G. Đorđević, P.B. Jovanić, Influence of mechanical activation on electrical properties of cordierite ceramics, *Sci Sinter*, 40, 2008, 47–53.
- [17] E. Yalamac, S. Akkurt, Additive and intensive grinding effects on the synthesis of cordierite, *Ceram Int*, 32, 2006, 825–832.
- [18] J. Wu, C. Hu, C. Ping, X. Xu, W. Xiang, Preparation and corrosion resistance of cordierite–spodumene composite ceramics using zircon as a modifying agent, *Ceram Int*, 44, 2018, 19590–19596.
- [19] B. Çitak, D. Kirsever, A. Ayday, H. Boussebha, A. Ş. Demirkıran, The corrosion kinetics of cordierite-based ZrO₂ composites obtained from natural zeolite in dilute HCl acid solution, *J Compos Mater*, 55(20), 2021, 2751–2763.
- [20] P. Balaz, *Mechanochemistry In Nanoscience And Minerals Engineering* (1. edition), 2008, Germany, Springer.
- [21] S. Vyazovkin, Isoconversional Kinetics, *Handbook of Thermal Analysis and Calorimetry*, Editors: M.E. Brown, P.K. Gallagher, 2008, Holland, Elsevier.
- [22] J. Wu, C. Lu, X. Xu, D. Wang, Y. Zhang, Y. Zhou, Preparation and characterization of cordierite ceramic from coal series kaolin for electronic application, *J Aust Ceram Soc*, 55, 2019, 943–952.
- [23] D. Tromans, J. A. Meech, Enhanced dissolution of minerals: microtopography and mechanical activation, *Miner Eng*, 12(6), 1999, 609–625.
- [24] D. Tromans, J.A. Meech, Enhanced dissolution of minerals: stored energy, amorphism and mechanical activation, *Miner Eng*, 14(11), 2001, 1359–1377.
- [25] E. Elmas, K. Yıldız, N. Toplan, H.Ö. Toplan, Effect of mechanical activation on mullite formation in an alumina-quartz ceramics system, *Mater Technol*, 47(4), 2013, 413–416.
- [26] L. Curkovic, M.F. Jelaca, Dissolution of alumina ceramics in HCl aqueous solution, *Ceram Int*, 35(5), 2009, 2041–2045.



A green liquid chromatographic method using ethanol in mobile phase for the determination of nimesulide and naproxen in gel formulations

Sercan Yıldırım* 

Karadeniz Technical University, Faculty of Pharmacy, Department of Analytical Chemistry, 61080, Trabzon, Türkiye

Abstract

Determination of nonsteroidal anti-inflammatory drugs (NSAIDs) in pharmaceutical formulations helps to ensure that they are manufactured to the correct specifications. Consequently, simple, reliable, and environmentally friendly analytical methods are needed for the quality control of NSAID formulations. In this study, a novel and green liquid chromatographic method was developed for the determination of nimesulide (NIM) and naproxen (NAP) in gel formulations by employing ethanol as a green alternative to hazardous methanol and acetonitrile. The high viscosity of ethanol was compensated by employing a Chromolith High Resolution RP18e monolithic column (100 × 4.6 mm) with low flow resistance. Box-Behnken design with desirability function was employed for the optimization of selected significant parameters: pH (2.8–4), ethanol ratio in the mobile phase (35–55%), and flow rate (0.7–1.5 mL/min). Under optimum conditions, satisfactory separation of analytes was achieved within 5 min. Calibration curves for both analytes were linear between 1–50 µg/mL. Accuracies of intra- and inter-day experiments at low-, middle-, and high-quality control levels ranged from 99.0–101.5% with relative standard deviation values lower than 2.3%. The detection limits were 0.27 and 0.62 µg/mL for NIM and NAP, respectively. The applicability of the method was demonstrated by analyzing gel formulations. The results of this study indicated that monolithic columns in combination with ethanol as a mobile phase component could be considered a desirable and green alternative for the routine analysis of NSAIDs in quality control laboratories.

Keywords: Anti-inflammatory drugs, liquid chromatography, pharmaceutical analysis, design of experiments

1. Introduction

Nimesulide (NIM) and naproxen (NAP) are nonsteroidal anti-inflammatory drugs (NSAIDs) commonly utilized for their potent analgesic, anti-inflammatory, and antipyretic effects. These medications exhibit distinct pharmacological effects and have been widely prescribed for various inflammatory conditions and pain management [1].

NIM selectively inhibits cyclooxygenase-2 (COX-2) enzyme, which is primarily responsible for the production of prostaglandins involved in inflammation and pain. This selectivity minimizes the adverse gastrointestinal effects often associated with nonselective NSAIDs, such as gastric irritation and ulceration. Nimesulide has also shown anti-inflammatory and analgesic properties, making it a valuable option for managing acute and chronic pain and musculoskeletal disorders [2,3]. On the other hand, NAP is a nonselective NSAID that inhibits both COX-1 and COX-2 enzymes, leading to a more comprehensive suppression of prostaglandin synthesis. The broader

spectrum of action of NAP is advantageous in treating several inflammatory conditions, particularly in rheumatoid arthritis and osteoarthritis [4,5].

Accurate quantification of drugs ensures that the formulations maintain their intended therapeutic potency. Additionally, quality control (QC) measures are essential to ensure drugs meet stringent regulatory standards. In this manner, there is a need for reliable analytical methodologies for the determination of NIM and NAP in pharmaceutical formulations. High-performance liquid chromatography (HPLC) with UV or diode array detector (DAD) detection has a leading position in the analysis of NSAIDs [6–15]. On the other hand, HPLC methods generally require the use of solvents such as methanol and acetonitrile, which present health and environmental issues and, therefore, are classified as “class 2” in the International Conference on Harmonization (ICH) guidelines [16].

Green analytical chemistry (GAC) is a field of science that focuses on minimizing the negative environmental

Citation: S. Yıldırım, A green liquid chromatographic method using ethanol in mobile phase for the determination of nimesulide and naproxen in gel formulations, Turk J Anal Chem, 5(2), 2023, 89–97.

 <https://doi.org/10.51435/turkjac.1364599>

Author of correspondence: sercanyildirim@ktu.edu.tr

Received: September 22, 2023

Tel: +90 (462) 377 8812

Accepted: November 04, 2023

Fax: +90 (462) 325 6717

impact of medical, environmental, food, and industrial analysis laboratories [17]. Today, there is a shift towards applying GAC concepts to replace conventional methods with eco-friendly ones displaying similar or better analytical performance [18]. In this manner, ethanol has been considered as a green mobile phase component in LC due to its wide availability, safety, and relatively low cost. It has an eluotropic strength and a UV cut-off value similar to acetonitrile and methanol, respectively [19]. Although ethanol has a high viscosity, which may lead to the formation of elevated column back pressures, this issue can be solved by using monolithic columns consisting of a single rod of high-purity polymeric silica gel, which creates significantly lower flow resistance compared to traditional particle-based columns due to bimodal pore structure of macro and mesopores [20,21]. For these reasons, there is a growing interest in the use of ethanolic mobile phases to separate various analytes, including natural compounds [22] and drugs [23–26].

In HPLC analysis, several chromatographic parameters influence separation efficiency, including mobile phase pH, organic solvent ratio, gradient slope, flow rate, temperature, etc. These parameters are generally optimized by employing a one-factor-at-a-time (OFAT) approach, which requires performing many experiments and is unable to detect factor interactions. In this manner, Design of Experiments (DOE) has recently attracted considerable interest in the analytical chemistry community as a reliable chemometric tool for the optimization of analytical procedures while conducting a minimal number of experiments [27]. Instead of the traditional OFAT approach, where factors are altered individually, DOE allows for the simultaneous exploration of the effects of multiple variations on one or more responses. While conventional optimization approaches are often empirical, DOE offers a systematic and multivariate experimental framework to comprehensively understand a process and assess the statistical significance of factors. By creating an experimental matrix, DOE enables faster visualization and the evaluation of multiple factors simultaneously. Furthermore, unlike OFAT, which assumes that factors act independently, DOE models can reveal potential interactions between these factors, enhancing the depth of process understanding. The optimization is conducted by employing response surface methodology with desirability function based on different designs such as Box-Behnken design (BBD) and central composite design (CCD) [28–30]. The BBD is a second-order response surface design proposed for optimizing processes and studying the relationship between multiple independent factors and three-level responses. The main advantage of the BBD over the CCD is its

simplicity and efficiency. The BBD requires fewer experimental runs compared to CCD, which makes it less resource-intensive and quicker to implement. It achieves this by omitting extreme factor combinations and focusing on factor settings closer to the center of the design space [30,31]. Many studies have been reported on using BBD to optimize chromatographic conditions [27,29].

The aim of this study is to develop a green HPLC method for the simultaneous determination of NIM and NAP in gel formulations. To our knowledge, ethanol was used for the first time as an eco-friendly mobile phase component for the separation of selected NSAIDs. The high viscosity of ethanol was compensated by employing a monolithic column with high permeability as the stationary phase. Chromatographic conditions were optimized by BBD with multi-response optimization based on the desirability function. The greenness of the method was examined by a recently reported assessment tool, i.e., AGREE [32]. The developed method was successfully applied to the determination of NIM and NAP in pharmaceutical formulations.

2. Material and methods

2.1. Chemicals and materials

All chemicals used in the present study were of analytical grade. Methanol, formic acid, NaOH, NAP, and NIM were purchased from Sigma Aldrich (St. Louis, MO, USA). Ethanol was obtained from Smyrna. Ultrapure water was produced by Arium pro UV (Sartorius Stedim, Göttingen, Germany). Mobile phase pH was adjusted by dropwise addition of 3 mol/L NaOH solution. Nimes gel containing 1% NIM and Naprosyn gel containing 10% NAP were purchased from a local pharmacy.

2.2. Standard solutions

Individual stock solutions of NAP and NIM were prepared in methanol at 1000 µg/mL. Standard solutions (1, 2.5, 5, 10, 20, 25, 30, 50 µg/mL) for optimization studies and method validation were obtained by mixing and diluting stock solutions with water. The solutions were kept at +4 °C and protected from daylight.

2.3. Instrumentation and apparatus

Chromatographic analyses were carried out by a Prominence-20 series HPLC system coupled with an SPD-20A DAD. LC solution 1.25 software (Shimadzu, Japan) was used for system control and data acquisition. An HI 2211 pH meter from Hanna Instruments, a magnetic stirrer, a vortex mixer, and an ultrasonic bath

from Isolab Laborgerte were used for the preparation of samples and solutions.

2.4. Chromatographic conditions

NIM and NAP were separated on a Chromolith High Resolution RP18e monolithic column (100 × 4.6 mm) with a mobile phase consisting of 0.1% formic acid in water (pH 4): ethanol (60:40, v/v). The mobile phase was pumped through the system at a 1.5 mL/min flow rate. Column oven temperature was kept at 25 °C. A total of 20 µL sample or standard solution was injected into the system. The DAD was operated at 272 nm with 0.24 s time constant and 3.125 Hz data sampling rate. Under optimum conditions, retention times of NIM and NAP were 3.0 and 3.7 min, respectively.

2.5. Preparation of samples

Two-hundred fifty milligrams of Nimes or Naprosyn gels corresponding to 2.5 mg NIM or 25 mg NAP, respectively, were accurately weighed and transferred to a 25 mL volumetric flask. 20 mL of ethanol was added, and the mixture was magnetically stirred for 15 min. Then, the flask was subjected to ultrasonication for 5 min. After cooling at room temperature, each flask was made up to volume with ethanol. Five milliliters of the extracts were centrifuged at 5000 rpm for 5 min. Clear supernatants obtained for Nimes and Naprosyn gels were diluted 4- and 40-fold with ultrapure water to obtain a final drug concentration of 25 µg/mL, respectively. Twenty microliter of diluted extract was injected into the system. It should be noted that centrifugation was found to be sufficient to obtain a clean and particle-free extract. Therefore, no filtration was performed during sample preparation, which both simplified the sample preparation procedure and reduced the analysis cost per sample.

2.6. Optimization strategy

The effect of three factors: pH, % ethanol in the mobile phase, and flow rate on analysis time, resolution (R_s), and capacity factor (k) of the early eluting analyte (NIM), using the BBD. The simultaneous optimization of multiple responses was performed by the desirability approach [33]. Experimental design, data analysis, and desirability function calculations were performed by Design Expert 11.1.2 (Stat-Ease, Minneapolis, MN, USA). Duplicate measurements were performed for each experimental run to ensure the accuracy of the results.

2.7. Method validation

Validation experiments were conducted in accordance with ICH guidelines and official pharmacopeias [34,35]. A system suitability test (SST) was performed before validation experiments. For this purpose, a 25 µg/mL

mixed standard solution of NIM and NAP was injected six times. The chromatographic performance was evaluated with regard to R_s , k , number of theoretical plates, tailing factor, selectivity factor, and repeatability of both retention times and peak areas. The linearity of the method was evaluated by analyzing mixed standard solutions of analytes at six concentrations (1, 5, 10, 25, 40, 50 µg/mL), each injected in triplicate. Regression parameters, including slopes, intercepts, and correlation coefficients, were obtained by Microsoft Excel. Intra- and inter-day accuracy and repeatability were evaluated by analyzing QC samples prepared at 20, 25, and 30 µg/mL corresponding to 80%, 100%, and 120% of final analyte levels in the extract, respectively. The intra-day measurements were assessed by four analyses at each concentration level within the same day, while inter-day measurements were evaluated by ten analyses in three consecutive days. Results for repeatability and accuracy were given as relative standard deviation (RSD) and % accuracy, respectively. The limits of detection (LOD) values were statistically calculated from the standard deviation of the y-intercept of the regression line and the slope of the corresponding calibration curve [36]. The limit of quantification (LOQ) for each drug was accepted as the lowest concentration level of the corresponding calibration curve. The specificity of the method was assessed by examining signals of potential interfering substances in the blank, standard, and sample solutions to ensure that the analyte peaks were free from interference.

3. Results and discussion

3.1. Optimization of chromatographic conditions by BBD

Based on its ability to generate second-order equations that establish correlations between the examined parameters and the observed responses, BBD was chosen as the experimental design method for optimizing the chromatographic separation of NIM and NAP. BBD is considered an attractive alternative to the CCD due to its capacity to yield appropriate mathematical models while reducing the number of required experimental runs. Unlike CCD, BBD avoids the utilization of extreme experimental conditions, which can sometimes yield undesirable outcomes [37]. In this study, we applied BBD to fine-tune the HPLC conditions, aiming to determine the shortest possible run time that still enables the acceptable separation of the NIM and NAP as well as the adequate retention for the first peak (NIM). After performing preliminary experiments, ethanol ratio (%) in the mobile phase, pH, and flow rate were selected as the main parameters that can affect the separation of analytes. Temperature was

Table 1. Experimental matrix and experimental plan of the BBD

Std order	Run order	Factor 1	Factor 2	Factor 3	Response 1	Response 2	Response 3
		A: pH	B: Ethanol ratio (%)	C: Flow rate (mL/min)	Rs of NAP	k of NIM	Retention time of NAP (min)
1	10	2.8	35	1.1	7.607	3.657	9.053
2	12	4	35	1.1	6.061	3.697	8.51
3	11	2.8	55	1.1	1.365	0.415	2.11
4	13	4	55	1.1	1.116	0.418	2.068
5	14	2.8	45	0.7	3.044	1.062	5.319
6	17	4	45	0.7	2.505	1.07	5.15
7	3	2.8	45	1.5	3.163	1.065	2.526
8	6	4	45	1.5	2.558	1.076	2.442
9	8	3.4	35	0.7	7.144	3.665	13.909
10	16	3.4	55	0.7	1.152	0.41	3.255
11	5	3.4	35	1.5	7.153	3.646	6.571
12	2	3.4	55	1.5	1.28	0.412	1.546
13	4	3.4	45	1.1	3.197	1.072	3.407
14	9	3.4	45	1.1	3.142	1.063	3.391
15	1	3.4	45	1.1	3.23	1.067	3.418
16	7	3.4	45	1.1	3.137	1.062	3.396
17	15	3.4	45	1.1	3.11	1.059	3.374

deliberately omitted from the experimental design since its influence can be reasonably anticipated through common sense and the understanding of chromatographic principles [38]. The R_s between NIM-NAP, k of NIM, and the retention time of NAP were selected as responses for the optimization by desirability function. The effect of selected factors was evaluated at low and high levels in the following ranges: pH (2.8-4), ethanol ratio (35-55%), and flow rate (0.7-1.5 mL/min). BBD matrix and experimental results are shown in Table 1.

The relationships between the factors and responses were modeled by the second-order polynomial equations after applying multiple regression analysis. The log₁₀ transformation was applied to all variables as it improved the models' ability to explain data. The model equations for the three responses are as follows:

$$\begin{aligned} \text{Log}_{10}(Y1) = & 0,500085 - 0,0453716A - 0,377591B + \\ & 0,00900645C + 0,00280017AB - 0,00189043AC + \\ & 0,0113027BC - 0,0300783A^2 - 0,00836831B^2 - \\ & 0,0224439C^2 \end{aligned}$$

$$\begin{aligned} \text{Log}_{10}(Y2) = & 0,0271826 + 0,00194682A - 0,473745B + \\ & 0,00043870C - 0,000399AB + 0,00030085AC + \\ & 0,00109267BC + 0,00282086A^2 + 0,0625462B^2 - \\ & 0,00133591C^2 \end{aligned}$$

$$\begin{aligned} \text{Log}_{10}(Y3) = & 0,531117 - 0,00803817A - 0,313257B - \\ & 0,162058C + 0,00453276AB - 0,000166231AC + \\ & 0,000580734BC - 0,00409804A^2 + 0,10462B^2 + \\ & 0,0299352C^2 \end{aligned}$$

where Y1, Y2, and Y3 are the responses of R_s , k , and retention time of NAP, respectively. A, B, and C represent the three chromatographic parameters: pH, ethanol ratio (%) in the mobile phase, and flow rate, respectively. Statistical evaluation of models was carried out by analysis of variance (ANOVA) with the results

presented in Table S1-3. All three models were statistically significant according to ANOVA ($p < 0.0001$). The determination coefficient (R^2), adjusted R^2 , and predicted R^2 values were higher than 0.99, demonstrating that the models adequately interpret the interactions between factors and responses. Lack-of-fit values were found to be insignificant ($p > 0.1$) compared to the pure error, implying that the model could accurately estimate the response of the evaluated factors.

As can be seen from the equations and response surfaces (Fig. 1), the most significant parameter in all models was the ethanol ratio in the mobile phase, which was inversely proportional to all responses, i.e., R_s of peaks, k of NIM, and retention time of NAP. The k of NIM increased with the increase in pH while it negatively affected the R_s of peaks and retention time of NAP. An increase in the flow rate enhanced the R_s , decreased the retention of NAP, and did not significantly affect the k of NIM.

The optimal condition was established by the optimization tool of Design-Expert software according to the desirability function of Derringer and Suich [33]. The aim of the optimization studies was to obtain an R_s higher than 2 for the NAP-NIM peak pair, achieve a k of at least 2 for NIM, and minimize the retention time of NAP. Optimum chromatographic conditions were estimated as follows: mobile phase pH: 4; ethanol ratio of mobile phase: 40 %; and flow rate: 1.5 mL/min. The optimum values for Y1, Y2, and Y3 were estimated as 3.98, 2, and 3.81 min, respectively. The chromatogram obtained under these conditions is presented in Fig. 2. For Y1, Y2, and Y3, there are 4.02%, 2.15%, and 2.36% differences between the predicted and experimentally obtained values, respectively, proving the validity of the

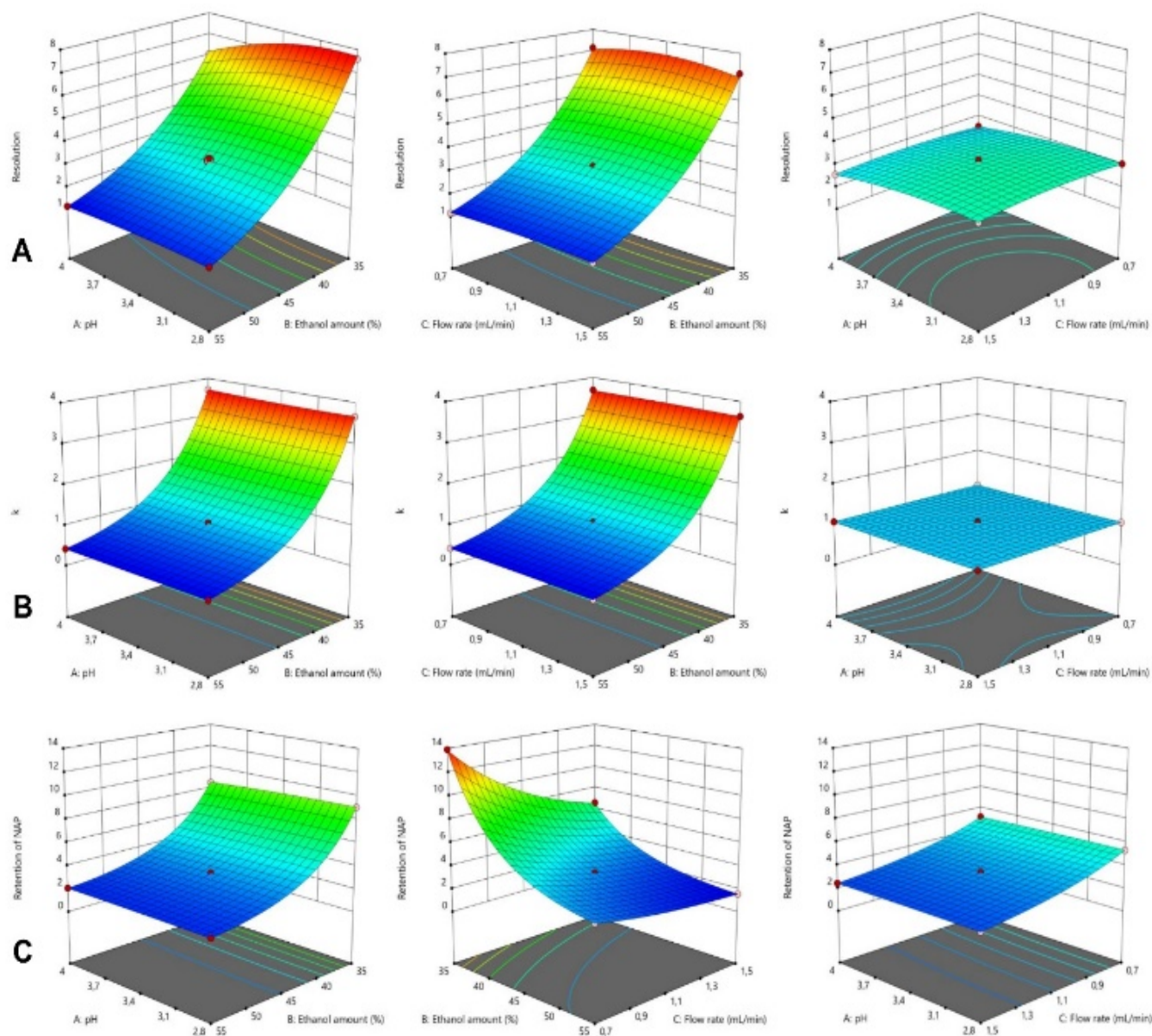


Figure 1. 3D-Response surface plots for (A) R_s of NAP, (B) k of NIM, and (C) Retention time of NAP

models used. Retention times of NIM and NAP were 3.0 and 3.7 min under optimum chromatographic conditions, respectively. The total run time was 5 min.

3.2. Method validation

In order to evaluate the appropriateness of the technique for the determination of NIM and NAP in pharmaceutical formulations, validation experiments were carried out as per the guidelines of ICH. An SST was performed as a control measure and an integral part of method validation. Results of SST studies obtained by injecting 10 $\mu\text{g/mL}$ standard solution six times are presented in Table 2. Under optimum conditions, both analytes were adequately retained on the column. R_s value for NAP was 4.3. Tailing factors (<1.4) indicated that symmetric peaks were obtained. RSD values for both retention time and peak area are lower than 1%. All evaluated parameters were found to be in accordance with USP requirements.

The results of linearity and sensitivity studies are depicted in Table 3. All calibration curves had correlation coefficients >0.999 , indicating that the developed method was linear. LOD values were 0.27 $\mu\text{g/mL}$ and 0.62 $\mu\text{g/mL}$ for NIM and NAP, respectively, while the lowest concentration of the calibration curve (1 $\mu\text{g/mL}$) was accepted as LOQ for both analytes.

Table 2. Results of system suitability tests for determination of NIM and NAP ($n = 6$)

	NIM	NAP	Recommended value
Retention time (min)	3.0	3.7	-
Tailing factor (T)	1.38	1.31	<2
Capacity factor (k)	2.0	2.7	>1
Resolution (R_s)	-	4.30	>2
Theoretical plates (N)	6012.9	6779.0	>2000
Selectivity factor (α)	-	1.36	>1.05
RSD% of retention time	0.85	0.92	<1
RSD% of peak area	0.52	0.48	<1

Table 3. Statistical evaluation of the calibration data of NIM and NAP

	NIM	NAP
Linear range ($\mu\text{g/mL}$)	1 – 50	1 – 50
Slope	15031	18146
Intercept	-1880.4	-2755.7
SE of slope	42.6	120.0
SE of intercept	1211.81	3412.2
Correlation coefficient (r)	0.9999	0.9996
LOD ($\mu\text{g/mL}$)	0.27	0.62
LOQ ($\mu\text{g/mL}$)	1.0	1.0

Table 4. Intra- and inter-day precision and accuracy for NSAIDs

Analyte	Concentration level ($\mu\text{g/mL}$)	Intra-day (n = 4)		Inter-day (n = 10)	
		Accuracy (%)	RSD (%)	Accuracy (%)	RSD (%)
NIM	20	99.2	2.05	99.0	2.29
	25	101.5	1.60	100.8	2.20
	30	99.1	1.54	99.4	1.33
NAP	20	100.3	2.03	99.8	1.80
	25	101.1	0.85	101.1	1.08
	30	101.0	1.23	100.9	1.01

Table 5. Assay data of NIM and NAP (n=3)

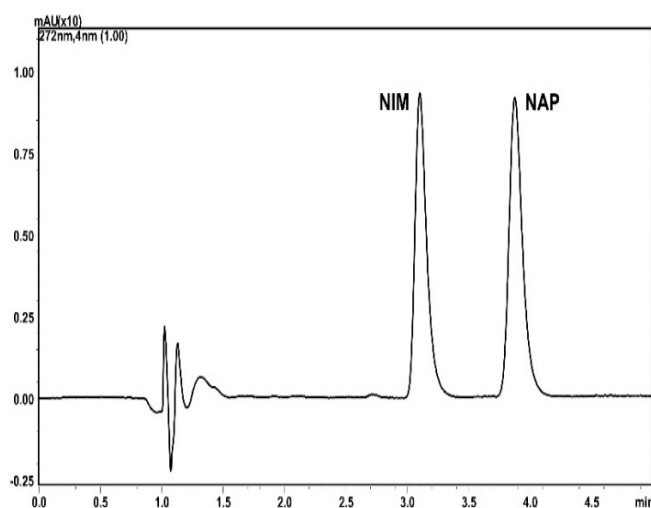
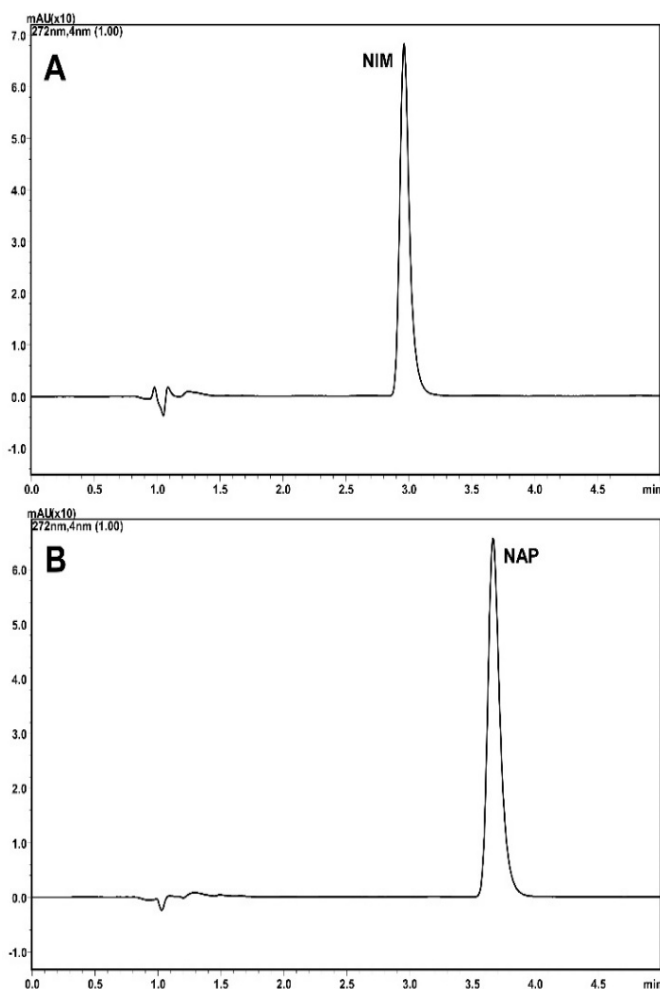
	Labeled amount (%) (w/w)	Observed amount (%) (w/w)	Recovery (%)	RSD (%)
NIM	1	0.989	98.95	0.88
NAP	10	9.921	99.22	0.20

QC solutions prepared at 20, 25, and 30 $\mu\text{g/mL}$ concentration levels for all analytes were analyzed on the same day and three consecutive days to evaluate the intra- and inter-day accuracy and repeatability (Table 4). Intra-day accuracies were in the range of 99.1 – 101.5%, while inter-day accuracies ranged from 99.0% to 101.1%. RSD values of intra- and inter-day experiments at three QC levels were in the ranges of 0.85 – 2.05% and 1.01 – 2.29%, respectively. Results demonstrated that the developed method is precise and accurate for determining NIM and NAP.

3.3. Application on real samples

The feasibility of the developed method was demonstrated by analyzing gel formulations of NIM and NAP in the market. Nimes gel includes disodium EDTA, carbomer 940, polyethylene glycol 400, triethanolamine, dimethyl sulfoxide, and glycerin as excipients, while Naprosyn gel contains carbomer 940, ethyl alcohol, triethanolamine, sodium metabisulfite, rose essence. Gel formulations were prepared as explained in section “2.5. The preparation of samples” and obtained extracts were analyzed by the developed HPLC method. Triplicate measurements were performed for each sample. Chromatograms of Nimes and Naprosyn gels were presented in Fig. 3.

No interferences were observed in the retention windows of NIM and NAP.

**Figure 2.** Chromatogram of a standard mixture (10 $\mu\text{g/mL}$) of NIM and NAP under optimized conditions at 272 nm**Figure 3.** Chromatograms of Nimes (A) and Naprosyn (B) gel formulations at 272 nm (25 $\mu\text{g/mL}$)

Additionally, peak purity values obtained from real sample analyses were >0.9999 for both analytes, demonstrating the specificity of the developed green LC method towards NIM and NAP. Table 5 summarizes the results of the gel formulation analysis. The quantities obtained were consistent with the manufacturers' claims.

3.4. Greenness evaluation

The selection of analytical methodologies for use in routine analyses within pharmaceutical research and QC laboratories is determined by various factors.

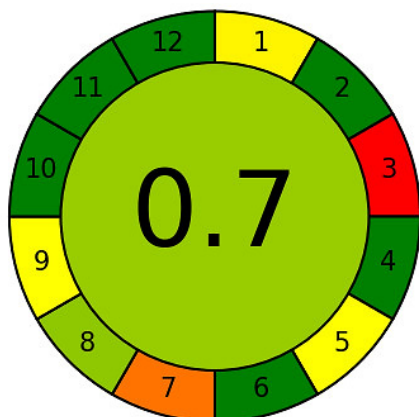


Figure 4. Greenness assessment of developed method using AGREE tool

Performance and throughput are paramount considerations. Cost efficiency is particularly critical for profit-seeking pharmaceutical entities. Recently, corporate social responsibility has become increasingly important, particularly with regard to the environmental impacts of business practices, including the regular implementation of analytical methods. Consequently, various metric tools have been introduced in order to accurately evaluate the "greenness" of analytical methods [39]. AGREE, introduced in 2020, stands as the latest comprehensive greenness assessment tool encompassing all 12 principles outlined by GAC [40]. As a result of the greenness assessment, the software generates a pictogram, which is divided into 12 adjustable sections, each marked by a distinct color scheme denoting its importance, from deep green (indicating a score of 1) to deep red (indicating a score of 0). The overall method greenness is depicted at the center of the circular pictogram as a final score ranging from 0 to 1. The closer the score is to one, the greener the method is considered [32].

The overall AGREE evaluation for the proposed HPLC-DAD method is shown in Fig. 4. An average score of 0.7 was achieved, demonstrating the environmental friendliness of the method. The lowest scores were obtained for the offline positioning of the analytical device (criteria 3) and waste production (criteria 7). It should be noted that offline sampling and sample transfer to the analysis laboratory are mandatory for QC laboratories to achieve separation of pharmaceutical production and QC sites [41]. Moreover, the generated waste during sample preparation and chromatographic separation mainly consists of ethanol, which is considered a safe and green solvent [42,43].

The method displayed prominent performance in terms of sections related to the use of safer solvents (criteria 2), high sample throughput (criteria 6), minimum energy consumption (criteria 8), and operator safety (criteria 10). The main advantages of the method are as follows: low sample amount (Criteria 2), reduced number of distinct steps (Criteria 4), the use of bio-based and non-toxic reagents (Criteria 10 and 11), and increased operator safety (Criteria 12).

4. Conclusion

A novel RP-HPLC-DAD method was developed for the simultaneous determination of NIM and NAP in pharmaceutical formulations. Chromatographic conditions were optimized to obtain adequate retention for both analytes with satisfactory R_s and run time by experimental design as a multivariate optimization tool that enables both the reduction of the total number of experiments and detection of the factor interactions. Satisfactory separation of analytes was achieved in a short time by using a monolithic column with a mobile phase containing ethanol, which was used as a strong organic component for the first time to separate NIM and NAP. Due to the porous structure of the monolithic column, acceptable column pressure was observed despite the relatively high viscosity of ethanol. The method was validated and successfully applied to determine NIM and NAP in commercial gels, demonstrating that satisfactory chromatographic performance and compliance with validation criteria can be achieved using green solvents. The calculated AGREE score of the method indicates the excellent greenness for pharmaceutical analysis as a result of using a greener solvent for sample and mobile phase preparation. The results of this study demonstrate that ethanol and water-based mobile phases can be used in pharmaceutical analysis, making it an important effort to reduce the toxicity levels of the HPLC process.

References

- [1] K. Brune, P. Patrignani, New insights into the use of currently available non-steroidal anti-inflammatory drugs, *J Pain Res*, 8, 2015, 105–118.
- [2] A.K. Singla, M. Chawla, A. Singh, Nimesulide: some pharmaceutical and pharmacological aspects—an update, *J Pharm Pharmacol*, 52, 2000, 467–486.
- [3] K.D. Rainsford, M. Bevilacqua, F. Dallegri, F. Gago, L. Ottonello, G. Sandrini, C. Tassorelli, I.G. Tavares, Pharmacological properties of nimesulide BT - Nimesulide — Actions and Uses, in: K.D. Rainsford (Ed.), Birkhäuser Basel, Basel, 2005: pp. 133–244.
- [4] S.A. Kumar, M. Debnath, J.V.L.N.S. Rao, D.G. Sankar, A New Bioanalytical Method Development & Validation for Simultaneous Estimation of Esomeprazole and Naproxen in

- Human Plasma by Using RP-HPLC, *J Pharm Res Int*, 4, 2014, 2312–2327.
- [5] D.J. Angiolillo, S.M. Weisman, Clinical Pharmacology and Cardiovascular Safety of Naproxen, *Am J Cardiovasc Drugs*, 17, 2017, 97–107.
- [6] M. Locatelli, V. Ferrone, R. Cifelli, R.C. Barbacane, G. Carlucci, Microextraction by packed sorbent and high performance liquid chromatography determination of seven non-steroidal anti-inflammatory drugs in human plasma and urine, *J Chromatogr A*, 1367, 2014, 1–8.
- [7] P. Gallo, S. Fabbrocino, F. Vinci, M. Fiori, V. Danese, A. Nasi, L. Serpe, Multi-residue determination of non-steroidal anti-inflammatory drug residues in animal serum and plasma by HPLC and photo-diode array detection, *J Chromatogr Sci*, 44, 2006, 585–590.
- [8] L. Escuder-Gilabert, Y. Martín-Biosca, S. Sagrado, R.M. Villanueva-Camañas, M.J. Medina-Hernández, Quality control of pharmaceuticals containing non-steroidal anti-inflammatory drugs by micellar liquid chromatography, *Chromatographia*, 55, 2002, 283–288.
- [9] C. Onal, G. Tırs, E.K. Tekkeli, A. Onal, Ultra fast liquid chromatographic analysis of nonsteroidal anti-inflammatory drugs with fluorimetric detection in tap water, urine, and pharmaceutical samples, *Int J Environ Anal Chem*, 2022, 1–11.
- [10] L.A. Al-Khateeb, W.E. Hakami, Reliable chromatographic determination of non-steroidal anti-inflammatory drugs in real samples matrices, *Int J Environ Anal Chem*, 101, 2021, 1785–1802.
- [11] S. Riaño, M.C. Alcudia-León, R. Lucena, S. Cárdenas, M. Valcárcel, Determination of non-steroidal anti-inflammatory drugs in urine by the combination of stir membrane liquid–liquid–liquid microextraction and liquid chromatography, *Anal Bioanal Chem*, 403, 2012, 2583–2589.
- [12] P.D. Tzanavaras, D.G. Themelis, Validated high-throughput HPLC assay for nimesulide using a short monolithic column, *J Pharm Biomed Anal*, 43, 2007, 1483–1487.
- [13] M.-S. Kim, Y.-S. Park, S.-H. Kim, S.-Y. Kim, M.-H. Lee, Y.-H. Kim, D.-W. Kim, S.-C. Yang, J.-S. Kang, Quantification of animesulide in human plasma by high-performance liquid chromatography with ultraviolet detector (HPLC-UV): application to pharmacokinetic studies in 28 healthy Korean subjects, *J Chromatogr Sci*, 50, 2012, 396–400.
- [14] R. Nageswara Rao, S. Meena, A. Raghuram Rao, An overview of the recent developments in analytical methodologies for determination of COX-2 inhibitors in bulk drugs, pharmaceuticals and biological matrices, *J Pharm Biomed Anal*, 39, 2005, 349–363.
- [15] M. Starek, J. Krzek, A review of analytical techniques for determination of oxicams, nimesulide and nabumetone, *Talanta*, 77, 2009, 925–942.
- [16] T.-V. Pham, X.-L. Mai, T.-A.-T. Le, J.-Y. Lee, G. Lee, D.-J. Kim, S.-B. Han, K.H. Kim, Development and validation of an HPLC method using a less hazardous mobile phase for the determination of some β -Lactams, *Bull Korean Chem Soc*, 40, 2019, 863–871.
- [17] M. Tobiszewski, Introduction to Green Analytical Chemistry, in: *Handb. Green Chem.*, 2018: pp. 103–116.
- [18] J.F. Farid, N.M. Mostafa, Y.M. Fayez, H.M. Essam, Systemic optimization and validation of normal and reversed-phase eco-friendly chromatographic methods for simultaneous determination of paracetamol and phenylephrine hydrochloride in the presence of paracetamol impurities, *J AOAC Int*, 105, 2022, 26–33.
- [19] M. Yabré, L. Ferey, T.I. Somé, O. Mercier, K. Gaudin, Green reversed-phase HPLC development strategy: Application to artesunate and amodiaquine analysis, *J Sep Sci*, 43, 2020, 4390–4404.
- [20] Z.H. Shar, G.A. Sumbal, S.T.H. Sherazi, H. Kara, M. Hussain, M.I. Bhangar, Determination of ochratoxin A in poultry feed by high-performance liquid chromatography with a monolithic column, *Anal Lett*, 48, 2015, 396–407.
- [21] M. Staniak, M. Wójciak, I. Sowa, K. Tyszczyk-Rotko, M. Strzemiński, S. Dresler, W. Myśliński, Silica-based monolithic columns as a tool in HPLC—an overview of application in analysis of active compounds in biological samples, *Molecules*, 25, 2020, 3149.
- [22] C.S. Funari, A.J. Cavalheiro, R.L. Carneiro, Coupled monolithic columns as an alternative for the use of viscous ethanol–water mobile phases on chromatographic fingerprinting complex samples, *Rev Bras Farmacogn*, 28, 2018, 261–266.
- [23] A.L. Assassi, C.-E. Roy, P. Perovitch, J. Auzerie, T. Hamon, K. Gaudin, Green analytical method development for statin analysis, *J Chromatogr A*, 1380, 2015, 104–111.
- [24] A. Dogan, C.C. Eylem, N.E.B. Akduman, Application of green methodology to pharmaceutical analysis using eco-friendly ethanol-water mobile phases, *Microchem J*, 157, 2020, 104895.
- [25] A.E. Ibrahim, H. Saleh, M. Elhenawee, Assessment and validation of green stability indicating RP-HPLC method for simultaneous determination of timolol and latanoprost in pharmaceutical dosage forms using eco-friendly chiral mobile phase, *Microchem J*, 148, 2019, 21–26.
- [26] A. Hemdan, R. Magdy, M. Farouk, N. V Fares, Central composite design as an analytical optimization tool for the development of eco-friendly HPLC-PDA methods for two antihypertensive mixtures containing the angiotensin receptor blocker Valsartan: Greenness assessment by four evaluation tools, *Microchem J*, 183, 2022, 108105.
- [27] S.B. Ganorkar, A.A. Shirkhedkar, Design of experiments in liquid chromatography (HPLC) analysis of pharmaceuticals: analytics, applications, implications and future prospects, 36, 2017, 20160025.
- [28] L. Latrous, Optimization and validation in liquid chromatography using design of experiments, *Chem Africa*, 5, 2022, 437–458.
- [29] P.K. Sahu, N.R. Ramiseti, T. Cecchi, S. Swain, C.S. Patro, J. Panda, An overview of experimental designs in HPLC method development and validation, *J Pharm Biomed Anal*, 147, 2018, 590–611.
- [30] D. Sansaltık Yaşın, A. Arslantürk Bingül, A. Karaküçük, Z.Ş. Teksin, Development and validation of an HPLC method using an experimental design for analysis of amlodipine besylate and enalapril maleate in a fixed-dose combination, *Turkish J Pharm Sci*, 18, 2021, 306–318.
- [31] S.L.C. Ferreira, R.E. Bruns, H.S. Ferreira, G.D. Matos, J.M. David, G.C. Brandão, E.G.P. da Silva, L.A. Portugal, P.S. dos Reis, A.S. Souza, W.N.L. dos Santos, Box-Behnken design: An alternative for the optimization of analytical methods, *Anal Chim Acta*, 597, 2007, 179–186.
- [32] F. Pena-Pereira, W. Wojnowski, M. Tobiszewski, AGREE-Analytical GREENness metric approach and software, *Anal Chem*, 92, 2020, 10076–10082.
- [33] G. Derringer, R. Suich, Simultaneous optimization of several response variables, *J Qual Technol*, 12, 1980, 214–219.
- [34] ICH Expert Working Group, International Conference on Harmonisation of Technical Requirements for Registration of Pharmaceuticals for Human Use Validation of Analytical Procedures: Text and Methodology Q2(R1), 2005.
- [35] M. (Michael E. Swartz, I.S. Krull, *Handbook of analytical validation*, CRC Press, 2012.
- [36] S. Yıldırım, A. Kadioğlu, A. Sağlam, A. Yaşar, H.E. Sellitepe, Fast determination of anthocyanins and free pelargonidin in fruits, fruit juices, and fruit wines by high-performance liquid chromatography using a core-shell column, *J Sep Sci*, 39, 2016.
- [37] V.R. de Almeida Borges, A.F. Ribeiro, C. de Souza Anselmo, L.M. Cabral, V.P. de Sousa, Development of a high performance liquid chromatography method for quantification of isomers β -

- caryophyllene and α -humulene in copaiba oleoresin using the Box-Behnken design, *J Chromatogr B*, 940, 2013, 35–41.
- [38] B. Jancic-Stojanovic, A. Malenovic, D. Ivanovic, T. Rakic, M. Medenica, Chemometrical evaluation of ropinirole and its impurity's chromatographic behavior, *J Chromatogr A*, 1216, 2009, 1263–1269.
- [39] R.E. Saraya, S. El Deeb, B.I. Salman, A.E. Ibrahim, Highly sensitive high-performance thin-layer chromatography method for the simultaneous determination of molnupiravir, favipiravir, and ritonavir in pure forms and pharmaceutical formulations, *J Sep Sci*, 45, 2022, 2582–2590.
- [40] A. Gałuszka, Z. Migaszewski, J. Namieśnik, The 12 principles of green analytical chemistry and the SIGNIFICANCE mnemonic of green analytical practices, *TrAC - Trends Anal Chem*, 50, 2013, 78–84.
- [41] I.E. Mikhail, H. Elmansi, F. Belal, A. Ehab Ibrahim, Green micellar solvent-free HPLC and spectrofluorimetric determination of favipiravir as one of COVID-19 antiviral regimens, *Microchem J*, 165, 2021, 106189.
- [42] E.A. Rashad, S.S. Elsayed, J.J.M. Nasr, F.A. Ibrahim, Factorial design optimized green reversed-phase high-performance liquid chromatography for simultaneous determination of aspirin and clopidogrel in pharmaceutical tablets, *Microchem J*, 190, 2023, 108610.
- [43] M. Wadie, E.M. Abdel-Moety, M.R. Rezk, M.A. Tantawy, Eco-friendly chiral HPLC method for determination of alfuzosin enantiomers and solifenacin in their newly pharmaceutical combination: Method optimization via central composite design, *Microchem J*, 165, 2021, 106095.

Supplementary Informations

Table S1. Analysis of variance (ANOVA) of Box–Behnken design (BBD) for resolution (Y1)

Source	Sum of Squares	df	Mean Square	F-value	p-value	
Model	1.17	9	0.1295	1341.62	< 0.0001	significant
A-pH	0.0165	1	0.0165	170.68	< 0.0001	
B-Ethanol amount	1.14	1	1.14	11821.06	< 0.0001	
C-Flow rate	0.0006	1	0.0006	6.73	0.0358	
AB	0.0000	1	0.0000	0.3251	0.5864	
AC	0.0000	1	0.0000	0.1482	0.7117	
BC	0.0005	1	0.0005	5.30	0.0549	
A ²	0.0038	1	0.0038	39.48	0.0004	
B ²	0.0003	1	0.0003	3.06	0.1239	
C ²	0.0021	1	0.0021	21.98	0.0022	
Residual	0.0007	7	0.0001			
Lack of Fit	0.0005	3	0.0002	3.68	0.1201	not significant
Pure Error	0.0002	4	0.0000			
Cor Total	1.17	16				
Std. Dev.	0.0098		R²	0.9994		
Mean	0.4714		Adjusted R²	0.9987		
C.V. %	2.08		Predicted R²	0.9930		
			Adeq Precision	112.2840		

Table S2. Analysis of variance (ANOVA) of Box–Behnken design (BBD) for capacity factor (Y2)




Source	Sum of Squares	df	Mean Square	F-value	p-value	
Model	1.81	9	0.2014	59152.35	< 0.0001	significant
A-pH	0.0000	1	0.0000	8.91	0.0204	
B-Ethanol amount	1.80	1	1.80	5.275E+05	< 0.0001	
C-Flow rate	1.540E-06	1	1.540E-06	0.4523	0.5228	
AB	6.370E-07	1	6.370E-07	0.1871	0.6783	
AC	3.620E-07	1	3.620E-07	0.1064	0.7539	
BC	4.776E-06	1	4.776E-06	1.40	0.2749	
A ²	0.0000	1	0.0000	9.84	0.0164	
B ²	0.0165	1	0.0165	4839.00	< 0.0001	
C ²	7.514E-06	1	7.514E-06	2.21	0.1809	
Residual	0.0000	7	3.404E-06			
Lack of Fit	7.021E-06	3	2.340E-06	0.5569	0.6709	not significant
Pure Error	0.0000	4	4.202E-06			
Cor Total	1.81	16				
Std. Dev.	0.0018		R²	1.0000		
Mean	0.0573		Adjusted R²	1.0000		
C.V. %	3.22		Predicted R²	0.9999		
			Adeq Precision	675.2656		

Table S3. Analysis of variance (ANOVA) of Box–Behnken design (BBD) for retention time of NAP (Y3)

Source	Sum of Squares	df	Mean Square	F-value	p-value	
Model	1.05	9	0.1164	18867.05	< 0.0001	significant
A-pH	0.0005	1	0.0005	83.82	< 0.0001	
B-Ethanol amount	0.7850	1	0.7850	1.273E+05	< 0.0001	
C-Flow rate	0.2101	1	0.2101	34068.76	< 0.0001	
AB	0.0001	1	0.0001	13.33	0.0082	
AC	1.105E-07	1	1.105E-07	0.0179	0.8973	
BC	1.349E-06	1	1.349E-06	0.2187	0.6542	
A ²	0.0001	1	0.0001	11.47	0.0117	
B ²	0.0461	1	0.0461	7472.91	< 0.0001	
C ²	0.0038	1	0.0038	611.82	< 0.0001	
Residual	0.0000	7	6.167E-06			
Lack of Fit	0.0000	3	8.356E-06	1.85	0.2792	not significant
Pure Error	0.0000	4	4.526E-06			
Cor Total	1.05	16				
Std. Dev.	0.0025		R²	1.0000		
Mean	0.5925		Adjusted R²	0.9999		
C.V. %	0.4191		Predicted R²	0.9996		
			Adeq Precision	499.1127		



Electrochemical properties of non-peripherally and peripherally tetra-[(1-benzylpiperidin-4-yl)oxy] substituted phthalocyanines

Asiye Nas¹ , Gülsev Dilber^{1*} , Zekeriya Biyiklioglu² 

¹Karadeniz Technical University, Maçka Vocational School, 61750, Maçka, Trabzon, Türkiye

²Karadeniz Technical University, Faculty of Science, Department of Chemistry, 61080 Trabzon, Türkiye

Abstract

In this study, 1-benzylpiperidin-4-oxy substituted non-peripheral and peripheral metal free (3, 7), chloro manganese (III) (4, 8), oxotitanium (IV) (5, 9) and Cu(II) (6, 10) phthalocyanine complexes are synthesized and electrochemical properties were examined. Novel phthalocyanines compounds have been characterized by Fourier transform infrared, electronic spectroscopy, and mass spectra. Electrochemistry of non-peripherally and peripherally tetra-[(1-benzylpiperidine-4-yl)oxy] substituted metal-free and metallophthalocyanines were investigated by cyclic voltammetry (CV). Owing to the redox inactivity of the metal-free and Cu²⁺ ion of metal free (3, 7) and Cu(II) (6, 10) phthalocyanines, Phthalocyanine based reductions and oxidation processes are recorded. Unlike, electrochemical analyses showed that chloro manganese (III) (4, 8) and oxotitanium (IV) (5, 9) phthalocyanines illustrated metal based redox processes in addition to the Pc ring based reactions. The manganese (III) (4, 8) and the oxotitanium (IV) (5, 9) phthalocyanines extra metal based redox processes were observed with those of Pc rings.

Keywords: Titanium, manganese, electrochemistry, redox-active, piperidine

1. Introduction

Phthalocyanines (Pcs), which have been the subject of many studies for many years, are very important compounds for technological systems and are considered to be key compounds in solving many problems in the future. Phthalocyanine (Pc) compounds are widely used in the production of high-tech materials thanks to their optical, electrical and thermal properties and have attracted great attention in many fields such as; photovoltaic cells, thin film, liquid crystal, gas sensor, chemical sensor, corrosion inhibitor, optical data storage, semiconductors in recent years [1–8]. Pcs are used in many areas of technology due to their interesting electrochemical properties [9], and for this reason, electrochemical investigations play an important role in their industrial applications. Since phthalocyanines are compounds with electron exchange capacity and interesting electrochemical properties, a great deal of work has been done on their usability in various electrochemical applications [10]. The phthalocyanine ring is a redox active ring that can be oxidized by donating electrons at the HOMO (a_{1u}) or reduced by taking electrons at the LUMO (e_g). The ring-centered

redox process of phthalocyanines results from the fact that reduction and oxidation reactions occur through the ring. In the alternating voltammograms of metal-free and metalated phthalocyanines, the characteristic reductions and oxidations of the ring-centered redox process are observed as redox peaks or pairs at certain potentials. By using working electrodes in electrochemical methods, it is possible to investigate the electrode reaction of many molecules and to elucidate their electrochemical behavior.

The electron transfer property of the phthalocyanine ring depends on both the type, position [11] and number of substituents and the interaction of the substituents with the phthalocyanine ring and the central metal ion [12–14]. For example, when metals or substituents are different, the HOMO-LUMO transition energies of Pc compounds can change significantly [15]. Electron donating ligands (such as amine, ether, thioether, methoxy groups) attached to the phthalocyanine ring increase the electron density of the center metal, facilitating oxidation and making reduction more difficult, while shifting the redox process to negative

Citation: A. Nas, G. Dilber, Z. Biyiklioglu, Electrochemical properties of non-peripherally and peripherally tetra-[(1-benzylpiperidin-4-yl)oxy] substituted phthalocyanines, Turk J Anal Chem, 5(2), 2023, 98–106.

 <https://doi.org/10.51435/turkjac.1387506>

*** Author of correspondence:** gdilber@ktu.edu.tr

Received: November 07, 2023 **Tel:** +90 (462) 377 76 60

Accepted: November 16, 2023 **Fax:** +90 (462) 512 35 52

potentials. It has been reported in the literature that metallophthalocyanines containing especially redox active metals in the ring center such as Co(II), Mn(III) and, Ti(IV)O etc. at the ring center exhibit excellent electrocatalytic properties [16,17].

For compounds containing the piperidine ring system in their chemical structure, many pharmacological activities such as antibacterial, antifungal, anticancer, antioxidant, antiulcer, and renin inhibitor have been reported [18–24]. In addition, the electrochemical properties of many groups of compounds containing piperidine rings have been examined and it has been reported that they show very different electrochemical properties [25–27].

In this work, the synthesis of the metal-free, Mn(III), oxotitanium (IV) and, Cu(II) Pc complexes containing non-peripheral and peripheral position piperidine moiety were carried out. The electrochemical properties of the new compounds were comparatively examined according to the bonding the position of the substituent to the Pc ring and changing central metal atom.

2. Experimental

2.1. Materials and methods

The materials and equipment used in this study were set out in the supplementary information to the article.

2.2. Synthesis

2.2.1. 1(4), 8(11), 15(18), 22 (23) – Tekrakis - [1-benzylpiperidin-4-yl) oxy] phthalocyanine (3)

3-[(1-benzylpiperidin-4-yl)oxy]phthalonitrile (1) (0.20 g, 0.63 mmol) was dissolved in 2 mL dry n-pentanol and three drops of 1,8-diazabicyclo[5.4.0]undec-7-ene were added to the reaction medium. The reaction mixture was stirred at 160 °C for 24 hours. After the mixture cooled to room temperature, n-hexane was added (20 mL) and the precipitate was filtered. The obtained green product was purified by column chromatography using chloroform-methanol (10:2) solvent system.

Yield: 22 mg (11 %), M.p.: >300 °C (decomposition). FT-IR $\nu_{\max}/\text{cm}^{-1}$: 3028 (Ar-H), 2922-2809 (Aliph. C-H), 1724, 1584, 1491, 1454, 1267, 1104, 1040, 1028, 975, 797, 743, 697. MALDI-TOF, m/z : Calc.: 1271,55 for $\text{C}_{80}\text{H}_{78}\text{N}_{12}\text{O}_4$, Found: 1271,05 [M]⁺. UV/vis (Chloroform, 1×10^{-5} M): λ , nm (log ϵ): 316 (4.85), 352 (4.72), 629 (4.48), 662 (4.61), 697 (5.05), 727 (5.10).

2.2.2. 1(4), 8(11), 15(18), 22 (23) – Tekrakis - [1-benzylpiperidin-4-yl) oxy] phthalocyaninato chloro manganese (III) (4)

3-[(1-benzylpiperidin-4-yl)oxy]phthalonitrile (1) (0.20 g, 0.63 mmol) was dissolved in 2 mL dry n-pentanol, than anhydrous MnCl₂ (0.1 g, 0.32 mmol) and three drops of

1,8-diazabicyclo[5.4.0]undec-7-ene were added to the reaction medium. The reaction mixture was stirred at 160 °C for 24 hours. After the mixture cooled to room temperature, n-hexane was added (20 mL) and the precipitate was filtered. The obtained green product was purified by column chromatography using chloroform-methanol (10:3) solvent system.

Yield: 36 mg (17%), M.p.: >300 °C (decomposition). FT-IR $\nu_{\max}/\text{cm}^{-1}$: 3023 (Ar-H), 2924-2803 (Aliph. C-H), 1586, 1486, 1323, 1228, 1118, 1040, 797, 739, 696. MALDI-TOF, m/z : Calc.: 1359,95 for $\text{C}_{80}\text{H}_{76}\text{N}_{12}\text{O}_4\text{MnCl}$, Found: 1324,09 [M-Cl]⁺. UV/vis (Chloroform, 1×10^{-5} M): λ , nm (log ϵ): 331(4.72), 358 (4.85), 543 (4.38), 687 (4.46), 765 (5.13).

2.2.3. 1(4), 8(11), 15(18), 22 (23) – Tekrakis - [1-benzylpiperidin-4-yl) oxy] phthalocyaninato oxotitanium (IV) (5)

3-[(1-benzylpiperidin-4-yl)oxy]phthalonitrile (1) (0.20 g, 0.63 mmol) was dissolved in 2 mL dry n-pentanol, than anhydrous Ti(OBu)₄ (0.22 mL, 0.63 mmol) and three drops of 1,8-diazabicyclo[5.4.0]undec-7-ene were added to the reaction medium. The reaction mixture was stirred at 160 °C for 24 hours. After the mixture cooled to room temperature, petroleum ether was added (20 mL) and the precipitate was filtered. The obtained green product was purified by column chromatography using chloroform-methanol (10:1) solvent system.

Yield: 29 mg (14 %), M.p.: >300 °C (decomposition). FT-IR $\nu_{\max}/\text{cm}^{-1}$: 3066-3028 (Ar-H), 2953-2852 (Aliph. C-H), 1724, 1584, 1488, 1455, 1267, 1081, 1040, 852, 745, 697. MALDI-TOF, m/z : Calc.: 1333.44 for $\text{C}_{80}\text{H}_{76}\text{N}_{12}\text{O}_5\text{Ti}$, Found: 1273,93 [M-TiO+2]⁺. UV/vis (Chloroform, 1×10^{-5} M): λ , nm (log ϵ): 321 (4.95), 355 (4.87), 661 (4.71), 694 (5.03), 728 (5.21).

2.2.4. 1(4), 8(11), 15(18), 22 (23) – Tekrakis - [1-benzylpiperidin-4-yl) oxy] phthalocyaninato copper (II) (6)

3-[(1-benzylpiperidin-4-yl)oxy]phthalonitrile (1) (0.20 g, 0.63 mmol) was dissolved in 2 mL dry n-pentanol, than anhydrous CuCl₂ (0.04 g, 0.32 mmol) and three drops of 1,8-diazabicyclo[5.4.0]undec-7-ene were added to the reaction medium. The reaction mixture was stirred at 160 °C for 24 hours. After the mixture cooled to room temperature, ethyl alcohol was added (20 mL) and the precipitate was filtered. The obtained blue-green product was purified by column chromatography using chloroform-methanol (10:2) solvent system.

Yield: 44 mg (21 %), M.p.: >300 °C (decomposition). FT-IR $\nu_{\max}/\text{cm}^{-1}$: 3063-3028 (Ar-H), 2954-2851 (Aliph. C-H), 1727, 1589, 1455, 1458, 1236, 1191, 1080, 853, 747, 696. MALDI-TOF, m/z : Calc.: 1333,10 for $\text{C}_{80}\text{H}_{76}\text{N}_{12}\text{O}_4\text{Cu}$, Found: 1333,90 [M]⁺. UV/vis (Chloroform, 1×10^{-5} M): λ , nm (log ϵ): 313 (4.75), 344 (4.74), 634 (4.60), 706 (5.23).

2.2.5. 2(3), 9(10), 16(17), 23(24)- Tetrakis- [1-benzylpiperidin-4-yl] oxy] phthalocyanine (7)

To synthesize compound **7**, the synthetic procedure of compound **3** was followed except that **2** was used instead of **1**. The amounts of the reagents were: 4-[(1-benzylpiperidin-4-yl)oxy]phthalonitrile (**2**) (0.20 g, 0.63 mmol). Solvent system for column chromatography; chloroform/methanol (10:2).

Yield: 23 mg (23%), M.p.: >300 °C (decomposition). FT-IR $\nu_{\max}/\text{cm}^{-1}$: 3065-3028 (Ar-H), 2927-280 (Aliph. C-H), 1607, 1470, 1338, 1232, 1093, 1042, 1007, 733, 696. MALDI-TOF, m/z : Calc.: 1271,55 for $\text{C}_{80}\text{H}_{78}\text{N}_{12}\text{O}_4$, Found: 1271,18 $[\text{M}]^+$. UV/vis (Chloroform, 1×10^{-5} M): λ , nm (log ϵ): 342 (4.80), 393 (4.50), 609 (4.39), 642 (4.55); 669 (4.91), 706 (4.97).

2.2.6. 2(3), 9(10), 16(17), 23(24)- Tetrakis- [1-benzylpiperidin-4-yl] oxy] phthalocyaninato chloro manganese (III) (8)

To synthesize compound **8**, the synthetic procedure of compound **4** was followed except that **2** was used instead of **1**. The amounts of the reagents were: 4-[(1-benzylpiperidin-4-yl)oxy]phthalonitrile (**2**) (0.20 g, 0.63 mmol), anhydrous MnCl_2 (0.1 g, 0.32 mmol). Solvent system for column chromatography; chloroform/methanol (10:3).

Yield: 72 mg (34 %), M.p.: >300 °C (decomposition). FT-IR $\nu_{\max}/\text{cm}^{-1}$: 3065-3023 (Ar-H), 2926-2806 (Aliph. C-H), 1603, 1463, 1404, 1333, 1230, 1052, 1036, 743, 697. MALDI-TOF, m/z : Calc.: 1359,95 for $\text{C}_{80}\text{H}_{76}\text{N}_{12}\text{O}_4\text{MnCl}$, Found: 1324,02 $[\text{M-Cl}]^+$. UV/vis (Chloroform, 1×10^{-5} M): λ , nm (log ϵ): 388 (4.75), 530 (4.33), 661 (4.43), 736 (5.04).

2.2.7. 2(3), 9(10), 16(17), 23(24)- Tetrakis- [1-benzylpiperidin-4-yl] oxy] phthalocyaninato oxotitanium (IV) (9)

To synthesize compound **9**, the synthetic procedure of compound **5** was followed except that **2** was used instead of **1**. The amounts of the reagents were: 4-[(1-benzylpiperidin-4-yl)oxy]phthalonitrile (**2**) (0.20 g, 0.63 mmol), $\text{Ti}(\text{O}i\text{Bu})_4$ (0.22 mL, 0.63 mmol). Solvent system for column chromatography; chloroform/methanol (10:1).

Yield: 40 mg (19 %), M.p.: >300 °C (decomposition). FT-IR $\nu_{\max}/\text{cm}^{-1}$: 3066-3028 (Ar-H), 2953-2852 (Aliph. C-H), 1724, 1584, 1488, 1455, 1267, 1081, 1040, 852, 745, 697. MALDI-TOF, m/z : Calc.: 1333.44 for $\text{C}_{80}\text{H}_{76}\text{N}_{12}\text{O}_5\text{Ti}$, Found: 1333,90 $[\text{M}]^+$, 1273,63 $[\text{M-TiO}+2]^+$. UV/vis (Chloroform, 1×10^{-5} M): λ , nm (log ϵ): 346 (4.96), 397 (4.68), 637 (4.70), 669 (4.95), 705 (5.27).

2.2.8. 2(3), 9(10), 16(17), 23(24)- Tetrakis- [1-benzylpiperidin-4-yl] oxy] phthalocyaninato copper (II) (10)

To synthesize compound **10**, the synthetic procedure of compound **6** was followed except that **2** was used instead of **1**. The amounts of the reagents were: 4-[(1-benzylpiperidin-4-yl)oxy]phthalonitrile (**2**) (0.20 g, 0.63 mmol), anhydrous CuCl_2 (0.04 g, 0.32 mmol). Solvent system for column chromatography; chloroform/methanol (10:2).

Yield: 71 mg (34%), M.p.: >300 °C (decomposition). FT-IR $\nu_{\max}/\text{cm}^{-1}$: 3061-3030 (Ar-H), 2921-2851 (Aliph. C-H C-H), 1607, 1467, 1399, 1341, 1230, 1116, 1093, 1043, 852, 744, 697. MALDI-TOF, m/z : Calc.: 1333,10 for $\text{C}_{80}\text{H}_{76}\text{N}_{12}\text{O}_4\text{Cu}$, Found: 1333,78 $[\text{M}]^+$. UV/vis (Chloroform, 1×10^{-5} M): λ , nm (log ϵ): 338 (4.97), 383 (4.41), 615 (4.72), 682 (5.24).

3. Results and discussion

3.1. Synthesis and characterization

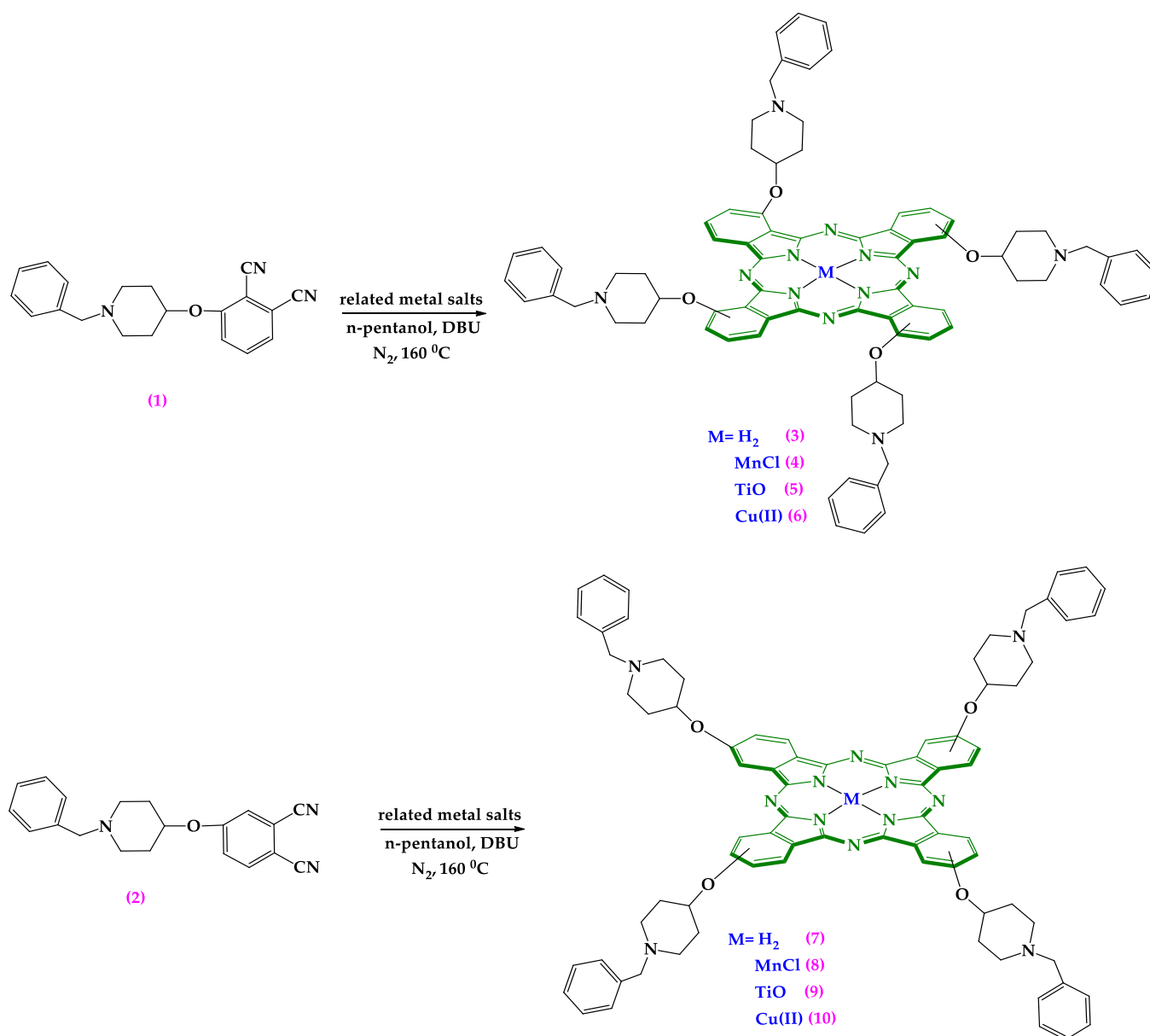
The phthalonitrile **1** [28] and **2** [29] were synthesized according to the procedures in a previously published paper. The synthesis method of Pc compounds is shown in detail in Scheme 1.

Structural characterization of the novel synthesized compounds was performed using FT-IR, UV-Vis, MALDI-TOF mass spectroscopic techniques.

Non-peripheral and peripheral metal-free (**3**, **7**), MnPc (**4**, **8**), TiPc (**5**, **9**) and CuPc (**6**, **10**) Pc compounds were accomplished by treatment of phthalonitrile **1** and **2** in the presence of the corresponding anhydrous metal salts; without metal, anhydrous MnCl_2 , $\text{Ti}(\text{O}i\text{Bu})_4$ and CuCl_2 . The reaction yields obtained for these compounds at 160 °C in dried *n*-pentanol are 11% for **3**, 17% for **4**, 29% for **5**, 21% for **6**, 23% for **7**, 34% for **8**, 19% for **9** and 21% for **10**, respectively. All synthesized Pc compounds were purified using column chromatography.

In the FT-IR spectra of non-peripheral (**3–6**) and peripheral (**7–10**) Pc compounds, the disappearance of $\text{C}\equiv\text{N}$ peak showed at 2233 cm^{-1} and 2230 of compounds **1** and **2** is an indication that cyclotetramerisation of phthalonitriles have occurred. The NMR spectra of **4**, **6**, **8** and **10** could not be determined because of the presence of paramagnetic manganese and copper atoms [30]. The spectra of the other's synthesized Pcs were not determined because of probable aggregation at the concentration for NMR measurements.

Mass spectra of Pc compounds (**3–10**) supported their proposed structures the appearance of molecular ion peaks at $1271,05$ as $[\text{M}]^+$ for **3** (Fig. S1), $1324,09$ as $[\text{M-Cl}]^+$ for **4** (Fig. S2), as $1273,93$ $[\text{M-TiO}+2]^+$ for **5** (Fig. S3), $1333,90$ as $[\text{M}]^+$ for **6** (Fig. 1), $1271,18$ as $[\text{M}]^+$ for **7** (Fig. 2), $1324,09$ as $[\text{M-Cl}]^+$ for **8** (Fig. S4), $1333,90$ as $[\text{M}]^+$, $1273,63$ $[\text{M-TiO}+2]^+$ for **9** (Fig. 3) and $1333,78$ as $[\text{M}]^+$ for **10** (Fig. S5).



Scheme 1. Synthesis of new phthalocyanines 3–10 (related metal salts; anhydrous MnCl₂, Ti(OBu)₄, CuCl₂)

3.2. UV-vis absorption spectra

UV-Vis spectroscopy is known to be one of the best methods to characterize Pc complexes. Two characteristic peaks called Q and B bands are observed in the UV spectra of Pcs [29]. In the UV region, the Q band generally appears at around 600–750 nm while the B band arises at about 300–450 nm. Absorption of the Q-band of the Pc compounds in the UV-vis spectrum is affected to a different degree by the central metal, ligand-bound in the axial position, solvent, binding position of the substituent and, aggregation [31].

The UV-vis spectra of the metal-free Pc complexes 3 and 7 showed intense double Q band absorption at λ_{max} : 727, 697 nm for 3 and 706, 669 nm for 7, as expected (Fig. 4). The B band signals of these compounds are at λ_{max} : 352, 316 nm for 3 and 393, 342 nm for 7. Metallophthalocyanine complexes 4–6 and 8–10 exhibited intense Q band caused by π - π^* transitions at λ_{max} : 765 (with single shoulders 687) nm for 4 (Fig. 5), 728

(with double shoulders 661 and 622) nm for 5 (Fig. 6), 706 (with single shoulders 634) nm for 6 (Fig. 7), 736 (with single shoulders 661) nm for 8 (Fig. 5), 705 (with double shoulders 669 and 606) nm for 9 (Fig. 6) and 682 (with single shoulders 661) nm for 10 (Fig. 7).

The B bands of these Pc were observed in the UV region at λ_{max} : 352, 316 nm for 3; 358 and 331 nm for 4; 355, 321 nm for 5; 344, 313 nm for 6; 393, 342 nm for 7, 388 nm for 8; 397, 346 nm for 9 and 383, 338 nm for 10.

When a comparison is made between these data obtained, the Q bands of the non-peripheral Pcs 3–6 are red shifted 11, 21, 23 and, 24 nm according to the corresponding peripheral substituted Pcs 7–10 respectively in chloroform. It is a well-known fact that the substitution of the Pcs at non-peripheral positions causes a significant degree red shifted of the Q band [32, 33].

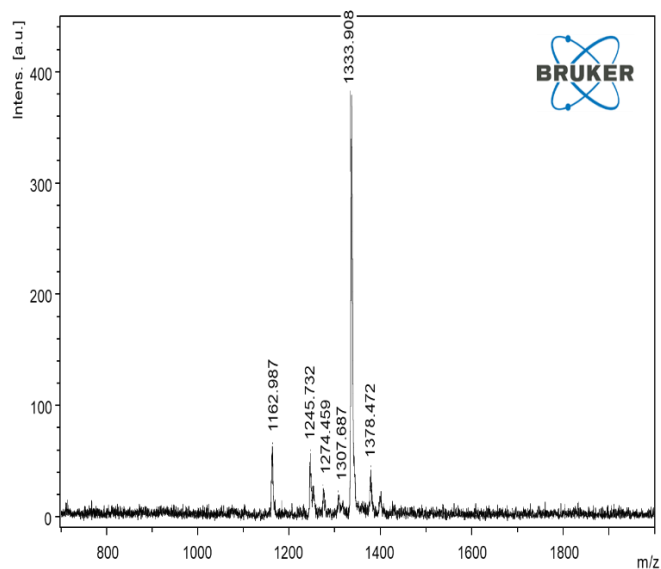


Figure 1. Mass spectrum of compound 6

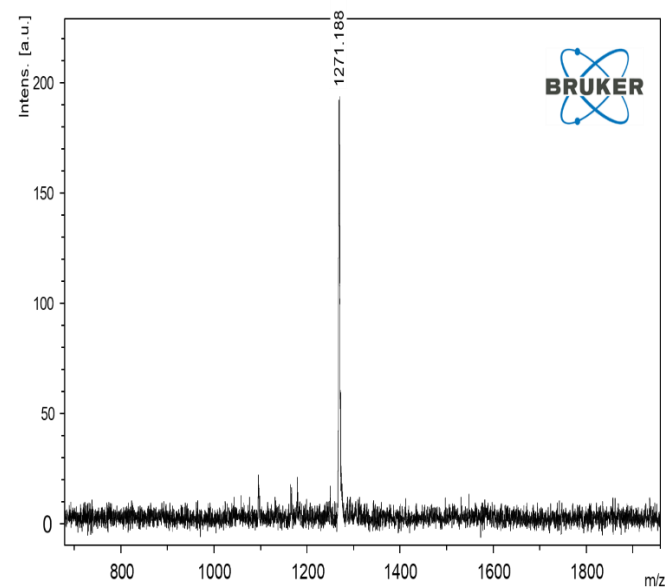


Figure 2. Mass spectrum of compound 7

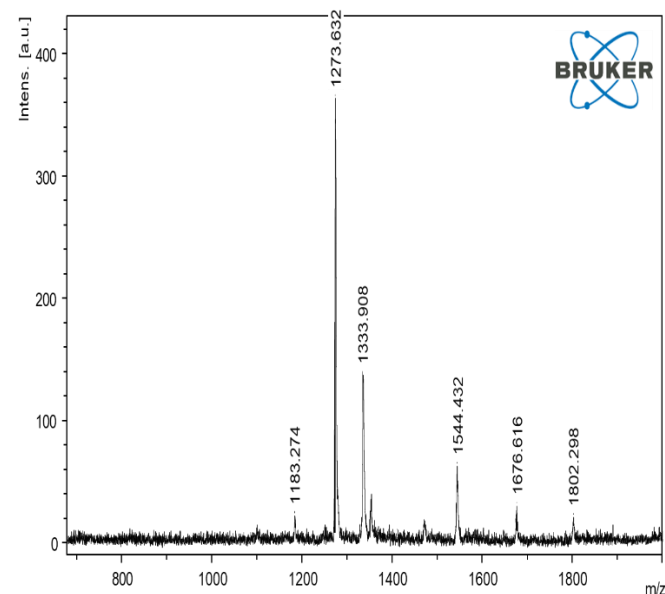


Figure 3. Mass spectrum of compound 9

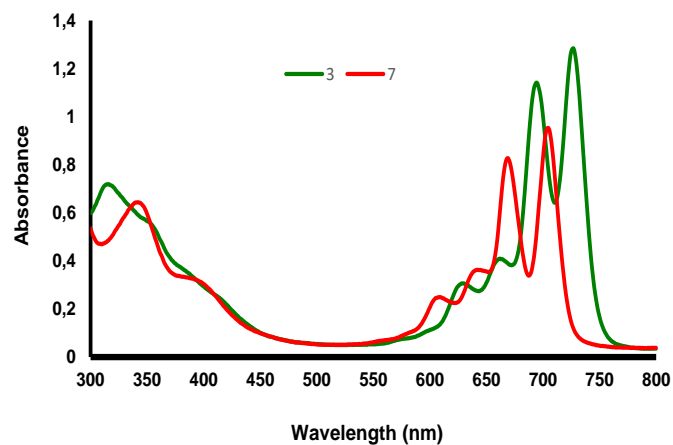


Figure 4. Absorption spectra of compounds 3 and 7 in chloroform at $1.10^{-5} M$

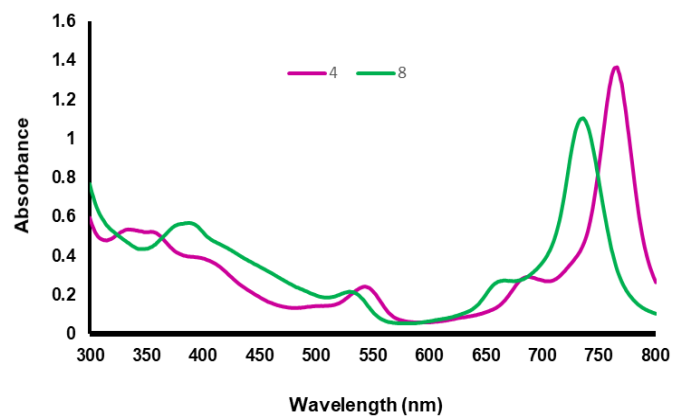


Figure 5. Absorption spectra of compounds 4 and 8 in chloroform at $1.10^{-5} M$

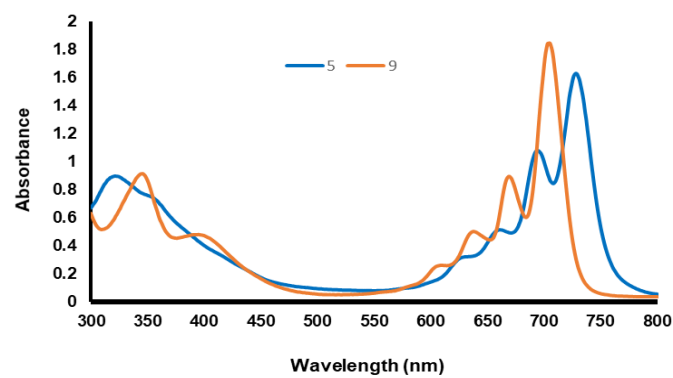


Figure 6. Absorption spectra of compounds 5 and 9 in chloroform at $1.10^{-5} M$

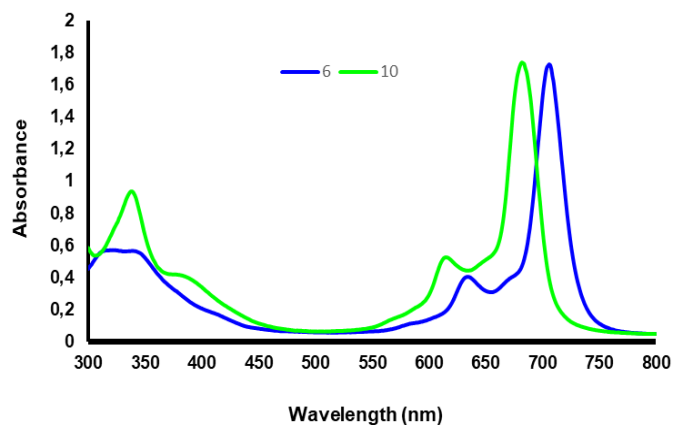


Figure 7. Absorption spectra of compounds 6 and 10 in chloroform at $1.10^{-5} M$

The manganese Pc complexes, unlike other Pc complexes, exhibit remarkable absorption properties in the UV-Vis spectrum. Although it is known in the literature that the main absorption Q bands of MnPc shift to red in the range of 710–890 nm [34]. We could see this shift of Q band in the UV spectrum of the **4** and **8** (at λ_{\max} : 765 and 736 nm, respectively) synthesized compounds (Fig. 5).

Additionally, the characteristic broad peak of the manganese Pcs between 470 nm and 570 nm appears in the region by the charge-transfer (CT) exciton owing to the existence of unsaturated manganese ions as a metal atom [35–37]. CT bands of the compounds **4** and **8** were observed as a broad peak at λ_{\max} : 543 and 530 nm, respectively.

3.3. Electrochemical studies

Electrochemical responses of non-peripherally and peripherally tetra-[(1-benzylpiperidine-4-yl)oxy] substituted metallophthalocyanines **3–10** were investigated using cyclic voltammetry (CV) in DCM/TBAP electrolyte at room temperature. The peak potential separation (ΔE_p), half-wave potential ($E_{1/2}$) and the potential difference between the first half-peak processes ($\Delta E_{1/2}$), are listed in Table 1.

Table 1. Voltammetric analysis results of the phthalocyanines.

Phthalocyanines	Label	^a $E_{1/2}$	^b ΔE_p (mV)	^c $\Delta E_{1/2}$
Metal-free 3	R ₁	-0.85	154	1.73
	R ₂	-1.24	162	
	O ₁	0.88	158	
Metal-free 7	R ₁	-0.82	83	1.75
	R ₂	-1.13	85	
	O ₁	0.93	166	
MnPc 4	R ₁	-0.18	142	1.04
	R ₂	-1.05	154	
	R ₃	-1.59	166	
	O ₁	0.86	150	
MnPc 8	R ₁	-0.22	80	1.14
	R ₂	-1.00	147	
	R ₃	-1.54	160	
	O ₁	0.92	171	
TiOPc 5	R ₁	-0.59	140	1.40
	R ₂	-0.80	145	
	R ₃	-1.00	154	
	R ₄	-1.20	148	
	O ₁	0.81	161	
TiOPc 9	R ₁	-0.77	160	1.62
	R ₂	-1.07	161	
	R ₃	-1.41	167	
	O ₁	0.85	150	
CuPc 6	R ₁	-0.96	159	1.83
	R ₂	-1.43	172	
	O ₁	0.87	161	
CuPc 10	R ₁	-0.93	87	1.94
	R ₂	-1.26	82	
	O ₁	1.01	164	

^a: $E_{1/2}$ values ($(E_{pa}+E_{pc})/2$) were given versus SCE at 0.100 V s⁻¹ scan rate. ^b: $\Delta E_p = E_{pa} - E_{pc}$. ^c: $\Delta E_{1/2} = E_{1/2}$ (first oxidation) - $E_{1/2}$ (first reduction)

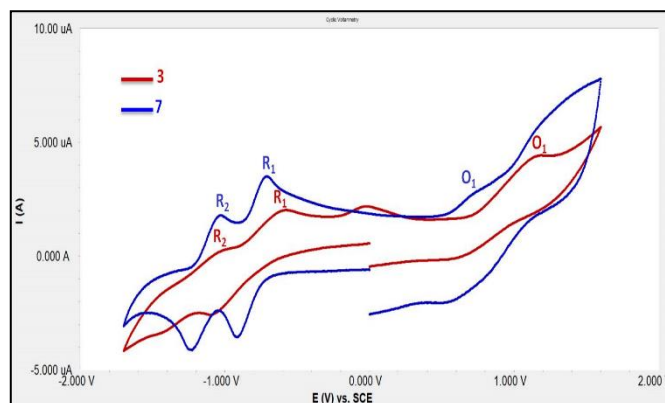


Figure 8. Cyclic voltammogram of metal-free phthalocyanines **3** and **7**

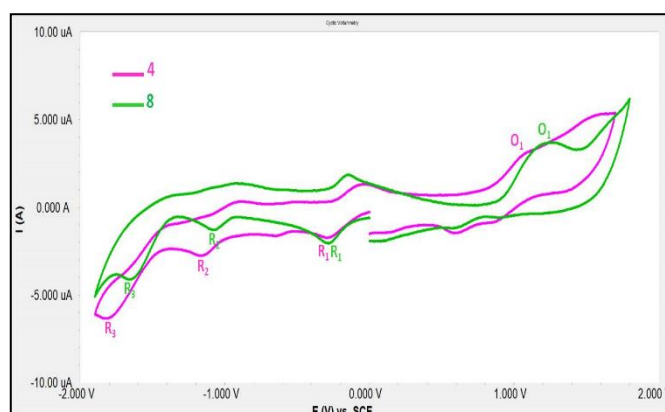


Figure 9. Cyclic voltammogram of manganese(III) phthalocyanines **4** and **8**

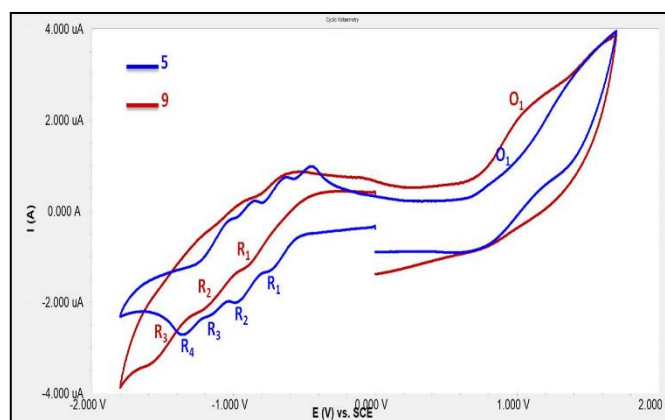


Figure 10. Cyclic voltammogram of titanium(IV) phthalocyanines **5** and **9**

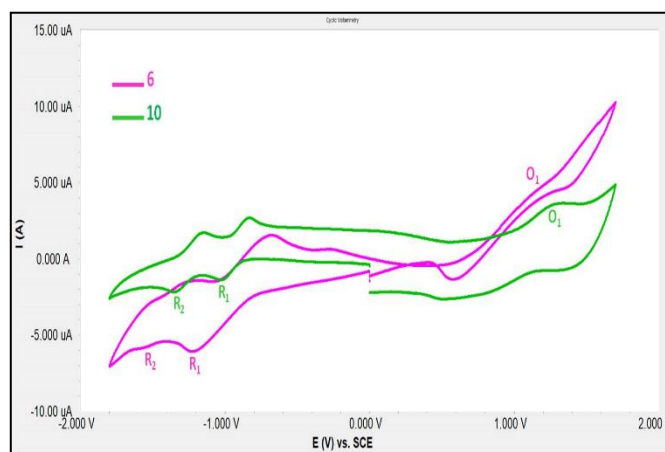


Figure 11. Cyclic voltammogram of copper(II) phthalocyanines **6** and **10**

Fig. 8 shows CV of non-peripherally and peripherally tetra-[(1-benzylpiperidine-4-yl)oxy] substituted metal-free Pcs compounds **3** and **7** in DCM/TBAP electrolyte on a Pt working electrode. When **Fig. 8** was examined, it was determined that metal-free Pcs (**3**, **7**) gave two Pc ring-based reduction peaks in the cathodic region. The half-wave peak potentials of the reduction peaks, expressed as R_1 and R_2 , are $E_{1/2}$: -0.85 V (R_1), -1.24 V (R_2) for the compound **3** and $E_{1/2}$: -0.82 V (R_1), -1.13 V (R_2) for the compound **7**. Based on the calculated ΔE_p values, it was determined that all of the reduction peaks denoted as R_1 and R_2 for metal-free Pcs (**3**, **7**) were quasi-reversible character. During the potential scanning in the anodic region, the half-wave peak potentials of the oxidation peaks symbolized by O_1 for metal-free Pcs (**3**, **7**) were calculated as $E_{1/2} = 0.88$ V for **3** and $E_{1/2} = 0.93$ V for **7**. Based on the ΔE_p values of the oxidation peaks symbolized by O_1 , it has been revealed that both of them have quasi-reversible character.

Fig. 9 shows CV of non-peripherally and peripherally tetra-[(1-benzylpiperidine-4-yl)oxy] substituted manganese(III) Pcs (**4** and **8**) in DCM/TBAP electrolyte on a Pt working electrode. Since manganese(III) and titanium(IV) Pcs have redox active metal ions, they show both ring and metal-based reduction processes [38–40]. During cathodic potential screening of MnPcs (**4**, **8**), it was determined that they gave two metal-centered reduction processes, $R_1 = -0.18$ V, $R_2 = -1.05$ V for **4** and $R_1 = -0.22$ V, $R_2 = -1.00$ V for **8**, respectively. Again, during the cathodic potential scan, it was determined that they gave Pc ring-centered reduction processes, with $R_3 = -1.59$ V for **4** and $R_3 = -1.54$ V for **8**, respectively. In addition, it has been observed that the reduction peaks indicated by R_1 , R_2 and R_3 for manganese(III) Pcs **4** and **8** have quasi-reversible character according to the calculated ΔE_p values. During the potential scan in the anodic region, the half-wave peak potentials of the oxidation peaks symbolized by O_1 for MnPcs (**4**, **8**) were calculated as $E_{1/2} = 0.86$ V for **4** and $E_{1/2} = 0.92$ V for **8**. Based on the ΔE_p values of the oxidation peaks, it was determined that both of them were quasi-reversible.

Fig. 10 shows CV of non-peripherally and peripherally tetra-[(1-benzylpiperidine-4-yl)oxy] substituted titanium(IV) Pcs (**5** and **9**) in DCM/TBAP electrolyte on a Pt working electrode. As shown in **Fig. 10**, non-peripheral substituted oxotitanium(IV) Pc compound **5** has 4 reduction peaks in the cathodic region ($R_1 = -0.59$ V, $R_2 = -0.80$ V, $R_3 = -1.00$ V, $R_4 = -1.20$ V) and 1 oxidation peak in the anodic region ($O_1 = 0.81$ V). Also, peripheral substituted oxotitanium(IV) Pc compound **9** has 3 reduction peaks ($R_1 = -0.77$ V, $R_2 = -1.07$ V, $R_3 = -1.41$ V) in the cathodic region and 1 oxidation peak ($O_1 = 0.85$ V) in the anodic region. During the cathodic potential screening of compound **5**, two metal-centered reduction

processes ($R_1 = -0.59$ V and $R_3 = -1.00$ V), two Pc ring-based reduction processes ($R_2 = -0.80$ V and $R_4 = -1.20$ V) were observed. During the cathodic potential scanning of compound **9** showed one metal-centered reduction process ($R_2 = -1.07$ V) and two Pc ring-based reduction processes ($R_1 = -0.77$ V and $R_3 = -1.41$ V).

Fig. 11 shows CV of non-peripherally and peripherally tetra-[(1-benzylpiperidine-4-yl)oxy] substituted copper (II) Pcs **6** and **10** in DCM. As shown in **Fig. 11**, CuPcs (**6** and **10**) gave 2 Pc ring-based reduction peaks in the cathodic region. The reduction peaks symbolized as R_1 and R_2 , respectively, are $E_{1/2}$: -0.96 V (R_1), -1.43 V (R_2) for compound **6** and $E_{1/2}$: -0.93 V (R_1), -1.26 V (R_2) for compound **10**. Based on the calculated ΔE_p values of the reduction peaks expressed as R_1 and R_2 for CuPcs (**6**, **10**), it was determined that they were semi-reversible for non-peripheral substituted copper (II) Pc **6** and reversible for peripheral substituted copper (II) Pc **10**. During the potential scanning in the anodic region, the half-wave peak potentials of the oxidation peaks symbolized by O_1 for CuPcs (**6**, **10**) were calculated as $E_{1/2} = 0.87$ V for **6** and $E_{1/2} = 1.01$ V for **10**. Based on the ΔE_p values of the oxidation peaks symbolized by O_1 , it was determined that both of them were semi-reversible.

Additionally, $\Delta E_{1/2}$ values, which determine the HOMO-LUMO energy levels, were calculated for the synthesized metal free Pcs (**3**, **7**), manganese (III) Pcs (**4**, **8**), oxotitanium(IV) Pcs (**5**, **9**) and copper (II) Pcs (**6**, **10**). The HOMO-LUMO energy level was calculated as $\Delta E_{1/2} = 1.73$ V, $\Delta E_{1/2} = 1.75$ V for metal free Pcs (**3**, **7**); $\Delta E_{1/2} = 1.04$ V, $\Delta E_{1/2} = 1.14$ V for MnPcs (**4**, **8**); $\Delta E_{1/2} = 1.40$ V, $\Delta E_{1/2} = 1.62$ V for TiPcs (**5**, **9**); and $\Delta E_{1/2} = 1.83$ V, $\Delta E_{1/2} = 1.94$ V for CuPcs (**6**, **10**).

4. Conclusion

In this paper, non-peripherally and peripherally tetra-[(1-benzylpiperidine-4-yl)oxy] substituted metal-free (**3**, **7**), manganese (III) (**4**, **8**), oxotitanium (IV) (**5**, **9**) and copper (II) (**6**, **10**) phthalocyanine compounds were presented. Characterization of these newly synthesized compounds was carried out using spectroscopic methods such as FT-IR, mass spectroscopy, UV/vis and, MALDI-TOF. Among the new compounds, especially the manganese (III) Pc compounds (**4** and **8**) showed a significant, red-shifted absorption of the Q-band in the UV region that this desired for the application of Pc compounds.

Electrochemical studies of non-peripherally and peripherally tetra-[(1-benzylpiperidine-4-yl)oxy] substituted metal-free (**3**, **7**), manganese (III) (**4**, **8**), oxotitanium (IV) (**5**, **9**) and copper (II) (**6**, **10**) Pc compounds were defined with voltammetric analysis.

According to the results, metal-free Pcs (**3**, **7**), and copper (II) Pcs (**6**, **10**) showed common Pc assigned electron transfer reactions. On the other hand, owing to the redox activity of Mn^{III} and Ti^{IV} metal centers of manganese (**4**, **8**), oxotitanium Pcs (**5**, **9**) compounds extra metal based redox processes were observed with those of Pc rings. Additionally, manganese (III) (**4**, **8**), oxotitanium (IV) Pcs (**5**, **9**) compounds with rich redox activity are important for electrochemical applications.

Acknowledgment

This study was supported by the Karadeniz Technical University Research Fund, Project No: FBA-2019-8429 (Trabzon-Turkey).

References

- [1] K.T. Cho, O. Trukhina, C. Roldán-Carmona, M. Ince, P. Gratia, G. Grancini, P. Gao, T. Marszalek, W. Pisula, Y.R. Paidi, T. Torres, M.K. Nazeeruddin, Molecularly Engineered Phthalocyanines as Hole-Transporting Materials in Perovskite Solar Cells Reaching Power Conversion Efficiency of 17.5%, *Adv Energy Mater*, 7, 2017, 1601733.
- [2] R.F. Chaabane, Effect of Measuring Environment on The Electrical Characteristics of NiPc Based Thin Film Transistors: The Effects of Ozone, *Mater Sci Eng C*, 26, 2006, 551–554.
- [3] M. Ozaki, M. Yoneya, Y. Shimizu, A. Fujii, Carrier transport and device applications of the organic semiconductor based on liquid crystalline non-peripheral octaalkyl phthalocyanine, *Liq Cryst*, 45, 2018, 2376–2389.
- [4] T. Sizun, M. Bouvet, Y. Chen, J.M. Suisse, G. Barochi, J. Rossignol, Differential study of substituted and unsubstituted cobalt phthalocyanines for gas sensor applications, *Sensor Actuat B-Chem*, 159, 2011, 63–170.
- [5] A. Şenocak, B. Köksoy, D. Akyüz, A. Koca, D. Klyamer, T. Basova, E. Demirbaş, M. Durmuş, Highly selective and ultra-sensitive electrochemical sensor behaviour of 3D SWCNT BODIPY hybrid material for eserine detection, *Biosens Bioelectron*, 128, 2019, 144–150.
- [6] P. Zhao, Q. Liang, Y. Li, Electrochemical, SEM/EDS and quantum chemical study of phthalocyanines as corrosion inhibitors for mild steel in 1 mol/l HCl, *Appl Surf Sci*, 252, 2005, 1596–1607.
- [7] Q. Luo, H. Tian, B. Chen, W. Huang, Effective non-destructive readout of photochromic bithienylethene-phthalocyanine hybrid, *Dyes Pigments*, 73, 2007, 118–120.
- [8] M.S. Kahouecha, K. Hrizb, S. Touaitia, J. Bassem, New anthracene-based-phthalocyanine semi-conducting materials: Synthesis and optoelectronic properties, *Mater Res Bull*, 75, 2016, 144–154.
- [9] Z. Biyiklioğlu, Non-aggregated and Water Soluble Amphiphilic Silicon Phthalocyanines With Two Axial Substituents and Their Electrochemical Properties, *Polyhedron*, 63, 2013, 1–8.
- [10] E. Demir, Ö. Göktug, R. İnam, D. Doyduk, Development and characterization of iron (III) phthalocyanine modified carbon nanotube paste electrodes and application for determination of fluometuron herbicide as an electrochemical sensor, *J Electroanal Chem*, 895, 2021, 115389.
- [11] D. Arıcan, M. Arıcı, A. L. Ugur, A. Erdogmus, A. Koca, Effects of peripheral and nonperipheral substitution to the spectroscopic, electrochemical and spectroelectrochemical properties of metallophthalocyanines, *Electrochim Acta*, 106, 2013, 541–555.
- [12] J.H. Zagal, F. Bedioui, J.P. Dodelet, *N4-Macrocyclic Metal Complexes*, Springer, New York, NY, 2006.
- [13] C.A. Caro, F. Bedioui, J.H. Zagal, Electrocatalytic oxidation of nitrite on a vitreouscarbon electrode modified with cobalt phthalocyanine, *Electrochim Acta*, 47, 2002, 1489–1494.
- [14] S. Griveau, F. Bedioui, Electrocatalytic oxidation of 2-mercaptoethanol by electropolymerized cobalt porphyrin film on vitreous carbon electrodes, *Electroanal*, 13, 2001, 253–256.
- [15] L'Her M. ve Pondaven A. "Electrochemistry of Phthalocyanines" (2003). *The Porphyrin Handbook*, K. M. Kadish, K. M. Smith, R. Guilard, Eds., Vol. 16, Elsevier (USA), pp. 104–169, ISBN 0-12-393220-3.
- [16] D. Cakir, O. Bekircan, Z. Biyiklioglu, 1,2,4-Triazole-substituted metallophthalocyanines carrying redox active cobalt(II), manganese(III), titanium (IV) center and their electrochemical studies, *Synthetic Met*, 201, 2015, 18–24.
- [17] A. Nas, G. Dilber, Z. Biyiklioglu, Electroanalytical characterization of chloroquinoline substituted redox-active phthalocyanines, *Turk J Anal Chem*, 5(1), 2023, 25–31.
- [18] Y.P. Yuan, S.B. Wang, G.H. Gong, Z.S. Quan, Synthesis and studies on anticonvulsant and antibacterial activities of 1-alkyl-4-(4H-1,2,4-triazol-4-yl) piperidine derivatives, *Lett Drug Des Discov*, 11, 2014, 1070–1078.
- [19] Z. Jiang, J. Gu, C. Wang, S. Wang, N. Liu, Y. Jiang, G. Dong, Y. Wang, Y. Liu, J. Yao, Z. Miao, W. Zhang, C. Sheng, Design, synthesis and 59 antifungal activity of novel triazole derivatives containing substituted 1,2,3-triazole-piperidine side chains, *Eur J Med Chem*, 82, 2014, 490–497.
- [20] P. Wang, J. Cai, J. Chen, M. Ji, Synthesis and anticancer activities of ceritinibanalogs modified in the terminal piperidine ring, *Eur J Med Chem*, 93, 2015, 1–8.
- [21] J.H. Kim, P.K. Shyam, M.J. Kim, H.J. Lee, J.T. Lee, H.Y. Jang, Enantioselective synthesis and antioxidant activity of 3,4,5-substituted piperidine derivatives, *Bioorg Med Chem Lett*, 26(13), 2016, 3119–3121.
- [22] M. Ahmad Bhat, M.A. Al-Omar, A.M. Naglah, Synthesis and in vivo antiulcer evaluation of some novel piperidine linked dihydropyrimidinone derivatives, *J Enzym Inhib Med Ch*, 33(1), 2018, 978–988.
- [23] X. Chen, P. Zhan, C. Pannecouque, J. Balzarini, E. De Clercq, X. Liu, Synthesis and biological evaluation of piperidine-substituted triazine derivatives as HIV-1 non-nucleoside reverse transcriptase inhibitors, *Eur J Med Chem*, 51, 2012, 60–66.
- [24] Y. Imaeda, M. Tawada, S. Suzuki, M. Tomimoto, M. Kondo, N. Tarui, T. Sanada, R. Kanagawa, G. Snel, C.A. Behnke, K. Kubo, T. Kuroita, Structure based design of a new series of N-(piperidin-3-yl)pyrimidine-5-carboxamides as renin inhibitors" *Bioorgan Med Chem*, 24, 2016, 5771–5780.
- [25] A. Wcislo, I. Dąbkowska, J. Czupryniak, T. Ossowski, D. Zarzeckańska, Unusual behavior in di-substituted piperidine and piperazineanthraquinones upon protonation-Spectral, electrochemical, and quantum chemical studies, *J Mol Liq*, 279, 2019, 154–163.
- [26] P. Niedziałkowski, E. Czaczyk, J. Jarosz, A. Wcislo, W. Biało-brzeska, J. Wietrzyk, T. Ossowski, Synthesis and electrochemical, spectral, and biological evaluation of novel 9,10-anthraquinone derivatives containing piperidine unit as potent antiproliferative agents, *J Mol Struct*, 1175, 2019, 488–495.
- [27] E. Hussain, H. Zhou, . Yang, S. Shahzad, C. Yu, Synthesis of regioisomerically pure piperidine substituted perylenebisimide NIR dyes: A comparative study of spectroscopic, electrochemical and crystalline properties, *Dyes Pigments*, 147, 2017, 211–224.
- [28] G. Dilber, M. Durmuş, H. Kantekin, Investigation of the photophysical and photochemical behavior of substituted zinc phthalocyanines and their water-soluble quaternized derivatives, *Turk J Chem*, 41, 2017, 917–930.
- [29] E.T. Saka, Z. Biyiklioğlu, Co(II) and Fe(II) phthalocyanines: synthesis, investigation of their catalytic activity towards

- phenolic compounds and electrochemical behaviour, *Appl Organomet Chem*, 29, 2015, 392–399.
- [30] D. Kulaç, M. Bulut, A. Altındal, A.R. Özkaya, B. Salih, Ö. Bekaroglu, Synthesis and characterization of novel 4-nitro-2-(octyloxy)phenoxy substituted symmetrical and unsymmetrical Zn(II), Co(II) and Lu(III) phthalocyanines, *Polyhedron*, 26, 2007, 5432–5440.
- [31] T. Nyokong, Electronic spectral and electrochemical behaviour of near infrared absorbing metallophthalocyanines. In: *Structure and Bonding: Functional Phthalocyanine Molecular Materials*, Editors: D.M.P Mingos, 2010, Germany, Springer.
- [32] A. Ogunsipe, T. Nyokong, M. Durmuş, Photophysical, photochemical and bovine serum albumin binding studies on water soluble gallium (III) phthalocyanine derivatives, *J Porphy Phthalocya*, 11, 2007, 635–44.
- [33] G. Dilber, M. Durmuş, H. Kantekin, Non-aggregated zwitterionic Zinc(II) phthalocyanine complexes in water with high singlet oxygen quantum yield, *Dyes Pigments*, 160, 2019, 267–284.
- [34] L.K. Lee, N.H. Sabelli, P.R. LeBreton, Theoretical characterization of phthalocyanine, tetraazaporphyrin, tetrabenzoporphyrin, and porphyrin electronic spectra, *J Phys Chem*, 86 1982, 3926–3931.
- [35] Y. Han, W. Ning, H. Du, J. Yang, N. Wang, Preparation, optical and electrical properties of PTCDA nanostructures, *Nanoscale*, 7, 2015, 17116–17121.
- [36] J. Obirai, N.P. Rodrigues, F. Bedioui, T. Nyokong, Synthesis, spectral and electrochemical properties of a new family of pyrrole substituted cobalt, iron, manganese, nickel and zinc phthalocyanine complexes, *J Porphy Phthalocya*, 7, 2003, 508–520.
- [37] M.J. Stillman, T. Nyokong, in: C.C. Leznoff, A.B.P. Lever (Eds.), *Phthalocyanines: Properties and Applications*, vol. 1, VCH, New York, 1989.
- [38] D. Akyüz, T. Keleş, Z. Biyıklıoğlu, A. Koca, Metallophthalocyanines Bearing Polymerizable {[5-((1E)-[4-(Diethylamino)phenyl]methylene)amino]-1-naphthyl]oxy} Groups as Electrochemical Pesticide Sensor, *Electroanal*, 29, 2017, 2913–2924.
- [39] T. Keleş, D. Akyüz, Z. Biyıklıoğlu, A. Koca, Electropolymerization of metallophthalocyanines carrying redox active metal centers and their electrochemical pesticide sensing application, *Electroanal*, 29, 2017, 2125–2137.
- [40] Akyüz, T Keleş, Z Biyıklıoğlu, A Koca, Electrochemical pesticide sensors based on electropolymerized metallophthalocyanines, *J Electroanal Chem*, 804, 2017, 53–63.

Supplementary Informations

1. Experimental

1.1. Materials and Methods

All reagents and solvents used were dried and purified as described in Perrin and Armarego. [1]. 1-benzylpiperidin-4-ol were purchased from commercial supplier. 3-nitrophthalonitrile [2], 4-nitro phthalonitrile [3], compound 1 [4] and compound 2 [5] were synthesized according to the procedures.

All electrochemical measurements were carried out with Gamry Interface 1000 potentiostat/galvanostat utilizing a three-electrode configuration at 25 °C. The working electrode was a Pt disc with a surface area of 0.071 cm². A Pt wire was served as the counter electrode and saturated calomel electrode (SCE) was employed as the reference electrode and separated from the bulk of the solution by a double bridge. Electrochemical grade tetrabutylammonium perchlorate (TBAP) in extra pure dichloromethane (DCM) was employed as the supporting electrolyte at a concentration of 0.10 mol/dm.

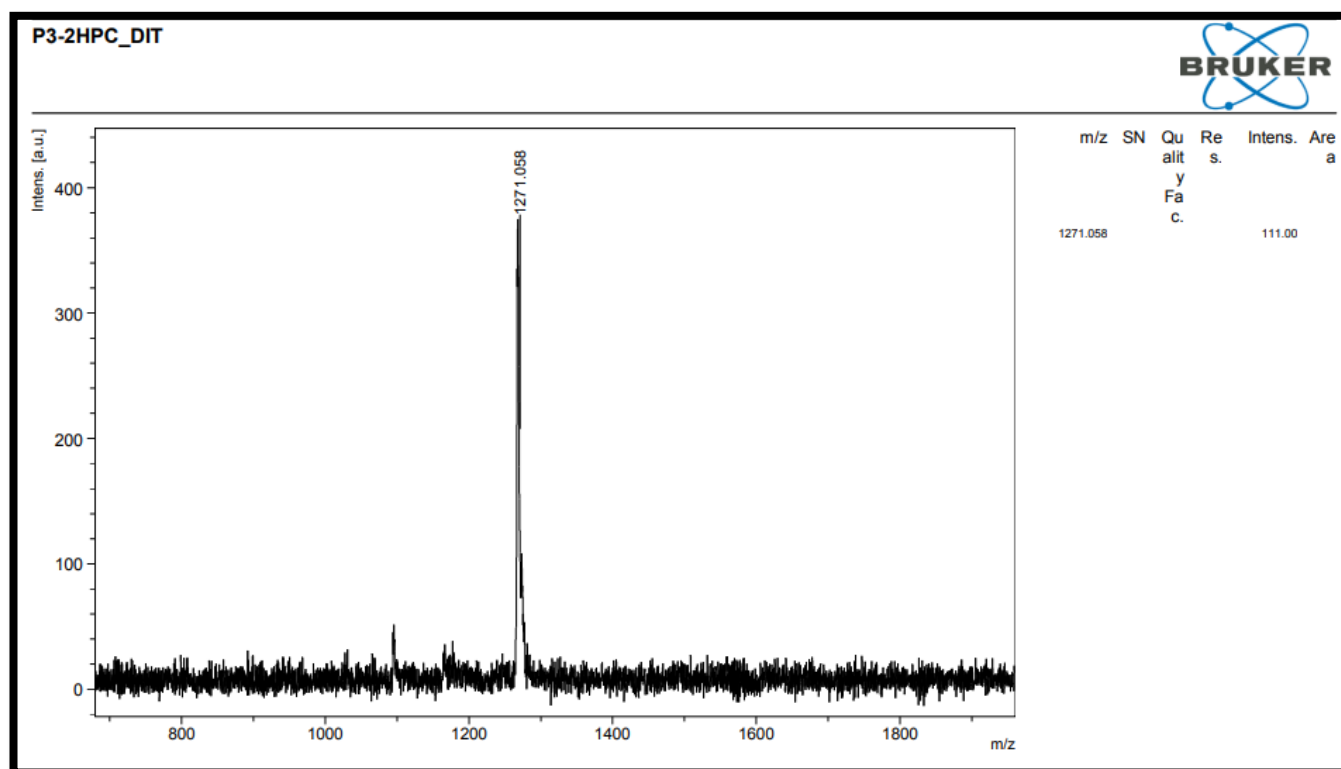
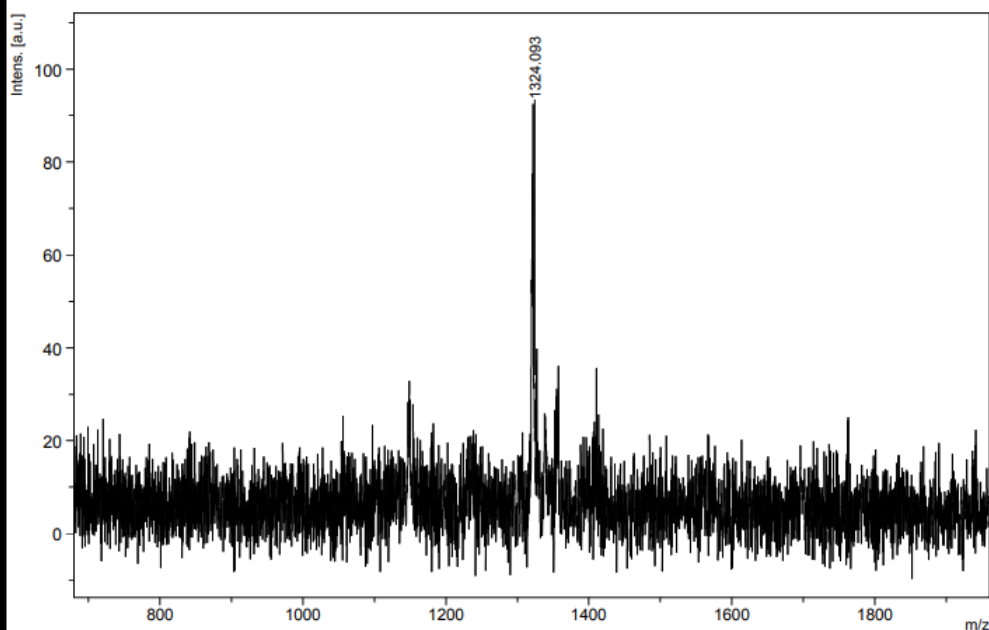


Figure S1. Mass spectrum of compound 3

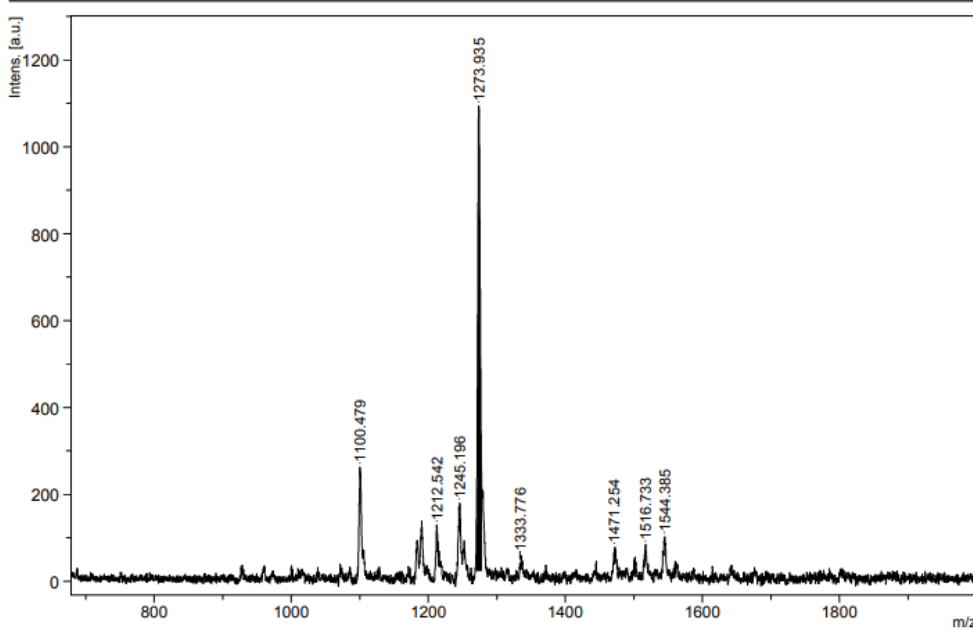
P3-MnPC_DIT



m/z	SN	Quality Factor	Res.	Intens.	Area
1324.093				17.87	

Figure S2. Mass spectrum of compound 4

P3-Ti-2_DIT



m/z	SN	Quality Factor	Res.	Intens.	Area
1100.479	12.1		1632	262.95	302
1190.045	5.2		1884	123.10	132
1212.542	5.5		804	130.33	229
1245.196	7.4		2107	173.71	159
1273.935	47.0		327	1094.10	4983
1333.776				38.62	
1471.254	3.0		2608	67.76	49
1516.733	3.7		4148	84.05	68
1544.385	4.3		2610	98.00	101

Figure S3. Mass spectrum of compound 5

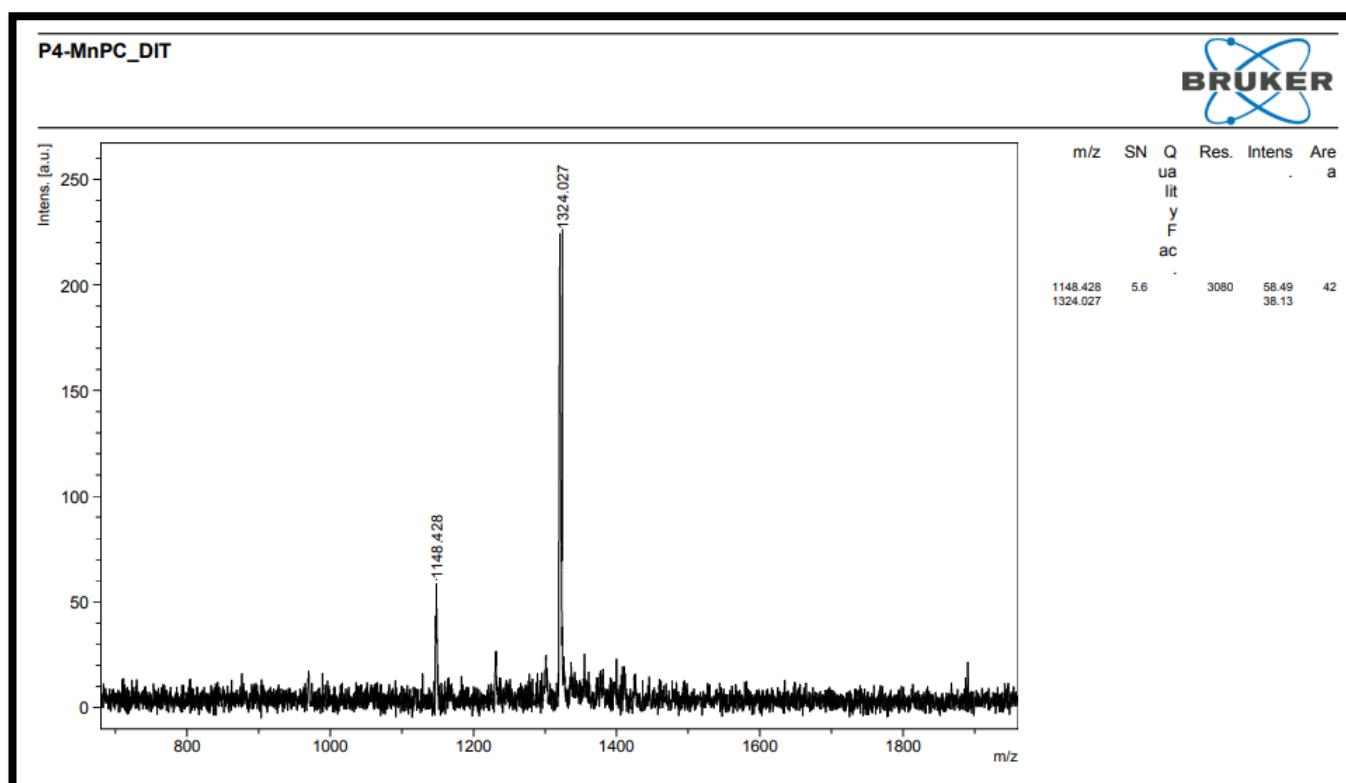


Figure S4. Mass spectrum of compound 8

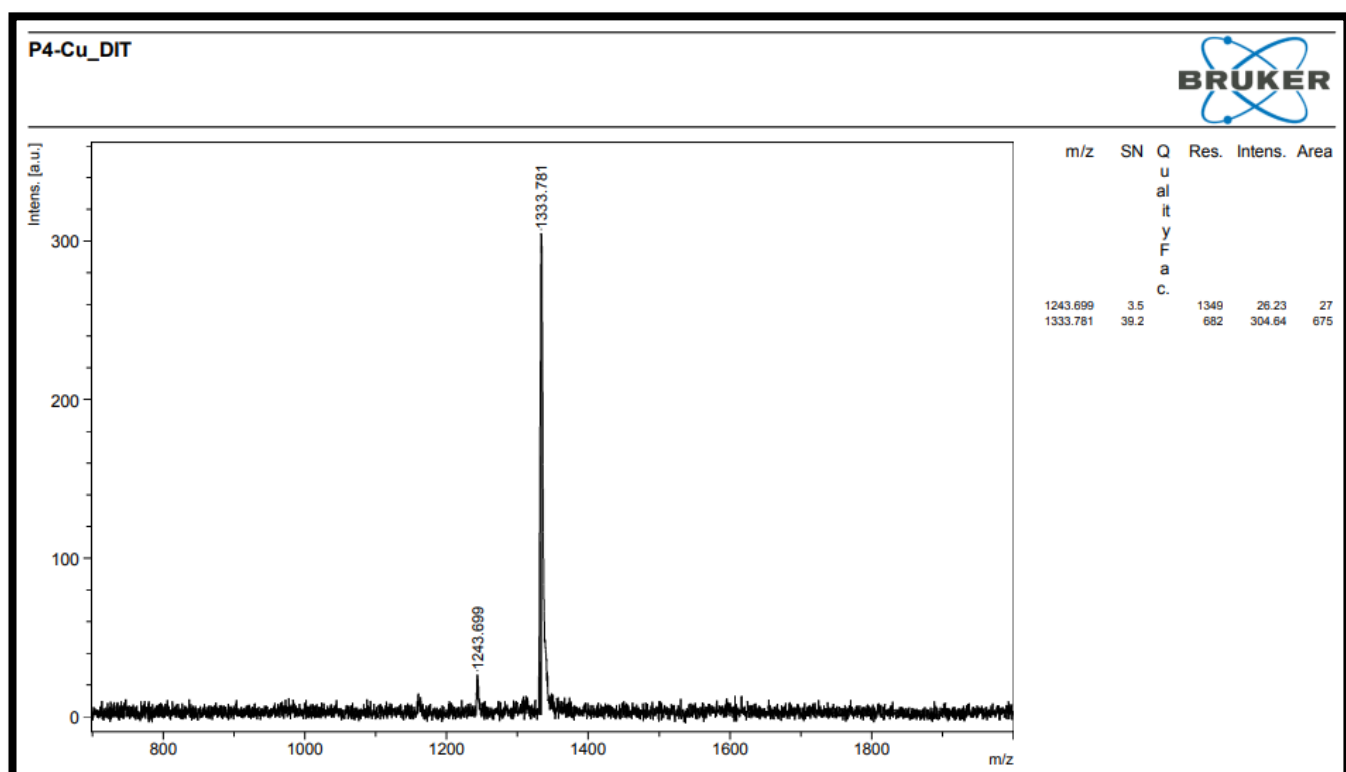


Figure S5. Mass spectrum of compound 10

References

- [1] Perrin DD, Armarego WLF, Purification of laboratory chemicals, Oxford, 1989, New York, Pergamon.
- [2] R.D. George, A.W. Snow, Synthesis of 3-nitrophthalonitrile and tetra- α -substituted phthalocyanines, *J Heterocyclic Chem*, 32, 1995, 495–498.
- [3] J.G. Young, W. Onyebuagu, Synthesis and characterization of di-disubstituted phthalocyanines, *J Org Chem*, 55, 1990, 2155–2159.
- [4] G. Dilber, M. Durmuş, H. Kantekin, Investigation of the photophysical and photochemical behavior of substituted zinc phthalocyanines and their water-soluble quaternized derivatives, *Turk J Chem*. 41 (2017) 917–930.
- [5] E.T. Saka, Z. Bıyıklıođlu, Co(II) and Fe(II) phthalocyanines: synthesis, investigation of their catalytic activity towards phenolic compounds and electrochemical behaviour, *Appl. Organomet. Chem*. 2015, 29, 392–399.



Adsorption of hexavalent chromium from aqueous solution onto corn cobs – activated carbon

Pinar Bozbeyoglu¹ , Ali Gundogdu^{2*} 

¹Gümüşhane University, Gümüşhane Vocational School, Department of Electronics and Automation, Biomedical Device Technology Program, 29100, Gümüşhane, Türkiye

²Karadeniz Technical University, Maçka Vocational School, Department of Pharmacy Services, 61750, Trabzon, Türkiye

Abstract

This study evaluated the performance of a new activated carbon (CCs-AC) produced from corn cobs by boric acid activation for the effective removal of hexavalent chromium, a heavy metal with high potential to pollute the environment, from wastewater. For this purpose, with the help of parameters such as solution pH, contact time, initial Cr(VI) concentration, CCs-AC dose, desorption, and temperature, the removal of Cr(VI) ions from aqueous solution by adsorption onto CCs-AC was investigated using equilibrium, kinetic, and thermodynamic approaches. As a result of the experiments, it was determined that the optimum solution pH was 2.0, the contact time was 4 hours, and the desorption solution was 3.0 M NaOH. From the kinetic data, it was determined that the adsorption was compatible with the pseudo-second order kinetic model. The maximum Cr(VI) adsorption capacity of 123.7 mg/g obtained from the Langmuir isotherm model showed that CCs-AC was competitive with the literature. R_L values between 0.42–0.03 indicated that Cr(VI) adsorption on CCs-AC was favorable. From the thermodynamic data, the ΔH value of 12.00 kJ/mol indicated that the adsorption was rather chemically driven, while the positive value indicated that the adsorption was endothermic. Negative ΔG values indicate that Cr(VI) adsorption occurs spontaneously with increasing temperature, while the ΔS value is interpreted as an increase in the amount of unused energy.

Keywords: Adsorption, corn cobs – activated carbon, equilibrium, hexavalent chromium, kinetics, thermodynamics

1. Introduction

Chromium is known as one of the most common and most hazardous toxic heavy metals in industrial wastewater. Chromium is widely used in various industrial applications such as leather tanning, batteries, steel metallurgy, petroleum refining, paint manufacturing, electroplating, and textile industry. The most stable known forms of chromium are the trivalent and hexavalent forms [1]. The hexavalent form of chromium, Cr(VI), is much more toxic than the trivalent form, Cr(III), and both forms are highly soluble in water. Especially in bodies exposed to Cr(VI), it can accumulate in the liver, kidneys and stomach and cause many bad diseases, including cancer [2]. The limit value for total chromium species reported by the World Health Organization (WHO) in 2017 under the title "Guidelines for drinking water quality" is 0.05 mg/L [3]. Therefore, it is vital to eliminate Cr(VI) as well as various pollutant species from industrial wastewater and to release these waters to nature after treatment in a way that does not cause health problems.

Various physicochemical and electrochemical methods have been developed to reduce heavy metal concentrations in wastewater to acceptable limits. Adsorption, membrane filtration, chemical precipitation, ion exchange, photocatalysis, electrodialysis, and nanotechnology, which has been developed in recent years, are some of the methods used to remove metal ions from aqueous media. Adsorption is the process of attaching a species, called adsorbate, to the surface of another material, called adsorbent [2]. For this purpose, activated carbon, which exhibits unique properties with its porosity, large surface area and rich functional groups in its active sites, ranks first among the preferences [4]. Due to these unique properties of activated carbon and its high performance in removing pollutants from water, its commercial production from various materials such as coal, wood, fruit seed shells, coconut shells, nut shells and polymer-based synthetic raw materials with high carbon content has become very common [5]. However, due to the high cost of

Citation: P. Bozbeyoglu, A. Gundogdu, Adsorption of hexavalent chromium from aqueous solution onto corn cobs – activated carbon, Turk J Anal Chem, 5(2), 2023, 107–117.

 <https://doi.org/10.51435/turkjac.1394304>

Author of correspondence: a.ramazan.gundogdu@gmail.com

Received: November 22, 2023

Tel: +90 (462) 512 35 35

Accepted: December 04, 2023

Fax: +90 (462) 512 35 52

commercial activated carbons, studies on the production of much lower cost and high-performance activated carbon from agricultural wastes or by-products are increasing day by day [6]. For example, many agricultural wastes such as apricot stones [7], cherry stones [8], palm oil stones [9], olive stones [10], grape seeds [11], almond shells [12], nut shells [13], corn cobs [14], rice husks [15], and sugarcane bagasse [16] have been used to produce activated carbon [17].

In today's technology, activated carbon is mainly produced by two methods: (i) chemical activation method using mineral acids, bases, or salts (such as HCl, NaOH, and ZnCl₂) as activating agents, and (ii) physical activation method using steam or CO₂ as activating agents. In chemical activation, the precursor (the starting material) is first impregnated with the activating agent and then subjected to carbonization in an N₂ atmosphere at temperatures in the range 400–1000 °C. In physical activation, activation and carbonization are carried out simultaneously. It requires carbonization of the precursor at temperatures above 700 °C followed by gasification in CO₂, steam, or a mixture thereof [18].

In this study, a new activated carbon was produced by chemical activation using boric acid from corn cobs as a precursor. When the literature is reviewed, it is observed that activated carbons with different properties have been produced from corn cobs using many activating agents, but the use of boric acid as a chemical activating agent is found in only one study and that study belongs to our group. In that study, the adsorption mechanisms of Cd metal and methylene blue on the activated carbon were investigated [19]. In this study, the main objective was to investigate the adsorption performance of the produced activated carbon for the removal of Cr(VI) ions from aqueous media by equilibrium, kinetic and thermodynamic parameters. Therefore, from this point of view, this study is also original.

2. Materials and methods

2.1. Preparation, production, and characterization of CCs-AC

Corn cobs (CCs) were obtained from corns collected from agricultural fields in Akçaabat district of Trabzon, Türkiye. CCs were washed thoroughly with tap water, rinsed with distilled water and dried in an oven at 105 °C for 24 hours after being left outdoors for 3 days. The dried CCs were ground in a knife grinder and sieved to a size of approximately 4–8 mm. 60 g CCs and 60 g boric acid (H₃BO₃) were mixed in 700 mL distilled/deionized water. The resulting mixture was converted into activated carbon by pyrolysis at 700 °C in N₂ atmosphere as detailed in the literature and labeled as CCs-AC (corn cobs – activated carbon) [19].

As reported in the literature, CCs-AC produced by boric acid activation was characterized by many parameters such as proximate-ultimate analysis, Boehm titration, pH-pHpzc determination, SEM images (Fig. 1), IR spectra and surface characterization analysis [19].

Fig. 1 shows SEM images of the original CCs and CCs-AC produced at 700 °C in N₂ atmosphere. Although there are roughnesses, indentations and protrusions in the structure of CCs, no porosity is visible. Activating agents such as boric acid act to dehydrate the structure at high temperatures in N₂ atmosphere and causing the formation of fractures, voids, channels, indentations, and protrusions and thus pores of a different character. This porosity of activated carbons, as well as the functional groups in the reorganized active sites on their surfaces, play a major role in making them unique adsorbents [20].

2.2. Adsorption tests

14.14 g K₂Cr₂O₇ (Merck, Darmstadt, Germany) was weighed, dissolved in distilled/deionized water and diluted to 1 L to prepare 5000 mg/L of a stock Cr(VI)

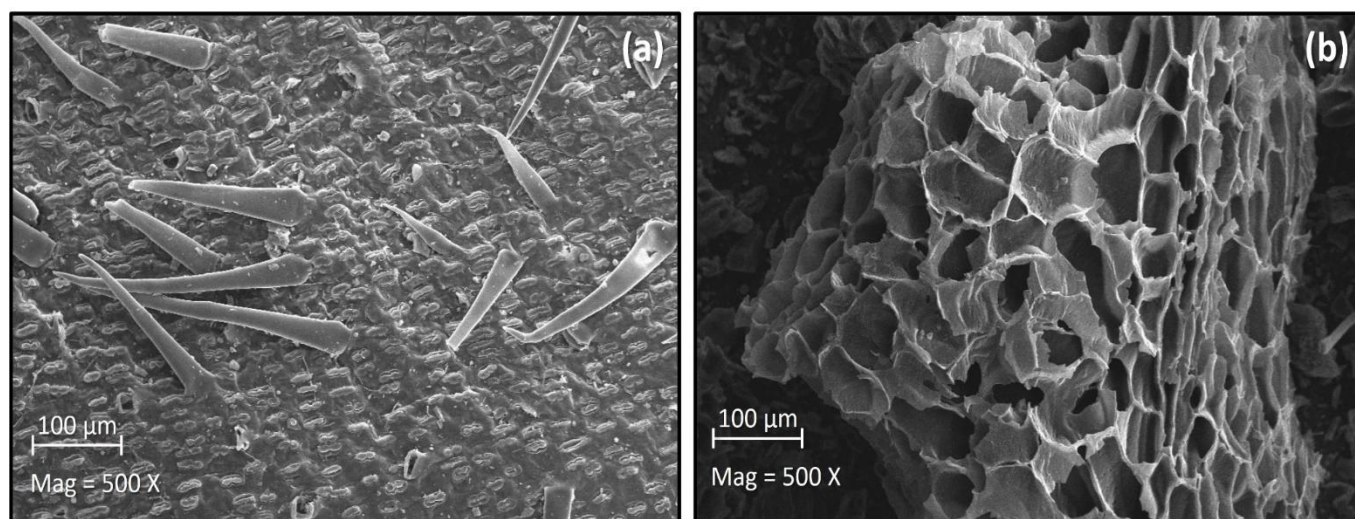


Figure 1. SEM images for (a) Corn cobs (CCs) and (b) Corn cobs – activated carbon (CCs-AC)

solution. The stock Cr(VI) solution was diluted in appropriate ratios and used in adsorption tests. Cr(VI) adsorption tests were carried out in batch mode.

10 mL of the solution prepared by diluting 5000 mg/L Cr(VI) stock solution to the desired ratio and 0.05 g of CCs-AC ground to $\leq 125 \mu\text{m}$ particle size were mixed in a polypropylene falcon tube of 15 mL volume (5.0 g/L suspension). The resulting mixture was shaken on a mechanical shaker for 4 hours. The solid-liquid mixture was separated by vacuum filtration and the concentration of Cr(VI) remaining unadsorbed in the solution was determined by microwave plasma-atomic emission spectrometry (MP-AES, Agilent Tech. 4200 model, Santa Clara, US).

Each test was repeated at least 3 times, and mean values were used. From MP-AES measurements, the amount of Cr(VI) adsorbed per gram of CCs-AC was calculated with the help of Equation (1).

$$Q_e = \frac{(C_o - C_e) \cdot V}{m} \quad (1)$$

Percent adsorption values were also calculated with the help of Equation (2) below.

$$\text{Adsorption (\%)} = \frac{C_o - C_e}{C_o} \cdot 100 \quad (2)$$

Where C_o is the initial Cr(VI) concentration (mg/L), C_e is the Cr(VI) concentration remaining in the solution at equilibrium (mg/L), Q_e is the amount of Cr(VI) adsorbed per unit CCs-AC (mg/g), V is the solution volume (L), and m is the amount of CCs-AC (g).

3. Results and discussion

3.1. Effect of pH on the adsorption of Cr(VI) ions from aqueous solution onto CCs-AC

In adsorption studies, the pH of adsorbate solutions is extremely important in terms of adsorbent capacity. A series of Cr(VI) solutions with a concentration of 100 mg/L and the pH values adjusted between 2 and 8 were prepared and 10 mL of these solutions were placed in 15 mL polypropylene tubes. 0.05 g CCs-AC was added to these solutions (5.0 g/L suspension), the tubes were capped and shaken for 12 hours. The suspensions were filtered by vacuum filtration and the supernatants were analyzed by MP-AES. The concentrations remaining in the supernatants were subtracted from the initial concentration (100 mg/L) and the percent adsorption values were calculated with the relevant formulas.

Fig. 2 reflects the performance of CCs-AC with varying pH. In parallel with many studies in the literature, Cr(VI) adsorption onto CCs-AC is more

favorable at low pH values [21–23]. In fact, it is normal to observe higher yields at lower pHs because Cr(VI) is present in anionic forms in aqueous solution. Between $1.0 < \text{pH} < 3.0$ the predominant form for Cr(VI) is HCrO_4^- , while at $\text{pH} > 6.0$ it is CrO_4^{2-} . As a result, whether the medium is acidic or basic, Cr(VI) is always in the anionic form. At low pHs, the surface of the adsorbent is positive due to the abundance of protons and therefore strong electrostatic interactions occur between Cr(VI) in anionic form and CCs-AC. Thus, the adsorption efficiency is quite high at low pHs. As a result, the adsorption efficiency is quite high at low pHs. As the solution pH increases, the net charge of the CCs-AC surface becomes negative, while Cr(VI) is still in negative form. Thus, the adsorption efficiency will gradually decrease due to electrostatic repulsions [24,25].

As it was clear from the pH screening that the optimum solution pH was 2.0, the following studies were carried out at this pH value.

3.2. Effect of contact time on the adsorption of Cr(VI) ions from aqueous solution onto CCs-AC and adsorption kinetics

The systems in which the adsorption mechanism is studied as a function of time are called adsorption kinetics. A 250 mL volume of Cr(VI) solution adjusted to pH 2.0 and 1.25 g CCs-AC (5.0 g/L suspension) were treated for 12 hours. The concentrations of the micropipetted aliquots at certain time intervals during the treatment were measured by MP-AES. The measured concentrations were subtracted from the initial Cr(VI) concentration and the amount of Cr(VI) adsorbed per unit adsorbent (Q_t , mg/g) was calculated with the relevant formulas.

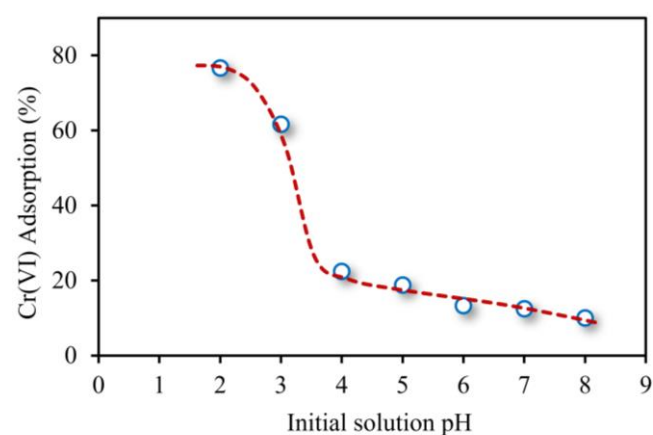


Figure 2. Effect of solution pH on the adsorption of Cr(VI) ions onto CCs-AC from aqueous solution (C_o : 100.0 mg/L; Agitation time: 12 h; CCs-AC dosage: 5.0 g/L; CCs-AC particle size: $\leq 125 \mu\text{m}$; temperature: 25°C)

Fig. 3 (a) illustrates the amount of Cr(VI) adsorbed on CCs-AC at different time periods. It is seen that the adsorption is quite fast in the first minutes of the process and the system reaches equilibrium after 2 hours.

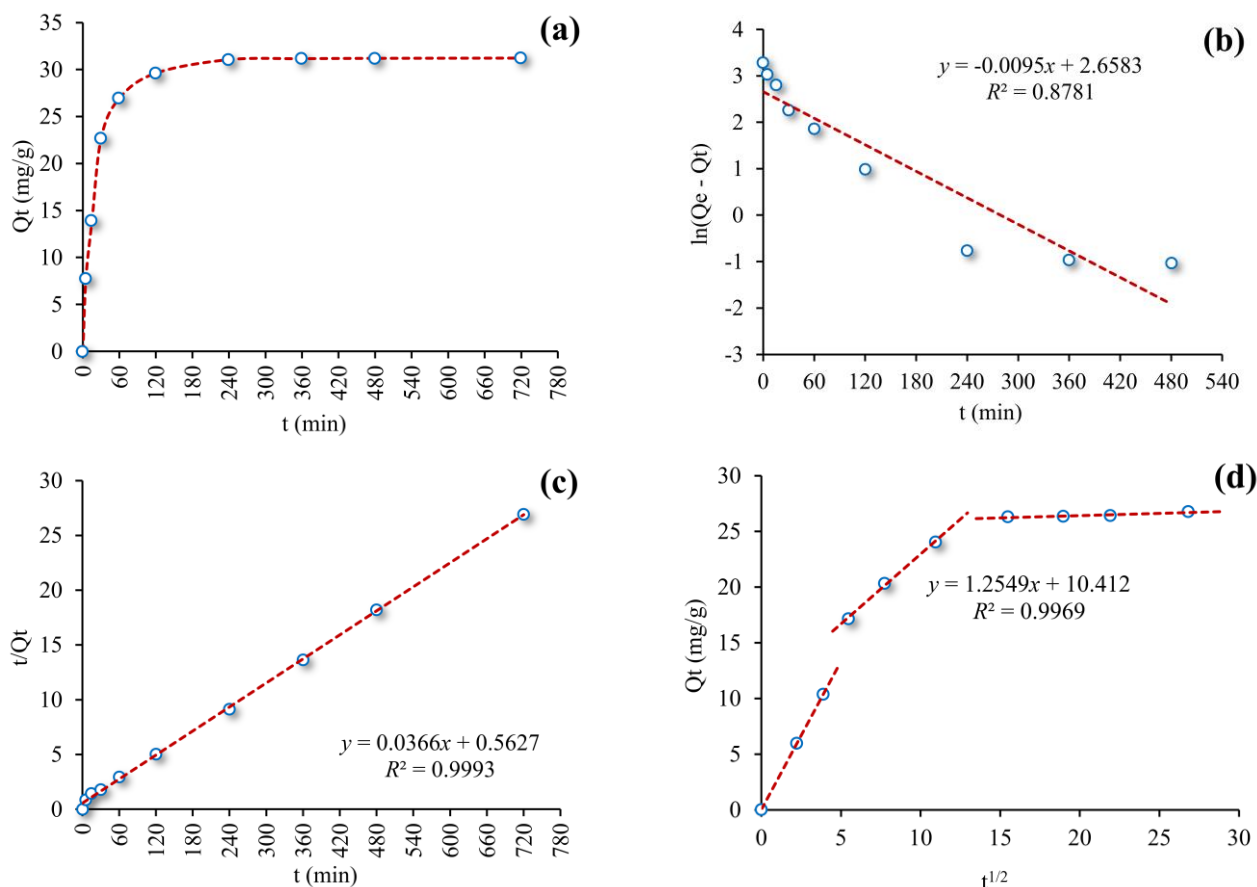


Figure 3. Contact time and adsorption kinetics of Cr(VI) ions onto CCs-AC: (a) Contact time; t vs Q_t graph, (b) Pseudo first-order kinetics; t vs $\ln(Q_e - Q_t)$ graph, (c) Pseudo second-order kinetics; t vs t/Q_t graph, (d) intraparticle diffusion kinetics; $t^{1/2}$ vs Q_t graph (Initial solution pH: 2.0; agitation time: 0–12 h; C_0 : 250.0 mg/L; CCs-AC dosage: 5.0 g/L)

However, an optimum contact time of 4.0 hours was deemed appropriate as a guarantee.

The behavior of Cr(VI) ions onto CCs-AC in terms of time dependence of adsorption was monitored by pseudo-first order, pseudo-second order and intraparticle diffusion kinetic models. The constants obtained from the relevant equations of these models are given in Table 1.

The mathematical equations of the pseudo-first order kinetic model is shown in Equation (3) and Equation (4). The second equation is a rearrangement and linearization of the first equation.

Table 1. Kinetic data for adsorption of Cr(VI) ions from aqueous solution onto CCs-AC

Kinetic models	Constants		Value
	Q_e (exp), mg/g	Q_e (cal), mg/g	
Pseudo first-order	k_1 , 1/min		0.00952
	R^2		0.8781
	Q_e (exp), mg/g		27.35
	k_2 , g/mg.min		0.00238
Pseudo-second order	R^2		0.9993
	k_{id} , mg/g.min ^{1/2}		1.255
	C , mg/g		10.41
Intraparticle diffusion	R^2		0.9969

$$\frac{dQ}{dt} = k_1(Q_e - Q_t) \quad (3)$$

$$\ln(Q_e - Q_t) = \ln(Q_e) - k_1 t \quad (4)$$

Where Q_e represents the amount of adsorbed material per gram of adsorbent at equilibrium (mg/g), Q_t represents the amount of adsorbed material per gram of adsorbent at any time t (mg/g), k_1 represents the first order rate constant (1/min) and t represents the contact time (min). The plot of $\ln(Q_e - Q_t)$ versus t forms a line and gives information about the fit of this kinetic model to the adsorption data. Q_e and k_1 can be found from the intercept and slope of the graph [26].

Equations for the curvilinear and linear forms of the pseudo-second-order kinetic model, another model used to describe the time dependence of the adsorption process from aqueous solution, are shown in Equation (5) and Equation (6).

$$\frac{dQ_t}{dt} = k_2(Q_e - Q_t)^2 \quad (5)$$

$$\frac{t}{Qt} = \frac{1}{k_2 Qe^2} + \frac{t}{Qe} \quad (6)$$

Where k_2 represents the second order rate constant (g/mg.min). The graph plotted between $t/Qt - t$ forms a line, which shows the agreement of the kinetic data with the second-order kinetic model. Q_e and k_2 can be determined from the slope and intercept of the line [27,28].

Fig. 3(b) shows that the adsorption kinetics is not compatible with the pseudo-first order kinetic model ($R^2 = 0.8781$). While this model gives better results for systems that have not yet reached equilibrium, it is insufficient to explain the adsorption rate of systems that can be saturated on porous structures such as activated carbon. This conclusion is also supported by the fact that the experimental Q_e value (26.75 mg/g) does not coincide with the theoretical Q_e value (14.27 mg/g) obtained from the pseudo-first order (Table 1).

The time-dependent adsorption of various pollutant species from the liquid phase on activated carbon and similar adsorbents gradually slows down and reaches equilibrium when saturation is reached within the capacity of the adsorbent. The adsorption rates of such equilibrium systems are in full agreement with the pseudo-second order kinetic model (Fig. 3(c); $R^2 = 0.9993$). In addition, the experimental Q_e value and the theoretical Q_e value obtained from this model are very close to each other (Table 1) [29].

In cases where the diffusion mechanism in porous structures cannot be clearly explained by pseudo-first and pseudo-second order equations or when these equations are insufficient, the intraparticle diffusion model may be preferred. This model is given by Equation (7) below.

$$Qt = k_{id}t^{1/2} + C \quad (7)$$

Where k_{id} (mg/g.min^{1/2}) is the intraparticle diffusion rate constant while C (mg/g) is a constant characterizing the boundary layer thickness. k_{id} and C can be determined from the slope and intercept of the graph plotted between Qt and $t^{1/2}$ [26,27].

In the intraparticle diffusion model, the time-dependent stages of adsorption can be estimated. Fig. 3(d) shows that adsorption takes place mainly in 3 stages. The fact that the adsorption rate is very high at the beginning indicates that the outer surface of the activated carbon, i.e. the film layer, is filled first. The second part is slower and here there is a movement of adsorbate ions into the pore interior. This movement is the rate-limiting step of adsorption and indicates the diffusion of adsorbate molecules into the pore interior. The last step is the equilibrium step where adsorption

reaches saturation. For the intraparticle diffusion model, the $t^{1/2}$ - Qt plot contains three lines with different slopes as shown in Fig. 3(d). This indicates that more than one process affects adsorption. The second line represents intraparticle diffusion. The C value found for the second line is different from zero (10.41 mg/g), suggesting that the adsorption rate is controlled by other mechanisms besides intraparticle diffusion [26,27].

3.3. Effect of adsorbent dose on the adsorption of Cr(VI) ions onto CCs-AC

In this parameter, it was investigated whether the amount of Cr(VI) adsorbed is linear with increasing amount of CCs-AC. Fig. 4 proves that this relationship is non-linear. The figure illustrates that the amount of Cr(VI) adsorbed per unit adsorbent decreases as the dose of CCs-AC increases due to a non-linear increase in the amount of Cr(VI) adsorbed. Therefore, in the light of these results, it is seen that the lowest CCs-AC dose (1.0 g/L) has the highest Cr(VI) adsorption capacity per unit adsorbent. This inverse relationship can be attributed to two reasons: (i) Increasing CCs-AC dose at constant Cr(VI) concentration in solution leads to the formation of unsaturated sites on the adsorbent surface. (ii) Agglomeration of CCs-AC particles at high dose leads to a decrease in the total surface area [30,31].

3.4. Effect of initial Cr(VI) concentration on the adsorption efficiency and adsorption isotherms

Increasing adsorbate concentration in aqueous solution at constant adsorbent dose will of course gradually increase the adsorption efficiency. However, as stated in the previous parameter, this increase will not be linear. As the adsorbate gradually reaches saturation, its capacity against the adsorbate of interest will be revealed. This parameter was applied to reveal the adsorption capacity of CCs-AC against Cr(VI) ions from aqueous solution.

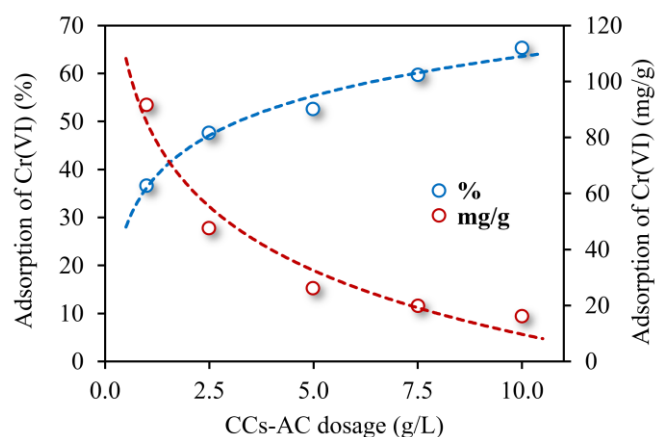


Figure 4. Effect of CCs-AC dosage on the adsorption of Cr(VI) ions onto CCs-AC from aqueous solution (Initial solution pH: 2.0; C_0 : 250.0 mg/L; agitation time: 4 h; CCs-AC dosage: 1.0–10.0 g/L; CCs-AC particle size: $\leq 125 \mu\text{m}$; temperature: 25 °C)

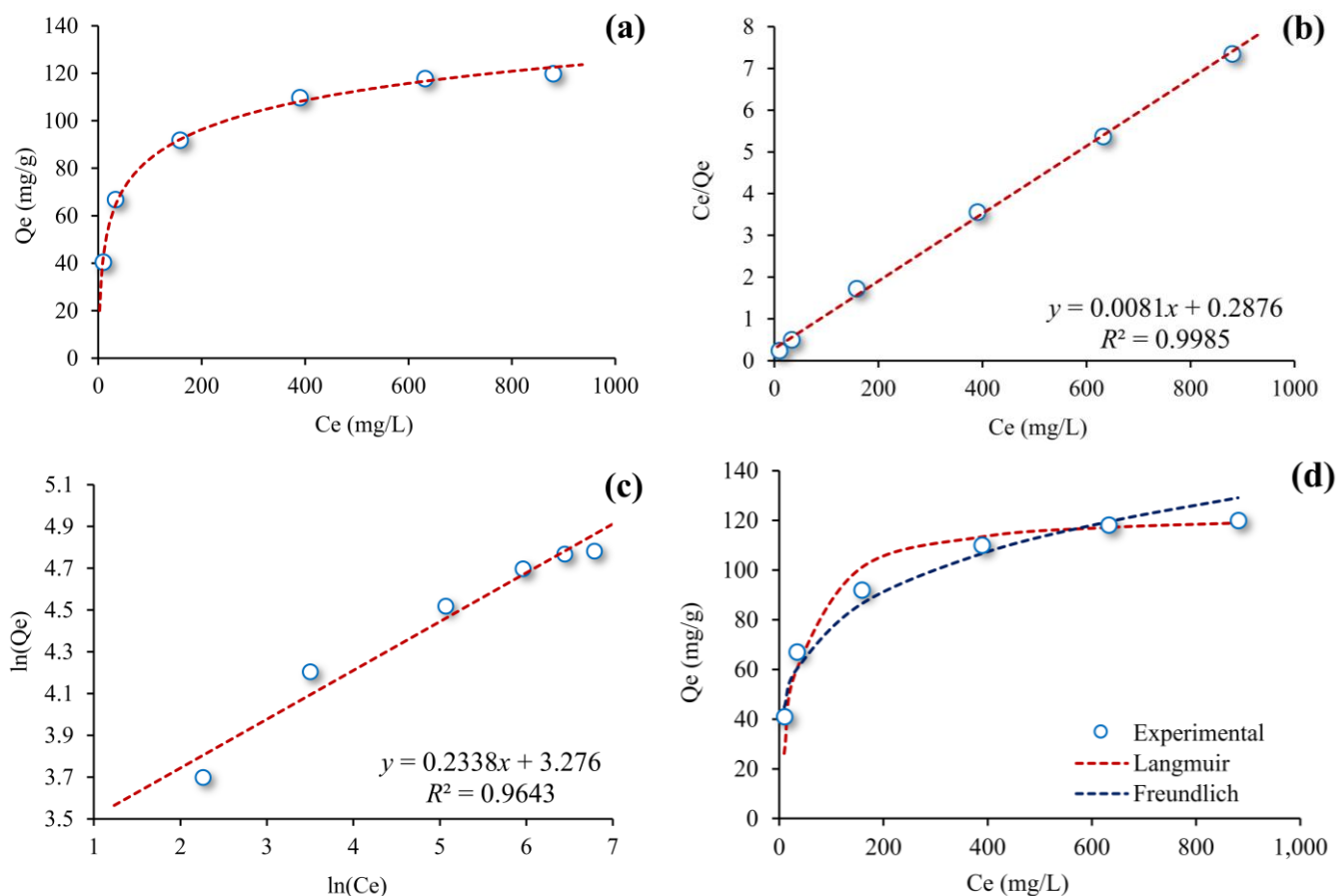


Figure 5. Concentration effect on the adsorption of Cr(VI) ions onto CCs-AC and the adsorption isotherms: (a) Ce – Qe graph, (b) Ce – Ce/Qe graph for Linear Langmuir isotherm, (c) ln(Ce) – ln(Qe) graph for Linear Freundlich isotherm, (d) Ce – Qe graph for non-linear Langmuir and Freundlich isotherms (Initial solution pH: 2.0; Co: 50–1000 mg/L; agitation time: 4 h; CCs-AC dosage: 1.0 g/L; CCs-AC particle size: $\leq 125 \mu\text{m}$; temperature: 25 °C)

The relationship between the adsorbate concentration remaining in the aqueous solution as a result of the adsorption process and the amount of adsorbate adsorbed per unit adsorbent is called adsorption isotherm.

Fig. 5(a) illustrates this relationship. As can be seen from the figure, the amount of Cr(VI) adsorbed per unit CCs-AC (mg/g) increases non-linearly with increasing initial Cr(VI) concentration in aqueous solution. The part of the graph where the adsorption reaches maximum saturation indicates the capacity of CCs-AC.

Langmuir and Freundlich isotherm models are more preferred than others in adsorption studies from aqueous solution. The Langmuir model is successfully applied to monolayer systems on homogeneous surfaces and to systems where relatively active sites have equal energy. The capacities of adsorbents that can comply with these conditions can be determined quite accurately with this model [29].

Langmuir adsorption model is given by Equation (8) below:

$$Q_e = \frac{bC_e}{1 + bC_e} \quad (8)$$

Equation (8) can be modified to derive its linear form in Equation (9):

$$\frac{C_e}{Q_e} = \frac{C_e}{Q_{\max}} + \frac{1}{bQ_{\max}} \quad (9)$$

Where C_e is the concentration of adsorbate remaining unadsorbed in solution (mg/L), Q_e is the amount of adsorbate adsorbed per unit adsorbent (mg/g), Q_{\max} is the maximum adsorption capacity (mg/g) and b is the constant related to the free energy or enthalpy of adsorption (L/mg).

The plot of C_e versus C_e/Q_e forms a line and indicates whether the adsorption follows the Langmuir model. Q_{\max} and b can be determined from the slope and the intercept, respectively. Q_{\max} will give the maximum adsorption capacity of the adsorbent of interest [32,33].

R_L , an important parameter of Langmuir isotherm, indicates whether the selected adsorbent-adsorbate relationship is suitable for adsorption. R_L is a dimensionless constant and is also called the separation factor or equilibrium parameter. R_L is expressed by Equation (10).

$$R_L = \frac{1}{1 + bC_0} \quad (10)$$

Where C_0 is the initial adsorbate concentration (mg/L). b is a constant (L/mg) derived from the Langmuir equation. The R_L value calculated from the formula is expected to be between 0 and 1 for the suitability of adsorption. In cases where R_L is greater than 1, it indicates that adsorption is not suitable for the selected adsorbent-adsorbate pair. When the R_L value is exactly equal to 1, it indicates that the adsorption is linear and when R_L is 0, it indicates that the adsorption is irreversible [7,15,29].

The other type of isotherm, Freundlich isotherm, is related to monolayer/multilayer adsorption from aqueous solution on heterogeneous surfaces. The mathematical expression of this model is as in Equation (11).

$$Q_e = K_f \times C_e^{1/n} \quad (11)$$

For simplicity of calculations in adsorption studies Equation (11) is usually used by taking the logarithm of both sides of the equation and transforming it into linear form (Equation 12).

$$\ln(Q_e) = \ln(K_f) + \frac{1}{n} \ln(C_e) \quad (12)$$

Where K_f (mg/g) and n are constants of this model and are related to adsorption capacity and adsorption density, respectively [32,33].

In this parameter, a series of Cr(VI) solutions prepared between 50–1000 mg/L and CCs-AC at a dose of 1.0 g/L were treated under optimum conditions. The Cr(VI) concentration remaining in the solution (C_e) after filtration and the amount of Cr(VI) adsorbed per gram of CCs-AC (Q_e) were calculated with the help of the relevant equations. Firstly, the graph in Fig. 4(a) was plotted as mentioned above. Then the linear graphs of Langmuir and Freundlich adsorption isotherms in Fig. 5(b) and Fig. 5(c) were plotted from the relevant linear formulas, respectively. The constants obtained from these graphs are given in Table 2.

As can be seen from Table 2, Fig. 5(b) and Fig. 5(c), the correlation coefficient for the linear Langmuir isotherm is larger than that obtained from the Freundlich isotherm. Therefore, it can be considered that

the experimental data are more compatible with the Langmuir model. However, in order to reach this conclusion definitively, the curvilinear forms of the related isotherm models should be compared. For this purpose, the constants obtained from the linear equations in Equation (9) and Equation (12) were used in the curvilinear equations Equation (8) and Equation (11) to theoretically re-derive the Q_e values. When these theoretical Q_e values and experimental Q_e values are shown on the same graph in Fig. 5(d), it can be said that the theoretical Q_e values that best represent the experimental Q_e values are mostly obtained from the Freundlich isotherm model. However, unlike the linear forms, no definite conclusion could be reached here. The adsorption behavior is more in agreement with the Freundlich model at relatively small concentrations and with the Langmuir model at high concentrations.

The Cr(VI) capacity value ($Q_{\max} = 123.7$ mg/g) derived by taking the inverse of the slope in the linear graph of the Langmuir isotherm model can be considered as quite high compared to the literature (Table 3). R_L values, another Langmuir parameter, were also calculated with the help of Equation (10). R_L values calculated for C_0 values between 50–1000 mg/L were found to be 0.42–0.03. This result shows the suitability of Cr(VI) adsorption onto CCs-AC.

3.5. Desorption of Cr(VI) ions adsorbed on CCs-AC

Desorption of adsorbate ions or molecules retained onto an adsorbent, in other words regeneration of the adsorbent used, is extremely important for the economy and usability of the system. Since Cr(VI) ions are in anionic form in solution at all pHs, they are adsorbed with much higher performance in the acidic region. Therefore, desorption efficiency will be very low with acidic characterized desorption solutions. As seen in the

Table 3. Comparison of Cr(VI) adsorption capacity of various activated carbon-based adsorbents

Precursor	Activating agent	Adsorbent dosage (g/L)	Q_{\max} (mg/g)	Reference
Rice husk	ZnCl ₂	2.0	56.82	[15]
Olive bagasse	Steam	2.0	109.89	[22]
Pomegranate husk	H ₂ SO ₄	2.0	35.2	[23]
Corn cob	CO ₂	5.0	57.37	[42]
Commercial AC	SiO ₂	1.0	60.9	[43]
Corn cob	ZnCl ₂ -NH ₄ Cl	0.5	34.48	[44]
Fir wood	KOH	0.4	180.3	[45]
Hazelnut shell	H ₂ SO ₄	2.5	170.0	[46]
Coconut shell	Chitosan	1.0	64.49	[47]
<i>Aloe vera</i> leaves	HNO ₃	2.0	59.88	[48]
Corn cob	H ₃ BO ₃	1.0	123.7	This work

pH study, the adsorption efficiency of Cr(VI) ions in the basic region is very low. Therefore, a series of NaOH solutions were prepared at concentrations between 0–3 mol/L for the desorption of Cr(VI) ions adsorbed onto CCs-AC.

Table 2. Langmuir and Freundlich constants for Cr(VI) ions

Langmuir constants				Freundlich constants		
Q_{\max} (mg/g)	Q_{\max} (mmol/g)	b (L/mg)	R^2	K_f (mg/g)	n	R^2
123.7	2.38	0.0281	0.9985	26.47	4.28	0.9643

CCs-AC at a dose of 5.0 g/L was placed in a series of polypropylene tubes. After adding 100 mg/L Cr(VI) solutions, they were shaken under optimum conditions. After filtration, the CCs-ACs in the tubes were air dried and then a series of NaOH solutions in the range of 0–3 M were added separately, and the desorption was carried out for 4 hours. The Cr(VI) concentrations desorbed into the solution were measured by MP-AES and after necessary calculations, Fig. 6 was plotted.

The results from Fig. 6 show that even the most concentrated NaOH solution (3.0 M) could not quantitatively desorb Cr(VI) ions adsorbed onto CCs-AC. This result proves that unlike typical cationic metal ions, Cr(VI) ions are much more strongly adsorbed onto CCs-AC. Since cationic metal ions bind to functional groups on many adsorbents by weak electrostatic interactions, their desorption can be achieved quantitatively even with very weakly acidic solutions. Cr(VI) ions, which are present in aqueous solution at relatively low pHs, mostly in the form of HCrO_4^- , bind to the adsorbent with much stronger interactions, especially chemically. Studies supporting this result are found in the literature [34–38].

3.6. Effect of temperature on the adsorption of Cr(VI) ions onto CCs-AC and adsorption thermodynamics

Temperature is an important indicator of whether the system works under all conditions, how well it performs under which ambient conditions, in short, how close its performance is to laboratory conditions in real applications. In addition, the study of temperature changes is an important parameter that is frequently applied in understanding the mechanism and energy of adsorption.

For this purpose, 5.0 g/L CCs-AC and a series of 250 mg/L Cr(VI) solutions were treated separately at temperatures ranging from 5–50 °C. The concentrations of Cr(VI) remaining unadsorbed in the solution after filtration were determined by MP-AES, from which the amount of Cr(VI) loaded per gram of adsorbent (mg/g) was calculated.

The temperature vs Q_e plot is given in Fig. 7(a). As can be seen from the figure, the adsorption behavior of Cr(VI) ions onto CCs-AC is via endothermic mechanism, that is, the increase in ambient temperature positively affects the adsorption efficiency.

The absorption and diffusion of energy during all kinds of events and chemical reactions, the transformation of one type of energy into another type and the relations between different types of energy in a system are the subject of thermodynamics. Thermodynamics determines the internal energy, enthalpy, entropy, and free energy values of the system during a physical or chemical transformation and examines their dependence on the reaction conditions.

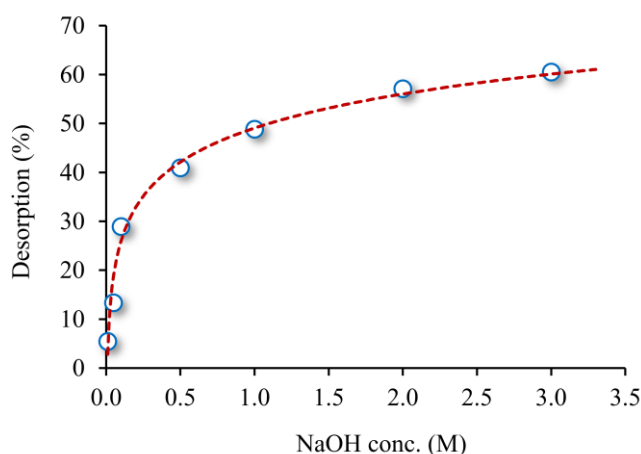


Figure 6. Desorption of Cr(VI) ions adsorbed on CCs-AC (Co: 100 mg/L)

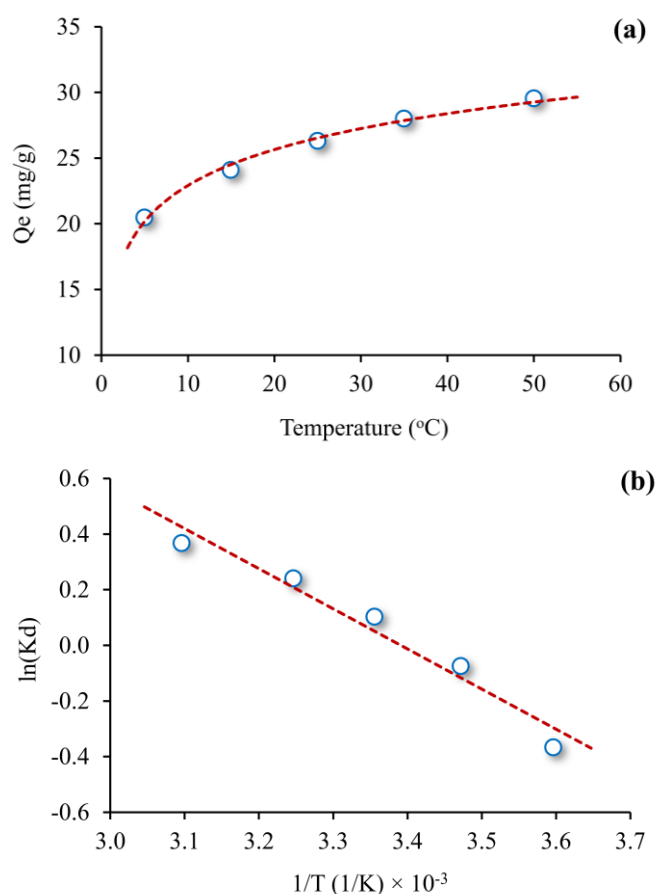


Figure 7. Effect of temperature on adsorption of Cr(VI) ions onto CCs-AC and thermodynamics: (a) Temp. – Q_e graph, (b) $1/T - \ln(Kd)$ graph for thermodynamic parameters (Co: 250 mg/L; pH: 2.0; CCs-AC dosage: 5.0 g/L; agitation time: 4 h; CCs-AC particle size: $\leq 125 \mu\text{m}$; temperature: 5–50 °C)

The sum of all kinds of energy that a substance stores in its structure is called enthalpy (H). In chemical reactions, the difference between the sum of the enthalpies of the products and the sum of the enthalpies of the reactants is called the enthalpy of reaction (ΔH). Entropy (ΔS) is the energy that cannot be converted into work in a physical system. The Gibbs free energy change (ΔG) is used to express the equilibrium state and willingness of a system. In spontaneous chemical

reactions and other physicochemical transformations, the free energy decreases, so the standard ΔG becomes negative. In short, for any system, all the energy is expressed by enthalpy (H), the available energy by free energy (G) and the unavailable energy by entropy (S). The equations derived for these concepts related to thermodynamics are given in Equations 13–16.

$$\Delta G = \Delta H - T\Delta S \quad (13)$$

$$\Delta G = -RT\ln(K_d) \quad (14)$$

$$K_d = \frac{C_a}{C_e} \quad (15)$$

$$\ln(K_d) = \frac{\Delta S}{R} - \frac{\Delta H}{RT} \quad (16)$$

Where T is the temperature (K), R is the gas constant (8.314 J/mol.K), K_d is the adsorption equilibrium constant, C_a is the concentration of adsorbate retained onto the adsorbent (mg/L), C_e is the adsorbate concentration remaining in the solution after adsorption (mg/L).

The graph of $\ln(K_d)$ vs $1/T$ forms a line (Fig. 7(b)). From the slope of this line ΔH and from the intercept ΔS can be found (Table 4), thus providing information about the reaction course.

The ΔG values in Table 4 become more negative in parallel with the increase in temperature. This indicates that adsorption occurs spontaneously. In cases where the adsorption efficiency is below 50%, $\ln(K_d)$ values are negative and therefore ΔG values are positive. As the adsorption efficiency increases above 50% with increasing temperature, $\ln(K_d)$ values are also positive. As a result, ΔG values will be negative.

The decrease in ΔG values with increasing temperature increases the feasibility of adsorption and the possibility of spontaneous formation. For the selected initial Cr(VI) concentration (250 mg/L), the feasibility of adsorption becomes more feasible at higher temperatures. Therefore, it is more important that ΔG decreases in relative value with increasing temperature rather than being positive or negative. This is not the case for low

Cr(VI) concentrations. At low Cr(VI) concentrations, room temperature is sufficient for the spontaneous formation of adsorption.

A positive ΔH value indicates that the adsorption of Cr(VI) ions onto CCs-AC is endothermic. The ΔH value can also help to decide whether the adsorption is chemical or physical. The enthalpy value of physical adsorption is generally not greater than 4 kJ/mol and for chemical adsorption not less than 20 kJ/mol [39,40]. The ΔH value is 12.0 kJ/mol (Table 4), which means that the adsorption of Cr(VI) ions on CCs-AC is slightly chemical rather than physical. Quantitative regeneration did not occur in the desorption study anyway.

A positive ΔS value (40.69 J/mol.K) increases the probability of randomization of the adsorption equilibrium occurring at the solid-liquid interface of the adsorbent during adsorption. In other words, this value indicates an increase in the amount of unused energy, i.e. an increase in the disorder of the system [41].

4. Conclusion

The data obtained from this study showed that activated carbon (CCs-AC) produced by chemical activation using boric acid from corn cobs, an agricultural waste by-product, can effectively remove Cr(VI) ions from aqueous solution. Moreover, with an adsorption capacity of 123.7 mg/g Cr(VI), CCs-AC has an even higher capacity than the activated carbons used in many studies in the literature.

As a result of optimization studies with model Cr(VI) solutions, it was determined that the optimum pH was 2.0 and the contact time was 4.0 hours. From the kinetic data, it was concluded that Cr(VI) adsorption on CCs-AC was consistent with the pseudo-second order kinetic model and the adsorption rate was controlled by the boundary layer diffusion together with the intraparticle diffusion.

From the thermodynamic data, it was determined that temperature had a positive effect on adsorption, thus, from the enthalpy value of 12.0 kJ/mol, the reaction was endothermic, and the adsorption process was rather chemically driven. The negative Gibbs free energy values proved that the adsorption was spontaneous.

This study is important in several ways: (i) Activated carbon was produced from corn cobs, an agricultural waste that is not used for any purpose, giving them an economic value. (ii) Possible damage to the environment from these wastes discharged into the environment was prevented. (iii) Recycling activities were encouraged by recycling wastes that have no economic value.

Table 4. Thermodynamic data for adsorption of Cr(VI) ions from aqueous solution onto CCs-AC

T (°C)	K_d	ΔG (kJ/mol)	ΔS (J/mol.K)	ΔH (kJ/mol)
5	0.69	0.85		
15	0.93	0.18		
25	1.11	-0.26	40.69	12.00
35	1.27	-0.62		
50	1.44	-1.85		

Acknowledgements

The authors are grateful to Prof. Dr. Mustafa Imamoglu (Sakarya University, Sakarya, Turkey) for his contribution in the production of activated carbon subjected to adsorption tests in this study. The authors would also like to thank Prof. Yunus Onal (Inonu University, Malatya, Turkey) for his contribution to the characterization analysis of the material and Assoc. Prof. Cemalettin Baltaci (Gümüşhane University, Gümüşhane, Turkey) for his contribution to the adsorption tests.

References

- [1] Y. Wang, C. Peng, E. Padilla-Ortega, A. Robledo-Cabrera, A. López-Valdivieso, Cr(VI) adsorption on activated carbon: Mechanisms, modeling and limitations in water treatment, *J Environ Chem Eng*, 8(4), 2020, 104031.
- [2] S. Sujatha, R. Sivarethinamohan, A critical review of Cr(VI) ion effect on mankind and its amputation through adsorption by activated carbon, *Materials Today: Proceedings*, 37(2), 2021, 1158–1162.
- [3] WHO, Guidelines for Drinking-water Quality, Fourth edition incorporating the first addendum, WHO Headquarters in Geneva, 2017.
- [4] R.C. Bansal, M. Goyal, Activated carbon adsorption, 2005, CRC Press, London, UK, Taylor and Francis.
- [5] Z.E. Sayın, C. Kumaş, B. Ergül, Activated carbon production from hazelnut shells (in Turkish), *AKU J Sci Eng*, 16, 2016, 025805(409–419).
- [6] C. Djilani, R. Zaghoudi, F. Djazi, B. Boucekima, A. Lallam, A. Modarressi, M. Rogalski, Adsorption of dyes on activated carbon prepared from apricot stones and commercial activated carbon, *J Taiwan Inst Chem E*, 53, 2015, 112–121.
- [7] M. Abbas, S. Kaddour, M. Trari, Kinetic and equilibrium studies of cobalt adsorption on apricot stone activated carbon, *J Ind Eng Chem*, 20(3), 2014, 745–751.
- [8] M. Koohestani, A. Salem, S. Salem, Decolorization of corn syrup in a dynamic system by activated carbon bed: Microwave-assisted impregnation of H₃PO₄ over cherry and date stones for efficient purification, *Sustain Chem Pharm*, 36, 2023, 101298.
- [9] A.C. Lua, J. Guo, Preparation and characterization of activated carbons from oil-palm stones for gas-phase adsorption, *Colloid Surface A*, 179(2–3), 2001, 151–162.
- [10] J. Serafin, B. Dziejarski, J. Sreńscek-Nazzal, An innovative and environmentally friendly bioorganic synthesis of activated carbon based on olive stones and its potential application for CO₂ capture, *Sustain Mater Technol*, 38, 2023, e00717.
- [11] I. Okman, S. Karagöz, T. Tay, M. Erdem, Activated carbons from grape seeds by chemical activation with potassium carbonate and potassium hydroxide, *Appl Surf Sci*, 293, 2014, 138–142.
- [12] H. Boulika, M.E. Hajam, M.H. Nabih, I.R. Karim, N.I. Kandri, A. Zerouale, Definitive screening design applied to cationic & anionic adsorption dyes on Almond shells activated carbon: Isotherm, kinetic and thermodynamic studies, *Materials Today: Proceedings*, 72(7), 2023, 3336–3346.
- [13] D.S.G.D. Senewirathna, S. Thuraisingam, S. Prabagar, J. Prabagar, Fluoride removal in drinking water using activated carbon prepared from palmyrah (Borassus flabellifer) nut shells, *Curr Res Green Sustain Chem*, 5, 2022, 100304.
- [14] A. Putranto, Z.W. Ng, T. Hadibarata, M. Aziz, J.Y.J. Yeo, S. Ismadji, J. Sunarjo, Effects of pyrolysis temperature and impregnation ratio on adsorption kinetics and isotherm of methylene blue on corn cobs activated carbons, *S Afr J Chem Eng*, 42, 2022, 91–97.
- [15] X. Zhang, S. Wu, Y. Liu, Z. Wang, H. Zhang, R. Xiao, Removal of Cr(VI) from aqueous solution by Rice-husk-based activated carbon prepared by Dual-mode heating method, *Carbon Res Conver*, 6(2), 2023, 76–84.
- [16] E.R. Raut, M.A. Bedmohata, A.R. Chaudhari, Comparative study of preparation and characterization of activated carbon obtained from sugarcane bagasse and rice husk by using H₃PO₄ and ZnCl₂, *Materials Today: Proceedings*, 66(4), 2022, 1875–1884.
- [17] P. Paraskeva, D. Kalderis, E. Diamadopoulou, Production of activated carbon from agricultural by-products, *J Chem Technol Biotechnol* 83(5), 2008, 581–592.
- [18] T.M. Alslaibi, I. Abustan, M.A. Ahmad, A.A. Foul, A review: production of activated carbon from agricultural byproducts via conventional and microwave heating, *J Chem Technol Biotechnol*, 88, 2013, 1183–1190.
- [19] A. Gundogdu, P. Bozbeyoglu, M. Imamoglu, C. Baltaci, C. Duran, V.N. Bulut, Characterization of the adsorption mechanism of cadmium(II) and methylene blue upon corncobs activated carbon, *Anal Lett*, 56(3), 2023, 433–448.
- [20] A. Sharma, N. Kumar, M. Sillanpää, P.R. Makgwane, S. Kumar, K. Kumari, Carbon nano-structures and functionalized associates: Adsorptive detoxification of organic and inorganic water pollutants, *Inorg Chem Commun*, 141, 2022, 109579.
- [21] C. Duran, D. Ozdes, A. Gundogdu, M. Imamoglu, H.B. Senturk, Tea-industry waste activated carbon, as a novel adsorbent, for separation, preconcentration and speciation of chromium, *Anal Chim Acta*, 688(1), 2011, 75–83.
- [22] H. Demiral, İ. Demiral, F. Tümsük, B. Karabacakoglu, Adsorption of chromium(VI) from aqueous solution by activated carbon derived from olive bagasse and applicability of different adsorption models, *Chem Eng J*, 144(2), 2008, 188–196.
- [23] A.E. Nemr, Potential of pomegranate husk carbon for Cr(VI) removal from wastewater: Kinetic and isotherm studies, *J Hazard Mater* 161(1), 2009, 132–141.
- [24] Y. Alvarez-Galvan, B. Minofar, Z. Futera, M. Francoeur, C. Jean-Marius, N. Brehm, C. Yacou, U.J. Jauregui-Haza, S. Gaspard, Adsorption of hexavalent chromium using activated carbon produced from sargassum ssp.: comparison between lab experiments and molecular dynamics simulations, *Molecules*, 27(18), 2022, 6040.
- [25] W. Liu, J. Zhang, C. Zhang, L. Ren, Preparation and evaluation of activated carbon-based iron-containing adsorbents for enhanced Cr(VI) removal: mechanism study, *Chem Engin J*, 189–190, 2012, 295–302.
- [26] H. Qiu, L. Lv, B.c. Pan, Q.j. Zhang, W.m. Zhang, Q.x. Zhang, Critical review in adsorption kinetic models. *J. Zhejiang Univ. Sci. A* 10, 2009, 716–724.
- [27] S. Mandal, J. Calderon, S.B. Marpu, M.A. Omary, S.Q. Shi, Mesoporous activated carbon as a green adsorbent for the removal of heavy metals and Congo red: characterization, adsorption kinetics, and isotherm studies, *J Contam Hydrol*, 243, 2021, 103869.
- [28] J. Wang, X. Guo, Adsorption kinetic models: physical meanings, applications, and solving methods, *J Hazard Mater*, 390, 2020, 122156.
- [29] D. Özdes, C. Duran, S.T. Ozeken, O. Kalkisim, Y. Top, Natural and H₂SO₄ modified plane sawdust as a low-cost adsorbent: removal of anionic and cationic dyes from aqueous solutions, *Turk J Anal Chem*, 5(1), 2023, 32–42.
- [30] G.B. Adebayo, H.I. Adegoke, S. Fauzeeyat, Adsorption of Cr(VI) ions onto goethite, activated carbon and their composite: kinetic and thermodynamic studies, *Appl Wat Sci*, 10, 2020, 213.
- [31] M.E. Goher, A.M. Hassan, I.A. Abdel-Moniem, A.H. Fahmy, M.H. Abdo, S.M. El-Sayed, Removal of aluminum, iron and manganese ions from industrial wastes using granular activated

- carbon and Amberlite IR-120H, Egypt J Aqu Res, 41(2), 2015, 155–164.
- [32] W. Somyanonthanakun, R. Ahmed, V. Krongtong, S. Thongmee, Studies on the adsorption of Pb(II) from aqueous solutions using sugarcane bagasse-based modified activated carbon with nitric acid: kinetic, isotherm and desorption, Chem Physics Impact, 6, 2023, 100181.
- [33] Y. Zhou, J. Lu, Y. Zhou, Y. Liu, Recent advances for dyes removal using novel adsorbents: a review, Environ. Pollut., 252 (2019), 352–365.
- [34] B. Singha, S.K. Das, Biosorption of Cr(VI) ions from aqueous solutions: Kinetics, equilibrium, thermodynamics and desorption studies, Colloid Surface B, 84(1), 2011, 221–232.
- [35] A. Tyłak, P. Oleszczuk, R. Dobrowolski, Sorption and desorption of Cr(VI) ions from water by biochars in different environmental conditions. Environ Sci Pollut Res 22, 2015, 5985–5994.
- [36] E. Daneshvar, M.J. Zarrinmehr, M. Kousha, A.M. Hashtjin, G.D. Saratale, A. Maiti, M. Vithanage, A. Bhatnagar, Hexavalent chromium removal from water by microalgal-based materials: adsorption, desorption and recovery studies, Biores Technol, 293, 2019, 122064.
- [37] J. Bayuo, M.A. Abukari, K.B. Pelig-Ba, Desorption of chromium (VI) and lead (II) ions and regeneration of the exhausted adsorbent. Appl Water Sci, 10, 2020, 171.
- [38] D. Ozdes, A. Gundogdu, B. Kemer, C. Duran, M. Kucuk, M. Soylak, Assessment of kinetics, thermodynamics and equilibrium parameters of Cr(VI) biosorption onto *Pinus brutia* Ten, Canadian J Chem Eng, 92, 2014, 139–147.
- [39] M. Khormaei, B. Nasernejad, M. Edrisi, T. Eslamzadeh, Copper biosorption from aqueous solutions by sour orange residue, J Hazard Mater, 149, 2007, 269–274.
- [40] P. Bozbeyoglu, C. Duran, C. Baltaci, A. Gundogdu, Adsorption of methylene blue from aqueous solution with sulfuric acid activated corn cobs: equilibrium, kinetics and thermodynamics assessment, Hittite Journal of Science and Engineering, 7(3), 2020, 239–256.
- [41] T. Karthikeyan, S. Rajgopal, L.R. Miranda, Chromium(VI) adsorption from aqueous solution by *Hevea Brasilinesis* sawdust activated carbon, J Hazard Mater, 124(1-3), 2005, 192–199.
- [42] S. Nethaji, A. Sivasamy A.B. Mandal, Preparation and characterization of corn cob activated carbon coated with nano-sized magnetite particles for the removal of Cr (VI), Biores Technol, 134, 2013, 94–100.
- [43] M. Karnib, A. Kabbani, H. Holaila, Z. Olamaa, Heavy metals removal using activated carbon, silica and silica activated carbon composite, Energy Procedia, 50, 2014, 113–120.
- [44] S. Tang, Y. Chen, X. Ruzhen, W. Jiang, Y. Jiang, Preparation of activated carbon from corn cob and its adsorption behavior on Cr(VI) Removal, Water Sci Technol, 73(11), 2016, 2654–2661.
- [45] L. Khezami, R. Capart, Removal of Chromium (VI) from aqueous solution by activated carbons: kinetic and equilibrium studies, J Hazard Mater, 123, 2005, 223–231.
- [46] M. Koby, Removal of Cr(VI) from aqueous solutions by adsorption onto hazelnut shell activated carbon: kinetic and equilibrium studies, Biores Technol, 91, 2004, 317–321.
- [47] Y. Liu, H. Shan, Y. Pang, H. Zhan, C. Zeng, Iron modified chitosan/coconut shell activated carbon composite beads for Cr(VI) removal from aqueous solution, Int J Bio Macromol, 224, 2023, 156–169.
- [48] A.K. Prajapati, S. Das, M.K. Mondal, Exhaustive studies on toxic Cr(VI) removal mechanism from aqueous solution using activated carbon of Aloe vera waste leaves, J Molecul Liq, 307, 2020, 112956.



Green synthesis and structural characterization of ZnO nanoparticles and ZnO@TiO₂ nanocomposites by *Cinnamomum verum* bark extract

Gökçenur Selva Keleşoğlu¹ , Mesut Özdiñçer² , Aslıhan Dalmaz³ , Kübra Zenkin¹ , Sefa Durmuş^{3*} 

¹Düzce University, Graduate Education Institute, Department of Chemistry, 81620, Düzce, Türkiye

²Düzce University, Graduate Education Institute, Faculty of Technology, Department of Composite - Materials, 81620, Düzce, Türkiye

³Düzce University, Faculty of Art and Science, Department of Chemistry, 81620, Düzce, Türkiye

Abstract

In this work, a facile and efficient approach for the green synthesis of ZnO@TiO₂ bimetallic oxide nanoparticles by exploiting the potential of *Cinnamomum verum* bark extract as a biogenic reducing agent is presented. The synthesized nanoparticles were subjected to an extensive characterization process involving various spectroscopic techniques. These techniques include X-ray diffraction analysis, Fourier transform infrared spectroscopy, Scanning electron microscopy and Energy dispersive X-ray spectroscopy. Based on the obtained results, it highlights the potential of green synthesized ZnO@TiO₂ nanocomposites as a promising material for many applications.

Keywords: *Cinnamomum verum*, ZnO@TiO₂ nanocomposites, ZnO NPs, green synthesis

1. Introduction

In recent years, the application of biosynthesis to the production of nanoparticles (NPs) has attracted attention as a more environmentally sustainable, safer and cost-effective alternative to traditional chemical and physical methods [1]. Plant extracts in particular hold great promise for 'green' production due to their widespread availability, affordability, ease of use and scalability [2,3]. These extracts contain a potent combination of antioxidants, including polyphenols, reducing sugars, nitrogenous bases and amino acids, which have the ability to reduce metal ions in a metal salt solution. The reduction of metal ions initiates the formation of nucleation centers which attract additional metal ions and incorporate neighboring nucleation sites, ultimately leading to the formation of nanoparticles. These particles are associated with organic substances from plant extracts which help to increase the stability of the particles. It has also been reported that these nanoparticles have no toxicity compared to those produced by traditional chemical methods [4]. Due to their unique properties compared to their bulk materials, there has been considerable interest in the synthesis and

characterization of these nanoparticles particularly metal oxide nanoparticles, in the last decades. The high surface to volume ratio of these nanoparticles is a major factor contributing to their distinctive properties [5–7]. Among metal oxide nanoparticles zinc oxide (ZnO), titanium dioxide (TiO₂) show particularly promising physical and chemical properties [8,19]. Their unique properties make them very important in a wide range of applications [10,11] and research endeavors. Various methods, including chemical [1], sonochemical [12,13], electrochemical, photochemical and microemulsion techniques, are used to produce them. However, many of these methods involve complex reaction conditions and the use of toxic chemicals, leading to environmental pollution problems. As a result, researchers have sought to develop environmentally friendly methods for the synthesis of nanoparticles

Cinnamomum verum (*C. verum*), commonly known as cinnamon, is a very abundant, economical and easily available plant. It is known to be rich in phytochemicals such as alkaloids, polyphenolic compounds, terpenoids and flavonoids, which act as stabilizing and capping

Citation: G.S. Keleşoğlu, M. Özdiñçer, A. Dalmaz, K. Zenkin, S. Durmuş, Green Synthesis and Structural Characterization of ZnO Nanoparticles and ZnO@TiO₂ Nanocomposites by *Cinnamomum verum* Bark Extract Turk J Anal Chem, 5(2), 2023, 118–123.

 <https://doi.org/10.51435/turkjac.1395817>

Author of correspondence: sefadurmus@duzce.edu.tr

Received: November 25, 2023

Tel: +90 (380) 541 24 04

Accepted: December 06, 2023

Fax: +90 (380) 541 24 03

agents during the synthesis process [14]. Moreover, the bark of *C. verum* contains a notable concentration of carboxylic and phenolic functional groups, such as bisabolol, cinnamic acid, heptanoic acid, hexadecenoic acid, linalool, and phytol [15]. However, it is of great importance to identify accurately the specific phytochemicals responsible for the formation of nanoparticles with controlled properties. This understanding can significantly contribute to the utilization of cinnamon in various applications, especially in the field of nanotechnology [16,17].

As a result, it has become essential to investigate synthesis routes for ZnO NPs and TiO₂ nanocomposites and to explore their properties and applications through extensive research. In this context, our study aims to investigate the synthesis of ZnO@TiO₂ nanocomposites using *C. verum* bark extract, which is a sustainable and environmentally friendly approach

2. Materials and methods

2.1. Reagents and chemicals

Cinnamomum verum, used as a stabilizing and reducing agent in the study (Fig. 1), was obtained from local markets in Düzce province. In addition, all of the chemical materials used in the study are of analytical purity. Sodium hydroxide, zinc nitrate hexahydrate and titanium(IV)isopropoxide chemicals used in the synthesis stage of metal oxide nanoparticles were obtained from Merck company.



Figure 1. Image of *Cinnamomum verum* bark

2.2. Apparatus

Heidolph brand magnetic stirrer was used to ensure homogeneous mixing of the solutions throughout the experimental studies. An Isolab brand pH meter was used to ensure that the nanoparticles precipitated appropriately. Elektromag M5040P brand oven was used to dry the synthesized products. Radwag brand electronic balance was used throughout the experimental studies. Separation of the products was carried out using a VWR brand centrifuge. Filtration of *C. verum* extract and nanoparticles obtained through the extract was carried out using an Isolab brand vacuum pump. The elemental composition of the nanoparticles

obtained as a result of the studies was determined by energy dispersive X-ray analysis (EDX), and their morphology and size were determined by scanning electron microscopy (SEM) (FEI Quanta FEG 250).

The functional groups present in the structure of the nanoparticles were recorded using a Perkin Elmer Spectra Two UATR Fourier transform infrared spectroscopy (FT-IR) spectrophotometer. X-ray diffraction (XRD) patterns of ZnO NPs and ZnO@TiO₂ nanocomposites were obtained using a Smart Lab instrument with Cu-K α radiation (1.5406 Å).

2.3. Preparation of *Cinnamomum verum* bark extract

Cinnamomum verum was first obtained from local markets and ground into powder. The powdered cinnamon was washed several times with deionized water to remove impurities. Following this step, to prepare extract, 2.5 g *C. verum* bark was heated in 100 mL deionized water for one hour in a magnetic stirrer. After this time, the extract (Fig. 2) was allowed to cool at room temperature and filtered with Whatman filter paper. It was stored in the refrigerator at 4 °C to be used for the synthesis of ZnO NPs and ZnO@TiO₂ nanocomposites.



Figure 2. Schematic representation of the preparation steps of *C. verum* bark extract

2.4. Green synthesis of ZnO NPs

In order to synthesize ZnO NPs, 25 mL *C. verum* bark extract was heated to 60 °C and 2.08 g Zn(NO₃)₂·6H₂O was dissolved in 25 mL deionized water and added. The resulting solution was stirred with a magnetic stirrer at 60 °C for one hour color change were observed. Following this step, 0.1 M NaOH was added to adjust the pH of the solution to 8. The mixture was centrifuged at 5000 rpm for 7 min. and then washed several times with deionized water. The resulting product was then dried in an oven at 60 °C for 24 hours. After the drying step was completed, it was subjected to calcination at 450 °C for 2.5 hours. The white-colored ZnO NPs formed as a result of calcination was stored in a desiccator at room temperature (Fig. 3).



Figure 3. Schematic representation of the preparation steps of ZnO NPs

2.5. Green synthesis of ZnO@TiO₂ nanocomposites

Cinnamomum verum bark extract was heated to 60 °C, then a solution of 2.97 g Zn (NO₃)₂·6H₂O in 10 mL deionized water was added slowly. To this solution 0.1 M NaOH was added until pH = 8, then 3 mL of titanium(IV) isopropoxide was added slowly and stirring was continued at 60 °C for one hour on a magnetic stirrer. The resulting mixture was centrifuged at 5000 rpm for 7 min. and the product was washed several times with deionized water to remove impurities. It was then placed in an oven to dry at 60 °C for 24 hours. The dried product was then subjected to calcination in a muffle furnace at 450 °C for 2.5 hours (Fig. 4) and the off-white-colored product was stored in a desiccator for analysis.



Figure 4. Schematic representation of the preparation steps of ZnO@TiO₂ nanocomposites

3. Results and discussion

3.1. FT-IR spectra

FT-IR spectroscopy analysis was carried out to determine the presence of functional biomolecular groups in *C. verum* extract and synthesized ZnO NPs and ZnO@TiO₂ nanocomposites. When the FT-IR spectrum of *C. verum* shown in Fig. 5 is examined, the bands at 3271 and 2928 cm⁻¹ are due to O-H stretching vibrations in the structure of polyphenols and asymmetric C-H stretching vibrations of -CH₃ groups in the structure of biomolecules. The presence of the O-H group in the structure of water is indicated by the peak at 1586 cm⁻¹ in the FT-IR spectrum. Also observed at 1408 cm⁻¹ and 1386 cm⁻¹ are peaks belonging to aliphatic C-H stretching and CH₃ symmetric bending vibrations. The C-O stretch vibration of hydroxy flavonoids in the biostructure of *C. verum* is seen at 1260 cm⁻¹, while the band at 1043 cm⁻¹ is related to the C-O stretch of primary alcohols. The peak corresponding to the C=C vibrations in the structure of the benzene ring was observed at 614 cm⁻¹ [18-20]. In the FT-IR spectrum of ZnO NPs, only the peak at 402 cm⁻¹ belonging to Zn-O bond was observed. Moreover, in the FT-IR spectrum of ZnO@TiO₂ nanocomposites, vibrations at 402 cm⁻¹ are attributed to Zn-O bond [21,22] and vibrations at 388 cm⁻¹ to Ti-O bond. When the FT-IR spectra of ZnO NPs and ZnO@TiO₂ nanocomposites

were analyzed, no vibrations belonging to organic compounds in the structure of cinnamon extract were observed.

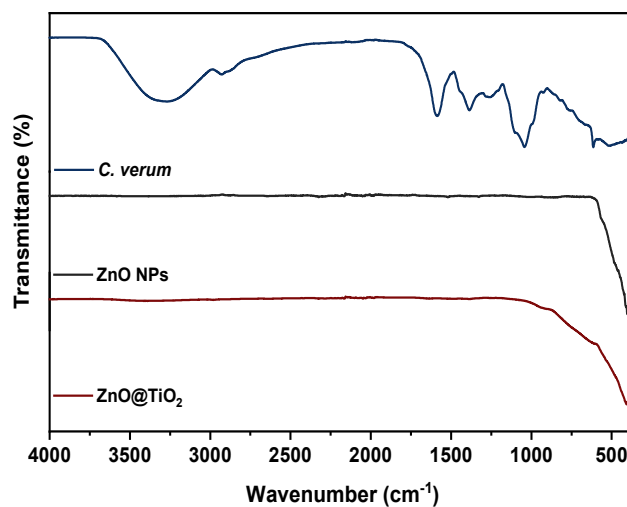


Figure 5. FT-IR spectra of dry *C. verum* extract, ZnO NPs and ZnO@TiO₂ nanocomposites

3.2. XRD analysis

In the XRD pattern of ZnO NPs and ZnO@TiO₂ nanocomposites are shown in Fig. 6. Different peaks were observed in the XRD pattern of ZnO NPs at 2θ=31.82°, 34.45°, 36.29°, 47.60°, 56.63°, 62.91°, 66.46°, 67.98°, 69.06°, 72.63° and 77.06°. These peaks were interrelated to (100), (002), (101), (102), (110), (103), (200), (112), (201), (004) and (202) hkl planes. All these diffraction peaks are consisted to wurtzite (hexagonal) structure compatible with JCPDS Card No. 036-1451 [23] and space group: P6₃mc [24]. Moreover, the cell parameters of the ZnO NPs a= b= 3.24 Å, and c= 5.20 Å. The absence of distinct peaks in the XRD pattern indicates that the nanoparticles do not contain impurities. In the XRD pattern of ZnO@TiO₂ nanocomposites, in addition to the peak belonging to ZnO NPs, 25.41° and the associated (101) hkl planes of the anatase phase (space group: I₄/amd) of TiO₂ with JCPDS card no. 21-1272 are shown [25].

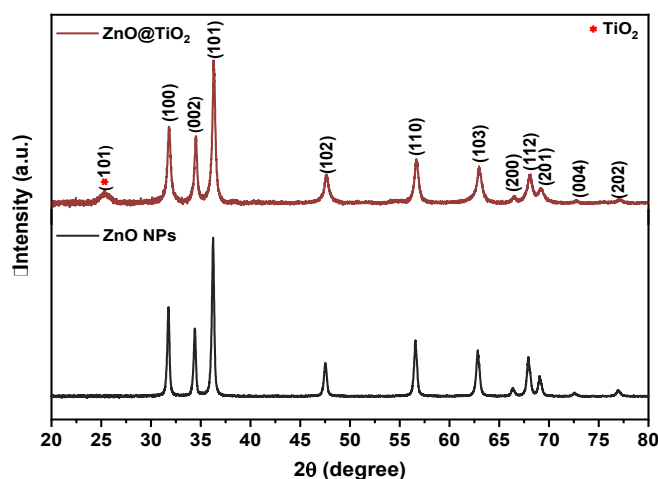
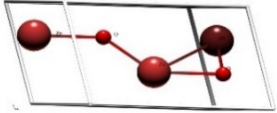
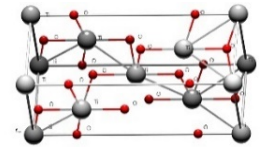


Figure 6. XRD pattern of ZnO NPs and ZnO@TiO₂ nanocomposites

Table 1. The structural parameters of ZnO and TiO₂ NPs.

Sample	JCPDS Card no:	Crystal Structure	Space Group	Lattice Parameters (Å)	Cell Volume (Å ³)	Unit Cell
ZnO	036-1451	Hexagonal	P6 ₃ mc	a= b= 3.24 c= 5.20	54.58	
TiO ₂	21-1272	Anatase	I4 ₁ /amd	a= b= 3.80 c= 9.61	138.76	

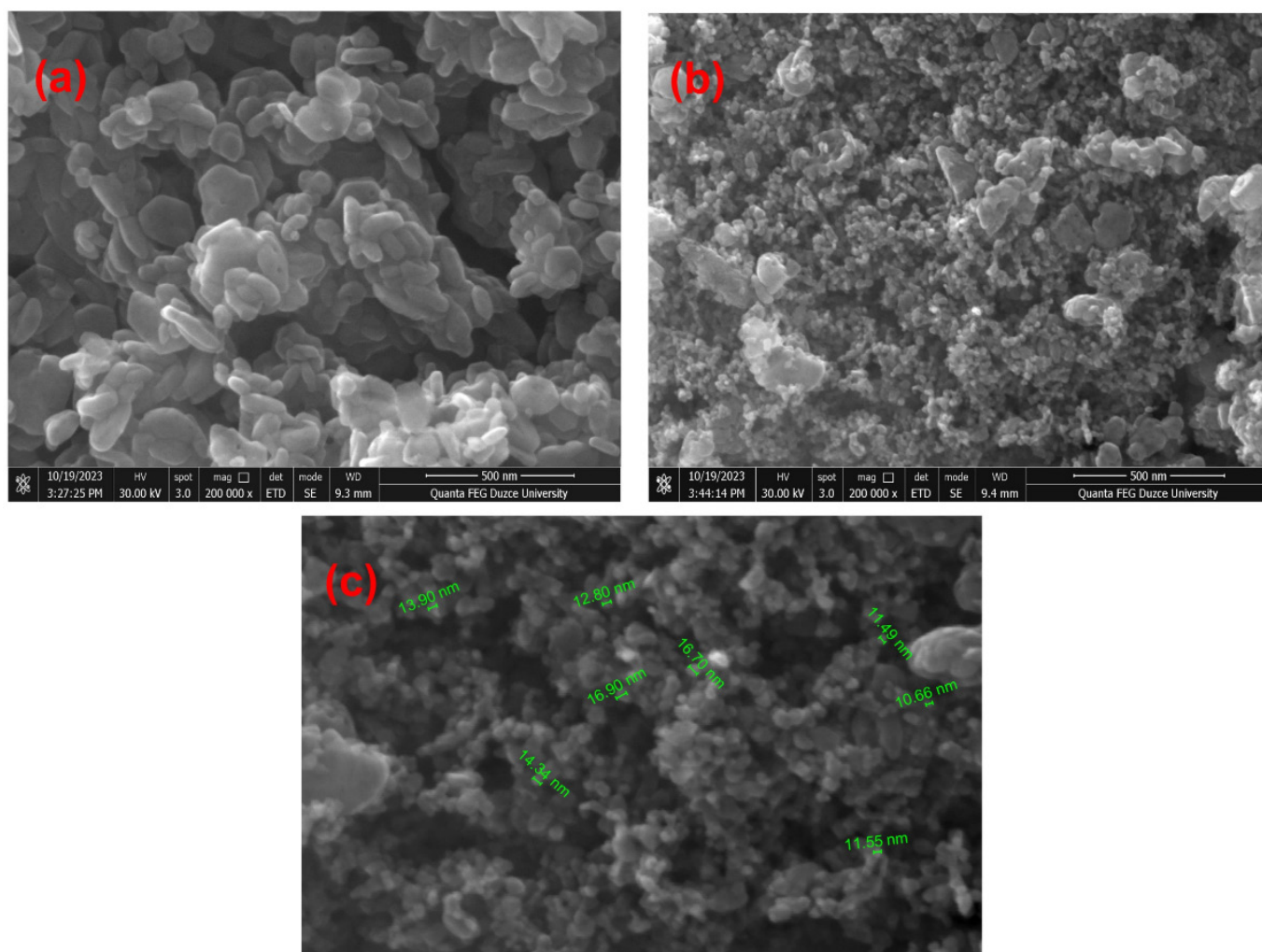
The cell parameters of the TiO₂ NPs a= b= 3.80 Å, and c= 9.61 Å as shown in Table 1. In addition, the weight fraction of ZnO@TiO₂ nanocomposites was determined using the Whole Powder Pattern Fitting (WPPF) method, which approximates the components and fraction of the sample based on the measured XRD pattern and the materials [26]. According to WPPF weight fraction analysis, ZnO@TiO₂ nanocomposites consists of 89% ZnO and 11% TiO₂ NPs.

3.3. SEM-EDX analysis

The SEM images in Fig. 7(a-c) depict the surface morphology of green-synthesized ZnO NPs and ZnO@TiO₂ nanocomposites using *C. verum* extract. The

ZnO NPs exhibit hexagonal and near-spherical shapes, with some irregularities indicating non-homogeneity [27,28]. The particle size of ZnO NPs falls within the range of 30 - 50 nm, and there is a noticeable tendency for slight agglomeration (Fig. 7(a)).

Recent studies have shown that there is an optimum amount of TiO₂ that is effective in inhibiting growth and phase transformation of ZnO NPs, leading to production of smaller ZnO NPs [29]. This method resulted in obtaining ZnO@TiO₂ nanocomposites with an average size of 20 nm, as shown in Fig. 7 (b, c). The surface morphology of the ZnO@TiO₂ nanocomposites shows the presence of both spherical and hexagonal shapes. In addition, TiO₂ NPs are widely dispersed on the surface of the ZnO@TiO₂ nanocomposites.

**Figure 7.** SEM images of the synthesized (a) ZnO NPs (b, c) ZnO@TiO₂ nanocomposites

Energy dispersive X-ray spectroscopy, a mode of operation of SEM, is used to determine the elemental composition of nanomaterials and provides information on the percentage of each element in the materials (Fig. 8). The presence of oxygen, titanium and zinc elements were observed in the EDX spectra of ZnO NPs and ZnO@TiO₂ nanocomposites. The stoichiometric ratios seen in the spectra are compatible with the proposed structure and it is seen from these ratios that the amount of TiO₂ doped corresponds to 10.8% [30].

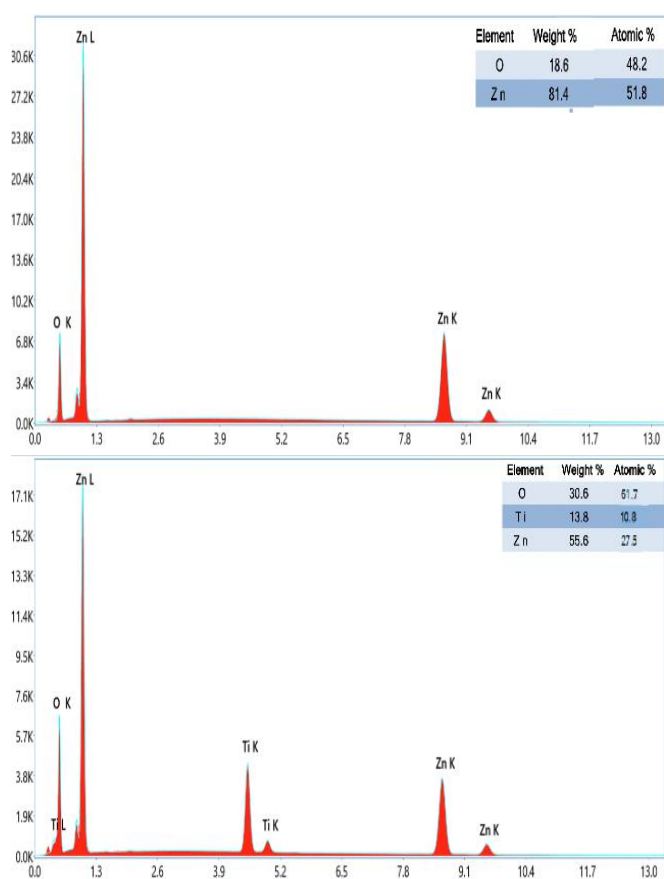


Figure 8. EDX analysis of the synthesized (a) ZnO NPs (b) ZnO@TiO₂ nanocomposites

4. Conclusion

In this study, ZnO NPs and ZnO@TiO₂ nanocomposites were synthesized using aqueous extract of *C. verum* as natural chelating agent that stabilizes and aid in the bioreduction of the nanoparticles without using any harmful surfactant. FT-IR and XRD results show that ZnO NPs and ZnO@TiO₂ nanocomposites are free from any organic compounds and impurities. According to SEM results, ZnO NPs and ZnO@TiO₂ nanocomposites have hexagonal, spherical particles with an average shape of 40 nm and 20 nm respectively. The EDX results indicated that, the amount of TiO₂ addition was found to be 10.8%, which is in agreement with the XRD analysis value calculated by the WPPF method. Furthermore, the EDX spectrum exhibited no impurities in the compound's structure. ZnO NPs and ZnO@TiO₂

nanocomposites have more extensive application in biotechnology, optical device, medical, sensors, coatings, catalysis and drug delivery. This green synthesis is a highly efficient approach, using fewer chemicals and controlling costs. This has led to additional research to investigate the further implementation of environmentally friendly nanoparticles.

Acknowledgement

This work is supported by Düzce University Scientific Project (Project no: 2022.05.03.1365).

References

- [1] L. Krishnia, P. Thakur, A. Thakur, Synthesis of nanoparticles by physical route, in synthesis and applications of nanoparticles (1. Edition), 2022, Singapore: Springer Nature.
- [2] L. Soltys, O. Olkhovyy, T. Tatarchuk, M. Naushad, Green synthesis of metal and metal oxide nanoparticles: principles of green chemistry and raw materials, *Magnetochem*, 7, 2021, 145.
- [3] M. Jamzad, B. Mokhtari, P.S. Mirkhani, Green synthesis of metal nanoparticles mediated by a versatile medicinal plant extract, *Chem Pap*, 77, 2022, 1457–1467.
- [4] D. Gnanasangeetha, M. Suresh, A review on green synthesis of metal and metal oxide nanoparticles, *Nat Environ Pollut Technol*, 19, 2020, 1789–1800.
- [5] M.P. Nikolova, M.S. Chavali, Metal oxide nanoparticles as biomedical materials, *Biomimetics*, 5, 2020, 27.
- [6] J.J. Xu, W.C. Zhang, Y.W. Guo, X.Y. Chen, Y.N. Zhang, Metal nanoparticles as a promising technology in targeted cancer treatment, *Drug Deliv*, 29, 2022, 664–678.
- [7] P. Prasannalakshmi, N. Shanmugam, Fabrication of TiO₂/ZnO nanocomposites for solar energy driven photocatalysis, *Mater Sci Semicond Process*, 61, 2017, 114–124.
- [8] N. Geetha, S. Sivaranjani, A. Ayeshamariam, M. Kavin Micheal, D. Saravankumar, S. A. Fowziya, A.M. Uduman Mohideen, M. Jayachandran, ZnO/TiO₂ nanocomposites semiconductor for bacterial applications and dye-sensitized solar cell applications, *J Adv Microsc Res*, 13, 2018, 3–11.
- [9] G.K. Upadhyay, J.K. Rajput, T.K. Pathak, V. Kumar, L.P. Purohit, Synthesis of ZnO:TiO₂ nanocomposites for photocatalyst application in visible light, *Vacuum*, 160, 2019, 154–163.
- [10] M. Özdiñçer, S. Durmuş, Fabrication, characterization and corrosion inhibition properties of SCW-based ZnO nanofluids, *Chem Eng Commun*, 2023, 1–16.
- [11] K. Akshaya, A. Rajasekar, S. Rajeshkumar, Antioxidant activity of zinc oxide nanoparticles synthesized using grape seed extract: An in vitro study, *Plant Cell Biotechnol. Mol Biol*, 21, 2020, 21–29.
- [12] A. Hassanjani-Roshan, M.R. Vaezi, A. Shokuhfar, Z. Rajabali, Synthesis of iron oxide nanoparticles via sonochemical method and their characterization, *Particuology*, 9, 2011, 95–99.
- [13] M. Darroudi, A. Khorsand Zak, M.R. Muhamad, N.M. Huang, M. Hakimi, Green synthesis of colloidal silver nanoparticles by sonochemical method, *Mater Lett*, 66, 2012, 117–120.
- [14] P.V. Rao, S.H. Gan, Cinnamon: A multifaceted medicinal plant, *Evid Based Complement Alternat Med*, 2014, 2014.
- [15] H.H. Phu, K. Pham Van, T.H. Tran, D.T.N. Pham, Extraction, chemical compositions and biological activities of essential oils of *Cinnamomum verum* cultivated in Vietnam, *Process*, 10, 2022, 1713.
- [16] M.A. Alghuthaymi, A.M. Diab, A.F. Elzahy, K.E. Mazrou, A.A. Tayel, S.H. Moussa, Green biosynthesized selenium

- nanoparticles by cinnamon extract and their antimicrobial activity and application as edible coatings with nano-chitosan, *J Food Qual*, 2021, 2021,1–10.
- [17] X. Zhu, K. Pathakoti, H.M. Hwang, Green synthesis of titanium dioxide and zinc oxide nanoparticles and their usage for antimicrobial applications and environmental remediation, *Green Synthesis, Characterization and Applications of Nanoparticles*, Editors: A.K Shukla, S. Iravani, 2018, Elsevier.
- [18] H. Özcan, A. Dalmaz, M. Özdiğer, K. Zenkin, S. Durmuş, Biosynthesis and characterization of α -FeOOH nanoparticles using Isabella grape (*Vitis labrusca* L.) extract, *Turk J Anal Chem*, 5, 2023, 43–49.
- [19] F. Mojarrad, A. Asadi, A. Abdolmaleki, S. Mirzaee, S. Zahri, Preparation of cinnamon-coated cerium oxide nanoparticles and evaluation of their anticonvulsant effect in rats, *Pharm Chem J*, 57, 2023, 648–655.
- [20] A. Sameen, S. Fathima, S. Ramlal, S. Kumar, F. Khanum, Nanopackaging of silver using spice extract and their characterization, *Sci Technol Arts Res J*, 3, 2014, 52–56.
- [21] R. Bekem, S. Durmuş, A. Dalmaz, G. Dülger, *Agaricus bisporus* Ekstraktı Kullanılarak ZnO Nanopartiküllerinin Yeşil Sentezi: Yapısal Karakterizasyonu ve Biyolojik Aktivitelerinin İncelenmesi, *DÜBİTED*, 11, 2023, 551–562.
- [22] S.N. Gençay, S. Durmuş, A. Dalmaz, G. Dülger, Ticari Bal Kullanılarak ZnO Nanopartiküllerinin Yeşil Sentezi, Yapısal Karakterizasyonu ve Biyolojik Aktivitelerinin İncelenmesi, *DÜBİTED*, 11, 2023, 1437–1445.
- [23] T. Bezrodna, G. Puchkovska, V. Shymanovska, J. Baran, H. Ratajczak, IR-analysis of H-bonded H₂O on the pure TiO₂ surface, *J Mol Struct*, 700, 2004, 175–181.
- [24] F.A. Alharthi, A.A. Alghamdi, N. Al-Zaqri, H.S. Alanazi, A.A. Alsyahi, A.E. Marghany, N. Ahmad, Facile one-pot green synthesis of Ag–ZnO nanocomposites using potato peel and their Ag concentration dependent photocatalytic properties, *Sci Rep*, 10, 2020, 20229.
- [25] S. Kumar, D. Arora, A. Dhupar, V. Sharma, J.K. Sharma, S.K. Sharma, A. Gaur, Structural and optical properties of polycrystalline ZnO nanopowder synthesized by direct precipitation technique, *J Nano-Electron Phys*, 12, 2020, 04027-1-04027-5.
- [26] R. Nawaz, H. Ullah, A.A.J. Ghanim, M. Irfan, M. Anjum, S. Rahman, S. Ullah, Z.A. Baki, V. Kumar Oad, Green synthesis of ZnO and black TiO₂ materials and their application in photodegradation of organic pollutants, *ACS Omega*, 8, 2023, 36076–36087.
- [27] D. Negrea, E. David, V. Malinovschi, S. Moga, C. Ducu, X-ray analysis of spent catalysts and recovered metals, *Environ Eng Manag J*, 9, 2010, 1235–1241.
- [28] D. Ramírez-Ortega, A.M. Meléndez, P. Acevedo-Peña, I. González, R. Arroyo, Semiconducting properties of ZnO/TiO₂ composites by electrochemical measurements and their relationship with photocatalytic activity, *Electrochim Acta*, 140, 2014, 541–549.
- [29] A. Hossain, Y. Abdallah, M.A. Ali, M.M.I. Masum, B. Li, G. Sun, Y. Meng, Y. Weng, Q. An, Lemon-fruit-based green synthesis of zinc oxide nanoparticles and titanium dioxide nanoparticles against soft rot bacterial pathogen *Dickeya dadantii*, *Biomol*, 9, 2019, 863.
- [30] M. Zamani, M. Rostami, M. Aghajanzadeh, H. Kheiri Manjili, K. Rostamizadeh, H. Danafar, Mesoporous titanium dioxide@zinc oxide–graphene oxide nanocarriers for colon-specific drug delivery, *J Mater Sci*, 53, 2018, 1634–1645.



Geochemical evaluation of the genetic relationship of Kısacık (Ayvacık, Çanakkale/Türkiye) epithermal gold mineralization using trace and rare earth elements

Alaaddin Vural 

Ankara University, Faculty of Engineering, Department of Geological Engineering, 06830, Gölbaşı, Ankara, Türkiye

Abstract

The Kısacık gold deposit is situated in the Biga Peninsula, Northwest Anatolia, Türkiye. The aim of this study is to investigate the genetic relationship between the Kısacık gold deposit and the surrounding rocks using trace element (TE) and rare earth element (REE) geochemistry. For this purpose, 48 samples directly and/or indirectly associated with the mineralization in the area were analyzed for major oxides, trace, and rare earth elements using inductively coupled plasma-atomic emission spectrometry (ICP-AES) and inductively coupled plasma-mass spectrometry (ICP-MS). Considering the laboratory conditions under which the analyses were performed, the limit of detection (LOD) values for metals varied between 0.01 and 0.04%, while those given in parts per million (ppm) varied between 0.002 and 0.1 ppm. In addition, the relative standard deviations (RSD) for all metals ranged from 0.38 to 5.52%. The results of the study revealed that the gold mineralizations in the Kısacık area have a compatible pattern with the Kısacık Volcanics and the Kuşçayırı plutonic rocks in the near vicinity of the area. The gold mineralizations in the Kısacık area are consistent with the TE and REE patterns of the upper continental and lower continental crust, as shown by comparison with spider diagrams normalized to different geological settings. The gold enrichments in the listvenites and silicified rocks in the area are also consistent with the TE and REE element patterns of these rock types. The results of this study support the conclusion that the gold mineralization in the Kısacık area is related to hydrothermal fluids that leached elements from the Kısacık volcanics. In addition, hydrothermal fluids from granitic rocks were also effective in the mineralization process. As a result, the gold mineralization in the Kısacık area is genetically related to both the upper continental crust and relatively the lower continental crust and is characterized as a multi-sourced and multi-process epithermal gold deposit.

Keywords: Kısacık epithermal gold mineralization, Trace-Rare Earth elements, Spider diagrams, Çanakkale, Türkiye

1. Introduction

Epithermal gold deposits are a type of gold mineralization that forms near the surface of the Earth due to the action of hydrothermal fluids. These fluids are heated by magmatic activity and can travel through fractures in rocks, dissolving and transporting minerals [1]. Trace elements (TEs) and rare earth elements (REEs) are often enriched in epithermal gold deposits, and their presence can provide valuable clues about the formation and potential richness of these deposits [2]. The geochemical behavior of TEs and REEs is an important factor in their association with epithermal gold deposits. These elements are typically found in minerals that dissolve easily in hydrothermal fluids, such as feldspars, micas, amphiboles, and pyroxenes. Once dissolved, TEs and REEs can be transported by hydrothermal fluids over long distances. During ore formation,

hydrothermal fluids cool, and pressure drops, causing the dissolved minerals to precipitate and form new minerals. TEs and REEs are often incorporated into these newly formed minerals, leading to their enrichment in epithermal gold mineralization. TEs and REEs are also found in a wide variety of rocks, but they are particularly abundant in volcanic rocks. This is because volcanic rocks are formed from molten magma, which contains high concentrations of these kinds of elements. When hydrothermal fluids interact with volcanic rocks, they dissolve TEs and REEs and carry them away. These elements can then be transported to sites of epithermal gold deposition [3,4]. They (TEs and REEs) can be used to trace the movement of hydrothermal fluids through the rocks and to identify the different types of alteration that have occurred, including propylitic, argillic, and

Citation: A. Vural, Geochemical evaluation of the genetic relationship of Kısacık (Ayvacık, Çanakkale/Türkiye) epithermal gold mineralization using trace and rare earth elements, Turk J Anal Chem, 5(2), 2023, 124–136.

 <https://doi.org/10.51435/turkjac.1397465>

Author of correspondence: alaaddinvural@hotmail.com

Received: November 30, 2023 **Tel:** +90 (456) 233 17 13

Accepted: December 17, 2023 **Fax:** +90 (456) 233 10 75

adularia-sericite alteration. This information can be used to better understand the formation of epithermal gold deposits and to identify potential exploration targets. The relationship between TEs and REEs, and epithermal gold deposits has several important implications for understanding of their genetic characteristics, and their exploration and evaluation. For example, the presence of these elements can be used to:

- Identify areas that have the potential to host epithermal gold deposits.
- Trace the movement of hydrothermal fluids and identify potential ore zones.
- Assess the potential richness of epithermal gold deposits.

By understanding the geochemical behavior of TEs and REEs, geologists can use these elements as valuable tools for exploring and evaluating epithermal gold deposits.

In addition to the factors discussed above, several other considerations are important when interpreting the relationship between TEs and REEs, and epithermal gold deposits. These include:

- The type of epithermal gold deposit (high-sulfidation, low-sulfidation, intermediate-sulfidation),
- The mineralogy of the deposit,
- The geological setting of the deposit.

So, trace and REEs are valuable indicators of epithermal gold deposits. Their chemical behavior, origin in rocks, and relationships with alteration in the field provide important clues about the formation and potential richness of these deposits.

Anatolia's strategic location and rich natural resources were key factors in its emergence as a cradle of civilizations in antiquity. The Biga Peninsula, located in the northwest of Western Anatolia, has been one of the most important mining regions in the Anatolian geography, both today and in the past [5]. The rich mineral potential of the region has triggered numerous studies in the fields of general geology and mining geology [6,7, 8–15,16–21]. The region is characterized by a diverse array of mineral deposits, evidenced by numerous abandoned mine workings and ongoing mining operations. These deposits, encompassing copper, lead, zinc, iron, gold, tungsten, molybdenum, antimony, and mercury, reflect the region's complex geological history, shaped by multiple phases of granite intrusions and volcanic activities that have resulted in a variety of mineralization styles. Mineral exploration activities continue in the region, conducted by both the Turkish Geological Survey (MTA) and numerous domestic and foreign private companies. One of the most recent discoveries made under an MTA-led

exploration project is the Kısacık gold deposit [14,22]. The Kısacık gold mineralization area is situated at Ayvacık-Çanakkale, Biga Peninsula, Northwest Anatolia (Türkiye).

The aim of this study is to contribute to the understanding of the genetic relationship of the Kısacık (Ayvacık, Çanakkale, Türkiye) epithermal gold deposit using TEs and REEs. To this end, the relationship between the deposit, wall rock, and source rock was investigated by using TEs and REEs patterns of the deposit, alteration, and surrounding rocks, as well as rocks that are thought to have influenced the potential mineralization process.

2. MATERIAL AND METHODS

2.1. Geological characteristics of the area

The Biga Peninsula, located in Northwest Anatolia, Türkiye, is home to a diverse array of geological units (Fig. 1) [15,22], including pre-Tertiary, Tertiary, and post-Tertiary rocks [23]. The pre-Tertiary units of the Biga Peninsula, Northwest Türkiye, were subdivided into three distinct tectonic zones by Okay et al. [23]: the Sakarya Tectonic Zone, the Ayvacık-Karabiga Zone, and the Ezine Zone, extending from northwest to southeast. The Sakarya Tectonic Zone is principally composed of the Kazdağ Group metamorphic rocks and the Karakaya Complex [24], overlying these metamorphic rocks and post-Triassic sediments. The Ayvacık-Karabiga Zone is characterized by an ophiolitic mélangé, the Çetmi Ophiolitic Mélangé. Eclogite blocks and Upper Triassic limestone blocks within the mélangé are distinctive features of the Ayvacık-Karabiga Zone. The Ezine Zone comprises continental-derived rocks, including a Permo-Carboniferous sedimentary sequence, the Karadağ Unit, metamorphosed under greenschist facies conditions, and an overlying ophiolite, the Denizgören Ophiolite, emplaced during the Permo-Triassic period in the western portion of the zone. Additionally, the Ezine Zone contains high-grade metamorphic rocks of sedimentary origin, the Çamlıca Mica schist [6,22,23].

The Tertiary and Post-Tertiary units in the region encompass magmatic and sedimentary rocks, commencing with middle Eocene neritic limestone. This is followed by Upper Eocene turbidites, interbedded andesite, and andesitic tuff, which concordantly overlie the neritic limestone. Volcanic rocks in the near vicinity of the study area were named Kuşçayır and Kısacık volcanics, respectively, based on their age differences. The older volcanics, which outcrop in the north, are named Kuşçayır volcanics, while the younger volcanics, which outcrop in the south, are named Kısacık volcanics. Eocene (?)/Oligo-Miocene calc-alkaline magmatism subsequently commenced in the region, marked by a disconformity plane [25–29]. Magmatic activity spanned

the Eocene (?)/Oligocene to Upper Pliocene Quaternary (?) period, encompassing plutonic and volcanic rocks along with their associated pyroclastics [22,30]. Notably, dacite, andesite, rhyolite, and acidic tuffs are exposed, often interbedded with sedimentary rocks containing coal in some areas. Sedimentary rocks, primarily lacustrine and terrestrial clastics, are found in Upper Miocene-Pliocene age terrains, and Quaternary alluvium is also present.

Granitic rocks are present outside the study area, in its northern part. Volcanic rocks, collectively known as the Kısacık volcanics [22], occur within the study area and exhibit varying degrees of alteration, including hematization and silicification. These rocks predominantly comprise andesite, latite, rhyolite, basaltic andesite, ignimbrite, basaltic trachyandesite lavas, and pyroclastic rocks. Lateral transitions between these volcanic rocks and fluvial conglomerates, as well as lacustrine sedimentary rocks, are observed. Geochronological studies by Siyako et al. [26] and Genç [29] indicate that these volcanic rocks belong to the Early-Middle Miocene period. Basalt, the youngest manifestation of magmatism in the region, is found in the western vicinity of the study area.

Known anomalous areas in the study area and its vicinity have been identified in the lisenitic zones north of the Kısacık ore field and in the veins and fractures of altered volcanic rocks in the southern part of the field. Hydrothermal alteration is widespread in the volcanic rocks in the Kısacık epithermal ore field and its vicinity.

A few samples from the Kısacık area analyzed for heavy mineral geochemistry by Pehlivan et al. [31] yielded Au values ranging from 60 ppb to 1100 ppb. In the study conducted by the principal investigator during his doctoral dissertation at the Kısacık gold field, the volcanic rocks were found to be extensively cut by capillary silica veins. Sericitic hydrothermal alteration was widespread in the volcanic rocks of the ore field, and hematitization and limonitization accompanied this alteration and mineralization.

In a study of the Kısacık gold ore field conducted by the corresponding author, Vural [22], it was determined that the formation temperatures of the orebodies ranged from 190 °C to 290 °C based on fluid inclusion studies. The salinity was found to be 0-7% NaCl equivalent, and sulfur isotope values were mostly close to zero. Therefore, it was proposed that the gold mineralization in the field is of the epithermal type.

2.2. Sampling and analytical procedure

As part of the mine geology study of the area, a detailed geology and mine geology map of the area was prepared. Observations were carried out to reveal the details of the mine geology of the area, and rock samples were collected for geochemical purposes, considering the sections where alteration and silicification are

present. In addition to geochemical samples, petrographic samples were collected to reveal the geology and lithology of the area, XRD samples to identify alteration, and ore microprobe samples to identify ore minerals. Petrographic studies were used to determine the rocks in the area, thus revealing the geology of the area. The results of these studies in detailed will be presented in a separate mine geology study of the region.

To elucidate the genetic relationship between the orebodies and the mineralization in the area, a total of 48 samples were collected from both orebodies and associated rocks (host rock, wall rock, and associated rocks). These samples were ground at the Gümüşhane University Central Laboratory and the MTA Laboratory before being sent to the ACME Analytical laboratory (Vancouver, Canada) for whole-rock major oxide, trace element (including heavy metals), and rare earth element (REE) analyses. Major oxide and trace element (including heavy metals) analyses were performed using inductively coupled plasma-atomic emission spectrometry (ICP-AES), while rare earth element (REE) analyses were performed using inductively coupled plasma-mass spectrometry (ICP-MS) at ACME Analytical Laboratories (Vancouver, Canada). The laboratory is accredited, and all analyses were conducted in accordance with international standards. To ensure the accuracy and sensitivity of the analyses, routine procedures were followed, and a t-test was performed to confirm that the certified values used during the analysis and the values obtained were statistically indistinguishable ($p \leq 0.05$) [32].

For major and trace element/heavy metal analyses, approximately 0.2 g of powdered sample was mixed with 1.5 g of LiBO₂ and analyzed after dissolving it in a solution containing 5% HNO₃. For rare earth element analysis, approximately 0.25 g of powdered sample was dissolved in four different acids and analyzed.

After the acidic solutions of the samples solubilized by the wet digestion method were obtained, they were measured in ICP-AES and ICP-MS devices. The measured values were converted into ppm and % units with the help of the formulas given in Equation 1 and Equation 2.

$$ppm = \frac{C \times V}{m} \quad (1)$$

$$\% = \frac{ppm}{10000} \quad (2)$$

ppm: part per million (mg/kg)

C: Concentration measured in mg/L by ICP-AES and ICP-MS

V: Final volume completed after wet digestion (mL)

m: Mass of sample weighed for wet digestion (g)

Table 1. The analysis results of the samples from the study area (1)

Analyte	K ₂ O	TiO ₂	P ₂ O ₅	Cr ₂ O ₃	Ba	Sum	Ni	Rb	Sr	Y	Zr	Nb	Cs	La	Ce
Unit	%	%	%	%	ppm	%	ppm	ppm	ppm	ppm	ppm	ppm	ppm	ppm	ppm
Sample/ LOD	0.01	0.01	0.01	0.0001	1.0	0.01	20.0	0.1	0.5	0.1	0.1	0.1	0.1	0.1	0.1
Kis20	3.35	0.13	0.03	0.001	271.7	100.01	1.8	96.1	50.1	12.7	77.9	10.6	3.4	29.2	52.2
BayG-1	4.37	0.21	0.06	0.001	1251	99.81	13.2	168.8	614.1	6.4	187.4	10.4	1.8	37.9	76.9
BayG-2	2.80	0.59	0.18	0.001	622.2	99.89	4.8	97.5	557.2	21.1	117.8	6.4	3.0	27.5	54.1
BayG-3	2.80	0.61	0.15	0.002	434.7	99.95	6.1	106.2	342.9	21.1	127.2	6.4	8.2	24.3	47.9
Kusvol-1	1.44	0.68	0.15	0.001	400.2	99.80	15.2	43.9	391.2	21.7	114.1	5.9	2.2	16.1	29.7
Kis21	2.82	0.76	0.19	0.002	630.0	99.91	11.2	101.3	174.1	24.3	92.9	11.2	9.9	31.8	57.6
Ter1	0.28	0.04	0.21	0.076	46.3	100.0	35.8	9.9	176.7	2.6	11.3	3.4	3.5	2.8	7.7
Kusvol-2	1.94	0.48	0.14	0.003	378.7	99.81	17.1	62.3	384.4	14.6	114.5	4.9	3.2	18.9	37.2
Lis1	0.34	0.03	0.01	0.253	92.0	99.90	1227.1	10.5	71.7	1.7	6.7	0.9	1.4	1.7	3.1
Kis1	2.93	0.11	0.02	0.001	191.4	100.0	2.3	83.1	25.8	11.7	67.8	7.8	3.8	21.1	36.2
Kis4	5.98	0.50	0.10	0.002	487.4	99.95	8.7	190.0	23.4	18.7	131.2	7.9	12.2	20.9	42.9
Lis2	0.05	0.01	0.01	0.131	50.5	99.86	410.1	2.4	662.1	0.9	0.8		1.0		0.9
Kar1	0.17	0.01	0.01	0.001	145.1	100.0	12.1	13.5	20.5	3.7		2.6	8.1	0.8	1.5
Kar2	1.96	0.44	0.15	0.001	591.4	99.78	5.7	80.6	426.6	17.4	133.3	7.5	7.8	27.1	50.2
Kar3	0.14	0.01	0.11	0.001	259.3	99.91	21.3	0.7	357.2	0.4	3.0	1.5	0.3	2.1	4.3
BayG-4	2.51	0.60				99.55								28.7	
Kusvol-3	3.00	0.80				99.25	20.1								
Kusvol-4	3.22	0.78				99.07	20.2								
Kusvol-5	2.90	0.80				98.20	20.3								
Kusvol-6	2.95	0.88				99.09	19.2							36.7	
Kis21	4.66	0.45				99.66	9.1								
Kis22	3.39	1.11				99.07	39.4								
Kis23	3.22	1.06				98.44	24.3								
Kis24	3.36	0.81				98.43	20.2							71.5	
BayG-5	5.49	0.26				100.3								63.3	
BayG-6	3.02	0.67				100.4								34.2	
BayG-7	3.06	0.81				100.3								35.1	
BayG-8	3.29	0.52				99.32	5.0								
BayG-9	2.80	0.55				99.03									
Kis2	2.85	0.10	0.04	0.002	228.2	100.0	8.0	86.0	71.6	9.2	49.0	5.0	3.6	14.2	26.3
Kis3	1.38	0.17	0.11	0.001	106.0	100.0	0.2	56.6	42.3	7.6	57.7	3.5	9.4	11.8	23.5
Kis5	1.82	0.11	0.04	0.003	200.3	100.0	7.5	62.6	72.0	3.6	30.6	3.7	7.5	4.7	10.1
Kis6	5.38	0.37	0.15	0.001	988.9	99.87	2.7	147.8	68.0	24.6	176.0	10.1	3.2	41.3	79.8
Kis7	0.04	0.01	0.02	0.120	26.9	100.0	633.1	1.1	133.4	0.5	1.3	1.6	0.5		
Kis8	0.03		0.01	0.113	22.1	99.96	643.2	0.7	120.7	0.4	1.4	1.7	0.4	0.6	0.3
Kis9	4.77	0.52	0.25	0.012	1114.3	99.81	37.3	166.5	453.8	14.2	216.1	9.8	3.3	45.5	77.9
Kis10	5.80	0.57	0.16	0.010	657.2	99.79	8.0	293.3	165.6	19.7	271.2	18.2	50.3	53.5	89.6
Kis11	3.30	2.31	0.50	0.022	1607.1	99.63	17.0	163.6	318.2	35.5	437.8	20.0	20.7	103.6	203.8
Kis12	2.95	0.16	0.03	0.012	267.3	99.96	2.5	82.7	27.2	13.3	87.8	12.6	4.1	21.7	33.3
Kis13	5.58	0.48	0.14	0.009	532.4	99.88	2.5	173.7	248.3	22.6	180.8	15.7	6.2	43.2	73.6
Kis14	6.39	0.44	0.07	0.009	946.3	99.88	4.8	184.2	146.0	22.7	179.5	9.4	6.1	32.7	62.3
Kis15	2.14	0.17	0.03	0.021	117.2	99.95	22.4	69.2	34.0	12.8	94.9	11	4.0	25.9	44.6
Kis16	2.83	0.77	0.18	0.003	747.4	99.84	10.8	97.2	157.6	21.9	94.3	11.8	8.8	31.4	52.2
Kis17	2.03	0.12	0.03	0.003	202.1	99.98	7.1	58.5	63.6	3.2	33.1	3.8	6.5	5.1	9.3
Kis19	3.26	0.13	0.03		241.2	99.96	1.7	85.9	42.1	10.9	74.6	10.1	2.6	27.6	43.3
Lis3	0.04	0.02	0.04	0.320		99.93		26.9	0.4	1.2	0.3	1.4	102	0.4	
Lis4	0.08	0.03	0.02	0.254		99.94		39.5	0.6	5.2	0.2	0.8	18.2	1.7	0.2
Lis5	0.01	0.01	0.02	0.142		99.95	1.3	16.2	0.3	3.3	0.9	1.3	11.1	0.7	

Table 2. The analysis results of the samples from the study area (2)

Analyte	Hf	Ta	Au	Pb	Th	U	Lu	Yb	Tm	Er	Ho	Dy	Tb	Gd	Eu	Sm	Nd	Pr
Unit	ppm	ppm	ppb	ppm	ppm	ppm	ppm	ppm	ppm	ppm	ppm	ppm	ppm	ppm	ppm	ppm	ppm	ppm
Sample/LOD	0.1	0.1	0.5	0.1	0.2	0.1	0.01	0.05	0.01	0.03	0.02	0.05	0.01	0.05	0.02	0.05	0.3	0.02
Kis20	3.1	1.1	3.6	7.1	27.1	3.5	0.27	1.74	0.22	1.32	0.36	1.75	0.24	1.39	0.27	2.10	13.9	4.70
BayG-1	5.5	1.2	0.8	11.3	30.3	4.5	0.11	0.62	0.09	0.61	0.22	1.12	0.23	1.57	0.73	3.31	22.4	6.83
BayG-2	3.3	0.6	1.5	6.6	14.9	3.4	0.32	2.13	0.30	2.12	0.69	3.41	0.64	3.75	1.21	4.62	23.3	5.87
BayG-3	3.7	0.6	4.1	9.4	10.3	3.4	0.35	2.22	0.31	2.27	0.70	3.65	0.63	3.86	1.04	4.10	20.1	5.20
Kusvl1	3.0	0.6	1.3	2.6	9.1	2.6	0.36	2.26	0.32	2.25	0.81	3.86	0.61	3.63	1.07	3.43	15.5	3.86
Kis21	2.5	0.7	106.5	9.7	7.0	1.0	0.42	2.61	0.38	2.66	0.87	4.21	0.72	4.31	1.16	4.31	21.9	5.94
Ter1		0.4	9470.5	22.0	0.9	2.1	0.04	0.25		0.28	0.11	0.46	0.09	0.44	0.16	0.60	4.0	1.15
Kusvl2	2.8	0.5	4.5	8.8	7.5	2.8	0.22	1.53	0.23	1.45	0.51	2.44	0.44	2.60	0.94	3.10	16.2	4.08
Lis1			20.8	1.2	1.8	0.6	0.03	0.17		0.17		0.25	0.04	0.20		0.20	1.0	0.32
Kis1	2.4	0.7	14.1	4.9	18.6	3.5	0.22	1.43	0.20	1.19	0.36	1.66	0.25	1.26	0.32	1.62	10.1	3.14
Kis4	3.8	0.6	6922.8	38.7	11.5	4.9	0.26	2.12	0.33	1.93	0.67	3.45	0.55	3.34	0.99	3.71	18.9	4.74
Lis2			12.0	3.3	0.2			0.09		0.08		0.14	0.02	0.06		0.11		0.10
Kar1			1592.1	3.7	0.3	0.2	0.05	0.31	0.07	0.37	0.11	0.39	0.04	0.34	0.06	0.22	1.0	0.22
Kar2	3.7	0.6		8.8	10.9	3.3	0.27	1.68	0.28	1.83	0.61	3.02	0.49	2.92	0.98	4.01	19.9	5.53
Kar3			8412.0	149.7	1.7	0.4						0.13	0.04	0.32	0.06	0.33	1.6	0.48
BayG-4		0.6		14.0		2.2		1.77									20.2	
Kusvl3																		
Kusvl4																		
Kusvl5																		
Kusvl6		0.5		22.0		4.9		3.05									34.4	
Kis21																		
Kis22																		
Kis23																		
Kis24		0.8		44.0		5.2		1.63									49.8	
BayG-5		1.9						0.88									30.2	
BayG-6		1.0						2.88									40.3	
BayG-7		0.9						1.87									29.3	
BayG-8																		
BayG-9																		
Kis2	1.5	0.7	1690.5	6.5	12.2	2.7	0.17	1.02	0.16	0.93	0.29	1.36	0.26	1.30	0.38	1.61	8.3	2.53
Kis3	1.7	0.5	1188.1	15.3	8.6	1.8	0.13	0.87	0.14	0.81	0.26	1.32	0.23	1.13	0.36	1.61	9.3	2.46
Kis5	0.8	0.2	189.9	6.2	2.8	1.4	0.05	0.37		0.41	0.13	0.61	0.10	0.54	0.20	0.82	4.4	1.06
Kis6	4.9	0.9	68.7	34.6	19.2	4.5	0.39	2.22	0.40	2.54	0.81	3.94	0.66	4.18	1.16	5.30	30.7	8.29
Kis7			140.9	1.9		0.1						0.08	0.01	0.09				0.05
Kis8			207.1	1.3		0.1				0.03				0.06				0.04
Kis9	4.9	0.6	15.9	23.2	17.8	3.5	0.26	1.67	0.25	1.54	0.53	2.49	0.47	3.19	1.05	4.29	27.1	8.22
Kis10	7.7	1.4	20.4	60.4	43.3	6.4	0.36	2.31	0.34	2.05	0.75	3.70	0.66	4.82	1.40	6.01	36.5	10.31
Kis11	10.4	1.2	7.6	47.9	37.9	10.1	0.50	3.30	0.54	3.71	1.31	7.49	1.56	12.31	3.44	18.22	102.3	26.62
Kis12	3.3	1.0	5.5	13.9	26.6	4.4	0.33	1.88	0.26	1.49	0.43	1.80	0.25	1.39	0.21	1.38	9.6	3.08
Kis13	5.2	1.3	0.7	11.0	29.7	8.1	0.47	2.83	0.41	2.60	0.83	3.67	0.63	4.10	1.09	4.75	27.8	8.24
Kis14	4.5	0.7	42.5	33.3	16.8	3.8	0.40	2.56	0.37	2.57	0.86	4.00	0.70	4.11	1.04	4.87	26.9	7.29
Kis15	3.3	0.9	9.0	10.5	27.2	5.4	0.29	1.69	0.25	1.40	0.44	1.83	0.31	1.98	0.42	2.04	13.0	4.33
Kis16	2.5	0.6	154.8	9.0	5.9	0.8	0.37	2.53	0.38	2.40	0.87	3.86	0.63	3.93	1.07	3.80	20.2	5.56
Kis17	0.9	0.1	376.5	6.4	2.7	1.5	0.06	0.34	0.05	0.34	0.11	0.56	0.10	0.64	0.16	0.73	4.2	1.07
Kis19	2.6	0.9	4.6	6.0	24.3	3.2	0.25	1.52	0.21	1.15	0.35	1.46	0.23	1.44	0.26	1.65	12.2	4.11
Lis3		1.5	0.7		0.2		0.08		0.04		0.05		0.06				0.1	61.10
Lis4		0.9	0.4				0.06		0.06		0.12		0.14	0.05	0.13	0.70	0.2	25.20
Lis5		2.0	0.5		0.1		0.05						0.05		0.11	0.30	0.1	11.01

Metal and metal oxides results measured by ICP-MS and ICP-AES at ACME Analytical Laboratory are given in Table 1 and Table 2. For geological considerations, the results for K, Ti, P and Cr metals are given by converting them into their oxides. Some cells in the tables are blank because the relevant metal contents of some samples were either not measured, or their values were below the LOD (Limit of detection).

The precision of the method was evaluated by calculating the relative standard deviation (RSD). The LOD values for metals metal oxides given in percentage units in Table 1 and Table 2, vary between 0.01–0.04%, while those given in ppm vary between 0.002–0.1 ppm. In addition, the relative standard deviations (RSD) for all metals and metal oxides ranged from 0.38–5.52% (Table 1 and Table 2). The accuracy of the method was verified by analyzing standard reference materials.

2.3. Evaluation of the data

The genetic characteristics of the gold mineralization in the Kısacık area were investigated using trace and rare earth elements (REE) in this study. The results of the previous genetic studies, which were conducted by the corresponding author as part of his doctoral dissertation, will be presented in a separate study. This study aims to verify the results of the previous studies and contribute to the understanding of the genesis of the gold mineralization in the area.

The rocks in the area, especially those that are thought to be associated with magmatism, were identified through field observations and mine geology studies. In this context, analyses of major oxides, TEs, REE, and metals were performed on samples from boreholes drilled by the MTA in the area, from sections with high gold anomalies, and from magmatic and other relevant rocks. Spider diagrams proposed by different researchers [33–36] were used to determine the genetic relationship between the mineralization and the host rocks [33–36].

The trace and REE contents of rock and ore samples were normalized to geological environment values, such as chondrite, normal mid-ocean ridge basalt (NMORB), upper crust, and lower crust.

3. Results and discussion

The TE and REE contents of rocks potentially associated with gold mineralization in the Kısacık area were assessed using spider diagrams normalized to various geological environments and materials (chondrites, NMORB, lower continental crust, bulk continental crust, upper continental crust), as proposed by different authors. Fig. 2 illustrates that the gold enrichments observed in the Kısacık field exhibit similar patterns in the spider diagram proposed by Sun and McDonough [33] and normalized to NMORB. Notably, two samples (Kıs7 and Kıs 8) from the ore-bearing silicifications near Baharlar Village, located south of the Kısacık field, displays a distinct pattern compared to the other samples (Fig. 2). Furthermore, the REE contents of the ore samples exhibit significant enrichment, reaching up to 10000 times NMORB for light REEs and up to 1/10 times NMORB for some heavy REEs (Fig. 2). Pb values were also enriched by 10 to 100 times compared to NMORB.

To investigate the relationship between the behavior patterns of the Kısacık gold deposit and other mineralizations in the region (mineralizations associated with listvenitization, gold mineralizations in the Kuşçayır area, gold mineralizations in ultramafic rocks), the TE and REE contents of the Kısacık gold deposit and other mineralizations were analyzed using spider diagrams normalized to NMORB values proposed by Sun and McDonough [33]. The NMORB spider diagram proposed by Sun and McDonough [33] is based on the

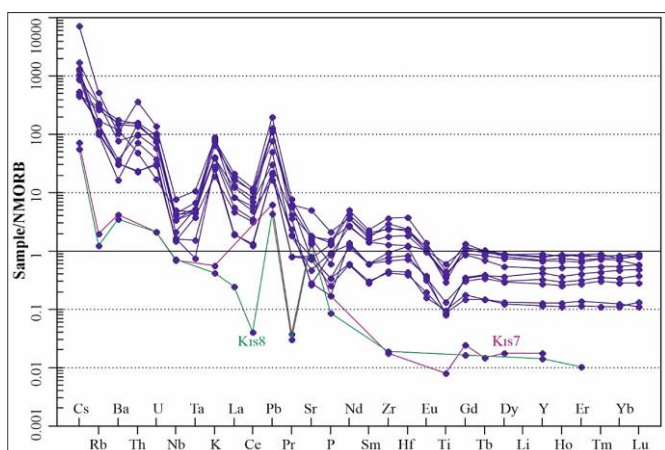


Figure 2. Spider diagram of rare earth element (REE) contents of ore samples from the Kısacık epithermal gold mineralizations, normalized to NMORB

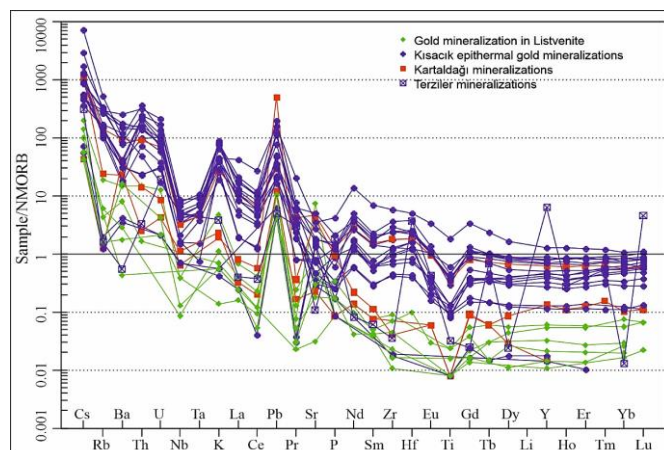


Figure 3. Spider diagram of TE and REE contents of Kısacık gold deposit and other mineralization in the close vicinity, normalized to NMORB.

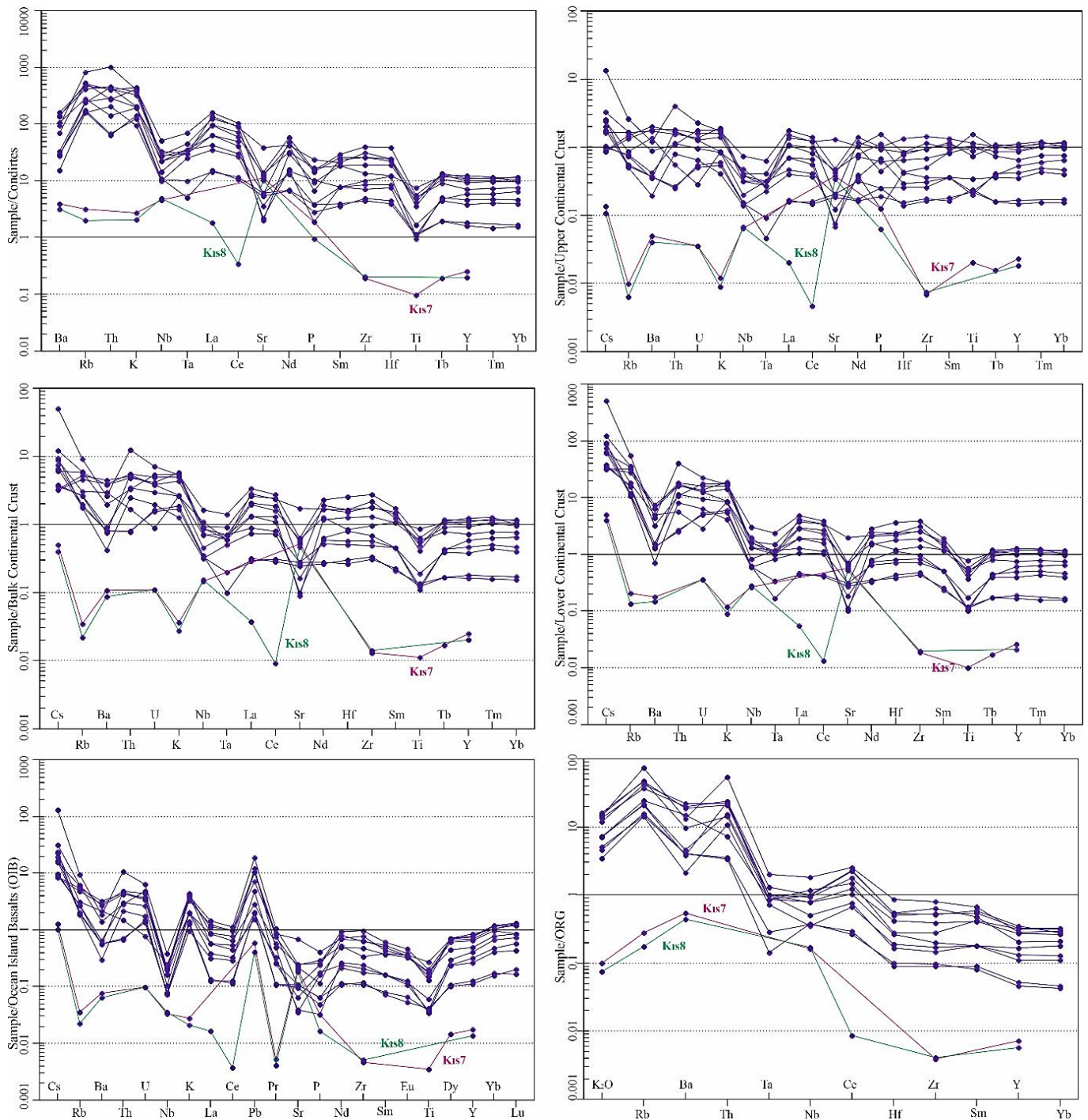


Figure 4. The spider diagrams of gold enrichments in volcanic rocks of the Kısacık area, normalized to chondrites and different geological settings.

compositions of 30 elements, including trace elements, REEs, and metals. This allows for the evaluation of a large number of elements simultaneously. The trace and REE patterns of the Kısacık deposit were found to be generally consistent with the patterns of gold enrichments in the listvenitizations in the northern part of the deposit, and to be relatively similar to the patterns of gold enrichments in quartz veins developed in schists in the Kuşçayır-Kartaldağı area, much further north of the Kısacık deposit. The mineralizations in the Terziler region were found to have a different pattern from the other mineralizations (Fig. 3). The coherence within each ore deposit group is also noteworthy.

The TE and REE contents of the Kısacık village gold enrichment samples are normalized to the chondrites proposed by Thompson [35] (Fig. 4). It is determined that they show a compatible pattern with each other, except for the samples Kıs7 and Kıs8. The Kısacık village gold enrichments are enriched in incompatible elements up to 1000 times compared to the chondrites, and light REEs are enriched by 10 to 100 times. For heavy REEs and some trace elements, enrichments exceeding 10 times have been observed (Fig. 4).

The trace and REE contents of Kısacık gold mineralization samples were also normalized to different geological settings proposed by various

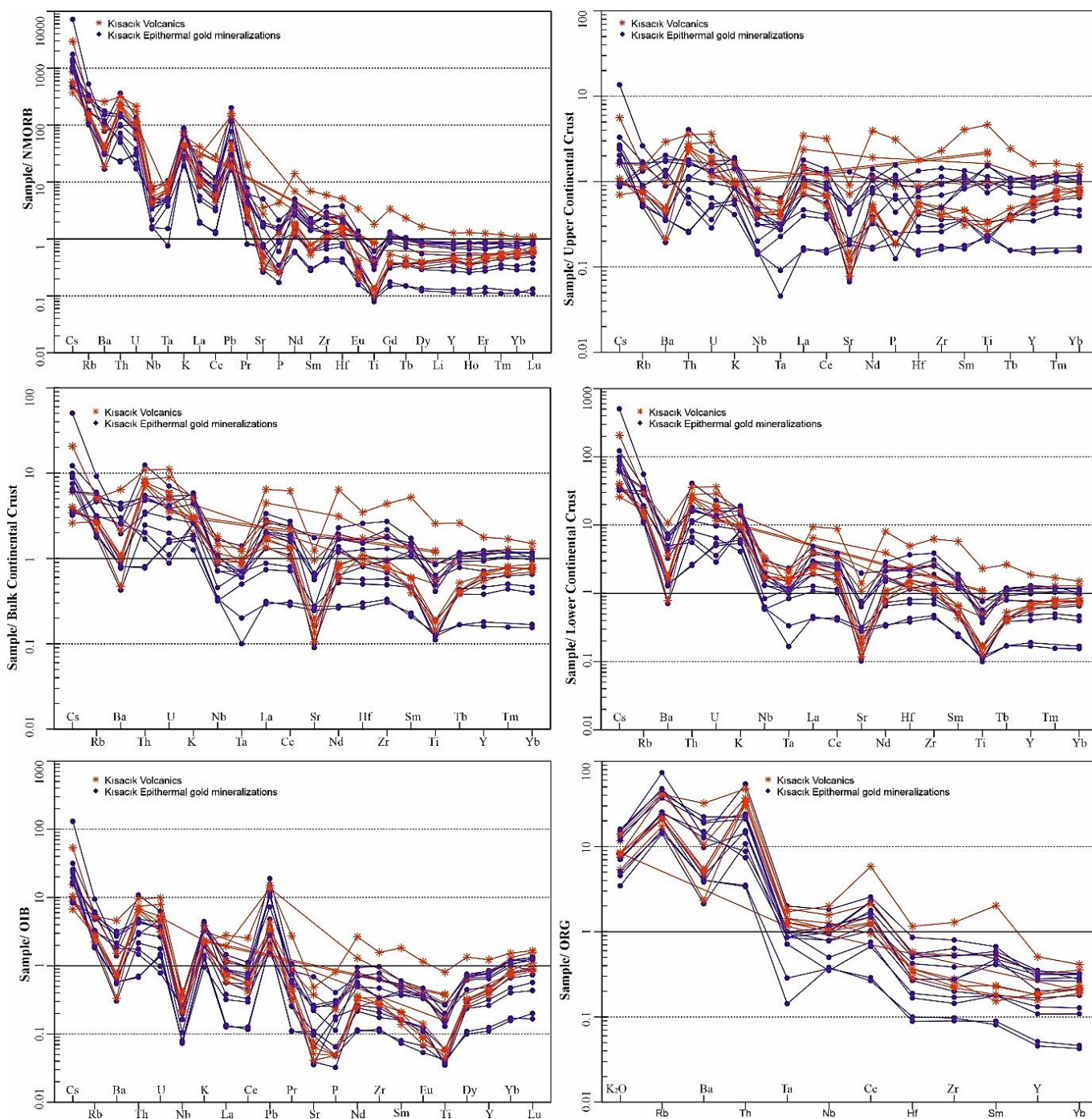


Figure 5. Spider diagrams of Kısacık volcanics and Kısacık epithermal gold mineralizations/enrichments normalized to NMORB, upper continental crust, bulk continental crust, lower continental crust, OIB, ORG.

authors, including chondrite, upper continental crust, Bulk continental crust, lower continental crust, Ocean Island Basalts (OIB) and Ocean Ridge Granites (ORG) (Fig. 4).

It is clear that samples Kıs7 and Kıs 8 have a different pattern than other Kısacık mineralization samples for all geological settings. Sample Kıs7 and Kıs8 are compatible with chondrites, while it shows depletion of up to 1/100 times, and sometimes 1/1000 times compared to upper continental crust and bulk continental crust values (Fig. 4). Kısacık ore samples are relatively compatible with upper continental crust normalized values and have a relatively good agreement with bulk continental

crust values. There are enrichments in incompatible elements according to lower continental crust values, while REE elements are relatively compatible (Fig. 4, Fig 5). Based on the data in Fig. 4, it can be said that the upper crustal effect is relatively high in Kısacık gold mineralization, and the genetic effect belonging to the lower crust is also relatively effective.

Trace and REE contents of gold enrichments in the Kısacık area and some gold enrichments in the vicinity of the study area were compared to the TE-REE contents of associated magmatic rocks in the region, normalized

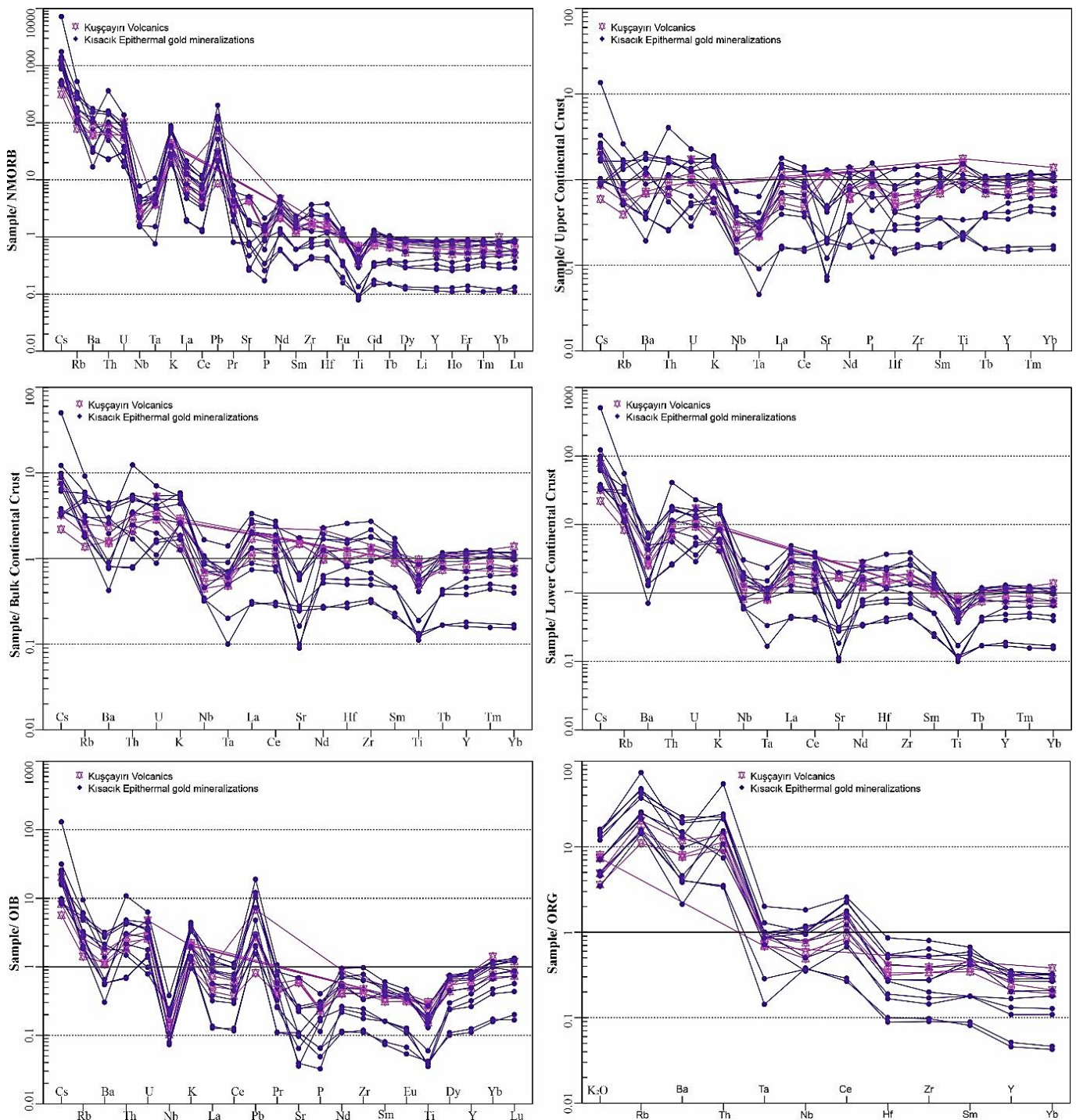


Figure 6. Normalized spider diagrams of the Kuşçayırı volcanics and Kısacık epithermal gold enrichments relative to NMORB, upper continental crust, bulk continental crust, lower continental crust, OIB and ORG tectonic settings.

to different geological settings. This was done to investigate the relationship between the Kısacık gold mineralization and the nearby gold enrichments and magmatism (Fig. 5, Fig. 6, Fig. 7). The contribution of ultramafic rocks to meteoric/hydrothermal leaching that affects mineralization was also investigated using trace-REE element spider diagrams of different geological settings for the relevant rock (Fig. 5, Fig. 6, Fig. 7).

When the spider diagrams of the Kısacık area gold enrichments and the Kısacık Volcanics are compared to each other, it is seen that the gold mineralizations in the Kısacık area have a compatible pattern with the Kısacık volcanics. The gold enrichments in the Kuşçayırı-

Kartaldağı area also have a close similarity to the Upper volcanic rocks (Fig. 5, Fig. 6, Fig. 7). It can be said that an important factor in the compatibility found in the spider diagrams is the leaching of elements from ultramafic rocks by meteoric effects in hydrothermal alteration processes and their contribution to the mineralization process.

When gold mineralization/enrichments are evaluated in the context of geological setting, it is seen that the patterns of both gold enrichment samples and the element patterns of the Kısacık Volcanics are compatible, especially with the lower continental crust. The NTE patterns of the enrichments seen in the volcanic rocks of

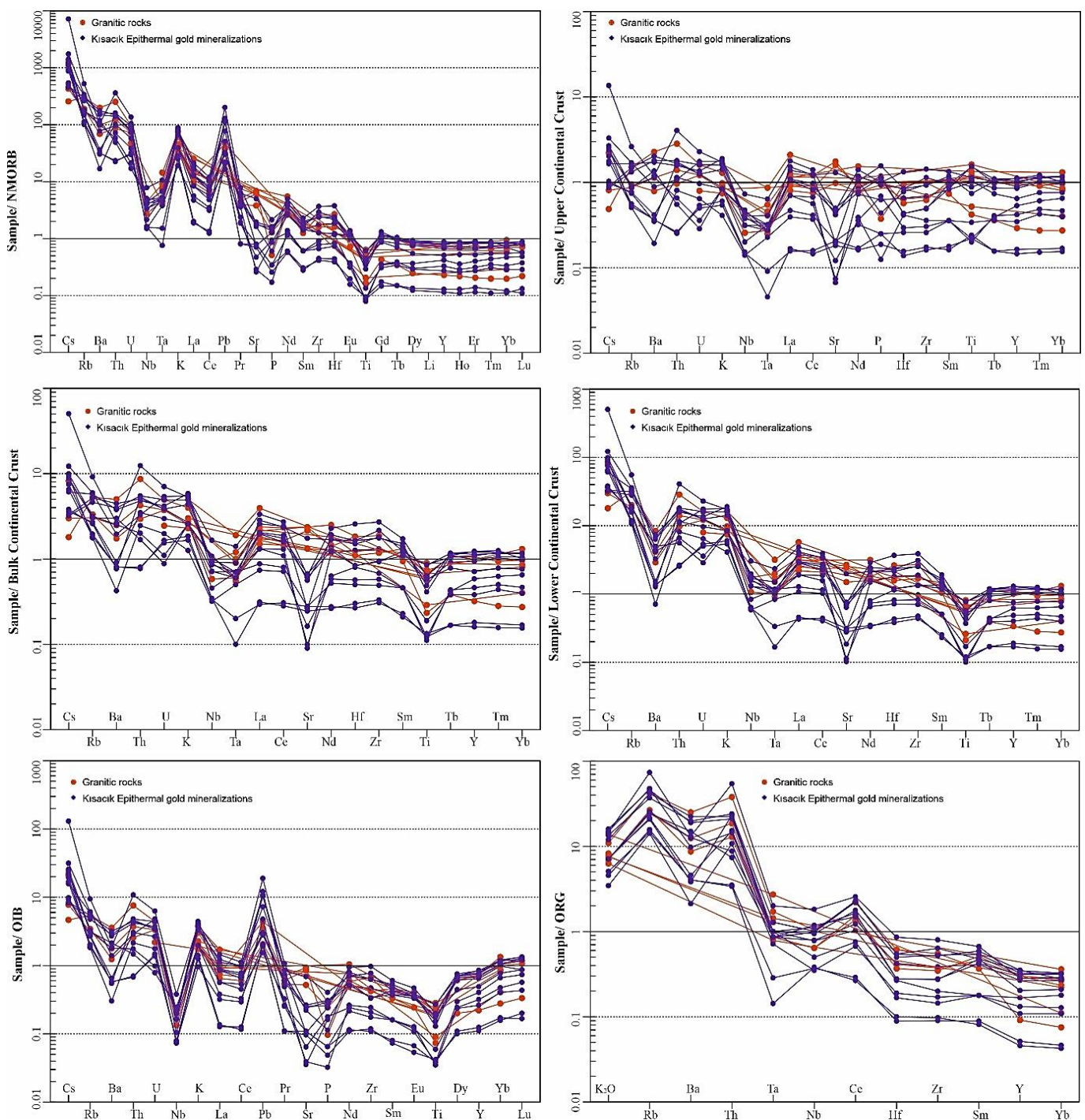


Figure 7. Spider diagrams of granitic rocks and Kısacık gold enrichments normalized to NMORB, upper continental crust, bulk continental crust, lower continental crust, OIB and ORG tectonic settings.

the Kısacık-Kırantepe area are compatible with the Lower volcanic rocks, while the patterns of the gold enrichments in the Kuşçayırı-Kartaldağı area and in the listvenites are not very compatible, with only one example being compatible. This indicates that there is at least a two-phase effect in the enrichments in the Kuşçayırı-Kartaldağı area, one of which is one of the phases that caused the gold mineralization in the volcanic rocks of the Kısacık area.

When the spider diagrams of the gold enrichments in the silicifications near the village of Baharlar and the gold enrichments in the listvenites are examined, it is seen

that they do not show compatibility with the enrichments in the volcanic rocks of the Kısacık area and the patterns of the gold enrichments in the Kuşçayırı-Kartaldağı area. While they have a discordant pattern with the other two gold enrichments, it has been determined that there is a compatibility within themselves (Fig. 5, Fig. 6, Fig. 7).

To investigate the relationship between the Kuşçayırı volcanics and the mineralizations in the Kısacık area, spider diagrams were examined. It is seen that the Kuşçayırı volcanics have a close relationship with the gold enrichments seen in the volcanic rocks of the

Kısacık area (Fig. 6). This relationship can be partially observed, albeit weakly, in other enrichments in the area. Both in the sections where gold enrichments are present and in the Kuşçayırı volcanics, there is an enrichment relative to NMORB. When the spider diagrams of the gold enrichments and the Kuşçayırı volcanics are examined relative to upper continental crust, bulk continental crust, lower continental crust, OIB and ORG, it is seen that the patterns of the Kuşçayırı volcanics are also in a harmony with the gold enrichments developed in the volcanic rocks of the Kısacık area. There is a compatibility with the lower crust, both in the volcanic rocks and in the gold enrichments. It is seen that there is a decrease from heavy to light REEs, an increase in Pb value relative to the NMORB. While the gold enrichments in the Kısacık area and the Kuşçayırı volcanics show values close to the Upper Continental Crust, the gold enrichments in the Kuşçayır-Kartaldağı area and the gold enrichments in the listvenite show a depletion in REEs relative to the Upper Continental Crust (see also Fig. 3).

To investigate the relationship between granitic rocks and the gold mineralizations/enrichments in the area, spider diagrams of both were constructed (Fig. 7). When the spider diagram patterns were examined, it was seen that the patterns of the granitic rocks were also compatible with the patterns of the gold enrichments in the Kısacık epithermal gold mineralization area. When the spider diagram patterns of the gold enrichments in the northern and near southern parts of the study area were considered, no significant differences were observed between the patterns. However, the most striking pattern similarity overlaps with those of the gold mineralizations in the Kısacık area (Fig. 7).

Spider diagrams of the gold enrichments and granitic rocks were constructed relative to NMORB, upper continental crust, bulk continental crust, lower continental crust, OIB and ORG tectonic settings. When the obtained spider diagrams were examined, it was determined that the patterns of the granitic rocks were also in good agreement with the patterns of the gold enrichments developed within the volcanic rocks in the Kısacık area. There is a compatibility with the upper continental crust and also relatively bulk continental crust, both in the volcanic rocks and in the gold enrichments. Compared to the NMORB, it is seen that it is enriched in light REEs, However, the enrichment trend decreases as it moves towards heavy REEs and approaches the NMORB values. It is seen that the REE values of the granitic rocks and the gold enrichments in the Kısacık area are compatible with the upper continental crust values (Fig. 7).

4. CONCLUSIONS

The TE and REE geochemistry of gold mineralizations in the Kısacık area suggests that they are of epithermal origin and have a multi-sourced genetic relationship. The gold enrichments in the Kısacık area are consistent with the TE and REE patterns of the upper continental and bulk continental crust and weakly lower continental crust. This suggests that the gold mineralization is related to hydrothermal fluids that leached elements from these crustal sources. The gold enrichments in the listvenites and silisified rocks (near Baharlar village) in the area are also relatively consistent with the TE and REE patterns of each others. This suggests that these mineralizations may have also been affected same sources in the mineralization process.

The findings of this study support the conclusion that the Kısacık gold deposit is a multi-sourced epithermal deposit that formed as a result of the interaction of hydrothermal fluids genetically related to both the upper continental crust and the relatively lower continental crust. Considering the TE and REE patterns of spider diagrams of other mineralizations in the region, which were also created according to different plate setting environments, it is understood that meteoric fluids were also active in the mineralization process.

Implications for exploration:

- The trace and REE geochemistry of gold mineralizations can be used to identify areas that have potential to host epithermal gold deposits.
- The presence of trace and REE elements in gold mineralizations can be used to trace the movement of hydrothermal fluids and identify potential ore zones.
- The trace and REE geochemistry of gold mineralizations can be used to assess the potential richness of epithermal gold deposits.

Future research:

- Further research is needed to better understand the genetic relationships between the different types of gold enrichments in the Kısacık area.
- Additional studies are needed to investigate the role of hydrothermal alteration in the mineralization process.
- Research is needed to determine the timing and temperature of gold mineralization in the Kısacık area.

Acknowledgements

This study is based on the data collected by the corresponding author during his doctoral dissertation, which was supported by the General Directorate of Mineral Research and Exploration (MTA) under the framework of mine exploration projects. The data used in this study were also obtained from a project supported by the Gümüşhane University Scientific Research Coordination Office (GÜBAP with the Grant number of 20.F5114.01.03). The author would like to thank the supporting organizations for their contributions.

References

- [1] F. Pirajno, *Hydrothermal Processes and Mineral Systems*, 2009.
- [2] A. Vural, *Relationship between the geological environment and element accumulation capacity of Helichrysum arenarium*, *Arab J Geosci*, 11, 2018, 258.
- [3] F. Pirajno, *Hydrothermal Mineral Deposits*, Springer Verlag, 1992.
- [4] L. Robb, *Introduction to Ore-Forming Processes*, Blackwell Publishing, 2005.
- [5] A. Vural, S. Kaya, N. Başaran, O.T. Songören, *Anadolu Madencilğinde İlk Adımlar*, Maden Tetkik ve Arama Genel Müdürlüğü, MTA Kültür Serisi-3, Ankara, Türkiye, 2009.
- [6] A. Vural, D. Aydal, *Determination of Lithological Differences and Hydrothermal Alteration Areas by Remote Sensing Studies: Kısacık (Ayvacık-Çanakkale, Biga Peninsula, Turkey)*, *J Eng Res Appl Sci*, 9, 2020, 1341–1357.
- [7] A.G. N, N. Köprübafii, E. Aldanmaz, *Karabiga (Çanakkale) granitoidinin jeokimyası Geochemistry of the Karabiga (Çanakkale) granitoid*, *Yerbilimleri* 29, 2004, 29–38.
- [8] G. Bozkaya, A. Gökçe, N.V. Grassineau, *Fluid inclusion and stable isotope characteristics of the Arapuçandere Pb-Zn-Cu deposits, Northwest Turkey*, *Int Geol Rev* 50, 2008, 848–862.
- [9] M. Akçay, H.M. Özkan, C.J. Moon, B.C. Scott, *Secondary dispersion from gold deposits in West Turkey*, *J Geochemical Explor*, 56, 1996, 197–218.
- [10] N. Bonev, L. Beccalotto, M. Robyr, P. Monié, *Metamorphic and age constraints on the Alakeçi shear zone: Implications for the extensional exhumation history of the northern Kazdağ Massif, NW Turkey*, *Lithos*, 113, 2009, 331–345.
- [11] H. Yılmaz, F.N. Sönmez, E. Akay, A.K. Şener, S. Tezel Tufan, *Low-sulfidation epithermal Au-Ag mineralization in the Sındırgı district, Balıkesir province, Turkey*, *Turkish J Earth Sci*, 22, 2013, 485–522.
- [12] G. Bozkaya, D.A. Banks, *Physico-chemical controls on ore deposition in the Arapuçandere Pb – Zn – Cu-precious metal deposit, Biga Peninsula, NW Turkey*, *Ore Geol Rev*, 66, 2015, 65–81.
- [13] A. Vural, T. Ünlü, *The geology and mineralogical/petrographic features of Umurbabadağ and its surroundings (Eşme, Uşak - Turkey)*, *J Eng Res Appl Sci*, 9, 2020, 1561–1587.
- [14] A. Vural, *An evaluation of elemental enrichment in rocks: in the case of Kısacık and its neighborhood (Ayvacık, Çanakkale/Türkiye)*, *J Geogr Cartogr*, 6, 2023, 1–20.
- [15] A. Vural, D. Aydal, *Soil geochemistry study of the listvenite area of Ayvacık (Çanakkale, Turkey)*, *Casp J Environ Sci*, 18, 2020, 205–215.
- [16] D. Aydal, A. Vural, İ. Taşdelen Uslu, E.G. Aydal, *Crosta Technique Application on Bayramiç (Alakeçi-Kısacık) Mineralized Area by Using Landsat 7 Etm+ Data*, *J Eng Archit Fac Selcuk Univ*, 22, 2007, 29–40.
- [17] M. Dönmez, A.E. Akçay, S.C. Genç, S. Acar, *Middle-Upper Eocene volcanism and marine ignimbrites in Biga Peninsula*, *Bull Miner Res Explor*, 131, 2005, 49–61.
- [18] Z. Karacık, Y. Yılmaz, *Geology of the ignimbrites and the associated volcano-plutonic complex of the Ezine area, Northwestern Anatolia*, *J Volcanol Geotherm Res*, 85, 1998, 251–264.
- [19] A.İ. Okay, E.J. Leven, *Stratigraphy and Paleontology of the Upper Paleozoic Sequences in the Pular (Bayburt) Region, Eastern Pontides*, *Turkish J Earth Sci*, 5, 1996, 145–155.
- [20] A.İ. Okay, M. Satir, *Covel plutonism and Metamorphism in a latest Oligocene metamorphic core complex in northwest Turkey*, *Geol Mag*, 137, 2000, 495–516.
- [21] A. Vural, *Güneyköy ve Çevresi (Eşme-Uşak) Arsenopirit Cevherleşmelerinin Maden Jeolojisi*, Ankara Üniversitesi, 1998.
- [22] A. Vural, *Bayramiç (Çanakkale) ve Çevresindeki Altın Zenginleşmelerinin Araştırılması*, Ankara Üniversitesi, 2006.
- [23] A.İ. Okay, M. Siyako, K.A. Bürkan, *Biga yarımadasının jeolojisi ve tektonik evrimi*, *Türkiye Pet Jeologları Derneği Bülteni*, 2, 1990, 83–121.
- [24] E. Bingöl, *Geology of Biga Peninsula and some characteristics of Karakaya Formation*, in: *Int. Geodyn. Proj. Rep. Turkey, Maden Tetkik ve Arama Genel Müdürlüğü*, Ankara, Turkey, 1975: pp. 71–77.
- [25] T. Ercan, *Batı Anadolu, Trakya ve Ege adalanndaki Senozoyik volkanizması*, *Jeol Mühendisliği*, 10, 1979, 117–137.
- [26] M. Siyako, K. Bürkan, A.İ. Okay, *Biga ve Gelibolu Yarımadalarının Tersiyer Jeolojisi ve hidrokarbon olanakları*, *Türkiye Pet Jeologları Derneği Bülteni*, 1, 1989, 183–200.
- [27] A.İ. Okay, M. Siyako, K.A. Burkan, *Geology and tectonic of the Biga Peninsula*, *Turk Assoc Pet Geol Bull*, 2, 1990, 83–121.
- [28] A.İ. Okay, M. Satir, *Coeval plutonism and metamorphism in a latest Oligocene metamorphic core complex in northwest Turkey*, *Geol Mag*, 137, 2000, 495–516.
- [29] Ş.C. Genç, *Evolution of the Bayramiç magmatic complex, Northwestern Anatolia*, *J Volcanol Geotherm Res*, 85, 1998, 233–249.
- [30] D. Aydal, A. Vural, İ. Taşdelen Uslu, E.G. Aydal, *Crosta Technique Application on Bayramiç (Alakeçi-Kısacık) Mineralized Area by Using Landsat 7 TM Data*, in: *30th Anniv. Fikret Kurtman Geol Symp, Konya, Türkiye*, 2006: p. 195.
- [31] N. Pehlivan, A. Çetin, T. Andıç, F. Kayhan, B. Demiray, N. Yüce, N. Karabalık, M. Demirdelen, *Edremit (Balıkesir)-Ezine-Bayramiç-Yenice (Çanakkale) Çevresinin Polimetal Altın Ağırıklı Polimetal ve Ağır Mineral Çalışmaları Raporu*, 1997.
- [32] D. Skoog, D. West, F. Holler, S. Crouch, *Fundamentals of analytical chemistry*, 8th ed., Brooks/Cole-Thomson Learning, Belmont, CA 94002, USA, 2004.
- [33] S.S. Sun, W.F. Mcdonough, *Chemical and isotopic systematics of oceanic basalts: implications for mantle composition and processes*, in: A.D. Saunders, M.J. Norry (Eds.), *Magmat. Ocean Basins.*, Geological Society, Special Publications 42, London, 1989: pp. 313–347.
- [34] S.R. Taylor, S.M. McLennan, *The geochemical evolution of the continental crust*, *Rev Geophys*, 33 (1995) 241–265.
- [35] R.N. Thompson, *Magmatism of the British Tertiary volcanic province*, *Scottish J Geol*, 18, 1982, 49–107.
- [36] J.A. Pearce, N.B.W. Harris, A.G. Tindle, *Trace element discrimination diagrams for the tectonic interpretation of granitic rocks*, *J Petrol*, 25 (1984) 956–983.



Synthesis of axially di- and peripherally tetra-(4-((1E)-(4-methoxyphenyl)methylene)amino)phenoxy) group substituted metallophthalocyanines and their electrochemistry

Hüseyin Baş* , Zekeriya Bıyıklıoğlu 

Karadeniz Technical University, Faculty of Science, Department of Chemistry, 61080, Trabzon, Türkiye

Abstract

In this study, the new phthalonitrile derivative, axially di-(4-((1E)-(4-methoxyphenyl)methylene)amino)phenoxy) substituted Si(IV) phthalocyanine and peripherally tetra-(4-((1E)-(4-methoxyphenyl)methylene)amino)phenoxy) substituted Cu(II), Mn(III) phthalocyanines have been synthesized and characterized. Then electrochemical measurements of axially di- and peripherally tetra-(4-((1E)-(4-methoxyphenyl)methylene)amino)phenoxy) group substituted Si(IV), Cu(II), Mn(III) phthalocyanines were investigated with cyclic voltammogram (CV) technique. The redox properties of Si(IV), Cu(II), Mn(III) phthalocyanines show that Mn^{III} center into the Pc cavity increased the redox richness of the phthalocyanines, with the addition of metal-based electron transfer processes to the ring-based ones while Si^{IV} and Cu^{II} show only ring-based electron transfer processes.

Keywords: Synthesis, phthalocyanine, silicon, manganese, cyclic voltammetry

1. Introduction

Phthalocyanines, which obey the Huckel rule ($4n+2$) with their $18-\pi$ electron system, constitute a unique class of macro heterocyclic compounds [1]. They are high-conjugated synthetic macrocyclic compounds containing four isoindole units with 18π electrons [2]. Also have very good thermal and chemical stability [3]. Because of their distinctive chemical structures and full aromatic delocalization, they are widely popular and used in many high-tech industries. [4]. For example, it is used in many fields such as thin film [5], non-linear optics (NLO) [6,7], dye-sensitized solar cells (DSSCs) [8,9], electrochemistry [10–12], photodynamic therapy (PDT) [13–15]. Although these compounds have a wide range of applications, they have low solubility and a high tendency to aggregate [16]. In other words, Pcs are poorly soluble in common organic solvents [17]. The synthesis of soluble Pcs by adding functional groups to the molecule has therefore been the focus of much research. Pcs can be easily substituted from peripheral, non-peripheral and axial positions [18]. The kind of the central metal atom and the location of the substituents on the phthalocyanine ring are used to categorize

phthalocyanines [19]. Tetra-substituted Pcs can be produced by various substitutions of peripheral or non-peripheral regions of the ring structure, while axially substituted ones can be obtained by bonding to the phthalocyanine ring at axial positions on the central metal atom. [20–22].

Phthalocyanines are known to have redox properties [23]. To improve these compounds' suitability for use in various electrochemical applications, it is important to improve the redox activity of metallophthalocyanines (MPcs) [24,25]. Complexation with redox-active metal cations has been observed to boost the redox activity of Pc [26]. The addition of redox-active groups to the Pc ring is another method of improving the redox properties of these molecules. [27,28]. In this way, the absorption of phthalocyanines shifts from the visible region to the near IR or UV region, causing optical transitions. [29,30]. As a result, phthalocyanines electrical and optical characteristics may be controlled and are used in a variety of application, including sensors, dye-sensitized solar cells (DSSCs), nanobiotechnology and nonlinear optics (NLO) [7].

Citation: H. Baş, Z. Bıyıklıoğlu, Synthesis of axially di- and peripherally tetra-(4-((1E)-(4-methoxyphenyl)methylene)amino)phenoxy) group substituted metallophthalocyanines and their electrochemistry, Turk J Anal Chem, 5(2), 2023, 137–142.

 <https://doi.org/10.51435/turkjac.1381022>

Author of correspondence: hsyn_bs@hotmail.com

Received: October 25, 2023

Tel: +90 (462) 377 25 25

Accepted: December 18, 2023

Fax: +90 (462) 325 31 96

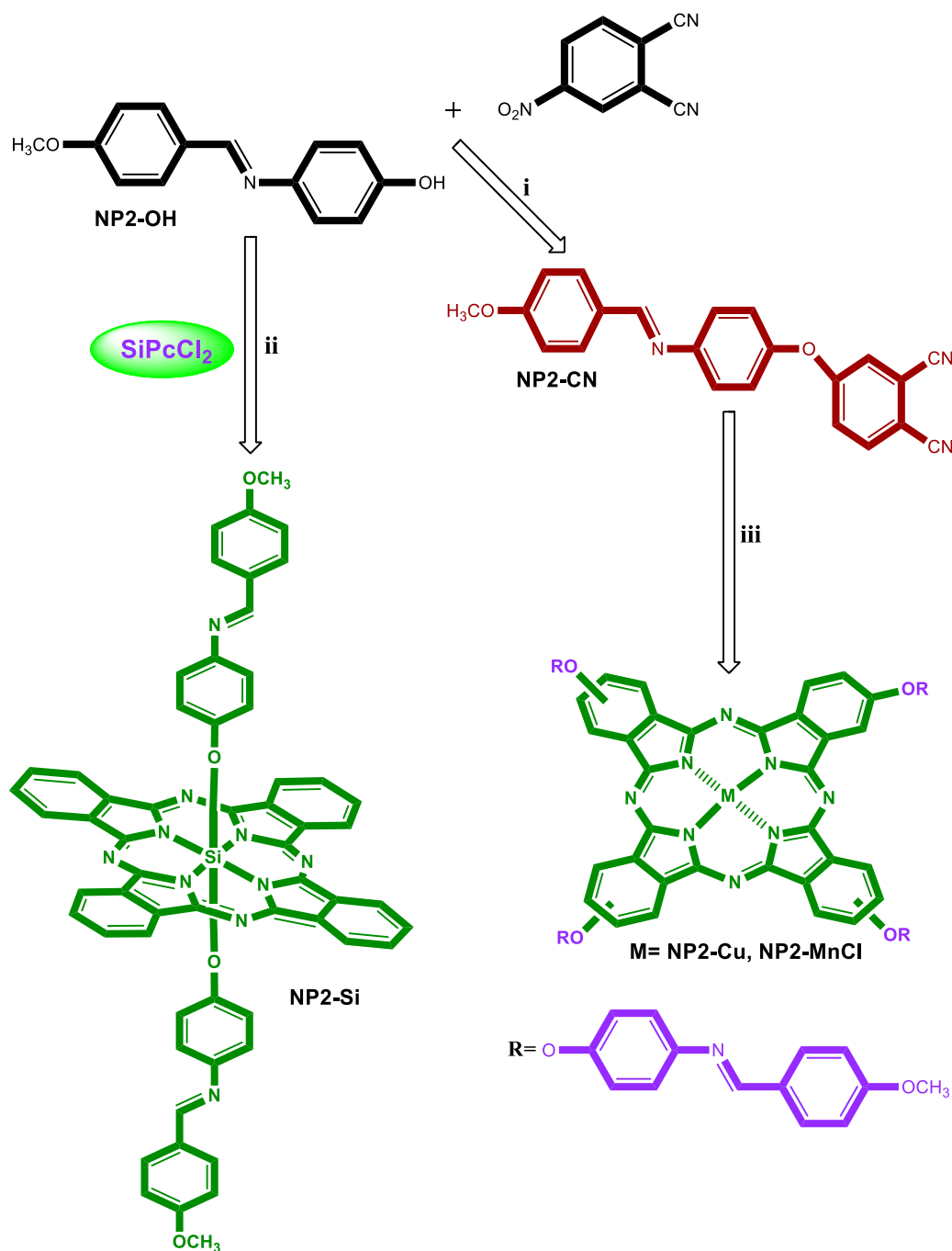


Figure 1. The synthesis of axially di- and peripherally tetra-(4-[(1*E*)-(4-ethoxyphenyl)methylene]amino)phenoxy) group substituted metallophthalocyanines (i) K₂CO₃, 60 °C, DMF. (ii) Toluene, NaH, 110 °C. (iii) n-pentanol, CuCl₂, MnCl₂, DBU, 160 °C

With this in mind, we have synthesised a new series of phthalocyanine derivatives to investigate their electrochemical properties. The electrochemical properties of the synthesised NP2-SiPc, NP2-MnPc and NP2-CuPc compounds were determined by cyclic voltammetry (CV) technique.

2. 2. Experimental

2.1. Synthesis

2.1.1. 4-(4-[(1*E*)-(4-methoxyphenyl)methylene]amino)phenoxy)phthalonitrile (NP2-CN)

NP2-OH (1.2 g, 5.3 mmol), 4-nitrophthalonitrile (915 mg, 5.3 mmol) and dry K₂CO₃ (2.2 g, 15.9 mmol) were dissolved in anhydrous DMF (20 mL) at 60 °C and under nitrogen atmosphere for stirred 4 days. Then, reaction mixture was poured into water. NP2-CN was crystallized from ethanol. Yield: 1.56 g (84%). FT-IR (ATR) ν (cm⁻¹): 3077 (Ar-H), 2970-2854 (Aliph. C-H), 2232 (C≡N), 1627, 1601, 1575, 1509, 1481, 1459, 1305, 1279, 1244, 1208, 1176, 1088, 1018, 952, 845, 828, 758. ¹H-NMR (400 MHz, DMSO-d₆), (δ): 8.58 (s, 1H, =CH), 8.12 (d, 1H, Ar-H), 7.91 (d, 2H, Ar-H), 7.80 (s, 1H, Ar-H), 7.42-7.36 (m, 3H, Ar-H), 7.24-7.09 (d, 2H, Ar-H), 7.09 (d, 2H, Ar-H), 3.84 (s, 3H, -OCH₃). ¹³C-NMR (100 MHz, DMSO-d₆),

(δ): 162.48, 161.81, 160.72, 151.87, 149.79, 136.77, 131.00, 129.30, 123.47, 122.93, 122.24, 121.68, 117.15, 116.39, 115.88, 114.76, 108.49, 55.90. MS (ESI), (m/z): 353.44 [M]⁺.

2.1.2. Synthesis of axially di-(4-[(1E)-(4-methoxyphenyl)methylene]amino)phenoxy substituted silicon(IV) phthalocyanine (NP2-Si)

SiPcCl₂ (100 mg, 0.16 mmol), NP2-OH (75 mg, 0.32 mmol) and NaH (7 mg, 0.32 mmol) in toluene (15 mL) was under nitrogen atmosphere stirred for 1 day at 110 °C. After evaporating the solvent, the product was subjected to column chromatography which is placed aluminium oxide using CHCl₃:CH₃OH (100:1) as solvent system. Yield: 91 mg (56%). IR (ATR) $\nu_{\max}/\text{cm}^{-1}$: 3052 (Ar-H), 2961-2850 (Aliph. C-H), 1603, 1575, 1508, 1493, 1429, 1335, 1292, 1254, 1160, 1122, 1095, 1078, 1018, 911, 882, 828, 759, 732. ¹H-NMR. (400 MHz, CDCl₃), (δ :ppm): 9.65-9.62 (m, 8H, Pc-H _{α}), 8.37-8.35 (m, 8H, Pc-H _{β}), 7.85 (d, 4H, Ar-H), 7.49 (s, 2H, Ar-H), 7.01 (d, 4H, Ar-H), 6.75 (d, 4H, Ar-H), 5.53 (d, 4H, Ar-H), 3.75 (s, 3H, -OCH₃). ¹³C-NMR (100 MHz, CDCl₃), (δ :ppm): 164.58, 156.82, 149.60, 135.56, 132.00, 131.12, 130.90, 129.78, 123.85, 119.75, 117.79, 114.29, 113.87, 55.58. UV-Vis (THF): λ_{\max} , nm (log ϵ): 676 (5.03), 609 (4.35), 352 (4.74). MALDI-TOF-MS m/z : 993.45 [M]⁺.

2.1.3. Synthesis of peripherally tetra-(4-[(1E)-(4-methoxyphenyl)methylene]amino)phenoxy substituted copper(II) phthalocyanine (NP2-Cu)

NP2-CN (100 mg, 0.28 mmol), dry CuCl₂ (19 mg, 0.14 mmol), dry n-pentanol (2 mL) and 1,8-diazabicyclo [5.4.0]undec-7-ene (DBU) (3 drops) was under nitrogen atmosphere stirred at 160 °C for 1 day. Then, NP2-Cu was precipitated with ethanol. NP2-Cu was purified by column chromatography (aluminum oxide) using CHCl₃:CH₃OH (100:2) solvent system. Yield: 33 mg (32%). FT-IR (ATR) $\nu_{\max}/\text{cm}^{-1}$: 3070 (Ar-H), 2919-2849 (Aliph. C-H), 1602, 1574, 1508, 1495, 1464, 1400, 1342, 1311, 1226, 1190, 1161, 1090, 1027, 949, 827, 746. UV-Vis (THF): λ_{\max} , nm (log ϵ) 678 (4.98), 610 (4.46), 337 (5.03). MALDI-TOF-MS m/z : 1476.35 [M]⁺.

2.1.4. Synthesis of peripherally tetra-(4-[(1E)-(4-methoxyphenyl)methylene]amino)phenoxy substituted manganese(III) phthalocyanine chloride (NP2-Mn)

NP2-Mn was prepared using same procedure for the NP2-Cu by using dry MnCl₂ instead of CuCl₂. Yield: 52 mg (50%). FT-IR (ATR) $\nu_{\max}/\text{cm}^{-1}$: 3034 (Ar-H), 2957-2836 (Aliph. C-H), 1602, 1574, 1508, 1495, 1464, 1399, 1335, 1311, 1225, 1160, 1073, 1026, 951, 886, 826, 743. UV-Vis (THF): λ_{\max} , nm (log ϵ) 723 (4.99), 638 (4.66), 498 (4.32), 342 (5.17). MALDI-TOF-MS m/z : 1468.48 [M -Cl]⁺.

3. Results and discussion

3.1. Synthesis and characterization

The general synthesis of peripherally tetra- and axially di-(4-[(1E)-(4-methoxyphenyl)methylene]amino)phenoxy group substituted metallophthalocyanines is given in Fig. 1. The preparation of NP2-CN was succeeded by the reaction of 4-[(1E)-(4-methoxyphenyl)methylene]amino]phenol [31] with 4-nitrophthalonitrile in anhydrous DMF with dry potassium carbonate. Silicon phthalocyanine dichloride was treated with NP2-OH in toluene and NaH led to axially di-(4-[(1E)-(4-methoxyphenyl)methylene]amino)phenoxy group substituted silicon phthalocyanine. Through a cyclotetramerization reaction in n-pentanol between NP2-CN and a metal salt, Cu(II) and Mn(III)Pcs with substituted 4-[(1E)-(4-methoxyphenyl)methylene]aminophenoxy groups were created peripherally. The typical nitrile stretching vibration was visible at 2232 cm⁻¹ when the FT-IR spectra of NP2-CN was investigated. The -OH stretching vibration of NP2-OH was vanished. Aromatic protons of NP2-CN were seen in the ¹H-NMR spectrum between 8.12 and 7.09 ppm. Also, =CH and -OCH₃ protons were observed at 8.58 and 3.84 ppm, respectively. In the ¹H-NMR spectrum of NP2-CN, the nitrile carbon atoms of the NP2-CN, were observed at 115.88 and 114.76 ppm. In addition, the carbon atom of methoxy group was seen at 55.90 ppm. The molecular ion peak in the mass spectra of NP2-CN was seen at m/z : 353.44 [M]⁺. The removal of the OH band in the IR spectrum provided unmistakable proof that NP2-Si had formed. In the ¹H NMR spectrum of NP2-Si, H _{α} and H _{β} protons of phthalocyanine ring was shown at 9.65-9.62, 8.37-8.35 ppm, respectively. The other aromatic protons were observed at 7.85, 7.49, 7.01, 6.75, 5.53 ppm. Also, protons of methoxy groups appeared at 3.75 ppm as singlet. In the ¹³C-NMR spectrum of NP2-Si indicated 13 number aromatic and 1 number aliphatic carbon signals. In MALDI-TOF MS spectrum of NP2-Si, the molecular ion peak was shown at 993.45 [M]⁺. The disappearance of the -C \equiv N vibration (2232 cm⁻¹) in the IR spectrum of NP2-Cu and NP2-Mn indicated the conversion of NP2-CN to the phthalocyanine ring. Owing to the paramagnetic nature of Cu(II) and Mn(III) ion, ¹H-NMR and ¹³C-NMR measurements of NP2-Cu and NP2-Mn could not be measured [32]. In MALDI-TOF MS spectra of NP2-Cu and NP2-Mn the molecular ion peaks were found at m/z 1476.35 [M]⁺, 1468.48 [M -Cl]⁺, respectively. The UV-Visible spectra of NP2-Si, NP2-Cu, NP2-Mn were recorded in THF at 1x10⁻⁵ M concentration (Fig. 2). All phthalocyanines (NP2-Si, NP2-Cu, NP2-Mn) showed the Q and B bands in the expected ranges. As seen in Fig. 2, the sharp Q bands of NP2-Si, NP2-Cu, NP2-Mn were seen at 676, 678, 723 nm, respectively. In addition, the peak at 498 nm for NP2-Mn was associated with charge transfer absorption [33]. On the other hand, the B bands of NP2-Si, NP2-Cu, NP2-Mn were observed at 352, 337, 342 nm, respectively.

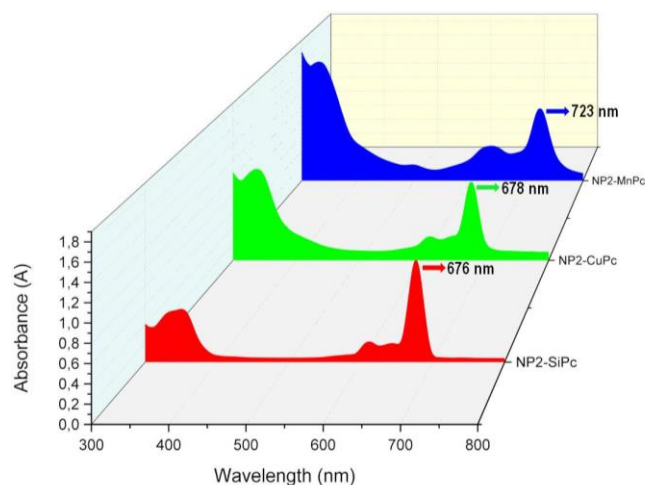


Figure 2. UV-Vis spectrum of NP2-Si, NP2-Cu, NP2-Mn in THF. (Concentration = 10×10^{-6} mol dm^{-3})

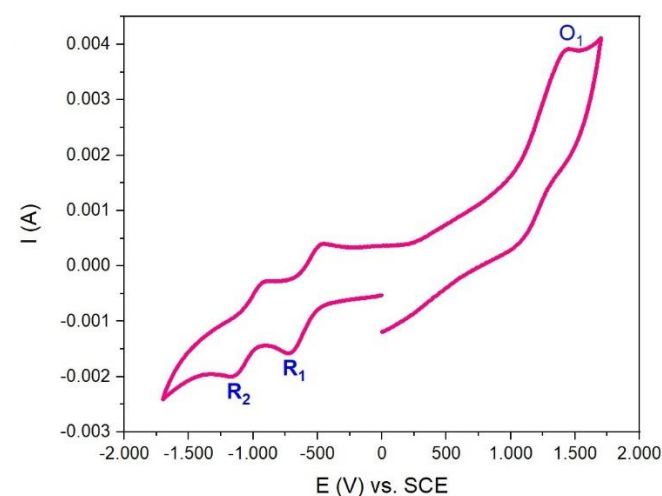


Figure 3. CV of NP2-Si

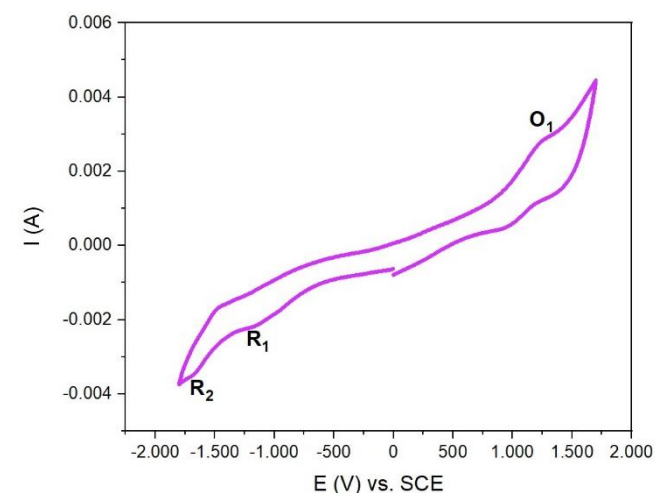


Figure 4. CV of NP2-Cu

3.2. Electrochemical Measurements

Electrochemical behaviors of axially di- and peripherally tetra-(4-[(1E)-(4-ethoxyphenyl) methylene] amino) phenoxy) group substituted metallophthalocyanines were recorded using cyclic voltammetry (CV) in DCM/TBAP electrolyte at room temperature. The peak potential separation (ΔE_p), half-wave potential ($E_{1/2}$), the potential difference between the first half-peak processes ($\Delta E_{1/2}$), are shown in Table 1.

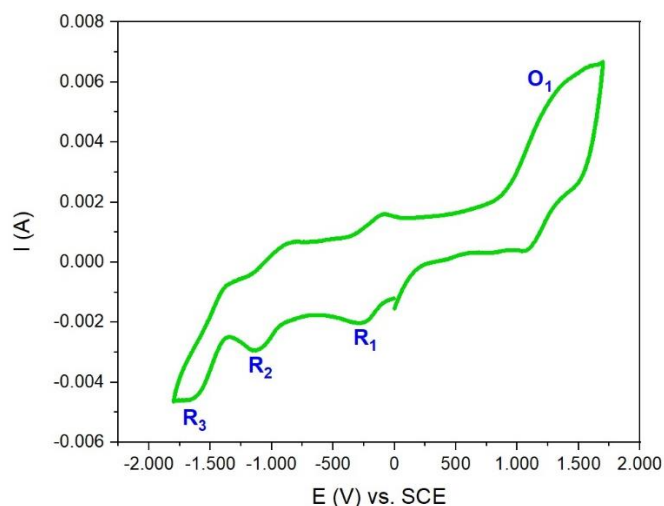


Figure 5. CV of NP2-Mn

Table 1. Electrochemical data of NP2-Si, NP2-Cu, NP2-Mn. All potentials were given versus SCE

Pcs	Redox Processes	Label	$^a E_{1/2}$ (V)	$^b \Delta E_p$ (mV)	$^c \Delta E_{1/2}$
NP2-Si	$[\text{L}_2\text{Si}^{\text{IV}}\text{Pc}^{2-}]/[\text{L}_2\text{Si}^{\text{IV}}\text{Pc}^{3-}]^{1-}$	R ₁	-0.60	135	
	$[\text{L}_2\text{Si}^{\text{IV}}\text{Pc}^{3-}]^{1-}/[\text{L}_2\text{Si}^{\text{IV}}\text{Pc}^{4-}]^{2-}$	R ₂	-1.04	141	1.86
	$[\text{L}_2\text{Si}^{\text{IV}}\text{Pc}^{2-}]/[\text{L}_2\text{Si}^{\text{IV}}\text{Pc}^{1-}]^{1+}$	O ₁	1.26	152	
NP2-Cu	$[\text{Cu}^{\text{II}}\text{Pc}^{2-}]/[\text{Cu}^{\text{II}}\text{Pc}^{3-}]^{1-}$	R ₁	-0.97	202	
	$[\text{Cu}^{\text{II}}\text{Pc}^{3-}]^{1-}/[\text{Cu}^{\text{II}}\text{Pc}^{4-}]^{2-}$	R ₂	-1.56	154	2.09
	$[\text{Cu}^{\text{II}}\text{Pc}^{2-}]/[\text{Cu}^{\text{II}}\text{Pc}^{1-}]^{1+}$	O ₁	1.12	156	
NP2-Mn	$[\text{Cl}^{1-}\text{Mn}^{\text{III}}\text{Pc}^{2-}]/[\text{Cl}^{1-}\text{Mn}^{\text{III}}\text{Pc}^{2-}]^{1-}$	R ₁	-0.17	96	
	$[\text{Cl}^{1-}\text{Mn}^{\text{III}}\text{Pc}^{2-}]^{1-}/[\text{Cl}^{1-}\text{Mn}^{\text{III}}\text{Pc}^{2-}]^{2-}$	R ₂	-1.01	129	1.29
	$[\text{Cl}^{1-}\text{Mn}^{\text{III}}\text{Pc}^{2-}]^{2-}/[\text{Cl}^{1-}\text{Mn}^{\text{III}}\text{Pc}^{3-}]^{3-}$	R ₃	-1.51	138	
	$[\text{Cl}^{1-}\text{Mn}^{\text{III}}\text{Pc}^{2-}]/[\text{Cl}^{1-}\text{Mn}^{\text{III}}\text{Pc}^{1-}]^{1+}$	O ₁	1.19	141	

^a: $E_{1/2}$ values ($(E_{pa}+E_{pc})/2$) were given versus SCE at 0.100 Vs^{-1} scan rate.

^b: $\Delta E_p = E_{pa} - E_{pc}$. ^c: $\Delta E_{1/2} = E_{1/2}$ (first oxidation) - $E_{1/2}$ (first reduction)

Fig. 3 shows cyclic voltammogram of axially di-((1E)-(4-methoxyphenyl)methylene]amino)phenoxy) substituted silicon(IV) phthalocyanine (NP2-Si) in DCM/TBAP electrolyte on a Pt working electrode. As shown in Fig. 3, NP2-Si illustrated two reduction ($R_1 = -0.60$ V, $R_2 = -1.04$ V) and one oxidation ($O_1 = 1.26$ V) reaction within the potential windows of the electrolyte. Here, axially di-((1E)-(4-methoxyphenyl) methylene] amino)phenoxy) substituted silicon(IV) phthalocyanine (NP2-Si) have redox inactive Si^{4+} metal centers. For this reason, NP2-Si illustrates only phthalocyanine ring based redox responses and the axial (4-[(1E)-(4-methoxyphenyl)methylene]amino)ligand on Si center do not considerably influence the redox response of the phthalocyanine ring [34]. According to the peak analyses and shape of the voltammogram, reduction and oxidation processes have quasi-reversible character.

Fig. 4 shows cyclic voltammogram of peripherally tetra-(4-[(1E)-(4-methoxyphenyl)methylene]amino) phenoxy) substituted copper(II) phthalocyanine (NP2-Cu) in DCM/TBAP electrolyte on a Pt working electrode. As shown in Fig. 4, two reduction and one oxidation processes are observed at -0.97 V (R_1), -1.04 V (R_2), and

1.26 V (O_1) with the cyclic voltammogram of **NP2-Cu**. These redox processes are easily attributed to the electron transfer reaction of phthalocyanine ring owing to the redox inactivity of the Cu^{2+} cation. According to the peak-to-peak separation (ΔE_p), R_1 has irreversible, R_2 and O_1 have quasi-reversible character.

Fig. 5 shows cyclic voltammogram of peripherally tetra-(4-[(1E)-(4-methoxyphenyl)methylene]amino)phenoxy substituted manganese(III) phthalocyanine chloride (**NP2-Mn**). Peripherally tetra-(4-[(1E)-(4-methoxyphenyl)methylene]amino)phenoxy substituted manganese(III) phthalocyanine chloride (**NP2-Mn**) shows different redox behaviors than **NP2-Si** and **NP2-Cu**, because **NP2-Mn** has redox active metal center (Mn^{3+}). For this reason, **NP2-Mn** shows metal-based reduction processes in addition to the phthalocyanine ring-based electron transfer reactions [35–37]. Here **NP2-Mn** shows two metal-based reductions at -0.17 V (R_1), -1.01 V (R_2) and one phthalocyanine ring-based reduction at -1.51 V (R_3) during the cathodic potential scans. On the other hand, during the anodic potential scans, one phthalocyanine ring-based oxidation at 1.19 V (O_1) is observed. According to the peak-to-peak separation (ΔE_p), R_1 has reversible, R_2 , R_3 and O_1 have quasi-reversible character.

4. Conclusion

In this work, Si(IV), Cu(II), Mn(III) phthalocyanines substituted with (4-[(1E)-(4 methoxyphenyl)methylene]aminophenoxy) groups were synthesized and analyzed by FT-IR, NMR, UV-Vis, mass spectroscopy. The redox behaviors of axially di- and peripherally tetra-(4-[(1E)-(4-methoxyphenyl)methylene]amino)phenoxy group substituted metallophthalocyanines were determined. Electrochemical results of **NP2-Si**, **NP2-Cu**, **NP2-Mn** were in compatible with the responses of the similar metallophthalocyanines. While **NP2-Si** and **NP2-Cu**, only showed phthalocyanine ring based redox processes, **NP2-Mn** showed rich redox responses and both metal-based and phthalocyanine ring based redox processes. **NP2-Mn** showed two metal-based and one phthalocyanine ring-based reduction reactions. The addition of Mn^{3+} cation to the phthalocyanine ring significantly changed the redox richness of phthalocyanines.

Acknowledgement

This study was not supported by any organization.






References

- [1] N. Kayir, S. Gorduk, Synthesis, characterization, and investigation photophysical properties of axially 2-hydroxymethyl-1,4-benzodioxan di-substituted Silicon(IV) phthalocyanine, *J Organomet Chem*, 990, 2023, 122661.
- [2] R. Balamurugan, J.H. Liu, B.T. Liu, A review of recent developments in fluorescent sensors for the selective detection of palladium ions, *Coord Chem Rev*, 376, 2018, 196–224.
- [3] T. Arslan, N. Çakır, T. Keleş, Z. Biyiklioglu, M. Senturk, Triazole substituted metal-free, metallo-phthalocyanines and their water soluble derivatives as potential cholinesterases inhibitors: Design, synthesis and in vitro inhibition study, *Bioorg Chem*, 90, 2019, 103100.
- [4] S. Temizel, T.Ç. Çanak, A.M. Sevim, Novel polymers with cobalt(II)phthalocyanine moieties as effective heterogeneous photocatalysts for visible-light-driven photodegradation of organic dyes in aqueous solutions, *J Photochem Photobiol A Chem*, 401, 2020, 112741.
- [5] R. Ishiura, A. Fujii, M. Arita, K. Sudoh, M. Ozaki, Study on energy level bending at heterojunction of solution-processed phthalocyanine thin film and n-Si by Kelvin probe force microscopy, *Org Electron*, 78, 2020, 105599.
- [6] R. Zugle, T. Nyokong, Physico-chemical properties of lutetium phthalocyanine complexes in solution and in solid polystyrene polymer fibers and their application in photoconversion of 4-nitrophenol, *J Mol Catal A Chem*, 358, 2012, 49–57.
- [7] M. Yahya, Y. Nural, Z. Seferoğlu, Recent advances in the nonlinear optical (NLO) properties of phthalocyanines: A review, *Dye Pigment*, 198, 2022, 109960.
- [8] E. Güzel, H. Baş, Z. Biyiklioglu, İ. Şişman, Dye-sensitized solar cells using silicon phthalocyanine photosensitizers with pyridine anchor: Preparation, evaluation of photophysical, electrochemical, and photovoltaic properties, *Appl Organomet Chem*, 35, 2021,.
- [9] B. Yıldız, B.S. Arslan, E. Güzel, M. Nebioğlu, N. Menges, İ. Şişman, M. Kasım Şener, Non-aggregating zinc phthalocyanine sensitizer with bulky diphenylphenoxy donor groups and pyrazole-3-carboxylic acid anchoring group for coadsorbent-free dye-sensitized solar cells, *Sol Energy*, 226, 2021, 173–179.
- [10] Z. Biyiklioglu, H. Bas, H. Alp, Non-aggregated axially disubstituted silicon phthalocyanines bearing electropolymerizable ligands and their aggregation, electropolymerization and thermal properties, *Dalt Trans*, 44, 2015, 14054–14062.
- [11] Z. Biyiklioglu, H. Alp, Electropolymerizable peripherally tetra-{2-[3-(diethylamino)phenoxy]ethoxy} substituted as well as axially (4-phenylpiperazin-1-yl)propanoxy-disubstituted silicon phthalocyanines and their electrochemistry, *Dalt Trans*, 44, 2015, 18993–18999.
- [12] Z. Biyiklioglu, I. Ömeroğlu, H. Alp, Synthesis, characterization and electrochemical properties of amphiphilic axially-disubstituted silicon(IV) phthalocyanines, *J Coord Chem*, 69, 2016, 354–362.
- [13] Y. Baygu, Y. Gök, Synthesis and characterization of new partially-aggregated water-soluble polyether-triazole linked zinc(II) phthalocyanines as photosensitizers for PDT studies, *Synth Met*, 260, 2020, 116256.
- [14] H. Kantekin, H. Yalazan, B. Barut, Ö. Güngör, D. Ünlüer, Ü. Demirbaş, A. Özel, M. Durmuş, Dual-purpose both peripheral and non-peripheral triazole substituted ZnII, MgII and PbII phthalocyanines: Synthesis, characterization, photophysical and acetylcholinesterase inhibitory properties, *Polyhedron*, 208, 2021, 115416.
- [15] A. Günsel, A.T. Bilgiçli, B. Barut, P. Taslimi, A. Özel, İ. Gülçin, Z. Biyiklioglu, M.N. Yarasir, Synthesis of water soluble tetra-substituted phthalocyanines: Investigation of DNA cleavage, cytotoxic effects and metabolic enzymes inhibition, *J Mol Struct*, 1214, 2020, 128210.

- [16] Z. Biyıklıoğlu, V. Çakır, D. Çakır, H. Kantekin, Crown ether-substituted water soluble phthalocyanines and their aggregation, electrochemical studies, *J Organomet Chem*, 749, 2014, 18–25.
- [17] R. Atajanov, B. Huraibat, Z. Odabaş, A.R. Özkaya, Electrochemical, spectroelectrochemical, and electrocatalytic properties of novel soluble phthalocyanines containing peripheral thymoxy and chloride units, *Inorganica Chim Acta*, 547, 2023, 121360.
- [18] H. Baş, Z. Biyıklıoğlu, B. Barut, C.Ö. Yalçın, A. Özel, Highly water soluble axial disubstituted silicon(IV) phthalocyanine, naphthalocyanine: Synthesis, DNA interaction and anticancer effects against human lung (A549), liver (SNU-398), melanoma (SK-MEL128), prostate (DU-145), breast (BT-20) cell lines, *Inorg Chem Commun*, 156, 2023, 111139.
- [19] A. Günsel, P. Taslimi, G.Y. Atmaca, A.T. Bilgiçli, H. Pişkin, Y. Ceylan, A. Erdoğan, M.N. Yarasir, İ. Gülçin, Novel potential metabolic enzymes inhibitor, photosensitizer and antibacterial agents based on water-soluble phthalocyanine bearing imidazole derivative, *J Mol Struct*, 1237, 2021, 130402.
- [20] S.M. Sudhakara, M.C. Devendrachari, F. Khan, S. Thippeshappa, H.M.N. Kotresh, Highly sensitive and selective detection of nitrite by polyaniline linked tetra amino cobalt (II) phthalocyanine surface functionalized ZnO hybrid electrocatalyst, *Surfaces and Interfaces*, 36, 2023, 102565.
- [21] R.A. Shoukat Ali, J. Keshavayya, A.S. Jagadisha, S.D. Umesha, K.N. Gujjar, S.A. Narasimha, D.G. Prasanna, E. Nagaraja, DC electrical conductivity studies of tetra 2-(furan-2-yl)-1,3,4-oxadiazole substituted metal (II) phthalocyanines, *Mater Today Proc*, 49, 2022, 644–649.
- [22] M.-R. Ke, J.-D. Huang, S.-M. Weng, Comparison between non-peripherally and peripherally tetra-substituted zinc (II) phthalocyanines as photosensitizers: Synthesis, spectroscopic, photochemical and photobiological properties, *J Photochem Photobiol A Chem*, 201, 2009, 23–31.
- [23] D. AlMarzouq, S. A. Majeed, Ö. Budak, A. Koca, Manganese phthalocyanine and its graphene quantum dot conjugate: Synthesis, characterization electrochemistry, spectroelectrochemistry, electropolymerization, and electrochromism, *Inorganica Chim Acta*, 527, 2021, 120558.
- [24] Y. Ünver, H. Baş, Z. Biyıklıoğlu, Non-peripherally 4-[(1E)-1-benzothien-2-ylmethylene]amino]phenol substituted zinc(II), manganese(III), cobalt(II) phthalocyanines: Synthesis and electrochemistry, *J Mol Struct*, 1178, 2019, 508–513.
- [25] S. Gorduk, A. Altındal, Non-peripherally tetra substituted phthalocyanines bearing carboxylic acid anchoring groups as photosensitizer for high efficient dye-sensitized solar cells, *J Mol Struct*, 1204, 2020, 127636.
- [26] S. Gorduk, Investigation of photophysical properties of non-peripherally tetra-substituted metal-free, Mg(II), Zn(II) and In(III)Cl phthalocyanines, *Polyhedron*, 189, 2020, 114727.
- [27] R. Bayrak, H.T. Akçay, Z. Biyıklıoğlu, İ. Değirmencioğlu, Substituted phthalocyanines and their electropolymerization properties, *Synth Met*, 220, 2016, 643–652.
- [28] M. Shumba, T. Nyokong, Electrode modification using nanocomposites of boron or nitrogen doped graphene oxide and cobalt (II) tetra aminophenoxy phthalocyanine nanoparticles, *Electrochim Acta*, 196, 2016, 457–469.
- [29] Ö. Kurt, A. Koca, A. Gül, M. Burkut Koçak, Synthesis, electrochemistry and in situ spectroelectrochemistry of novel hexadeca-substituted phthalocyanines with three different groups, *Synth Met*, 206, 2015, 72–83.
- [30] A. Günsel, M. Kandaz, A. Koca, B. Salih, Peripheral and non-peripheral-designed multifunctional phthalocyanines; synthesis, electrochemistry, spectroelectrochemistry and metal ion binding studies, *Polyhedron*, 30, 2011, 1446–1455.
- [31] G.H. Hegazy, H.I. Ali, Design, synthesis, biological evaluation, and comparative Cox1 and Cox2 docking of p-substituted benzylideneamino phenyl esters of ibuprofenic and mefenamic acids, *Bioorg Med Chem*, 20, 2012, 1259–1270.
- [32] H. Fazlı, Ç. Akkol, S.C. Osmanogulları, Z. Biyıklıoğlu, E.T. Saka, O. Bekircan, Synthesis of water soluble copper(II), manganese(III) phthalocyanines and their photocatalytic performances in benzyl alcohol photooxidation, *J Organomet Chem*, 983, 2023, 122553.
- [33] Z. BIYIKLIOĞLU, H. BAŞ, Synthesis and effect of substituent position, metal type on the electrochemical properties of (3-morpholin-4-ylpropoxy) groups substituted cobalt, manganese phthalocyanines, *TURKISH J Chem*, 44, 2020, 687–694.
- [34] G. Gümrükçü Köse, G.K. Karaoğlu, Y. Erdağ Maden, A. Koca, Novel silicon phthalocyanine photosensitizers containing carboxylic acid based axial anchoring groups: Electrochemistry, spectroelectrochemistry, and dye sensitized solar cell performance, *Dye Pigment*, 207, 2022, 110686.
- [35] H. Yalazan, Y.E. Maden, A. Koca, H. Kantekin, Multi-step syntheses, electrochemistry and spectroelectrochemistry of peripheral CoII, CuII and MnIII Cl phthalocyanines bearing pyrazoline, *J Mol Struct*, 1269, 2022, 133788.
- [36] D. Akyüz, Ü. Demirbaş, O. Bekircan, Metallo-phthalocyanines Containing 1,3,4-oxadiazole Substituents: Synthesis, Characterization, Electrochemical and Spectroelectrochemical Properties, *ChemistrySelect*, 8, 2023, e20220459.
- [37] G. Dilber, A. Nas, Ö. Budak, A. Koca, Chloromanganese and oxo-Titanium (IV) phthalocyanines: Synthesis, electrochemistry and Spectroelectrochemistry, *Polyhedron*, 242, 2023, 116495.



Antioxidant activity and in vitro/in silico acetylcholinesterase and urease enzyme inhibition effects of amygdalin

Zehra Can^{1*} , Yakup Kara² , Halil İbrahim Güler³ , Ceren Birinci² , Sevgi Kolaylı² 

¹ Bayburt University, Faculty of Applied Sciences, Department of Emergency Aid and Disaster Management, 69000, Bayburt, Türkiye

² Karadeniz Technical University, Faculty of Science, Department of Chemistry, 61080, Trabzon, Türkiye

³ Karadeniz Technical University, Faculty of Science, Department of Molecular Biology and Genetics, 61080, Trabzon, Türkiye

Abstract

This study investigated the acetylcholinesterase, urease enzyme inhibition and, these enzymes' molecular docking as well as the antioxidant activity of commercially available amygdalin. While Amygdalin displayed effective anti-urease activity compared to acetohydroxamic acid anti-acetylcholine esterase activity was a little ineffective compared to donepezil. The molecular docking was performed to check binding interactions between the amygdalin and the enzymes. DPPH and FRAP assays were preferred to determine the antioxidant activity. The antioxidant activity ($3.39 \pm 0.33 \mu\text{mol Fe}_2\text{SO}_4 \cdot 7\text{H}_2\text{O} / \text{g}$, $\text{SC}_{50} 18.74 \pm 0.72 \text{ mg/mL}$ using the FRAP and DPPH assays, respectively). Amygdalin's *in vitro* and *in vivo* studies are needed to demonstrate that is a therapeutic agent for the treatment of various diseases.

Keywords: Acetylcholinesterase, urease, molecular docking, antioxidant activity, amygdalin

1. Introduction

Amygdalin is a naturally occurring chemical compound found in the kernels of various fruits, such as apricots, peaches, cherries, and plums, as well as in bitter almonds. It has a molecular weight of 457.42g/mol and, a chemical formula $\text{C}_{20}\text{H}_{27}\text{O}_{11}$. Amygdalin, also known as laetrile or Vitamin B17, has garnered attention in recent years due to claims of its potential anti-cancer, anti-inflammatory, antibacterial and antioxidant properties [1,2]. Amygdalin is classified as a cyanogenic glycoside, meaning it contains both a sugar molecule and a cyanide group. When metabolized, amygdalin breaks down into glucose, benzaldehyde, and hydrogen cyanide. While amygdalin itself is harmless, the release of hydrogen cyanide (HCN) during its enzymatic hydrolysis can be harmful. Recent studies have shown that HCN is released in normal cells, indicating that it may not be safe for the human body [3].

Amygdalin is a cyanogenic disaccharide [4]. There are numerous studies in the literature regarding its high therapeutic effects, such as anti-inflammatory and analgesic effects in neurodegenerative diseases [5]. Studies have shown positive effects of amygdalin in the treatment of various diseases such as leprosy, colorectal

cancer, asthma, and bronchitis [6,7]. Numerous studies have also revealed its anticancer and anti-inflammatory effects [8,9]. Amygdalin has been used as a therapeutic agent in cancer treatment for many years [10,11,12]. For example, it has been reported to have a curative effect in the treatment of prostate cancer as well as a positive effect in the treatment of colon cancer.^[13] In another study, it was found that amygdalin derived from Apricot (*Prunus armeniaca*) inhibited breast, lung, and bladder cancer cell [14].

Alzheimer's disease (AD) is the most common form of dementia, which is a progressive neurological condition characterized by the gradual degeneration and loss of brain cells. Despite numerous studies on the treatment of this disease, a complete cure has not yet been found [15,16,17]. Acetylcholinesterase (AChE) is an enzyme responsible for breaking down the neurotransmitter acetylcholine in the nervous system. Inhibiting AChE activity is a key mechanism of action for drugs used in the treatment of Alzheimer's disease.

Helicobacter pylori (*H. pylori*) infection occurs when *H. pylori* bacteria infect your stomach. *H. pylori* is a widespread cause of stomach ulcers, also known as

Citation: Z. Can, Y. Kara, H.İ. Güler, C. Birinci, S. Kolaylı, Antioxidant activity and in vitro/in silico acetylcholinesterase and urease enzyme inhibition effects of amygdalin, Turk J Anal Chem, 5(2), 2023, 143–150.

 <https://doi.org/10.51435/turkjac.1390923>

Author of correspondence: zehracan61@gmail.com

Received: October 25, 2023

Tel: +90 (458) 211 11 53 → 2549

Accepted: December 18, 2023

Fax: +90 (458) 333 20 43

peptic ulcers, and it is estimated that it could be found in over half of the world's population [18]. Persistent infection with *H. pylori* has been linked to the onset of gastric cancer, primarily attributed to the formation of DNA damage caused by oxidative and nitrosative processes [19]. Urease is an enzyme that the breakdown of urea into ammonia and carbon dioxide through hydrolysis. It holds significant importance as a target for the advancement of anti-ulcer medications.

In the treatment of Alzheimer's disease, drugs such as tacrine, donepezil, rivastigmine, and galantamine are used as they effectively inhibit the AChE enzyme [20]. Similarly, inhibitor drugs are also used for the urease enzyme, which plays a role in the development of diseases like stomach cancer and ulcers. However, due to the significant side effects of these drugs, natural products are preferred for the treatment of these diseases. In this study, we evaluated commercially purchased amygdalin for its *in vitro* inhibition of urease, and acetylcholinesterase enzymes, as well as its antioxidant activity. In our planned study, we investigated the inhibitory potential of amygdalin, which has limited studies in the literature, on acetylcholinesterase and urease enzymes, as well as its molecular docking. Additionally, its antioxidant activity was also determined.

2. Material and methods

2.1. Acetylcholinesterase inhibition assay

The inhibition of acetylcholinesterase (AChE) was determined using Ellman's method [21] reported with slight modification as by Kantar et al. [22]. Initially, 50 μ L of 2.5U/mL enzyme, 50 μ L of the sample, 3 mL of pH:8 100 mM phosphate buffer was mixed and left for 5 minutes. Subsequently, the reaction was initiated by the addition of 100 μ L of a 10 mM solution of 5,5-dithio-bis(2-nitrobenzoic) acid (DTNB) and, 20 μ L of a 75 mM solution of acetyl thiocholine chloride (ATCI). After 30 minutes, absorbance values were recorded at 412 nm. Donepezil was used as the standard.

2.2. Urease enzyme inhibition assays

The inhibition effect of the urease enzyme was determined according to Weatherburn [23] with slight modifications. In brief, a reaction mixture comprising 500 μ L of buffer solution (pH 8.2), 200 μ L of urease enzyme solution, and 100 μ L of the sample was incubated for 15 minutes in a tube. Then, 500 μ L of a phenol reagent and 600 μ L of an alkali reagent were added to each tube and incubated for 50 minutes in a dark room. The increase in absorbance at 625 nm was measured at the end of the incubation period using a UV-Vis spectrophotometer. Acetohydroxamic acid was

used as the inhibitor. The IC₅₀ value corresponds to the concentration of a compound that effectively inhibits 50% of the maximum activity observed.

2.3. Molecular Docking Studies

In order to investigate the potential binding modes of amygdalin against both human acetylcholinesterase (AChE) and urease enzymes, a molecular docking (MD) technique was employed using Auto Dock 4.2 software [24]. The three-dimensional structure of human acetylcholinesterase (AChE) complexed with donepezil was obtained from the Protein Data Bank (PDB) website (<https://www.rcsb.org/>) with the identifier 4EY7 (Chain A, Res: 2.35 Å). The other receptor, urease in complex with Acetohydroxamic Acid, was downloaded from Protein Data Bank, which was denoted 4H9M (Chain A, Res: 1.52Å). The 3D structures of the reference molecules, acetohydroxamic acid and donepezil, were downloaded from the PubChem database (<https://pubchem.ncbi.nlm.nih.gov/>) in sdf format and converted to pdb file format using OpenBabelGUI 2.4.1 software [25].

After energy minimization, the protein structures were prepared for docking by removing water molecules, ions, and other ligands, and adding polar atoms of hydrogen and Kollman charges. The prepared structures were then converted to PDBQT file format for docking. Possible docking modes between molecules and target proteins were studied using Auto Dock 4.2 software with the Lamarckian genetic algorithm employed for all docking simulations. For the standard docking procedure, the target protein was kept rigid while all ligands were kept flexible with torsion angles of 150 independent runs per ligand. Docking studies were performed with a population of 150 individuals, maximum energy evaluations of 2,500,000, and maximum generation of 54,000.

Additionally, the active site of AChE was covered with a grid box of dimension 60 Å x 60 Å x 60 Å and -14.1, -43.83, 27.66 points in the x, y, and z directions with a grid spacing of 0.375 Å. To cover the urease active site, a grid box of dimension 70 Å x 70 Å x 70 Å and -19.84, -58.46, -22.38 points in the x, y, and z directions with a grid spacing of 0.375 Å was applied. Default settings were applied for all other parameters. The results of the molecular calculations elucidated the binding affinity of each ligand to the targeted proteins, as determined by the docking score and hydrogen/hydrophobic binding interactions. The binding energies of docked conformations and post-docking analyses of each ligand against the target protein were assessed using BIOVIA Discovery Studio Visualizer 2018 [26].

2.4. Antioxidant activity assays

2.4.1. Ferric-reducing antioxidant power (FRAP)

The FRAP method is the most common method for determining antioxidant activity due to its simplicity and low cost. The ferric-reducing antioxidant capacity of amygdalin was determined according to the method described in the literature [27]. To create the FRAP reagent, a mixture was prepared using the following components: 2.5 mL of 10 mM (2,4,6-Tris(2-pyridyl)-s-triazine) TPTZ, 2.5 mL of 20 mM FeCl_3 , and 25 mL of 0.3 M acetate buffer at pH 3.6. Then, 50 μL of the sample and 1.5 mL of the FRAP reagent were combined. After 4 minutes, the absorbance was measured at 595 nm. $\text{Fe}_2\text{SO}_4 \cdot 7\text{H}_2\text{O}$ was used for calculating the antioxidant activity. FRAP result was expressed as $\mu\text{mol Fe}_2\text{SO}_4 \cdot 7\text{H}_2\text{O} / \text{g}$.

2.4.2. DPPH assay

DPPH• (1,1-diphenyl-2-picrylhydrazyl) radical scavenging activity was investigated using the method described in the literature [28]. The sample was prepared at six different concentrations. A 10 mM DPPH solution was prepared in methanol. Subsequently, 750 μL of each sample and 750 μL of the stock DPPH solution were combined and incubated for 50 minutes in a dark room. Following the completion of the incubation period, absorbance measurements were obtained at a wavelength of 517 nm. Lower absorbance values indicate greater free radical scavenging activity. Trolox® was employed as a positive reference in the experiment.

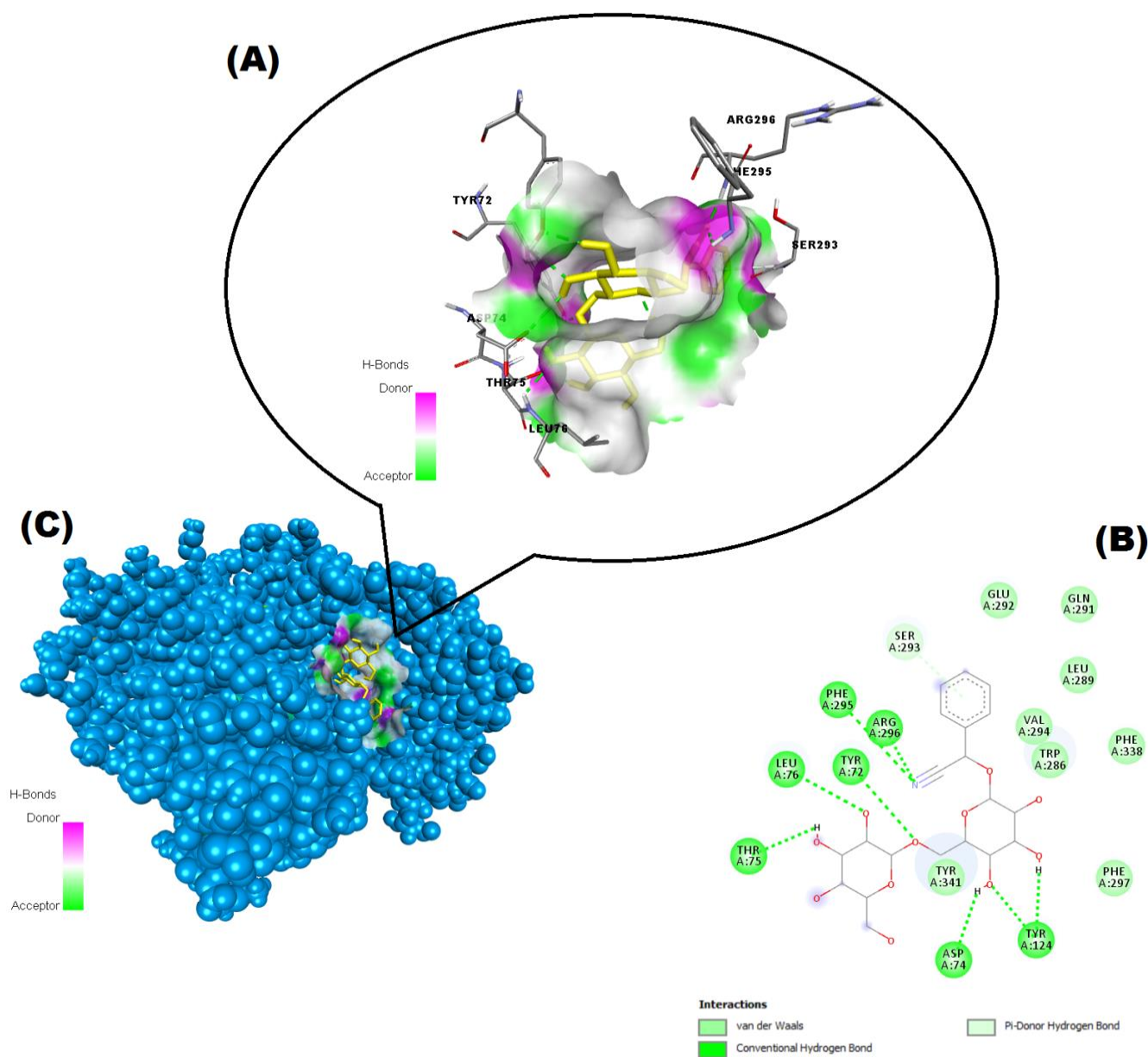


Figure 1. Binding pose profile of amygdalin in the target protein AChE (C), blue shaped molecule represents the receptor and yellow shaped molecule indicates the ligand. The two-dimension (2D) (B) and three-dimension (3D) (A) interactions analysis of human acetylcholinesterase (AChE) with amygdalin.

Table 1. Acetylcholinesterase and urease and enzyme inhibition of Amygdalin

Sample	Acetylcholinesterase Inhibition IC ₅₀ (M)	Urease Inhibition IC ₅₀ (M)
Amygdalin	>1	0.11 ± 0.01
Donepezil	39.84 ± 0.21	—
Acetohydroxamic acid	—	28.6 ± 0.78

2.5. Statistical analysis

All experiments were carried out in triplicates, and the results are presented as mean ± standard deviation (SD). SPSS version 22.0 (SPSS Inc., Chicago, IL, USA) of the Windows software was executed for statistical analysis.

3. Results and discussion

3.1. Acetylcholinesterase and urease enzyme inhibition

Acetylcholinesterase is an enzyme that plays a vital role in the breakdown of the neurotransmitter acetylcholine. Acetylcholine is a critical molecule involved in the transmission of nerve signals within the nervous system, including the brain, spinal cord, and peripheral nerves. Inhibition of acetylcholinesterase can have therapeutic implications in the treatment of conditions such as Alzheimer's disease. Donepezil and rivastigmine are very widely used AD remedies targeting the AChE enzyme. However, both are known to have various side effects [29,30]. The use is widespread of synthetic AChE inhibitors (such as donepezil, rivastigmine, and galantamine) and urease inhibitors (like thio-ureas, hydroxamic acids, etc.) however, they are associated with several side effects. Therefore, there is a growing demand to explore natural sources for the development of AChE and urease inhibitors that exhibit strong therapeutic effects with minimal to no toxicity, aiming to treat diseases caused by these enzymes effectively. For this reason, amygdalin was investigated for its ability to inhibit AChE (acetylcholinesterase) and urease. According to our findings we may say that amygdalin has the potential to inhibit the activity of AChE, which may have therapeutic implications for the treatment of Alzheimer's disease, and also the urease enzyme, which is vital in addressing conditions like gastric cancer, gastritis, and peptic ulcers as a potential

inhibitor. Table 1 shows that amygdalin exhibited an inhibition effect against acetylcholinesterase and urease. Several studies have reported that Amygdalin has the potential to act as an acetylcholinesterase inhibitor. Vahedi-Mazdabadia et al. [31] reported that both sweet and bitter extracts of apricot kernels had inhibitory effects on cholinesterase (ChE) enzymes in vitro.

The aqueous extract of the bitter type had the best inhibition effect, with an IC₅₀ value of 134.93 ± 2.88 µg/mL. Another study reported that kernels extracted from fruits of 20 different peach cultivars had IC₅₀ values ranging from 0.67 to 5.85 (mg of dried seeds). A study was conducted to investigate the neuroprotective and neurotogenic effects of amygdalin. Initially, the study demonstrated that amygdalin enhanced the process of nerve growth factor (NGF)-induced neuritogenesis and also reduced the neurotoxicity induced by 6-hydroxydopamine (6-OHDA) in rat dopaminergic PC12 cells [32].

A camp formulation consisting of *P. armeniaca* L. has been investigated for its neuroprotective abilities and its potential to improve learning difficulties and synaptic loss in AD (Alzheimer's disease) patients. It was found that synergistic effects play a significant role in directly activating neurons [33].

The enzyme urease functions in the process of converting urea to ammonia and carbon dioxide through its catalytic activity. Inhibition of urease can have potential applications in the treatment of various medical conditions, including urinary tract infections and gastric ulcers. The inhibition of urease by amygdalin at a concentration of (IC₅₀) 0.11 M. As a result of, we suggest that amygdalin may have moderate potential as a urease inhibitor.

In a study, the methanol and aqueous extracts of five apricot cultivars were investigated for their effects against the urease enzyme involved in treating stomach conditions such as carcinomas and ulcers. In the study, it was found that both methanol and aqueous extracts exhibited inhibitory effects on the urease enzyme, with IC₅₀ values ranging from 20.763 to 195.437 mg/mL [34].

Table 2. Description of amygdalin and reference molecules against different enzymes with binding energy, K_i and interacting residues in the binding site

Receptor Name	PDB ID	Ligand name	Binding Energy (kcal/mol)	K _i	No of H bonds	Interacted residues with ligand
Human acetylcholinesterase (AChE)	4EY7	Amygdalin	-9.35	140.66 nM	7	Asp74, Trp86, Asn87, Pro88, Tyr124, Gly126, Tyr341
		*Donepezil	-12.09	1.37 nM	2	Tyr72, Trp86, Trp286, Leu289, Ser293, Phe295, Tyr337, Phe338, Tyr341, His447
		Amygdalin	-6.13	32.19 µM	8	Arg439, His492, Met588, Leu589, Val591, His593, Arg609, Asp633, Ala636
Urease	4H9M	*Acetohydroxamic Acid	-5.04	200.49 µM	6	Glu547, Gly548, Ala549, Gly550, Glu618

*Reference molecules

3.2. In silico analysis

Molecular docking is widely used to investigate binding interactions between potential drugs and different sites or active sites on target molecules. Various types of interactions, such as H-bonds, π - π interactions, and amide- π interactions, are evaluated to determine the binding efficiency of a ligand molecule with a target. The hydrogen bonding pattern and the nature of residues present in the active site play a crucial role in explaining the binding affinity of a ligand with a target molecule. Binding free energy (kcal/mol) is used to examine and compare the binding affinity of different ligands with their respective target receptor molecules. When the binding energy is lower, it signifies a greater affinity of the ligand towards the receptor [35,36]. In this study, molecular docking was performed to evaluate amygdalin against AChE and urease enzymes. The simulation results provided predicted protein-ligand binding energies, K_i values, and identified potential ligand binding sites (Table 2). After successfully docking amygdalin and reference molecules (Table 2), significant interactions of the ligand with the receptor proteins were

Table 3. Antioxidant Activity of Amygdalin

Sample	FRAP ($\mu\text{mol Fe}_2\text{SO}_4 \cdot 7\text{H}_2\text{O/g}$)	DPPH SC_{50} (mg/mL)
Amygdalin	3.39 \pm 0.33	18.74 \pm 0.72
Trolox	—	0.004 \pm 0.00

observed. When examining the interaction of amygdalin with AChE, it was found that the ligand effectively binds to the receptor with a low binding energy of -9.35 kcal/mol, while the reference molecule, donepezil, binds strongly with an even lower binding energy (-12.09 kcal/mol). Both the reference molecule and amygdalin appear to form strong interactions with Trp86 and His341 residues in the active site of AChE. Amygdalin forms five conventional hydrogen bonds, two carbon hydrogen bonds, two Pi-sigma bonds, and two donor-donor bonds with AChE, with one of these bonds having an atomic distance lower than 2 Å. On the other hand, when examining the docking poses with urease enzyme and amygdalin, it is evident that the ligand binds to the receptor more effectively than the reference molecule, acetohydroxamic acid. Amygdalin forms six conventional hydrogen bonds with urease, three of

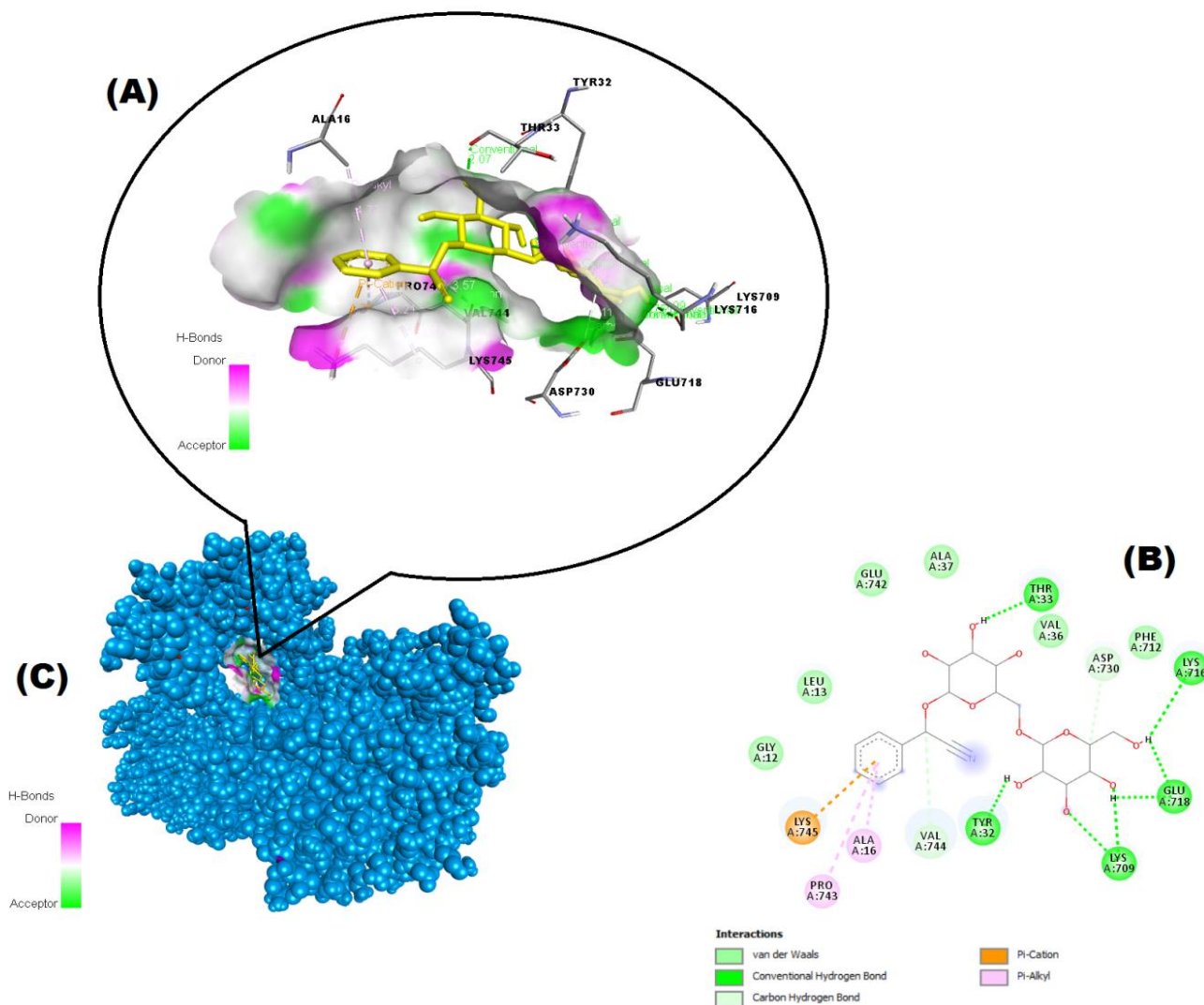


Figure 2. Binding pose profile of amygdalin in the target protein Urease (C), blue shaped molecule represents the receptor and yellow shaped molecule indicates the ligand. The two-dimension (2D) (B) and three-dimension (3D) (A) interactions analysis of Urease with amygdalin

which have atomic distances lower than 2 Å (Fig. 2). Additionally, the ligand forms two carbon hydrogen bonds, two pi-alkyl bonds, two donor-donor bonds, one pi-cation bond, one pi-anion bond, and one pi-pi t-shaped bond with the receptor. It appears that Met588 plays a crucial role by forming two conventional hydrogen bonds with lengths of 1.99 and 1.88 Å. Fig. 1 and Fig. 2 provide the docked poses of the best hits in each target receptor, the residues they interact with, and the corresponding interactions.

3.3. Antioxidant activity of amygdalin

Amygdalin has been observed to demonstrate antioxidant activity in numerous *in vitro* and *in vivo* studies. It is a natural compound found in the seeds of many fruits, such as apricots, peaches, and almonds, as well as in other plants. Apricot seeds contain antioxidant, Angiotensin I converting enzyme (ACE) inhibitor, and hypocholesterolemic peptides [37]. In our study, we performed DPPH and FRAP tests to assess the antioxidant activity of commercially purchased amygdalin. The FRAP value was determined as $3.39 \pm 0.33 \mu\text{mol Fe}_2\text{SO}_4 \cdot 7\text{H}_2\text{O/g}$, while the DPPH value was determined as $\text{SC}_{50} 18.74 \pm 0.72 \text{ mg/mL}$ (Table 3). When the numerical value of the DPPH value is low, it signifies a potent capability to scavenge free radicals. When comparing our study with the Trolox standard, we could see that the DPPH value is effective.

In an *in vivo* study, the effects of amygdalin at different doses on antioxidant gene expression and suppression of oxidative damage were evaluated in mice. The results of found that low and moderate doses of amygdalin did not cause toxicity in hepatic and testis tissues, and they did not have any adverse effects on the oxidative balance [38].

In a study conducted by Sushma et al. [39], amygdalin was extracted from *Prunus dulcis* and tested for its antioxidant and cytotoxic properties *in vitro*. Multiple antioxidant experiments revealed that the amygdalin extract from *P. dulcis* exhibited potent antioxidant characteristics. Zhang et al. [40] investigated the different varieties of apricot kernels. The researchers found that all the tested varieties had antioxidant activity, with some varieties showing higher levels than others. The study also suggested that the antioxidant activity of apricot kernels may be due to their high levels of phenolic compounds. A study was conducted to determine the amygdalin levels in different genotypes of bitter and sweet almonds. The results showed that bitter almonds had a higher amygdalin content compared to sweet almonds. Additionally, the study found that bitter almonds were rich in phenolic content. These findings suggest that it can be concluded that the amygdalin content affects the phenolic content [41].

Another study assessed the biological activities of amygdalin extracted from the organs of three cassava varieties that are commonly produced in Benin (BEN, RB, and MJ). HPLC analysis was employed to measure the amygdalin content in cassava organs and derivatives. The results indicated that the organs of all three cassava varieties contained glycosides, flavonoids, saponins, steroids, tannins, coumarins, and cyanogenic derivatives. Among these, young stems and fresh cassava leaves exhibited the highest concentrations of amygdalin, with 11,142.99 μg per 10 g and 9251.14 μg per 10 g, respectively. The antioxidant activity results showed that the amygdalin extracts were DPPH radical scavengers with IC_{50} values ranging from 0.18 mg/mL to 2.35 mg/mL [42]. Based on these results, it can be concluded that these extracts possess a considerably high concentration of amygdalin.

4. Conclusion

In summary, the purpose of this present study was to emphasize the enzyme inhibitory properties of amygdalin, as well as its antioxidant activity. In this study, the potential of amygdalin to act as an inhibitor for acetylcholinesterase and urease enzymes was investigated *in vitro*, as well as its molecular docking binding capacity. And the antioxidant capacity of amygdalin was determined. Based on the findings of our study, we can say that amygdalin holds significant potential as a valuable agent in pharmaceutical and food-related applications. Amygdalin, to be recommended for the treatment of human diseases, its safety and efficacy as a potential therapeutic agent must undergo thorough evaluation in clinical trials.

Funding:

None.

Conflicts of Interest:

The authors declare no conflict of interest.

Authors Contributions:

ZC: Methodology, Investigation, Data curation, Writing – original draft.

YK: Investigation of *in vitro* enzyme inhibition and antioxidant activity.

HİG: Investigation of molecular docking, writing,

CB: Investigation of antioxidant activity and enzyme inhibition.

SK: Writing

References

- [1] B. Orlikova, N. Legrand, J. Dicato, M. Diederich, Anti-inflammatory and anticancer drugs from nature. In *Advances in Nutrition and Cancer*, 3, 2014,123–14.
- [2] H. Barakat, Amygdalin as a plant-based bioactive constituent: A Mini-Review on Intervention with Gut Microbiota, Anticancer Mechanisms, Bioavailability, and Microencapsulation. *Proceedings*, 15, 2020, 61.
- [3] A. Kolesarova, S. Baldovska, S. Roychoudhury S, The multiple actions of amygdalin on cellular processes with an emphasis on female reproduction. *Pharm*, 14(9), 2021, 881.
- [4] M. Andrianarison, L. Tika, I.M. Ranaivo, M. Razakanaivo, L.S. Ramarozatovo, F. Rafaramino, R.F. Rapelanoro, Les cancers cutanés à Madagascar: OÙ en sommes-nous? *Pan Afr. Med*, 2019, 34, 167.
- [5] G. Viorica-Mirela, C. Socaciu, I. Jianu, R. Florica, F. Florinela, Identification et évaluation quantitative de l'amygdaline des huiles et noyaux d'abricot, de prune et de pêche. *Bulletin USAMV-CN*, 62, 2006, 246–253.
- [6] X.B. Li, C.H. Liu, R. Zhang, X.T. Huang, Y.Y. Li, L. Han, M.L. Xu, S.Q. Mi, N.S. Wang, Determination and pharmacokinetics of amygdalin in rats by LC–MS–MS, *J. Chromatogr Sci* 52, 2014,476–481.
- [7] Z. Song, X. Xu, Advanced research on anti-tumor effects of amygdalin. *J Cancer Res*, 10 (1), 2014, 3–7.
- [8] H.K. Chang, M.S. Shin, H.Y. Yang, J.W. Lee, Y.S. Kim, M.H. Lee, J. Kim, K.H. Kim, C.J. Kim, Amygdalin induces apoptosis through regulation of Bax and Bcl-2 expressions in human DU145 and LNCaP prostate cancer cells. *Biol Pharm Bull*, 29 (8), 2006,1597–602.
- [9] A. Moslehi, T. Komeili-movahed, M. Moslehi, Antioxidant effects of amygdalin on tunicamycin-induced endoplasmic reticulum stress in the mice liver: Cross talk between endoplasmic reticulum stress and oxidative stress. *J Rep Pharm Sci*, 8(2), 2019, 298–302.
- [10] J.C. Holland, Why patients seek unproven cancer remedies: a psychological perspective *CA Cancer J Clin*, 32 (1), 1982, 10–14.
- [11] I. London-Shafir, S. Shafir, D. Shafir, Eisikowitch, Amygdalin in almond nectar and pollen e facts and possible roles. *Plant Systematics and Evolution*, 238, 2003, 87–95.
- [12] A.M.A. Adam, An in vitro study of amygdalin alone and complexed with Se (IV), Au (III), Ru (III), and V (III) ions: Structure, morphology, and pharmacology. *J Molecular Struc*, 1195, 2019, 43–57.
- [13] H.J. Park, S.H. Yoon, L.S. Han, L.T. Zheng, K.H. Jung, Y.K. Uhm, J.H. Lee, J.S. Jeong, W.S. Joo, S.V. Yim, J.H. Chung, S.P. Hong, Amygdalin inhibits genes related to cell cycle in SNU-C4 human colon cancer cells. *World J Gastroenterol*, 11 (33), 2005, 5156–5161.
- [14] C. Zhou, L. Qian, H. Ma, X. Yu, Y. Zhang, Enhancement of amygdalin activated with β -d-glucosidase on HepG2 cells proliferation and apoptosis, *Carbohydr Polym*, 90, 2012, 516–523.
- [15] C.M. Henstridge, B.T. Hyman, T.L. Spires-Jones, Beyond the neuron–cellular interactions early in alzheimer disease pathogenesis. *Nat Rev Neurosci*, 20 (2), 2019, 94–108.
- [16] J.M. Long, D.M. Holtzman, Alzheimer disease: an update on pathobiology and treatment strategies. *Cell*, 2019, 179.
- [17] T. Taskin, M. Dogan, B.N. Yilmaz, I. Senkardes, Phytochemical screening and evaluation of antioxidant, enzyme inhibition, anti-proliferative and calcium oxalate anti-crystallization activities of *Micromeria fruticosa* spp. brachycalyx and *Rhus coriaria*. *Biocatalysis Agric Biotechnol*, 27, 2020, 101670.
- [18] W.D. Chey, G.I. Leontiadis, C.W. Howden, S.F. Moss, ACG clinical guideline: treatment of *Helicobacter pylori* infection. *Am J Gastroenterol*, 112 (2), 2017, 212–239.
- [19] D. Oral, A. Yirün, P. Erkekoğlu, Epigenetic and genetic changes caused by helicobacter pylori and their roles in gastric carcinogenesis. *J Faculty Pharmaceu Ankara*, 43(3): 2019, 285–308.
- [20] A. Saxena, A.M. Redman, X. Jiang, O. Lockridge, B.P. Doctor, Differences in active site gorge dimensions of cholinesterases revealed by binding of inhibitors to human butyrylcholinesterase. *Chemico-Biol Interact*, 36 (48), 1997,14642–14651.
- [21] G.L. Ellman, K.D. Courtney, R.M. V Andres Jr, Featherstone, A new and rapid colorimetric determination of acetylcholinesterase activity, *Biochem Pharmacol*, 1961, 7–88.
- [22] C. Kantar, N. Baltas, O.K. Dereci, S. Şaşmaz, Urease and acetylcholinesterase enzyme inhibitor novel phthalonitrile azo compounds. *Indian J Chem*, 61 (11), 2022, 1188.
- [23] M.W. Weatherburn, Phenol-hypochlorite reaction for determination of ammonia. *Anal Chem*, 1967,39, 971–974.
- [24] G.M. Morris, R. Huey, W. Lindstrom, M.F. Manner, R.K. Belew, D.S. Goodsell, A.J. Olson, AutoDock4 and AutoDockTools4: Automated docking with selective receptor flexibility. *J Comput Chem*, 30, 2009, 2785–2791.
- [25] M. O'Boyle, M. Banck, C.A. James, C. Morley, T. Vandermeersch, G.R. Hutchison, Open Babel: An open chemical toolbox. *J Cheminformatics*, 2011, 3, 33.
- [26] Dassault Systèmes BIOVIA, Discovery studio modeling environment, Release 2017, San Diego: Dassault Systèmes, 2016.
- [27] I.F.F. Benzie, J.J. Strain, The ferric reducing ability of plasma (FRAP) as a measure of “antioxidant power”: the FRAP assay, *Anal Biochem*, 1996,239–70.
- [28] P. Molyneux, The use of the stable free radical diphenylpicrylhydrazyl (DPPH) for estimating antioxidant activity. *Songklanakarın J Sci Technol*, 2004,26, 211.
- [29] H.O. Tayeb, H.D. Yang, B.H. Price, F.I. Tarazi, Pharmacotherapies for Alzheimer's disease: beyond cholinesterase inhibitors. *Pharmacol. Therapeu*, 134(1), 2012, 8–25.
- [30] M. Farlow, F. Veloso, M. Moline, J. Yardley, E. Brand-Schieber, F. Bibbiani, H. Zou, T. Hsu, A. Satlin, Safety and tolerability of donepezil 23 mg in moderate to severe Alzheimer's disease. *BMC Neurol*,2011, 11(1):57.
- [31] Y. Vahedi-Mazdabadi, E. Karimpour-Razkenari, T. Akbarzadeh, H. Lotfian, M. Toushah, N. Roshanravan, M. Saeedif, A. Ostadrahimi, Anti-cholinesterase and neuroprotective activities of sweet and bitter apricot kernels (*Prunus armeniaca* L.). *Iranian J Pharm Res*, 19(4), 2020, 216–224.
- [32] Y. Cheng, C. Yang, J. Zhao, H.F. Tse, J. Rong, Proteomic identification of calcium-binding chaperone calreticulin as a potential mediator for the neuroprotective and neurotogenic activities of fruit-derived glycoside amygdalin. *J Nutr Biochem*, 26, 2015,146–54.
- [33] C. Tohda, T. Tamura, K. Komatsu, Repair of amyloid β (25–35)-induced memory impairment and synaptic loss by a Kampo formula, *Zokumei-to. Brain Res*, 2003,990, 141–7.
- [34] A.A. Karaçelik, Phytochemical profiling, antioxidant activities and in vitro/in silico enzyme inhibitory potentials of apricot cultivars grown in Iğdır/Turkey. *S Afr J Bot*, 156, 2023, 257–267.
- [35] D. Chen, N. Oezguen, P. Urvil, C. Ferguson, S.M. Dann, T.C. Savidge, Regulation of protein-ligand binding affinity by hydrogen bond pairing. *Scie Adv*, 2(3), 2016, 1501240.
- [36] S. Raj, S. Sasidharan, V.K. Dubey, P. Saudagar, Identification of lead molecules against potential drug target protein MAPK4 from *L. donovani*: An in-silico approach using docking, molecular dynamics and binding free energy calculation. *PLoS one*, 2019,14(8).
- [37] M.C. Garcia, E. Gonzalez-Garcia, R. Vasquez-Villanueva, M.L. Marina, Apricot and other Seed Stones: Amygdalin Content and the Potential to Obtain Antioxidant, Angiotensin I Converting

- Enzyme Inhibitor and Hypocholesterolemic Peptides. *Food Funct*, 7, 2016, 4693–4701.
- [38] S. Albogami, A. Hassan, N. Ahmed, A. Alnefaie, A. Alattas, L. Alquthami, A. Alharbi, Evaluation of the effective dose of amygdalin for the improvement of antioxidant gene expression and suppression of oxidative damage in mice. *Peer J*, 8, 2020, e9232.
- [39] P. Sushma, B. Jacob, R.T. Narendhirakannan, Evaluation of antioxidant and cytotoxicity properties of amygdalin extracted from *Prunus dulcis*. *Kongunadu Res J*, 6, 2019, 8–12.
- [40] S. Zhang, Y. Zhang, C. Lv, J. Sun, Y. Zhao, Phenolic composition and antioxidant activity of different varieties of apricot kernels. *Food Chem*, 245, 2018, 1148–1156.
- [41] A.N. Yıldırım, B. San, F. Koyuncu, F. Yıldırım, Variability of phenolics, α -tocopherol and amygdalin contents of selected almond (*Prunus amygdalus* Batsch.) genotypes, *J Food Agric Environ*, 8 (1), 2010, 76–79.
- [42] H. Lehmane, A.N. Kohonou, A.P. Tchogou, R. Ba, D. Dah-Nouvlessounon, O. Didagbé, H. Sina, M. Senou, A. Adjanohoun, L. Baba-Moussa, Antioxidant, anti-inflammatory, and anti-cancer properties of amygdalin extracted from three cassava varieties cultivated in Benin. *Molecules*, 28(11), 4548, 2023.



Evaluation of biological activities of silver nanoparticles (AgNPs) synthesized by green nanotechnology from birch (*Betula* spp.) branches extract

Burçin Özçelik* , Aslı Kara 

Hitit University, Faculty of Science and Literature, Department of Molecular Biology and Genetic, 19100, Corum, Türkiye

Abstract

Green synthesis of silver nanoparticles (AgNPs) provide superiority due to their usage of various biological applications. The aim of this study is synthesizing the silver nanoparticles by using Birch (*Betula* spp.) branches extract with an ecofriendly, cost-effective, simple, and cheap green method. Even *Betula* is wide-spread tree with rich in phenolic compounds, data on the use of *Betula* branches is limited. Within this scope, this study is the first for using *Betula* branches extracts which take part as reducing and capping agent to synthesize the silver nanoparticles to evaluate the antimicrobial activity and antiproliferative efficiency. The biosynthesized AgNPs were characterized by various characterization methods such as UV-visible spectroscopy, dynamic light scattering (DLS), Fourier transform infrared (FTIR) spectroscopy and scanning electron microscopy (SEM). The characterization analysis has revealed the phenolic compounds of *Betula* extract acted as reducing and capping agent for formation of AgNPs.

The synthesized selected AgNPs were exhibited spherical shape with 103.2 ± 5.2 and 69.2 ± 12.7 nm according to DLS and SEM analysis, respectively. Also, the biological activity of biosynthesized AgNPs were evaluated by antimicrobial and antiproliferative tests on selected microorganisms and cell line, respectively. The IC₅₀ values of B3-4 AgNPs was determined as 64.27 µg/mL on HT29 colorectal cancer cells. And also, the antimicrobial activity results of AgNPs have revealed the dose-dependent inhibition for all studied test microorganisms.

In conclusion, this study evidently suggests the use of silver nanoparticles biosynthesized from *Betula* branches extract as a potential agent for antimicrobial and anticancer studies.

Keywords: *Betula* spp., silver nanoparticles, green synthesis, antiproliferative, colorectal cancer, antimicrobial

1. Introduction

Nanotechnology is a multidisciplinary field of science and engineering that deals with the design, manufacture and control of nanometer-scale materials, the smallest building blocks of matter. A nanometer is a unit of measurement that is one billionth of a meter, and this scale is an ideal size for understanding and manipulating the properties of materials at the atomic and molecular level. The main goal of nanotechnology is to enable the production of new and advanced products by utilizing the unique properties of materials of these small sizes. The properties of nanomaterials differ from those of large-scale materials and offer several advantages in their electrical, mechanical, thermal and optical properties. These properties allow nanotechnology to be used in a range of industrial, scientific and medical applications [1–5]. The applications of nanotechnology in the field of health aim to treat diseases more effectively, increase the rate of

early diagnosis and overcome limitations in the field of medicine. Nanotechnology enables the development of drug carrier systems that enable more effective transport and delivery of drugs to targeted sites in the body, the development of high-resolution imaging and diagnostic tools, the development of nano-sized sensors that allow the detection of biological analytes at low concentrations, and the design of nanorobots or nanomachines used in surgical operations [6–11]. Among the nanotechnological products that have application areas in many sectors, silver nanoparticles play an important role in many applications, especially in the field of medicine due to their unique properties. One of the most remarkable properties of silver nanoparticles is their strong antimicrobial effects. Silver disrupts the cell membrane of microorganisms and prevents them from multiplying. This property provides antibacterial, antiviral and antifungal effects, which

Citation: B. Özçelik, A. Kara, Evaluation of biological activities of silver nanoparticles (AgNPs) synthesized by green nanotechnology from birch (*Betula* spp.) branches extract, Turk J Anal Chem, 5(2), 2023, 151–161.

 <https://doi.org/10.51435/turkjac.1401931>

Author of correspondence: burcinozcelik@hitit.edu.tr

Received: December 8, 2023 **Tel:** +90 (364) 227 70 00

Accepted: December 26, 2023 **Fax:** +90 (364) 227 70 05

makes silver nanoparticles preferred in many applications such as wound healing, medical devices and antibacterial coatings. In addition, silver nanoparticles are generally biocompatible, meaning that they can be used in a compatible manner with biological systems. This property allows them to cause minimal toxic effects in the body and optimize their interaction with biological tissues. This allows silver nanoparticles to be used safely in medical applications. The surface plasmon resonance (SPR) properties of silver nanoparticles enable their use in imaging and sensor technologies. Silver nanoparticles can be well dispersed in various solvents. This property allows nanoparticles to be homogeneously used and dispersed in various medical applications. Nano-sized silver particles have large surface areas, which increases their reactivity. This feature enables silver nanoparticles to be effective in antimicrobial and catalytic applications. The high surface area enhances the antibacterial effect by increasing the interaction with microorganisms. In addition, these properties allow them to be used in drug transport and targeting studies. Moreover, silver nanoparticles attract attention with their anticancer activities. Silver nanoparticles have the capacity to stop the cell cycle of cancer cells. It has been reported that with this property, they stop the uncontrolled growth of cancer cells by preventing the division and proliferation of cells. Silver nanoparticles can increase oxidative stress in cancer cells. This may cause damage to cancer cells by increasing the production of free radicals in the cells. Silver nanoparticles can trigger the degradation of the genetic material of cancer cells and the process of apoptosis. Considering all these features, silver nanoparticles are widely used in studies such as imaging and diagnostics, drug delivery and targeting, tissue regeneration and rehabilitation, anti-microbial applications, development of sensitive and unique nanosensors that detect tumor markers [12–21].

The methods used for the preparation of silver nanoparticles include chemical reduction, thermal reduction, microwave heating, and electrochemical synthesis methods. In these methods, silver salts are reduced from solutions under special conditions to obtain nanoparticles. However, these traditional methods have problems with the use of toxic chemicals, energy intensity, high cost, long response times and scalability. Chemical reduction and thermal reduction methods are generally not environmentally friendly and the use of toxic agents is contrary to the principles of green chemistry. The microwave heating method may involve disadvantages in terms of equipment cost and energy consumption. Electrochemical synthesis requires specialized equipment and can sometimes result in uncontrolled particle growth. In recent years, green

synthesis method has been used to synthesize silver nanoparticles. Green synthesis represents an eco-friendly and sustainable approach and involves the use of herbal extracts, microorganisms or substances of natural origin for the synthesis of silver nanoparticles. In this method, environmentally friendly reducing agents are used. Green synthesis reduces the environmental impact of conventional synthesis methods, minimizes the use of toxic chemicals and enables medical and biological applications of silver nanoparticles with their biocompatibility properties. Green synthesis is an important step in the development of sustainable nanotechnology [14, 21–28].

Colorectal cancer is a type of cancer that develops in the large intestine (colon) or rectum. This type of cancer is recognized as a major health problem worldwide. Its incidence is increasing and it is a condition where early diagnosis is vital. Colorectal cancer is usually caused by abnormal cell masses called polyps, which can become cancerous over time. Risk factors include age, genetic predisposition, family history, inflammatory bowel diseases, poor eating habits and obesity. Methods used in the treatment of colorectal cancer include surgical intervention, chemotherapy, radiotherapy and targeted therapies. Surgery involves an operation to remove tumoral masses. Chemotherapy involves drugs used to kill cancer cells or control their growth. Radiotherapy is a treatment method that aims to destroy or shrink cancer cells by targeting them with high-energy rays. However, traditional treatment methods have various disadvantages. Disadvantages of surgery include the invasiveness of surgery, the patient's long recovery period, the serious side effects of chemotherapy and radiotherapy, and damage normal tissues. These methods often have a broad range of action and can also affect healthy cells. Additionally, in some cases, resistance to treatment may develop. Therefore, the development of new and more specific treatment strategies is an important area of research [29–31].

Betula is a genus of plants belonging to the Betulaceae family and includes tree and shrub species native to temperate climate regions. *Betula* tree has very valuable components, and the components may vary depending on the type of plant, growing conditions and extraction methods. *Betula* extracts contain triterpenoid components such as betulin and betulinic acid, flavonoids, phenolic acids, essential oils, minerals and vitamins. *Betula* tree extracts, through their various components, are an important biological resource in terms of reducing silver nitrate and stabilizing the silver nanoparticles formed by the green synthesis method [32, 34].

Taking all this into account, the aim of this study was to synthesize and to characterize silver nanoparticles,

which may have potential use in the treatment of infectious diseases and colorectal cancer, using green synthesis. It was also aimed to evaluate the antimicrobial and anticancer effects of silver nanoparticles synthesized and characterized by the green synthesis method.

2. Materials and Methods

2.1. Materials

Silver nitrate (AgNO_3), Muller Hilton Broth, 3-(4,5-dimethylthiazol-2-yl)-2,5-diphenyltetrazolium bromide (MTT), and dimethyl sulfoxide (DMSO) were purchased from Sigma-Aldrich (St Louis, MO, USA). Dulbecco's Modified Eagle's Medium (DMEM), high glucose, and pyruvate were purchased from Gibco (Waltham, MA, USA). *Escherichia coli* (ATCC 25922), *Pseudomonas aeruginosa* (ATCC 27853), gram-positive bacteria, *Staphylococcus aureus* (ATCC 25923), *Enterococcus faecalis* (ATCC 29212) and a yeast, *Candida albicans* (ATCC 10231) strains were purchased for antimicrobial studies. HT29 (ATCC HTB-38) colorectal cancer cell line was purchased for antiproliferative studies and L929 mouse fibroblast cell line was also purchased for *in vitro* biocompatibility from ATCC Cell Bank (USA). All other chemicals which used in study were analytical grade.

2.2. Methods

2.2.1. Preparation of *Betula* spp. extract from branches

Betula tree branches were collected from Van province, Türkiye. The purification of branches was done under the distilled water by washing twice and dried under room temperature in the shade. The dried samples were grounded in an electric grinder and weighed. After that dried ground samples were weighed to 25 g and mixed with 250 mL distilled water for extraction. The extraction was carried out in Soxhlet Extractor at 80 °C for 8 hours. Then the extract was filtered by using Whatman No. 1 filter paper and stored at 4 °C in amber colored bottle for further use [34]. The experiment was carried out in duplicate.

2.2.2. Synthesis of silver nanoparticles (AgNPs)

The synthesis of silver nanoparticles from branches was carried out with some modifications as reported before [35]. Silver nitrate (AgNO_3) was used as precursor salts to obtain silver nanoparticles. To prepare silver nanoparticles, various concentrations (1 mM, 3 mM, and 5 mM) of AgNO_3 solutions were incubated with *Betula* extracts in the ratio 1:10 for 24 hours. Also, the effect of temperature on the formation of silver nanoparticles was performed by changing the temperature from room temperature to 80 °C. Finally, the formation of silver nanoparticles was confirmed by color changes on different reaction solutions. After color change, the

reaction was stopped and silver nanoparticles were purified by centrifugation (Sigma 3-30KS, Germany). Therefore, the mixtures were centrifuged at 13500 rpm for 20 minutes twice to remove unreacted silver ions. Then the supernatant was discarded and the pellet was air dried in incubator overnight to obtain powder. The experiment was carried out in duplicate.

2.2.3. Characterization of AgNPs

The obtained silver nanoparticles were characterized by UV-Vis spectrophotometer (Rayto, RT, 2100C, China), particle size analyzer (Zetasizer Nano ZS, Malvern, UK), Fourier transform infrared (FTIR) spectrophotometer (Thermo Scientific / Nicolet IS50, China), Scanning electron microscopy (SEM) (FEI / Quanta 450 FEG, Japan).

2.2.3.1. UV-Vis spectroscopy

The reduction of silver ions in the presence of *Betula* extract was determined by measuring the spectrum of the reaction medium. The green synthesized silver nanoparticles were characterized by UV-Vis spectroscopy. UV-Vis spectrum of obtained silver nanoparticles were measured in the range of 200–800 nm by using UV-visible spectrometer. Three replicates of experiments were carried out.

2.2.3.2. Particle size analysis

The particle size, zeta potential and distribution of silver nanoparticles were analyzed by dynamic light scattering using Zetasizer Nano ZS (Malvern). The samples for measurement were prepared fresh each time and were analyzed at 25 °C. Three replicates of experiments were carried out.

2.2.3.3. FT-IR Analysis

Analysis of synthesized silver nanoparticles by FT-IR (Fourier Transform Infrared Spectroscopy) spectrometer provided information about structural properties of these nanoparticles. The measurements were carried out in the range of 400–4000 cm^{-1} at a resolution of 4 cm^{-1} by using KBr pellet method to introduce the bioreduced silver nanoparticles.

2.2.3.4. Scanning Electron Microscopy (SEM)

The synthesized silver nanoparticles from *Betula* spp. branches were analyzed by scanning electron microscopy to determine the formation, stability and surface morphology of nanoparticles.

2.2.4. Antiproliferative activity of AgNPs against HT-29 colorectal cancer cell

Antiproliferative activity of (AgNPs) against HT-29 colorectal cell (CRC) was evaluated using a MTT (3-(4,5-

dimethylthiazol-2-yl)-2,5-diphenyltetrazolium bromide) assay. 1×10^4 cells/well were plated in 96-well plates and were incubated in DMEM medium supplemented with 10% FBS, and 1% antibiotics (100 U/mL penicillin, 100 µg/mL streptomycin) at 37 °C in a humidified atmosphere containing 5% CO₂. Medium was changed every 48 h. When the cells reached about 70–80% confluency, they were serum-starved over-night before AgNPs exposure and medium was changed with serum supplemented medium (100 µL). Then, cells were exposed to 100 µL of AgNPs which dispersed in serum free medium at different concentrations (20–100 µg/mL) for 24 and 48 h. Serum free medium was used as a control. After the incubating period, 20 µL of 5 mg/mL MTT solution was added to each well and incubated at 37 °C and 5% CO₂ for 4 h. Then, the culture media was aspirated and 200 µL DMSO was added to solubilize the formazan crystals. The plate was read in a plate reader at 570 nm. Results are standardized using control group values. The viability (%) of the exposed cells was defined as the percentage of absorbance compared to control unexposed cells. Three replicates of experiments were carried out.

2.2.5. Biocompatibility of AgNPs

Healthy fibroblast cells were used to determine the biocompatibility of synthesized nanoparticles in living cells. For this purpose, L929 (Mouse Fibroblast cell line) cells in DMEM containing 10% FBS were grown in 96-well plates. After 2 days, the cells were washed and AgNPs obtained at different concentrations were applied to the cells. Cell culture medium not treated with AgNP was used as a control. After 4 hours, the cells were washed twice and the MTT test was performed according to the manufacturer's instructions. The absorbance value was measured in a microplate reader at 570 nm. Three replicates of experiments were carried out.

2.2.6. Antibacterial and antifungal activity of AgNPs

The antibacterial and antifungal activities of AgNPs were investigated using gram-negative bacteria, *Escherichia coli* (ATCC 25922), *Pseudomonas aeruginosa* (ATCC 27853), gram-positive bacteria, *Staphylococcus aureus* (ATCC 25923), *Enterococcus faecalis* (ATCC 29212) and a yeast, *Candida albicans* (ATCC 10231) as test microorganisms by the Kirby–Bauer Disk method. In brief, bacterial and fungal suspensions were inoculated at 10^6 cfu/spot on Mueller–Hinton Agar (MHA) and Sabouraud Dextrose Agar plates, respectively. Next, sterile paper disks were placed on the agar surface and different volumes of AgNPs stock solution (1 mg/mL)

were added to disks to get the concentration of 5–20 µg/disk prior to microdilution method. 10 µg/disk gentamicin and 10 µg/disk of fluconazole were used as positive controls for bacteria and fungi, respectively. The negative control consisted of disk treated with serum free medium. After incubation at 37 °C for 24 h for bacteria and at 30 °C for 48 h for yeast, the diameters (in mm) of the inhibition zone of were determined. Three replicates of experiments were carried out.

2.2.7. Minimal inhibitory concentration (MIC) of AgNPs against test microorganisms

The microdilution method is a widely used method to systematically and sensitively evaluate the antimicrobial properties and MIC values of AgNPs. MIC of the AgNPs against test microorganisms was evaluated using broth microdilution method. Briefly, the test microorganisms (1×10^4 CFU/mL) were incubated with AgNPs diluted in MHB with the concentration gradients from 0.046–60 µg/mL. The wells not treated with AgNP was used as a control. The 96 micro-well plates were incubated at 37 ± 1 °C for 24 h. The first well without microbial growth was defined as the MIC, expressed in µg /mL. The tests were carried out in triplicate for sampling.

2.2.8. Statistical analysis

All data were given as mean \pm standard deviation and the results were expressed by repeated analyses. Cell culture analysis results were evaluated by one-way ANOVA (* $p < 0.05$) and considered statistically significant.

3. Results and Discussion

Firstly, the formation of silver nanoparticles was confirmed based on color change of the solution that usually occurs as a result of a chemical reaction. These reactions are usually based on a redox reaction and lead to the reduction of silver ions of AgNO₃ to form silver nanoparticles. The phenolic compound of *Betula* branches act as a reducing agent which resulted with formation of silver nanoparticles [34]. During these reduction reactions, the size, shape and arrangement of the nanoparticles change, leading to a marked change in their optical properties.

In this study we used three different AgNO₃ concentrations (1 mM, 3mM and 5 mM) to determine the color changes depending on the formation of silver nanoparticles. When the *Betula* branches extract was added to various AgNO₃ solutions color has changed from yellow to dark upon to AgNO₃ solution for 24 h at room temperature (Fig. 1A).

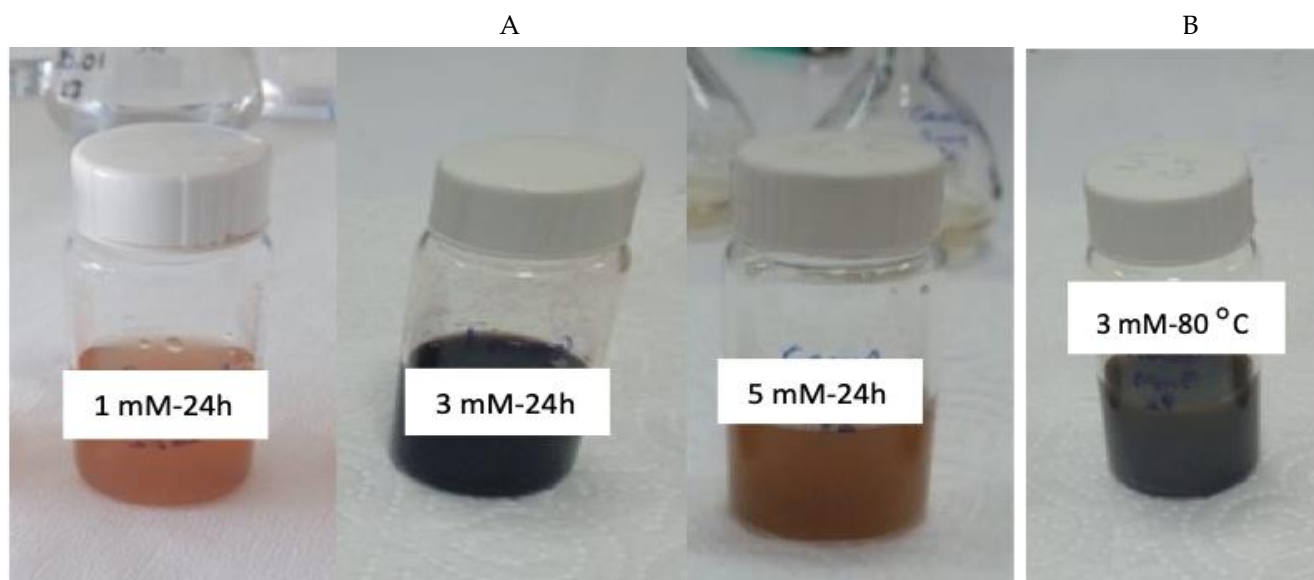


Figure 1. A. Color changes of *Betula* branches extract in the presence of various AgNO_3 concentrations (1 mM, 3 mM and 5mM) for 24 h at room temperature B. 3 mM AgNO_3 at 80°C (B3-4).

As shown in Fig. 1 the darker brown color was obtained by 3 mM AgNO_3 concentration (B3-4 formulation) at 24 h. The obtained darker color between the different concentrations indicated the biosynthesis of AgNPs by more reduction-induced silver nanoparticle formation by reducing silver ions to Ag^0 nanoparticles [36,37].

Also, the effect of the temperature on formation of AgNPs, the reaction was carried at 80 ° C which observed by also color changes. These results consistent with the previous reports that increasing temperature of the reaction mixture decreases largely the reaction times to 4 h (Fig. 1B) [38]. And this outcome suggesting that the nanoparticle size would be decrease to the same extent. These findings revealed that the phenolic compounds of the *Betula* branches exhibits reducing agent.

Formulations (B3-4 and B3-24) in which color change occurred depending on different temperature and silver nitrate concentrations were selected and continued with the following characterization method.

3.1. UV-Vis spectroscopy

Selected AgNPs were characterized for their structural analysis by UV-vis spectroscopy which is most commonly used analytical method. In this study, the reduction of AgNO_3 silver ions to the AgNPs in existence of *Betula* extract was analyzed by UV-Vis spectroscopy in the range of 200–800 nm. While the UV-Vis profile of *Betula* plant branches extract did not show any absorbance peak, the maximum absorbance peak was obtained at 425 nm with B3-4 formulation (Fig. 2). Among the various AgNO_3 concentrations, 3mM AgNO_3 treated extracts exhibited higher reduction activity. This may be due to the fact that only fixed *Betula* extract can

reduce the sufficient amount of AgNO_3 . These findings compatible with the literature that higher concentration of plant extracts introduce more reducing activity in the presence of higher AgNO_3 concentration [39].

The color changes and the presence of a sharp absorption peak at 425 nm also revealed the formation of AgNPs which related with the surface plasmon resonance (SPR) because of the release of free electrons [40]. Our results were also compatible with the previous reports that silver nanoparticles were formed in the range 420–430 nm according to UV-Vis spectroscopy technique [41–43]. The formation of selected AgNPs were verified depending on color changes by also UV-Vis spectroscopy.

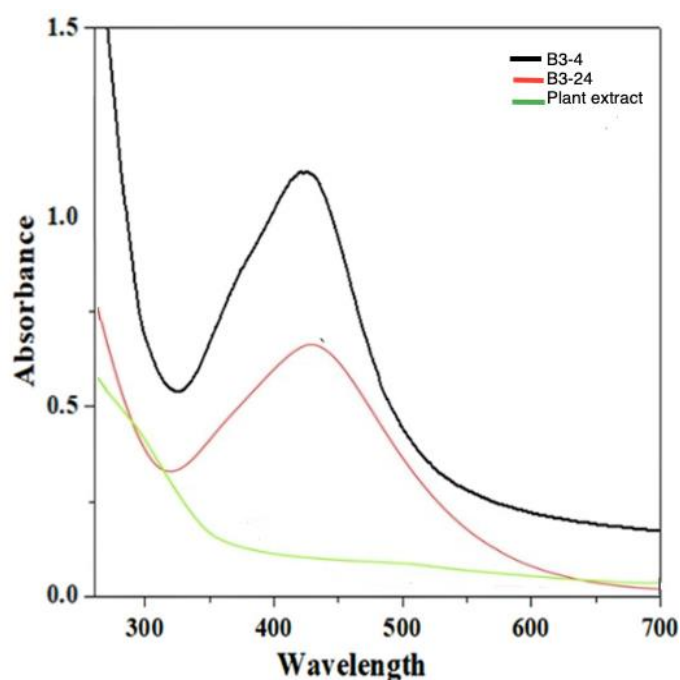


Figure 2. UV spectrum of the different *Betula* extracts according to synthesis temperature and AgNPs synthesized plant extract

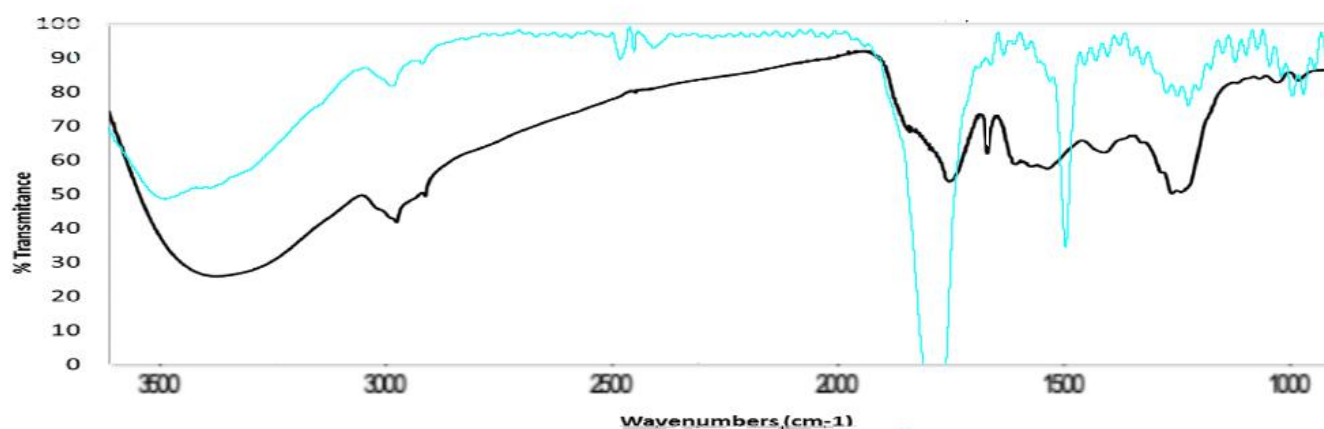


Figure 3. FTIR spectrum of *Betula* branches extract (Blank line) and AgNPs (Blue line)

3.2. Particle size analysis

In this study, AgNPs were synthesized based on the reducing power of the plant extract. However, there are various parameters that affect the physicochemical properties of nanoparticles synthesized with this method. In this study, the effect of initial AgNO_3 concentration on the mean particle size, zeta potential and distribution of AgNPs was evaluated. Next, the effect of reaction temperature on the size and preparation time was evaluated. Once the formation of colloidal AgNPs was confirmed by UV–vis spectroscopy, physicochemical properties of synthesized nanoparticles were analyzed by dynamic light scattering (DLS) method. Table 1 shows the synthesis conditions and physicochemical properties of AgNPs. As it can be clearly seen from the results, mean particle size and reaction time was significantly decreased by the increasement in reaction temperature. Therefore, formulation B3-4 was selected for further studies. Our results differed from the study that synthesized silver nanoparticles using aqueous extract of *Acacia cyanophylla*. In the study, relatively large nanoparticles were obtained when the reaction temperature increased from 35 °C to 100 °C [37]. Our results revealed that this synthesis method led to formation of monodispersed nanoparticles. The AgNPs demonstrated an acceptable particle uniformity indicating homogeneity. No shifts in dispersity of nanoparticles were observed with the increase of reaction temperature. The results were in agreement with those reported by Salvioni *et al* [44]. Nanoparticles were also evaluated in terms of zeta potential to determine the surface charge and the stability of nanoparticles. Results revealed that all formulations

were negatively charged and reaction temperature had no significant effect on zeta potential.

3.3. FT-IR analysis

Functional groups contained in phytocomponents in plant extracts are responsible for the reduction of silver ions to AgNP [41,42]. In this context, *Betula* is wealthy plant that contains tannis and other phenols with hydroxyl groups (-OH) which is responsible for bioformation of silver nanoparticles [35].

In present work, we used Fourier transform infrared (FTIR) spectroscopy analysis to identify the functional groups present in the *Betula* branches extract involved in the reduction and capping of silver nanoparticles. The FTIR spectrum of the *Betula* branches extract exhibited distinctive absorption peaks in the range of 800–1650 cm^{-1} . The determined characteristic fingerprint absorption peaks of *Betula* extract at 1628–1640 cm^{-1} are related with the phenolic components of plant extract such as lignin, as indicated previous literatures [45,46]. Also, the fingerprint peaks at 1440 cm^{-1} indicated the methyl groups and 1200 cm^{-1} indicated the alcohol groups. These alcohol groups which found in plant extract presents the bioreduction of silver ions to AgNPs.

The main absorption peaks which determined at 3400, 2934, 1728 and 1008 cm^{-1} has revealed the formation of AgNPs (Fig. 3). Our reported results were also compatible with earlier publications [47,48].

3.4. Scanning electron microscopy (SEM)

Morphological characterization of the biosynthesized AgNPs was also determined by using SEM technique. Fig. 4 showed SEM images of the B3-4 with particle sizes ranging between 60–90 nm. When the results were

Table 1 Physicochemical properties of AgNPs synthesized at different conditions. Data was represented as the mean \pm SEM values of three independent batches

Formulation code	AgNO_3 concentration	Reaction temperature	Reaction time	Size (nm)	Polydispersity index	Zeta potential (mV)
B3-24	3 mM	23 °C	24 h	117.7 \pm 14.4	0.28 \pm 0.09	-21.0 \pm 2.7
B3-4	3 mM	80 °C	4 h	103.2 \pm 5.2	0.26 \pm 0.01	-21.5 \pm 4.8

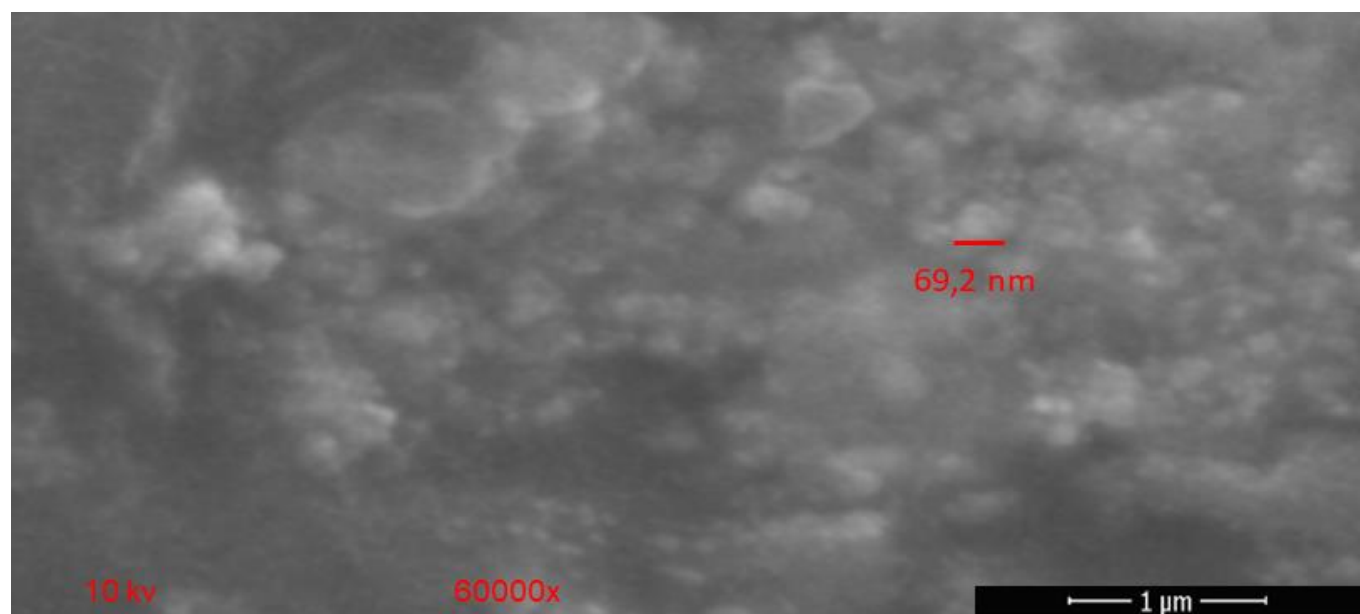


Figure 4. Scanning electron microphotographs of B3-4

compared to DLS method, the mean size of both biosynthesized nanoparticles were considerably smaller as a result of SEM analysis. In general, the size of nanoparticles determined by SEM analysis is approximately 20% smaller than those determined by the DLS method. The difference between the results regarding the size of the nanoparticles is due to the different analysis conditions of the two techniques. Through the DLS method, the average sizes of nanoparticles dispersed in liquid are analyzed. The presence of dispersants causes an increase in the size of the particles. SEM analysis is generally performed under vacuum and the sample must be dried during this process. Additionally, during SEM analysis, samples are usually coated with a thin metal layer. This coating process can lead to particle size reduction by sealing and flattening the surface of the particles [49]. Furthermore, when the morphology of the AgNPs was examined, it was seen that they exhibited spherical morphology. It also could be clearly observed that Ag-NPs partly aggregated.

3.5. Antiproliferative activity of AgNPs against HT-29 colorectal cancer cell

After characterization of the biosynthesized AgNPs, B3-4 formulation was evaluated for its cytotoxicity on malignant cells. For this purpose, HT-29 CRC cells were exposed to various concentrations of B3-4 AgNPs for 24 h and 48 h. After the indicated incubation period, MTT assay was performed to determine the half-maximal inhibitory concentration (IC_{50}). As it can be clearly seen in the Fig. 5, B3-4 AgNPs exhibited a dose and time-dependent cytotoxicity on HT-29 CRC cells. There was significant difference in cell viability between 24 hours and 48 hours incubation periods ($p < 0.05$). The IC_{50} value of B3-4 AgNPs was 64.27 $\mu\text{g/mL}$ after 48 h of treatment.

Our results corresponded well with the study, in which biosynthesized AgNPs were evaluated for the antiproliferative activity against HT-29 CRC cell [50]. Our results were also in agreement with the antiproliferative activity of AgNPs biosynthesized using *Acacia nilotica* extract against two colon cancer cell line [51]. Similar results were reported by Shathviha *et al* [52]. They reported that β -sitosterol mediated AgNPs induced concentration-dependent cytotoxicity in HT-29 cells. Our results are in contrast to research conducted by Durai *et al* [53]. They reported that lower concentration of AgNPs had an antiproliferative effect on both HT-29 and HCT15 CRC cells (IC_{50} : 8 $\mu\text{g/mL}$).

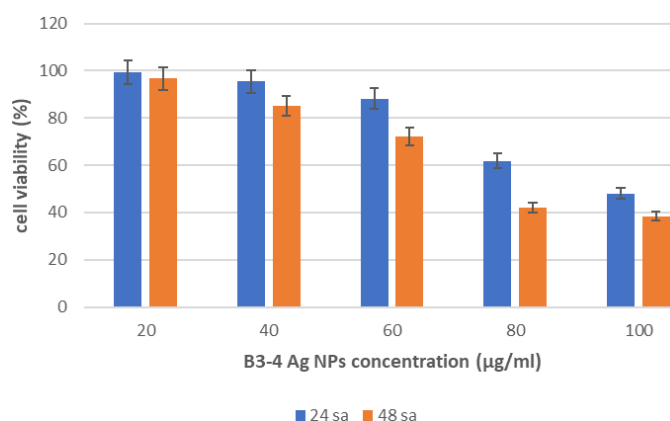


Figure 5. Determination of % cell viability of HT-29 CRC cells following treatment with different concentrations of B3-4 AgNPs

3.6. Biocompatibility of AgNPs

To evaluate the biocompatibility of B3-4 AgNPs, L929 mouse fibroblast cell line were exposed to various concentrations of nanoparticles. The effect of different concentrations of nanoparticles on L929 cell viability was determined with MTT assay. Fig. 6 showed the cell viability of L929 cells following 24 and 48 h incubation with B3-4 AgNPs.

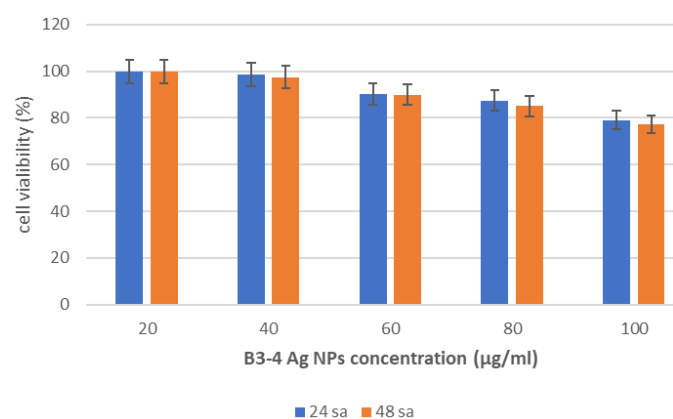


Figure 6. Determination of % cell viability of L929 cells following treatment with different concentrations of B3-4 AgNPs

The results clearly demonstrated that nanoformulations showed dose dependent toxicity. The IC_{50} value of B3-4 AgNPs was 142.67 $\mu\text{g}/\text{mL}$ after 48 h of treatment. Survival rate of L929 cells did not show significant difference between 24 h and 48 h incubation periods ($p > 0.05$). Our results was similar to the study in which biosynthesized AgNPs did not exhibit any harmful interaction to L929 mouse fibroblast cell line and the IC_{50} value was established as 64.5 $\mu\text{g}/\text{mL}$ [54].

3.7. Antibacterial and antifungal activity of AgNPs

Silver nanoparticles are important nanosized materials that exhibit a strong antimicrobial effect against both gram-positive and gram-negative bacteria. Various studies show that the antimicrobial potential of silver nanoparticles is effective on different types of bacteria. Previous studies showed that silver nanoparticles were effective on important Gram-positive pathogens such as *Staphylococcus aureus* and *Streptococcus pneumoniae* [55]. On the other hand, there are many studies showed that silver nanoparticles are effective on gram-negative species such as *Escherichia coli* and *Pseudomonas aeruginosa* [56]. Another striking feature about silver nanoparticles is that these nanoparticles have an antimicrobial effect even at low concentrations. For these reasons, silver nanoparticles synthesized by the green synthesis method were first screened by the disk-diffusion method for their antimicrobial activity. For this purpose, different concentrations of AgNPs were evaluated for inhibitory activity. As seen in Table 2, AgNPs showed significant zones of inhibition against all test organisms. AgNPs showed maximum inhibition zones of 18 mm, 19 mm, 11 mm, 20 mm and 20 mm in *Escherichia coli*, *Pseudomonas aeruginosa*, *Staphylococcus aureus*, *Enterococcus faecalis* and *Candida albicans*, respectively. The results revealed that *Enterococcus faecalis* and *Candida albicans* were the most susceptible strains against AgNPs whereas *Staphylococcus aureus* is the most resistant strain. AgNPs exhibited greater inhibition zones against *Pseudomonas aeruginosa* and *Staphylococcus aureus* compared to the reference

Table 2. The mean zone diameters of AgNPs as measured by disk diffusion method

Test microorganisms	Average zones of inhibition (mm)					
	AgNPs ($\mu\text{g}/\text{disk}$)				Gentamicin Fluconazole ($\mu\text{g}/\text{disk}$)	
	5	10	15	20	10	10
<i>Escherichia coli</i>	10	12	13	18	18	—
<i>Pseudomonas aeruginosa</i>	15	17	19	19	12	—
<i>Staphylococcus aureus</i>	3	8	9	11	20	—
<i>Enterococcus faecalis</i>	15	19	20	20	19	—
<i>Candida albicans</i>	12	14	17	20	—	15

antibiotic gentamicin. Our results were in agreement with the studies in which inhibitory effect of AgNPs was evaluated against *Escherichia coli* and *Pseudomonas aeruginosa* [57,58].

3.8. Minimal inhibitory concentration (MIC) of AgNPs against test microorganisms

Minimum Inhibitory Concentration (MIC), the lowest inhibitor concentration of B3-4 AgNPs, was determined by the microdilution method for the test microorganisms. Serial dilutions of the B3-4 AgNPs solution were prepared to adjust the concentrations in the range of 0.046–60 $\mu\text{g}/\text{mL}$. As seen in Table 3 MIC values for *Escherichia coli* and *Pseudomonas aeruginosa* were 3.75 $\mu\text{g}/\text{mL}$ and 1.875 $\mu\text{g}/\text{mL}$, respectively. A similar results were found in the research carried out by Panacek *et al*, in which *Escherichia coli* and *Pseudomonas aeruginosa* exposed to AgNPs with a mean size of 28 nm and MIC values was found 3.38 $\mu\text{g}/\text{mL}$ and 1.69 $\mu\text{g}/\text{mL}$, respectively [59]. The results were also in agreement with the study determined the MIC values of AgNPs against foodborne pathogens [60]. *Staphylococcus aureus* was found to be most tolerant isolate to B3-4 AgNPs with MIC value of 60 $\mu\text{g}/\text{mL}$. Our results were in contrast to previous study in which MIC value of AgNPs biosynthesized from lyophilized hydroalcoholic extract of *Syzygium cumini* against *Staphylococcus aureus* was 250 $\mu\text{g}/\text{mL}$ [61]. The result for *Candida albicans* showed that B3-4 AgNPs caused a slight decrease in yeast cell growth rates at low concentrations (0.12 $\mu\text{g}/\text{mL}$). A significant inhibitory effect was observed at high concentrations (15 $\mu\text{g}/\text{mL}$). Similar result was found in the research conducted by Arsène *et al*, in which MIC values of AgNPs ranged from 16 $\mu\text{g}/\text{mL}$ to 32 $\mu\text{g}/\text{mL}$ for clinical isolates of *Candida albicans* [62].

Table 3. The MIC values for the AgNPs prepared using *Betula*

Test microorganisms	MIC values ($\mu\text{g}/\text{mL}$)
<i>Escherichia coli</i>	3.75
<i>Pseudomonas aeruginosa</i>	1.875
<i>Staphylococcus aureus</i>	60
<i>Enterococcus faecalis</i>	0.94
<i>Candida albicans</i>	3.75

4. Conclusion

Green nanotechnology is an ecofriendly, low-cost and efficient method to synthesize the silver nanoparticles from biological components such as plants. In this scope, the silver nanoparticles were synthesized from the extract of *Betula* branches by bioreduction of silver ions. This is the first study for synthesis of AgNPs from *Betula* branches extract which collected from Van province, Türkiye. In this study *Betula* branch extract which is reachable in all seasons and rich in phenolic compounds, successfully reduced silver ions to silver nanoparticles and the presence of nanoparticles was confirmed by various characterization methods such as color change, UV-vis spectroscopy and FTIR analysis, particle size analysis and morphological analysis. The effect of AgNO₃ concentration and the temperature changes was evaluated in the scope of contribution to the formation of silver nanoparticles. Additionally, the antimicrobial activity and the anticancer efficiency studies have revealed that the green synthesized silver nanoparticles exhibit dose-dependent biological activity.

As a conclusion, the efficiency of silver nanoparticles obtained from a poorly studied plant part has been successfully demonstrated which can be used for further studies in terms of antimicrobial and anticancer properties.

References

- [1] S. Bayda, M. Adeel, T. Tuccinardi, M. Cordani, F. Rizzolio, The History of Nanoscience and Nanotechnology: From Chemical-Physical Applications to Nanomedicine, *Molecules*, 2020, PMC6982820.
- [2] M. K. Sahu, R. Yadav, S. P. Tiwari, Recent advances in nanotechnology, *International Journal of Nanomaterials, Nanotechnology and Nanomedicine*, 2023, 3492.000053.
- [3] H. Özcan, A. Dalmaz, M. Özdiğer, K. Zenkin, S. Durmuş, Biosynthesis and characterization of α -FeOOH nanoparticles using Isabella grape (*Vitis Labrusca L.*) extract, *Turk J Anal Chem*, 2023, 2687–6698.
- [4] S. Nimesh, *Nanotechnology: an introduction*, Gene Therapy, 2013, USA, Elsevier.
- [5] A. Afkhami, T. Madrakian, M. Ahmadi, Chapter - Nanotechnology and analytical chemistry, *Analytical Nanochemistry*, 2023, India, Elsevier.
- [6] A. Surendiran, S. Sandhiya, S.C. Pradhan, C. Adithan, Novel applications of nanotechnology in medicine, *Indian J Med Res*, 2009, A229530832.
- [7] U. Yezdani, M. G. Khan, N. Kushwah, A. Verma, F. Khan, Application of Nanotechnology in Diagnosis and Treatment of Various Diseases and Its Future, *World J Pharm Pharm Sci*, 2018, 2278 – 4357.
- [8] S. Zaib, J. Iqbal, *Nanotechnology: Applications, techniques, approaches, and the advancement in toxicology and environmental impact of engineered nanomaterials, Importance and Applications of Nanotechnology*, 2019, MedDocs Publishers LLC, USA.
- [9] W. Abdussalam-Mohammed, Review of Therapeutic Applications of Nanotechnology in Medicine Field and its Side Effects, *J Chem Reviews*, 2019.
- [10] S. Malik, K. Muhammad, Y. Waheed, *Emerging Applications of Nanotechnology in Healthcare and Medicine*, 2023, PMC10536529.
- [11] E. Abbasi, M. Milani, S. Fekri Aval, M. Kouhi, A. Akbarzadeh, H. Tayefi Nasrabadi, P. Nikasa, S.W. Joo, Y. Hanifehpour, K. Nejati-Koshki, M. Samiei, Silver nanoparticles: Synthesis methods, bio-applications and properties. *Crit Rev Microbiol*, 24937409.
- [12] K.C. Hembram, R. Kumar, L. Kandha, P.K. Parhi, C.N. Kundu, B.K. Bindhani, Therapeutic prospective of plant-induced silver nanoparticles: application as antimicrobial and anticancer agent, *Artif Cells Nanomed Biotechnol*, 2018, 30001158.
- [13] S.H. Lee, B.H. Jun, Silver Nanoparticles: Synthesis and Application for Nanomedicine. *Int J Mol Sci*, 2019, 3078156.
- [14] S.M. Mousavi, S.A. Hashemi, Y. Ghasemi, A. Atapour, A.M. Amani, A. Savar Dashtaki, A. Babapoor, O. Arjmand, Green synthesis of silver nanoparticles toward bio and medical applications: review study. *Artif Cells Nanomed Biotechnol*, 2018, 30328732.
- [15] L.M. Nieves, J.C. Hsu, K.C. Lau, A.D.A. Maidment, D.P. Cormode, Silver telluride nanoparticles as biocompatible and enhanced contrast agents for X-ray imaging: an in vivo breast cancer screening study, *Nanoscale*, 2021, 33325953.
- [16] A.S. Jain, P.S. Pawar, A. Sarkar, V. Junnuthula, S. Dyawanapelly, Bionanofactories for Green Synthesis of Silver Nanoparticles: Toward Antimicrobial Applications. *Int J Mol Sci*, 2021, 34769419.
- [17] A.S. Takamiya, D.R. Monteiro, L.F. Gorup, E.A. Silva, E.R. de Camargo, J.E. Gomes-Filho, S.H.P. de Oliveira, D.B. Barbosa, Biocompatible silver nanoparticles incorporated in acrylic resin for dental application inhibit *Candida albicans* biofilm, *Mat Sci Eng C-Mater*, 2021, 33254968.
- [18] I.A. Wani, T. Ahmad, A. Khosla, Recent advances in anticancer and antimicrobial activity of silver nanoparticles synthesized using phytochemicals and organic polymers, *Nanotechnology*, 2021, 34340224.
- [19] R.R. Miranda, I. Sampaio, V. Zucolotto, Exploring silver nanoparticles for cancer therapy and diagnosis. *Colloids and Surfaces B: Biointerfaces*, 2022, 34896692.
- [20] R. Sharma, N. Srivastava, Plant Mediated Silver Nanoparticles and Mode of Action in Cancer Therapy: A Review. *Anticancer Agents Medicinal Chem.* 2021, 33292139.
- [21] D. Kovács, N. Igaz, M.K. Gopisetty, M. Kiricsi, Cancer Therapy by Silver Nanoparticles: Fiction or Reality? *Int J Mol Sci*, 2022.
- [22] R.B. Patil, A. D. Chougale, Analytical methods for the identification and characterization of silver nanoparticles: A brief review, *Materialstoday: proceedings*, 2021.
- [23] A.C.D. Filho, J. de Jesus Soares, M.R.S. Carriço, G.P. Viçozzi, W.H. Flores, C.C. Denardin, R. Roehrs, E.L.G. Denardin, Green synthesis silver nanoparticles *Bougainvillea glabra* Choisy/LED light with high catalytic activity in the removal of methylene blue aqueous solution. *Environ Sci Pollut R*, 2023, 36547835.
- [24] M. Naveed, B. Bukhari, T. Aziz, S. Zaib, M.A. Mansoor, A.A. Khan, M. Shahzad, A.S. Dabool, M.W. Alruways, A.A. Almalki, A.S. Alamri, M. Alhomrani, Green Synthesis of Silver Nanoparticles Using the Plant Extract of *Acer oblongifolium* and Study of Its Antibacterial and Antiproliferative Activity via Mathematical Approaches, *Molecules*, 2022, 35807470.
- [25] M. Chandhru, R. Logesh, S. Kutti Rani, N. Ahmed, N. Vasimalai, Green synthesis of silver nanoparticles from plant latex and their antibacterial and photocatalytic studies, *Environ Technol*, 2022, 33825663.
- [26] N. Willian, S. Syukri, Z. Zulhadjri, H. Pardi, S. Arief, Marine plant mediated green synthesis of silver nanoparticles using mangrove *Rhizophorastylosa*: Effect of variable process and their antibacterial activity, *F1000Research*, 2022, 37359252.

- [27] M. Arif, R. Ullah, M. Ahmad, A. Ali, Z. Ullah, M. Ali, F.A. Al-Joufi, M. Zahoor, H. Sher, Green Synthesis of Silver Nanoparticles Using *Euphorbia wallichii* Leaf Extract: Its Antibacterial Action against Citrus Canker Causal Agent and Antioxidant Potential, *Molecules*, 2022, 35684463.
- [28] U. Habib, A. Ahmad Khan, T.U. Rahman, M.A. Zeb, W. Liaqat, Green synthesis, characterization, and antibacterial activity of silver nanoparticles using stem extract of *Zanthoxylum armatum*, *Microsc Res Techniq*, 2022, 36125078. Epub 2022 Sep 20.
- [29] E. Dekker, P.J. Tanis, J.L.A. Vleugels, P.M. Kasi, M.B. Wallace, Colorectal cancer, *Lancet*, 2019, 31631858.
- [30] F. Baidoun, K. Elshiyw, Y. Elkerai, Z. Merjaneh, G. Khoudari, M.T. Sarmini, M. Gad, M. Al-Husseini, A. Saad, Colorectal Cancer Epidemiology: Recent Trends and Impact on Outcomes, *Curr Drug Targets*, 2021, 33208072.
- [31] R. Sinha, Colorectal cancer, *Clin Radiol*, 2021, 34579868.
- [32] D. Penkov, V. Andonova, D. Delev, I. Kostadinov, M. Kassarova, Antioxidant Activity of Dry Birch (*Betula Pendula*) Leaves Extract, *Folia Medica*, 2018, 31188766.
- [33] Y.A. Heo, Birch Bark Extract: A Review in Epidermolysis Bullosa, *Drugs*, 2023, 37658982.
- [34] S. Hradilova, A. Panacek, R. Zboril, Green Synthesized Silver Nanoparticles Derived From an Extract of the *Betula Pendula* Tree, *Nanocon*, Oct 17-19, Brno, 2018, Czech Republic.
- [35] P. Devaraj, P. Kumari, C. Aarti, A. Renganathan, Synthesis and Characterization of Silver Nanoparticles Using Cannonball Leaves and Their Cytotoxic Activity against MCF-7 Cell Line, *J Nanotechnol*, 2013, 598328.
- [36] S. Azizi, F. Namvar, M. Mahdavi, M.B. Ahmad, R. Mohamad, Biosynthesis of Silver Nanoparticles Using Brown Marine Macroalga, *Sargassum Muticum* Aqueous Extract, *Materials*, 2013, 28788431.
- [37] J. Jalab, W. Abdelwahed, A. Kitaz, R. Al-Kayali, Green synthesis of silver nanoparticles using aqueous extract of *Acacia cyanophylla* and its antibacterial activity, *Heliyon*, 2021, 2405–8440.
- [38] Z. E. Jiménez Pérez, R. Mathiyalagan, J. Markus, Y. Kim, H.M. Kang, R. Abbai, K.H. Seo, D. Wang, V. Soshnikova, D.C Yang, Ginseng-berry-mediated gold and silver nanoparticle synthesis and evaluation of their in vitro antioxidant, antimicrobial, and cytotoxicity effects on human dermal fibroblast and murine melanoma skin cell lines. *Int J Nanomed*, 2017, 12:709–723.
- [39] E. F. Apriani M. Mardiyanto, A. Hendrawan, Optimization of Green Synthesis of Silver Nanoparticles From *Areca Catechu* L. Seed Extract With Variations of Silver Nitrate and Extract Concentrations Using Simplex Lattice Design Method, *Farmacia*, 2022.
- [40] M. Bilal, T. Rasheed, H.M.N. Iqbal, C. Li, H. Hu, X. Zhang, Development of silver nanoparticles loaded chitosan-alginate constructs with biomedical potentialities. *Int J Biol Macromol*, 2017, 28705499.
- [41] S. Jain, M.S. Mehata, Medicinal Plant Leaf Extract and Pure Flavonoid Mediated Green Synthesis of Silver Nanoparticles and their Enhanced Antibacterial Property, *Sci Rep*, 2017, 29158537.
- [42] G. Shumi, T.B. Demissie, R. Eswaramoorthy, R.F. Bogale, G. Kenasa, T. Desalegn, Biosynthesis of Silver Nanoparticles Functionalized with Histidine and Phenylalanine Amino Acids for Potential Antioxidant and Antibacterial Activities, *ACS Omega*, 2023, 37457474.
- [43] K. Anandalakshmi, J. Venugobal, V. Ramasamy, Characterization of silver nanoparticles by green synthesis method using *Pedaliun murex* leaf extract and their antibacterial activity, *Appl Nanoscience*, 2016.
- [44] L. Salvioni, E. Galbiati, V. Collico, G. Alessio, S. Avvakumova, F. Corsi, P. Tortora, D. Prosperi, M. Colombo, Negatively charged silver nanoparticles with potent antibacterial activity and reduced toxicity for pharmaceutical preparations, *Int J Nanomed*, 2017, 28408822.
- [45] A. Casas, M. Virginia Alonso, M. Oliet, E. Rojo, F. Rodríguez, FTIR analysis of lignin regenerated from *Pinus radiata* and *Eucalyptus globulus* woods dissolved in imidazolium-based ionic liquids, *J Chem Technol Biot*, 2012, 472–480.
- [46] H. Yang, R. Yan, H. Chen, D. H. Lee, C. Zheng. Characteristics of hemicellulose, cellulose and lignin pyrolysis, *Fuel*, 2007.
- [47] K. Raja, A. Saravanakumar, R. Vijayakumar, Efficient synthesis of silver nanoparticles from *Prosopis juliflora* leaf extract and its antimicrobial activity using sewage, *Spectrochim Acta A*, 2012, 490–494.
- [48] P.R. Rathi Sre, M. Reka, R. Poovazhagi, M. Arul Kumar, K. Murugesan, Antibacterial and cytotoxic effect of biologically synthesized silver nanoparticles using aqueous root extract of *Erythrina indica* lam, *Spectrochim Acta A*, 2015, 1137–1144.
- [49] T. G. F. Souza, V. S. T. Ciminelli, N. D. S. Mohallem, A comparison of TEM and DLS methods to characterize size distribution of ceramic nanoparticles, *Journal of Physics: Conference Series*, 29 November-2 December, 2016, Bento Gonçalves, Brazil.
- [50] J. Bao, Z. Jiang, W. Ding, Y. Cao, L. Yang, J. Liu, Silver nanoparticles induce mitochondria-dependent apoptosis and late non-canonical autophagy in HT-29 colon cancer cells, *Nanotechnol Rev*, 2022, 1781–1788.
- [51] N.S. Alduraihem, R.S. Bhat, S.A. Al-Zahrani, D.M. Elnagar, H.M. Alobaid, M.H. Daghestani, Anticancer and Antimicrobial Activity of Silver Nanoparticles Synthesized from Pods of *Acacia nilotica*, *Processes*, 2023.
- [52] P.C. Shathviha, D. Ezhilarasan, S. Rajeshkumar, J. Selvaraj, β -sitosterol Mediated Silver Nanoparticles Induce Cytotoxicity in Human Colon Cancer HT-29 Cells, *Avicenna J Med Biotechnol*, 2021, 33680372.
- [53] P. Durai, A. Chinnasamy, B. Gajendran, M. Ramar, S. Pappu, G. Kasivelu, A. Thirunavukkarasu, Synthesis and characterization of silver nanoparticles using crystal compound of sodium parahydroxybenzoate tetrahydrate isolated from *Vitex negundo*. L leaves and its apoptotic effect on human colon cancer cell lines, *Eur J Med Chem*, 2014, 25016231.
- [54] M. Składanowski, P. Golinska, K. Rudnicka, H. Dahm, M. Rai, Evaluation of cytotoxicity, immune compatibility and antibacterial activity of biogenic silver nanoparticles, *Med Microbiol Immunol*, 2016, 7620485.
- [55] F.M. Aldayel, M.S. Alsobeg, A. Khalifa, In vitro antibacterial activities of silver nanoparticles synthesised using the seed extracts of three varieties of *Phoenix dactylifera*, *Brazilian J Biol*, 2022, 34346959.
- [56] O.M. Bondarenko, M. Sihtmäe, J. Kuzmičiova, L. Ragelienė, A. Kahru, R. Daugelavičius, Plasma membrane is the target of rapid antibacterial action of silver nanoparticles in *Escherichia coli* and *Pseudomonas aeruginosa*, *Int J Nanomed*, 2018, 30498344.
- [57] M. Adil, T. Khan, M. Aasim, Evaluation of the antibacterial potential of silver nanoparticles synthesized through the interaction of antibiotic and aqueous callus extract of *Fagonia indica*, *AMB Express*, 2019.
- [58] M.A. Al Mashud, M. Moinuzzaman, M.S. Hossain, Green synthesis of silver nanoparticles using *Cinnamomum tamala* (Tejpata) leaf and their potential application to control multidrug resistant *Pseudomonas aeruginosa* isolated from hospital drainage water, *Heliyon*, 2022, 35855998.
- [59] A. Panáček, L. Kvítek, M. Směkalová, Bacterial resistance to silver nanoparticles and how to overcome it, *Nat Nanotechnol*, 2018, 29203912.
- [60] M. Zarei, A. Jamnejad, E. Khajehali, Antibacterial effect of silver nanoparticles against four foodborne pathogens. *Jundishapur J Microb*, 2014, 25147658.
- [61] W.L.C. Bernardo, M.F.G. Boriollo, C.C. Tonon, Biosynthesis of silver nanoparticles from *Syzygium cumini* leaves and their

potential effects on odontogenic pathogens and biofilms, *Frontier Microbiol*, 2022, 36246249.

- [62] M.M.J. Arsène, P.I. Viktorovna, M. Alla, Antifungal activity of silver nanoparticles prepared using Aloe vera extract against *Candida albicans*. *Veterinary World*, 2023, 36855352.

